

# Construction and noise behaviour of ultra-stable optical systems for space interferometers

Von der Fakultät für Mathematik und Physik der  
Gottfried Wilhelm Leibniz Universität Hannover  
zur Erlangung des Grades

**Doktorin der Naturwissenschaften**  
**- Dr. rer. nat -**

genehmigte Dissertation  
von

**Dipl. -Phys. Marina Dehne**  
geboren am 25. Mai 1981 in Hannover

2012

Referent: Prof. Dr. Karsten Danzmann  
Korreferent: Prof. Dr. Christian Ospelkaus  
Tag der Promotion: 16.11.2012



# Abstract

This thesis is written in the context of the space missions LISA and GRACE follow-on. The Laser Interferometer Space Antenna (LISA) is a space-borne interferometric gravitational wave detector, which aims to survey the low-frequency gravitational wave sky from 0.1 mHz to 1 Hz. A follow-on mission for the Gravity Recovery and Climate Experiment (GRACE), on the other hand, aims to monitor the spatial and time variable of Earth's gravity field with an unprecedented accuracy. Both missions rely on ultra-stable optical systems capable of measuring tiny displacements with picometre and nanometre resolution, respectively.

In the framework of this thesis, several stable optical benches were developed by applying the hydroxide-catalysis bonding technique in combination with a suitable Coordinate Measuring Machine. One optical system was used to experimentally demonstrate the compatibility of polarising interferometry for LISA. Various noise sources were experimentally investigated and successfully suppressed. A displacement sensitivity of better than  $1 \text{ pm}/\sqrt{\text{Hz}}$  for frequencies from 3 mHz to 1 Hz was demonstrated. The noise investigations were extended throughout this work with respect to thermally induced phase noise and periodic phase errors. As an alternative, several noise sources were subtracted in data post-processing. It was shown that under non-ideal conditions it was still possible to reach the required noise performance, which leads to an improved robustness for satellite missions.

The phase measurement systems of space-based laser interferometer need to be able to cope with large dynamic ranges of the order of  $10^9$ . Thus, the readout is based on a tracking phase measurement system implemented as a digital PLL on an FPGA. Research carried out was devoted on the optical linearity tests of such systems. An optical bench consisting of three identical and symmetric interferometers in a hexagonal configuration has been developed and the experimental investigations are described in detail.

A basis for ultra-stable optical systems to be used in future space-based gravity measurements at the the Huazhong University of Science and Technology in Wuhan, China, has been provided. The construction of a prototype test bench combining two heterodyne Mach-Zehnder interferometer and the initial results are presented.

Keywords: gravitational waves, interferometry, hydroxide-catalysis bonding



# Kurzzusammenfassung

Die vorliegende Arbeit wurde im Rahmen der Weltraummissionen LISA und der GRACE Nachfolgermission verfasst. LISA (Laser Interferometer Space Antenna) ist ein weltraum-gestützter interferometrischer Gravitationswellendetektor, der es zum Ziel hat, Gravitationswellen im Frequenzbereich zwischen 0.1 mHz und 1 Hz zu detektieren. Die GRACE (Gravity Recovery and Climate Experiment) Nachfolgermission dagegen hat das Ziel, die räumliche und zeitliche Variable des Erdschwerefeldes mit einer bisher unerreichten Genauigkeit zu beobachten. Beide Missionen erreichen ihr Ziel durch eine präzise Messung von Längenänderungen und sind daher auf ultra-stabile optische Systeme angewiesen. Diese müssen in der Lage sein, winzige Längenunterschiede pikometer- bzw. nanometergenau zu messen.

Im Laufe dieser Arbeit wurden mit Hilfe der sogenannten *hydroxide-catalysis bonding* Technik in Kombination mit einer Koordinaten-Messmaschine mehrere quasi-monolitische optische Bänke hergestellt. Ein so aufgebautes optisches System wurde verwendet, um experimentell zu zeigen, dass polarisierende Interferometrie mit den technischen Anforderungen der LISA Mission vereinbar ist. Verschiedene Rauschquellen wurden experimentell untersucht und erfolgreich unterdrückt. Eine Stabilität von besser als  $1 \text{ pm}/\sqrt{\text{Hz}}$  für Frequenzen zwischen 3 mHz und 1 Hz wurde erreicht. Weiterhin wurden periodische Nichtlinearitäten und thermisch induziertes Phasenrauschen untersucht. Beide Effekte werden detailliert in der Arbeit beschrieben. Als Alternative zu einer aktiven Rauschunterdrückung wurden mehrere Subtraktionsmodelle überprüft. Es hat sich gezeigt, dass es auch unter nicht idealen Bedingungen möglich ist, die anspruchsvollen Anforderungen zu erreichen. Diese Erkenntnis führt zu einer verbesserten Robustheit bei Satellitenmissionen.

Laser Interferometer werden mit einem digitalen Phasemeter ausgelegt, welches in der Lage sein muss, mit einem großen dynamischen Bereich der Größenordnung von  $10^9$  fertig zu werden. Ein Teil dieser Arbeit behandelt die optische Untersuchung der Linearität solcher Phasemeter. Dafür wurde eine optische Bank, bestehend aus drei identischen, symmetrischen Interferometern in einer hexagonalen Konfiguration hergestellt. Ablauf und Verfahren der Herstellung der Bank, sowie deren experimentelle Untersuchung sind Teil dieser Arbeit.

Im Rahmen dieser Arbeit wurde an der der Huazhong University of Science

---

and Technology in Wuhan (China) die Grundlage für den Aufbau von ultra-stabilen optischen Systeme geschaffen. Diese sollen zukünftig dafür verwendet werden, weltraum-gestützte Messungen des Erdschwerefeldes durchzuführen. Der Bau eines quasi-monolitischen Prototypen, bestehen aus zwei heterodynem Mach-Zehnder-Interferometern, und ersten Ergebnisse werden vorgestellt.

Schlüsselwörter: Gravitationswellen, Weltrauminterferometrie, Silicate Bonden

# Contents

<b>Abstract</b>	<b>i</b>
<b>Kurzzusammenfassung</b>	<b>iii</b>
<b>Contents</b>	<b>v</b>
<b>List of Figures</b>	<b>ix</b>
<b>List of Tables</b>	<b>xiii</b>
<b>List of Abbreviations</b>	<b>xvii</b>
<b>1. Introduction</b>	<b>1</b>
1.1. Space-borne laser metrology systems . . . . .	3
LISA . . . . .	3
LISA Pathfinder . . . . .	4
GRACE follow-on . . . . .	5
1.2. Outline of this thesis . . . . .	6
<b>Part I: Alignment strategies and construction methods for precision interferometers</b>	<b>9</b>
<b>2. Techniques for alignment and construction of precision interferometers</b>	<b>11</b>
2.1. Hydroxide-catalysis bonding process . . . . .	12
2.2. Template bonding . . . . .	15
2.3. Precision bonding . . . . .	19
2.3.1. Alignment tool . . . . .	19
2.3.2. Coordinate measuring machine . . . . .	20
2.3.3. The coordinate frames . . . . .	23
2.3.4. Adjustable bonding . . . . .	25
2.3.5. Adjuster aided bonding to heterodyne signals . . . . .	27
2.4. Appraisal of achievable accuracies . . . . .	29

<b>3. Absolute metrology of beam propagation axis</b>	<b>33</b>
3.1. Measurement principle of a CQP . . . . .	36
3.2. CQP design . . . . .	38
3.3. CQP architecture . . . . .	40
3.4. Calibration . . . . .	41
3.4.1. Calculation of the beam direction . . . . .	47
3.4.2. Calculation of the beam centroid . . . . .	48
3.4.3. Repeatability of the calibration . . . . .	50
3.5. Reliability of the CQP . . . . .	54
3.6. Conclusion . . . . .	57
<b>Part II: Verification of polarising optics for heterodyne interferometry</b>	<b>59</b>
<b>4. Design, analysis and construction of the test bed</b>	<b>61</b>
4.1. Periodic non-linearities . . . . .	65
4.2. Design . . . . .	74
4.2.1. Stray light analysis . . . . .	78
4.2.2. Properties of the optical components . . . . .	85
4.3. Description of the experimental setup . . . . .	87
4.4. First experimental setup based on an aluminium baseplate . . . . .	89
4.5. Quasi-monolithic setup . . . . .	93
4.6. Characterisation of the optical bench . . . . .	99
4.7. Summary . . . . .	102
<b>5. Experimental investigations</b>	<b>103</b>
5.1. Characterisation of phase measurement noise . . . . .	104
5.2. Reduction of environmental influences . . . . .	106
5.3. Beam pointing fluctuations . . . . .	110
5.4. Reduction of sideband-induced noise . . . . .	113
5.5. Control of the polarisation state stability . . . . .	115
5.6. Impact of frequency noise on longitudinal phase noise . . . . .	117
5.7. Impact of laser intensity noise . . . . .	121
5.8. Noise performance . . . . .	123
5.9. Periodic phase errors . . . . .	125
5.10. Summary . . . . .	127
<b>6. Performance investigations in data post-processing</b>	<b>129</b>
6.1. Subtraction of spurious beat note signals . . . . .	129
6.2. Laser frequency noise subtraction . . . . .	134
6.3. Amplitude noise subtraction . . . . .	137

6.4. Angular noise subtraction . . . . .	138
6.5. Impact of temperature fluctuations . . . . .	139
6.5.1. Temperature noise subtraction . . . . .	140
6.5.2. Coupling factor between temperature of PBS and longitudinal phase signal . . . . .	141
6.6. Resulting noise performance . . . . .	144
<b>7. Conclusion</b>	<b>147</b>
<b>Part III: The way towards an ultimate phasemeter test</b>	<b>149</b>
<b>8. Assembly of a hexagonal interferometer for optically testing a phase measurement system</b>	<b>151</b>
8.1. Design of the prototype optical bench . . . . .	153
8.1.1. Design considerations . . . . .	153
8.1.2. Layout of a hexagonal optical bench . . . . .	154
8.1.3. Properties of components used . . . . .	157
8.2. Construction . . . . .	159
8.2.1. Input beam alignment . . . . .	159
8.2.2. Alignment of the template . . . . .	160
8.2.3. Alignment of less critical components . . . . .	162
8.2.4. Alignment of the beam combiners . . . . .	162
8.3. Description of the experimental setup . . . . .	163
8.3.1. Phase measurement system . . . . .	164
8.3.2. Digital offset frequency lock . . . . .	165
8.3.3. ADC time jitter noise . . . . .	167
8.4. Noise performance . . . . .	168
8.5. Beam pointing fluctuations . . . . .	169
8.6. Conclusion and Outlook . . . . .	170
<b>Part IV: Ultra-stable interferometers for future geodesy missions</b>	<b>173</b>
<b>9. Joint efforts towards a transponder-type intersatellite laser ranging system</b>	<b>175</b>
9.1. Laboratory facilities . . . . .	177
9.2. The quasi-monolithic interferometer design . . . . .	177
9.3. Manufacturing process . . . . .	180
9.3.1. Alignment of non-critical components . . . . .	180
9.3.2. Alignment of critical components . . . . .	183

9.4. Characterisation of the optical bench . . . . .	187
9.5. Description of the experimental setup . . . . .	188
9.6. Initial noise performance . . . . .	190
9.7. Conclusion . . . . .	191
<b>10. Summary and Conclusion</b>	<b>193</b>
<b>Part V: Appendices</b>	<b>197</b>
<b>A. CMM measurement strategies</b>	<b>199</b>
A.1. Probing strategy . . . . .	199
A.2. Alignment strategy . . . . .	200
<b>B. Measurement uncertainty for Coordinate Measuring Systems</b>	<b>203</b>
B.1. Sources of CMM uncertainties . . . . .	206
B.2. Performance evaluation . . . . .	211
<b>C. CMM measurement program for adjustable bonding</b>	<b>217</b>
<b>D. Alignment plan</b>	<b>227</b>
<b>Bibliography</b>	<b>231</b>
<b>List of publications</b>	<b>243</b>
<b>Acknowledgements</b>	<b>245</b>
<b>Curriculum Vitae</b>	<b>247</b>



# List of Figures

1.1. Schematic of LISA orbit . . . . .	3
1.2. LISA Satellite . . . . .	4
1.3. LISA Pathfinder Satellite . . . . .	4
1.4. Photograph of the LTP. . . . .	4
1.5. GRACE with the Earth's gravity field . . . . .	5
1.6. Schematic of GFO . . . . .	7
2.1. Bonding procedure . . . . .	13
2.2. Degrees of freedom: 'in-plane' and 'out-of-plane' . . . . .	15
2.3. CAD drawing of a template model . . . . .	16
2.4. Bonding template for the non-critical components . . . . .	17
2.5. Alignment tool combined with its bridge . . . . .	18
2.6. CAD model of the alignment tool . . . . .	19
2.7. Photograph of the CMM . . . . .	21
2.8. Measuring process with the CMM . . . . .	22
2.9. The defined coordinate systems . . . . .	24
2.10. Illustration of moving mark and reference point . . . . .	25
2.11. Alignment procedure for adjustable bonding . . . . .	27
2.12. Three-point-reference for a beam combiner. . . . .	28
3.1. Illustration of beam alignment in the normal way . . . . .	34
3.2. Schematic of a quadrant photodiode . . . . .	34
3.3. Schematic of beam with a Gaussian transverse irradiance profile . . . . .	35
3.4. Principle of the CQP . . . . .	36
3.5. Photograph of the hexapod . . . . .	37
3.6. OptoCad model of the calibrated quadrant photodiode pair . . . . .	38
3.7. CAD model of the CQP . . . . .	39
3.8. Photograph of the final CQP . . . . .	40
3.9. Schematic of desired offset parameters at CQP calibration . . . . .	41
3.10. Schematic of auxiliary coordinate frames for the CQP . . . . .	42
3.11. Calibration: first step . . . . .	44
3.12. Calibration: second step . . . . .	45
3.13. Calibration: third step . . . . .	45
3.14. Flow chart of the calibration . . . . .	46

3.15. Residuals of a set of calibrations (one day) . . . . .	51
3.16. Drifts in the calibration parameters as a function of time . . . . .	54
3.17. Principle: CQP measurements along a beam . . . . .	55
3.18. Verifying CQP accuracy: measurements along a beam . . . . .	56
4.1. Current design of the LISA elegant breadboard (EBB) . . . . .	62
4.2. Two possibilities for test mass readout . . . . .	63
4.3. Two possibilities for beam separation in the science interferometer	63
4.4. Baseline design for a future geodesy mission . . . . .	65
4.5. Phase vs. travelled distance in an non-ideal interferometer . . . . .	66
4.6. Michelson setup to discuss non-linearities . . . . .	67
4.8. Polarisation mixing in a heterodyne interferometer . . . . .	69
4.9. Beam components: polarisation and frequency mixing . . . . .	69
4.10. Phasor diagram of the first and second harmonic non-linearity . . . . .	71
4.11. Analysis of non-linearity on the LISA EBB . . . . .	73
4.12. OptoCad models of the polifo part I . . . . .	76
4.13. OptoCad models of the polifo part II . . . . .	77
4.14. Stray light analysis of the optical bench made with OptoCad. . . . .	79
4.15. Ratio of ghost beams to beat signal @ $PD_{\text{npol}}$ . . . . .	80
4.16. Ratio of ghost beams to beat signal @ $PD_{\text{pol}}$ . . . . .	81
4.17. Stray light sources of the polarising interferometer . . . . .	82
4.18. Stray light analysis including wedged components . . . . .	84
4.19. Influence of wedged optics onto the path length noise . . . . .	85
4.20. Deformation analysis of a 50 mm thickness Clearceram <sup>®</sup> bench . . . . .	86
4.21. Schematic of the modulation bench . . . . .	88
4.22. Photograph of the modulation bench . . . . .	89
4.23. Schematic of the optical bench based on aluminium. . . . .	90
4.24. Photograph of the initial setup based on aluminium . . . . .	91
4.25. Displacement noise performed with the initial interferometer . . . . .	92
4.26. Glueing the fibre injectors (polifo) . . . . .	95
4.27. Photograph of the fibre injector assembly . . . . .	96
4.28. Photographs of several cleaning processes . . . . .	97
4.29. A selection of adjustable bonded optical components . . . . .	97
4.30. Photograph of the polarising components on the optical bench. . . . .	98
4.31. Photographs of the alignment of a beam combiner . . . . .	99
4.32. Final bonded optical bench (polifo) . . . . .	100
5.1. Photograph of the hardware-based phasemeter (PM3) . . . . .	105
5.2. Comparison of phasemeter noise using different input signal levels	106
5.3. Photograph of the vacuum chamber and the thermal shield . . . . .	107
5.4. Interferometer performance with and without vacuum and TS . . . . .	108
5.5. Temperature measurements in- and outside the vacuum chamber	109

5.6. Implementation of the optical bench in its vacuum environment	110
5.7. Beam pointing fluctuations within the polarising interferometer	111
5.8. DWS coupling coefficients . . . . .	112
5.9. Minimising electronic cross-talk . . . . .	113
5.10. Interferometer performance with and without an OPD stabilisation	114
5.11. Time series of OPD fluctuations . . . . .	115
5.12. Spectral densities of OPD fluctuations with/without stabilisation	115
5.13. Interferometer performance with/without polarisation control .	116
5.14. Polarisation measurements of optical fibres . . . . .	117
5.15. Free-running laser frequency noise along with reached stability.	118
5.16. Open loop gain of the frequency stabilisation . . . . .	119
5.17. Interferometer performance with/without frequency stabilisation	120
5.18. Relative intensity noise with DC stabilisation and without . . .	121
5.19. Interferometer performance with/without DC noise stabilisation	122
5.20. Schematic of the actual experimental setup . . . . .	123
5.21. Interferometer performance with/without DC noise stabilisation	124
5.22. Performance comparison of both measurement interferometers .	125
5.23. Photograph of the non-linearity experiment . . . . .	126
5.24. Comparison between measured and PZT displacement . . . . .	127
6.1. Phasor diagram: principle of balanced detection . . . . .	130
6.2. Interferometer performance with/without stray light correction I	132
6.3. Interferometer performance with/without stray light correction II	133
6.4. Noise performance with/without frequency noise correction . .	135
6.5. Example: Frequency stability and RIN . . . . .	136
6.6. Performance with laser intensity and angular noise correction .	137
6.7. Example: Angular noise subtraction . . . . .	138
6.8. Example: Angular noise and thermal stability . . . . .	139
6.9. Performance with/without temperature noise correction . . . .	140
6.10. Photograph of the polarising components on the optical bench.	141
6.11. Sketch of transmission and reflection at the PBS while heated .	142
6.12. Final noise performance with corrections applied in data post- processing . . . . .	144
6.13. Final noise performance with actively stabilisations and data corrections applied in data post-processing . . . . .	145
8.1. Schematic of electrical linearity test of PMS . . . . .	152
8.2. Stray light in an hexagonal layout with rectangular BS . . . . .	154
8.3. Iterative procedure towards an optimum hexagonal layout . . .	155
8.4. Design and analysis of the hexagonal interferometer . . . . .	156
8.5. Deformation analysis of a 25 mm thickness Zerodur <sup>®</sup> bench . . .	157
8.6. Beam alignment: hexagonal interferometer . . . . .	158

8.7. Template used to position the BSs of the hexagonal interferometer	161
8.8. RBS alignment: hexagonal interferometer . . . . .	161
8.9. Photographs of the hexagonal interferometer bonded . . . . .	162
8.10. Experimental setup: hexagonal interferometer . . . . .	163
8.11. Schematic of one DPLL core . . . . .	164
8.12. Photograph of the PM used for the offset frequency lock . . . . .	165
8.13. Open loop gain of digital frequency lock . . . . .	166
8.14. Setup for ADC jitter correction . . . . .	167
8.15. Initial performance of the hexagonal interferometer . . . . .	168
8.16. Fibre injector assembly used at the hexagonal and polarising interferometer . . . . .	169
8.17. Comparison of raw DWS signals between polarising and hexag- onal interferometer . . . . .	170
9.1. Working environment at HUST . . . . .	176
9.2. OptoCad model of the test bed towards an inter-satellite laser ranging system. . . . .	178
9.3. Photograph of the template used . . . . .	179
9.4. Test facility for verifying the machining accuracy of the template	180
9.5. Evaluation of template accuracy: $\delta x$ . . . . .	181
9.6. Evaluation of template accuracy: $\delta y$ . . . . .	181
9.7. Gluing process of the fibre injector assemblies . . . . .	182
9.8. Beam alignment: part I . . . . .	183
9.9. Beam alignment: part II . . . . .	183
9.10. Assembly of the alignment tool used in China . . . . .	184
9.11. Photograph of the beam combiner alignment procedure: I . . . . .	185
9.12. Photograph of the beam combiner alignment procedure: II . . . . .	186
9.13. Block diagram showing the phasemeter used . . . . .	188
9.14. Non-linearity of the piezo used at HUST . . . . .	188
9.15. Noise performance of PMS (HUST) . . . . .	188
9.16. Photograph of the picometre positioning control system. . . . .	189
9.17. Displacement noise measured at HUST . . . . .	190
9.18. Displacement measurement for 50 pm step motions . . . . .	191
9.19. OptoCad model of a modified optical bench . . . . .	192
A.1. Strategy of defining a datum reference frame: manual . . . . .	201
A.2. Strategy of defining a datum reference frame: cnc . . . . .	201
B.1. Illustration of measurement uncertainty . . . . .	204
B.2. Sources of uncertainty: workpiece . . . . .	207
B.3. Sources of uncertainty: CMM . . . . .	208
D.1. Alignment plan (polifo) . . . . .	229

# List of Tables

3.1.	Computed normal vectors for calculating the beam direction . .	52
3.2.	Example of computed corners with their residuals . . . . .	53
3.3.	Angular errors of a CQP measurement . . . . .	57
4.1.	Stray light analysis PD <sub>npol</sub> . . . . .	80
4.2.	Stray light analysis PD <sub>pol</sub> . . . . .	81
4.3.	Accuracy characterisation of the bonded optical bench: I . . . .	101
4.4.	Characterisation of the beam combiner's position . . . . .	102
6.1.	Frequency coupling coefficients (polifo) . . . . .	134
9.1.	Accuracy characterisation of the bonded optical bench: II . . .	187
A.1.	Number of probing points required to define a particular geometry	200
A.2.	Two alignment strategies for a datum reference frame . . . . .	202
B.1.	Example of measurement uncertainty: adjuster . . . . .	212
B.2.	Example of measurement uncertainty: optical component . . . .	214
B.3.	Example of measurement uncertainty: CQP . . . . .	216



# List of Abbreviations

AAF	Anti-Aliasing Filter
ACF	Adjuster Coordinate Frame
ACF	Polarisation-maintaining AND Absorption-reducing
ADC	Analogue-to-Digital converter
AEI	Albert Einstein Institute (in Hannover)
AL	Aluminium
AR	Anti-Reflective
BS	Beam Splitter
CAD	Computer Aided Design
CMM	Coordinate Measuring Machine
CNC	Computer Numerical Control
CQP	Calibrated Quadrant Photodiode Pair
DAC	Digital-to-Analogue Converter
DAQ	Data Acquisition
DCC	Direct Computer Control
DFT	Discrete Fourier Transform
DMIS	Dimensional Measurement Interface Specification
DoF	Degree of Freedom
DPLL	Digital Phase-Locked Loop
DRS	Disturbance Reduction System
DTU	Technical University of Denmark
DWS	Differential Wavefront Sensing
EBB	Elegant Breadboard
ESA	European Space Agency
FFT	Fast Fourier Transform
FIOS	Fibre Injector Optical Sub-Assembly

FPGA	Fast Programmable Gate Array
GFO	(fast) GRACE Follow-on to be launched in 2017
GOCE	Gravity field and steady-state ocean circulation explorer
GRACE	Gravity Recovery And Climate Experiment
GRACE FO	GRACE Follow-on
GUI	Graphical User Interface
HCF	Hexapod Coordinate Frame
HV	High Voltage
IBS	ION-Beam Sputtering
ICF	IfoCad Coordinate Frame
ifo	Interferometer
JPL	Jet Propulsion Laboratory
LISA	Laser Interferometry Space Antenna
LMS	LISA Metrology System
LO	Local Oscillator
LP	Low-pass Filter
LPF	LISA Pathfinder
LPSD	Linear Power Spectral Density
LRI	Laser Ranging Interferometer
LTP	LISA Technology Package
LTPDA	LTP Data Analysis
MCS	Machine Coordinate System
MPE	Maximum Permissible Error
NASA	National Aeronautics and Space Administration
NCO	Numerically Controlled Oscillator
Nd:YAG	Neodymium-Doped Yttrium Aluminium Garnet
OB	Optical Bench
OBF	Optical Bench Frame
OPD	Optical Path length Difference
PBS	Polarising Beam Splitter
PC	Personal Computer



PD	Photodiode
PI	Physics Instruments
PI	Proportional-Integral (controller)
PIR	Phase Increment Register
PLL	Phase-Locked Loop
PMS	Phase Measurement System
pp	peak-to-peak
ppm	parts per million
QPD	Quadrant Photodiode
S/C	Spacecraft
SBDFt	single-bin Discrete Fourier Transform
TDI	Time Delay Interferometry
UGL	University of Glasgow
ULE	Ultra Low Expansion

*For the sake of clear reference, a measurement code (m-code) is introduced. This code will specify the measures and stabilisations performed as well as the applied noise subtraction models in post-processing. It is applied for all displacement measurements shown in Chapters 5 and 6.*

Reduction of external influences		Data post-processing	
Vacuum	V	Stray light	s
Thermal shield	T	Laser intensity noise	a
Polarisation control:	P	DWS	d
only on modulation bench	P <sub>M</sub>	Frequency noise	f
only on optical bench	P <sub>OB</sub>	Temperature noise	t
Active stabilisation		<i>Example: [m-code: VFs]</i>	
OPD	O	Measurement conducted in vacuum and actively frequency stabilised. The balance detection is applied in post-processing.	
Frequency fluctuations	F		
Intensity fluctuations	A		



## Chapter 1

# 1 Introduction

The first publication by Einstein on his General Theory of Relativity in 1916 [1] paved the way for the prediction of the existence of gravitational waves. A consequence of this theory was that any mass distribution with a time-dependent quadrupole or higher multipole moment will emit gravitational waves. These are perturbations in spacetime which propagate at the speed of light. A passing gravitational wave changes the local spacetime metric such that measured distances between free falling test masses will vary as a function of time. This relative change is extremely small, as General Relativity states that spacetime is an elastic but stiff medium meaning that in order to produce measurable differences from flat space in the metric, the associated quadrupole moment must be extremely large. The stiffness of spacetime will cause the gravitational wave signals to interact only very weakly with matter. Thus the gravitational waves will reach us virtually unperturbed from every part of the universe, leading to a unique insight into various astrophysical processes that cannot be obtained from electromagnetic radiation. Since the amplitude of a gravitational wave is related to the magnitude of the variations in the quadrupole moment, compact objects such as binary neutron stars and black holes are the most promising sources [2].

In the same year, long before laser technology came into being, Albert Einstein established also the theoretical foundations for the laser [3]. Einstein explored the process by a re-derivation of Planck's law of radiation. With his exploration of this process based on the probability coefficients also known as *Einstein coefficients* for the absorption, spontaneous emission, and stimulated emission of electromagnetic radiation, he provided the basis for later laser technology development. Einstein suggested that forcing radiation past a group of atoms stimulates them to release energy. This energy will travel in the direction of the stimulating source and be of the same frequency as the source.

It was, however, only after half a century that the optical laser was invented [4–6], now the workhorse in a broad field such as astrophysics and geoscience. Both make use of laser technology as a high precision metrology device. Such metrology systems use laser interferometers, capable of measuring a relative change in length between two points in space to a precision of a few picometre. In the field of astronomy they are used in order to directly detect gravitational waves. For this purpose a network of long-baseline laser interferometers serving as gravitational wave detectors are installed around the world, such as GEO 600 (German-British collaboration [7, 8]), LIGO (USA [9]), VIRGO (Italy [10]), TAMA 300 and CLIO (Japan [11, 12]). All detectors to date are based on Michelson-type kilometre-scale interferometers most of them with long Fabry-Perot resonant cavities as arms. Gravity gradient noise, induced by variations in the gravitational field of the Earth as well as seismic background noise restrict the measurement bandwidth of Earth-based detectors to frequencies above a few hertz (measurement band  $\approx 10$  to  $10^3$  Hz). Though going underground with the detectors would partly reduce the seismic noise and thus the gravity gradient noise [13], local excitations would still be a potential source of gravity gradient noise resulting in a sensitivity restriction for frequencies below a few Hz. Consequently, it is planned to build space-borne detectors capable of detecting gravitational waves in the low-frequency range, such as the Laser Interferometer Space Antenna.

Another highly demanding application of precision laser metrology can be found in the field of Earth observation. The Gravity Recovery and Climate Experiment (GRACE) has successfully demonstrated that inter-satellite microwave ranging enables monitoring the time variations of the Earth’s gravity field on a global scale [14]. For future gravity field missions it is desired not only to realise a long-term monitoring but also to improve the precision. The sensitivity of GRACE is mainly limited by accelerometer noise for frequencies between the orbit frequency ( $\sim 200$   $\mu$ Hz) and a few mHz, whilst above a few mHz the microwave system noise, primarily thermal noise in the receiver, dominates [15]. For this reason it is beneficial, if future GRACE-like missions will use interferometric laser ranging instead of microwave ranging. One of the main reasons for doing so is the significant reduction in operating wavelength (a factor of 10.000 w.r.t. to the microwave ranging system) and the resulting improved measurement accuracy. Thus it will be possible to detect much smaller changes, for instance in water mass distribution, and to enable a higher spatial resolution. However, using a smaller wavelength is connected to stringent requirements for beam pointing because of the lower beam divergence.

A consequence for space-borne missions based on laser interferometry is the

demand for ultra stable optical systems to survive the liability of damage during launch into orbit. The construction and noise behaviour of such systems is the main issue of this thesis. The following section provides a brief overview of the three satellite missions directly related to the work carried out throughout this thesis.

## 1.1. Space-borne laser metrology systems

### LISA:

The Laser Interferometer Space Antenna (LISA) is a space-borne interferometric gravitational wave detector [16, 17]. The goal of LISA is to survey the low-frequency gravitational wave sky from 0.1 mHz to 1 Hz and to detect individual astrophysical sources such as coalescing massive black holes, inspirals of stellar-mass black holes, ultra compact Galactic binaries and possibly unforeseen sources such as relic radiation from the early Universe [18].

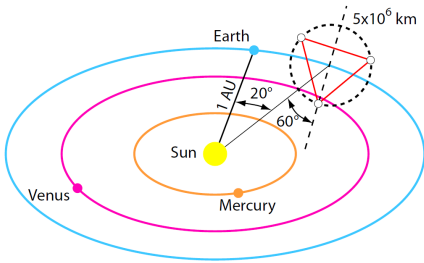


**Figure 1.1.:** Schematic of LISA orbit (not to scaled). Image credit: NASA.

In LISA light beams will propagate between three spacecraft orbiting the Sun at 50 million km behind the Earth in a near-equilateral triangle constellation of 5 million km side length [19], as sketched (not to scaled) in Figure 1.1. The three spacecraft bidirectionally linked by laser light will act as a Michelson interferometer having a strain sensitivity of  $\approx 10^{-20}/\sqrt{\text{Hz}}$  corresponding to optical path length noise of  $\approx 10 \text{ pm}/\sqrt{\text{Hz}}$  [20]. In the case of a passing gravitational wave the separation of two freely floating points in space will be changed. In order to detect this effect, in LISA each spacecraft will house two test masses, maintained in near free-fall, and two identical optical benches including polarising components connected via optical fibres to each other and to the two laser sources. The laser link between two spacecraft is realised by a laser beam at  $\lambda = 1064 \text{ nm}$  sent through a 40 cm telescope to the distant one, and heterodyne interferometry between the incoming and the local laser beam is performed. The phase of the resulting carrier-to-carrier beat note in the MHz range, carrying the desired information about the gravitational waves, is measured using heterodyne interferometry with a noise budget of about microcycle/ $\sqrt{\text{Hz}}$ . One laser link between two satellites is illustrated in Figure 1.2.

LISA relies on novel technologies that cannot be properly verified on the ground. This is due to the Earth's gravity and seismic environment which

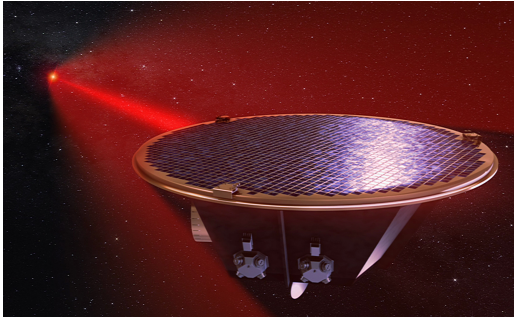


**Figure 1.2.:** LISA Satellite with one laser link.  
Image credit: Milde-Marketing

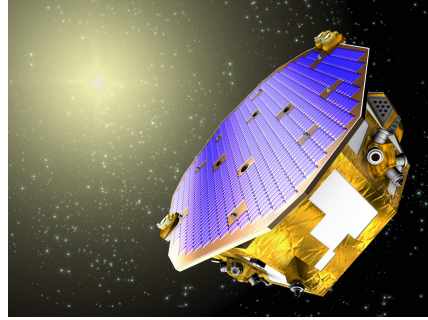


**Figure 1.3.:** LISA Pathfinder Satellite.  
Image credit: ESA

would overwhelm the test results. In order to prove that the requirements are realistically possible and to further demonstrate new technologies, the ESA has scheduled a precursor mission: LISA Pathfinder.

### LISA Pathfinder:

LISA Pathfinder (LPF) consists of one satellite, as depicted in Figure 1.3, and its launch is planned for 2014 on-board a VEGA vehicle [21, 22]. The operational orbit will be the halo orbit around the first Sun-Earth Lagrange point L1 located 1.5 million km from Earth. The mission challenge is to place two enclosed test masses in a nearly perfect gravitational free-fall and to maintain them there. For this purpose, the test mass attitude will be measured and controlled with unique accuracy by using state-of-the-art technologies such as highly stable drag-free attitude control, a laser metrology system, and precise micro-Newton propulsion systems.

Aboard LISA Pathfinder will be two payloads: the European LISA Technology

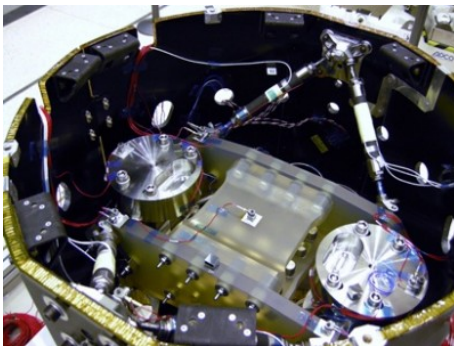


**Figure 1.4.:** Photograph of the LTP assembled in the LISA Pathfinder science module structure. Image credit: ESA.

(DRS) [23]. The DRS consists of a set of colloidal micro-thrusters and an on-board computer for controlling the spacecraft position to follow a geodesic within a fraction of a wavelength of light. This technology is not only required for enabling the LISA, but also of importance for a future geodesy mission for mapping the Earth's gravity field. The core instrument of LTP, in turn, includes the two test masses positioned on either side of an optical bench and thus serving

as end-mirrors of the laser interferometer. Their relative displacement is interferometrically measured serving as inertial reference for the satellite drag-free control system. Each test mass is enclosed in an electrode housing which is embedded in a non-magnetic titanium vacuum enclosure, as shown in Figure 1.4. Inside this chamber the caging mechanism for one test mass is located, which holds the test mass during launch and releases it on orbit.

In contrast to LISA, LPF will use a Mach-Zehnder heterodyne interferometer in a non-polarising scheme. Thus, the beams probing the test mass will have a slight angle to allow separation of the incident and reflected beams. LPF will in this way verify the heterodyne interferometer concept at kHz for LISA, which is analogous to a single LISA arm, with the baseline shrunk from 5 million km to about 40 cm. The aim of LISA Pathfinder is to demonstrate the technical readiness for LISA.

Whereas LISA Pathfinder is similar to a single LISA arm in one satellite, the first inter-satellite interferometer, in turn, will fly on-board a GRACE follow-on mission for precise monitoring of the spatial and temporal variability of Earth's gravity field.

### GRACE follow-on:

Various geophysical processes generate gravity anomalies with extensive spatial variations over the surface of the Earth. The resulting gravity field is known as the long-term average (or mean) gravity field. Measurement of these gravity anomalies provides, for example, a better understanding of the structure of the solid Earth. Shorter-term mass fluctuations such as the variation in water content of the Earth's crust are known as the time-variable gravity field. It helps, among other things, to study the global sea level changes or the polar ice sheet balance. These changes have a significant impact on relevant climatic issues. The joint US-German Gravity Recovery and Climate Experiment (GRACE) was successfully launched in 2002 to monitor these changes [14]. GRACE consists of two identical satellites, one 220 km ahead of the other in the same orbit at an altitude of approximately 500 km, as illustrated in Figure 1.5. Temporal and spatial changes in the Earth's gravity field cause small variations in the inter-

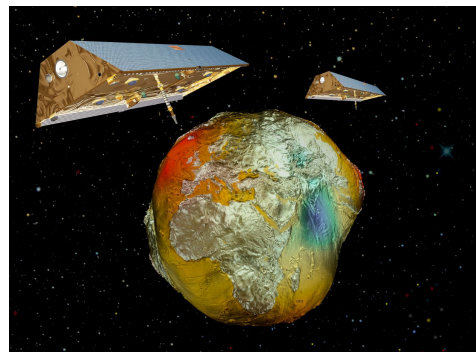


**Figure 1.5.:** Illustration of GRACE with the Earth's gravity field (vertically enhanced) calculated from CHAMP data. Image credit: Astrium/GFZ

spacecraft separation, which are measured in order to determine the Earth's gravity field. The relative distance and velocity changes are measured with a microwave interferometer in the K-Band with an accuracy of  $1\ \mu\text{m}$ . Thus the Earth's gravity field can be determined with a spatial resolution of about 200 km and a temporal resolution of typically one month.

GRACE was initially planned with a lifetime of five years, but was subsequently extended until the end of its on-orbit life (approximately 2013/2014). For the last decade GRACE has produced a wealth of useful data allowing a deeper insight into geophysics, hydrology, climate research, and many other fields. This success has led to the demand of a follow-on mission being launched as early as possible to minimise the gap in data stream and thus loss of valuable data. In order to allow such a fast mission, a GRACE follow-on mission, also referred to as *GFO*, will be an essential rebuild of the original GRACE mission with a few modifications. The primary instrument for measuring changes of the inter-satellite distance will indeed remain the microwave ranging (on-axis), but a laser ranging interferometer (LRI) will be additionally included as a technology demonstrator (off-axis), as shown in Figure 1.6. It will deliver a complementary set of ranging data with less noise and high-precision data of the alignment between the two satellites. The LRI aims at a noise performance of about  $80\ \text{nm}/\sqrt{\text{Hz}}$  over an inter-satellite distance of up to 270 km [24]. As the LRI serves only as a demonstrator and because of the GFO's limited lifetime, an interest in developing a follow-on mission with a superior performance still exists.

To achieve this, the primary metrology system for the distance measurement between the satellites needs to be replaced by laser interferometry [25–28] with nanometre precision, and it is beneficial to reduce the inter-satellite distance to improve spatial resolution [29]. Also a lower altitude is desirable, since the short-scale gravity field components diminish rapidly with increasing height. The disadvantage of a lower orbit is the significant atmospheric drag which then must be compensated. Therefore, a suitable drag-free control system needs to be developed. In order to provide a constant thermal environment and to avoid sunlight radiation coupling onto the optical axis between the two satellites, a sun synchronous near-circular orbit would be suitable.

## 1.2. Outline of this thesis

This thesis discusses the development and implementation of several metrology techniques involving precise measurements of displacement as well as laser beam propagation axes in space. The thesis is split into four parts:



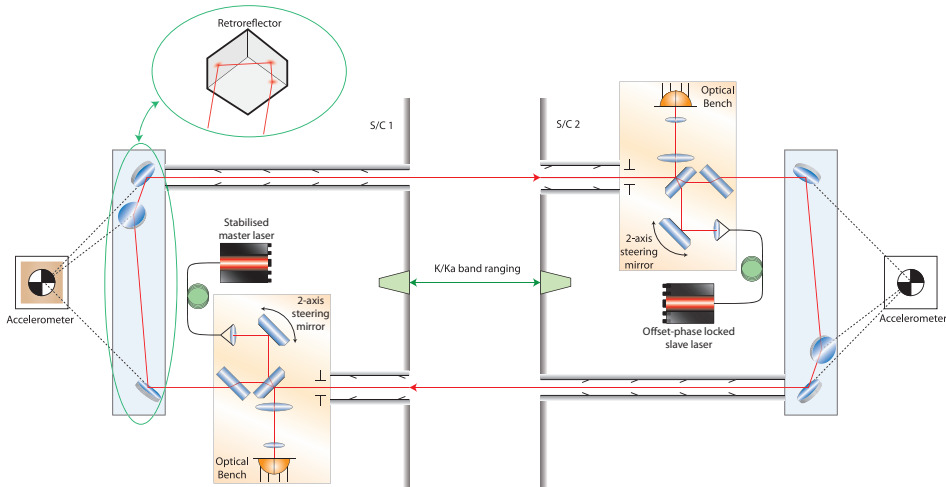


**Figure 1.6.:** Schematic of the proposed layout for the off-axis laser ranging instrument on board GRACE follow-on. The primary measurement instrument is the microwave ranging system and labelled K/Ka band ranging. Figure taken from [15].

**Part I**, comprising Chapters 2 and 3, introduces the techniques used for alignment and construction of ultra-stable optical systems. By applying the hydroxide-catalysis bonding technique one can build quasi-monolithic interferometers. For this purpose, several alignment techniques including a device for an absolute positional measurement of laser beams have been developed.

**Part II**, comprising Chapters 4 to 7, deals with the verification of polarising components for heterodyne interferometers. To this end an optical bench consisting of four interferometers has been designed and built using the hydroxide-bonding technique. Different noise sources have been identified and partly cancelled. These investigations have been performed within the framework of the ESA project: *LISA Optical Bench Development*.

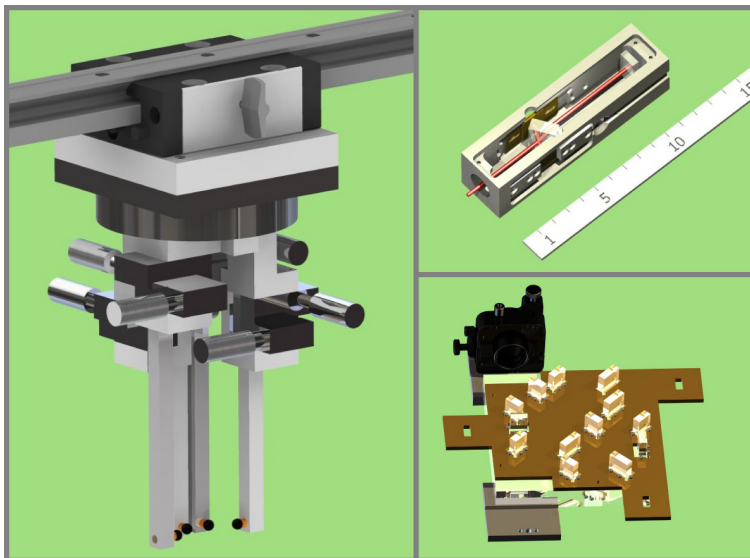
**Part III**, comprising Chapter 8, presents the efforts done for setting up a test bed for an ultimate linearity test of phase measurement systems. A hexagonal interferometer has been designed and built by adopting the template bonding technique. First tests in air to validate the measurement concept are presented.

**Part IV**, comprising Chapter 9, reports the joint efforts with the Huazhong University of Science and Technology (HUST) towards an optical system for measuring the Earth's gravitational field. As a first step, the hydroxide-catalysis bonding technique has been introduced in their laboratories, and an

optical bench forming two Mach-Zehnder interferometers has been designed and bonded. Initial displacement measurements performed at HUST are presented.

## Part I

## Alignment strategies and construction methods for precision interferometers





## Chapter 2

## 2 Techniques for alignment and construction of precision interferometers

Since precision interferometers are desired in various applications such as gravitational wave detectors on Earth as well as in space, the intrinsic stability of such interferometers is of crucial importance. Broadly, to reach an interferometric readout sensitivity down to a few pm/ $\sqrt{\text{Hz}}$  at frequencies below 1 Hz, an assembly of interferometers combined on an ultra-low expansion ceramic baseplate is required. Not only is it vitally important for the baseplate material to be ultra-stable, but the techniques used to attach optical components must be ultra-stable as well. One such technique is to *optically contact* a component onto a baseplate [30, 31]. In the case of two highly polished glass substrates, ideally to better than  $\lambda/10$ <sup>[1]</sup>, the surfaces will stick to each other on pressing them together. The interaction between the two surfaces is caused by molecular adhesion, in particular by van der Waals forces. Although optical contacting has proven to be an adequate method to reach low noise levels [32], such a method is not applicable in space science for precision metrology. Its breaking strength is much lower than for other bonding techniques [33], which has to be considered during the launch into space. Another method to fuse two surfaces with high strength is known as silicate bonding [34]. Since this method was invented for the optical telescope of the Gravity Probe B mission, it has already proven that silicate bonded assemblies can withstand the accelerations during launch into orbit [35–37]. Thus, it is possible to use silicate bonding to adhere optical components in other spaced-based missions. In addition, the ground-based gravitational-wave detectors GEO 600 [38] and Advanced LIGO [39] are using fused silica suspension stages. A small piece (the so-called ear)

<sup>[1]</sup>For the specification on the optical flatness, it is common to use a wavelength  $\lambda$  of 633 nm.

is silicate bonded to enhance the stability and to reduce the mechanical loss [40–43].

Although all experiments performed for this thesis are based on ground, silicate bonding is adopted as the baseline method for building ultra-stable optical benches that are adaptable for space missions such as LISA. The design and manufacture of such stable optical benches is crucial to comply with a stringently required noise performance at picometre level. Therefore, the construction of quasi-monolithic interferometers involves some challenging requirements. One of them involves the precise positioning of each optical component, classified either as non-critical or critical, at the few  $\mu\text{m}$  up to  $100\ \mu\text{m}$  level corresponding to a few  $\mu\text{rad}$  up to several hundred  $\mu\text{rad}$  level. A component is classified as non-critical, when its misalignment can be compensated by another component at a later stage in the bonding. Typically, this is the case for optics only reflecting or transmitting the beam to other optics. In contrast, the beam combiners as well as components directing the beam to a readout target such as a test mass are categorised as critical. A more precise alignment for such optics is necessary.

As the University of Glasgow (UGL) has successfully completed the LISA Pathfinder flight model and is currently working on the prototype for the LISA optical bench, a variety of alignment techniques have already been developed [44]. For instance, non-critical components have been bonded by using a template, while critical components have been positioned on the optical bench with adjusters. The use of a coordinate measuring machine (CMM) enabled them to measure the characteristics of the template in order to align it relative to the optical bench as well as to already bonded components. However, stable interferometers were also built in the past at the AEI by applying the silicate bonding technique [45]. For this purpose, several construction methods had been adopted, such as the so-called *template bonding* as well as simple adjusters. In the course of this thesis a CMM has been integrated in the AEI laboratory and its application has been further developed. The subsequent sections will give an overview of the silicate bonding process and will describe the various alignment techniques applied.

### 2.1. Hydroxide-catalysis bonding process

In order to understand the demanding alignment techniques, it is necessary to have some background knowledge of the silicate bonding method, although it would go beyond the scope of this thesis to describe this technique in detail. It is intended to specify only the basic principle and the resulting consequence.

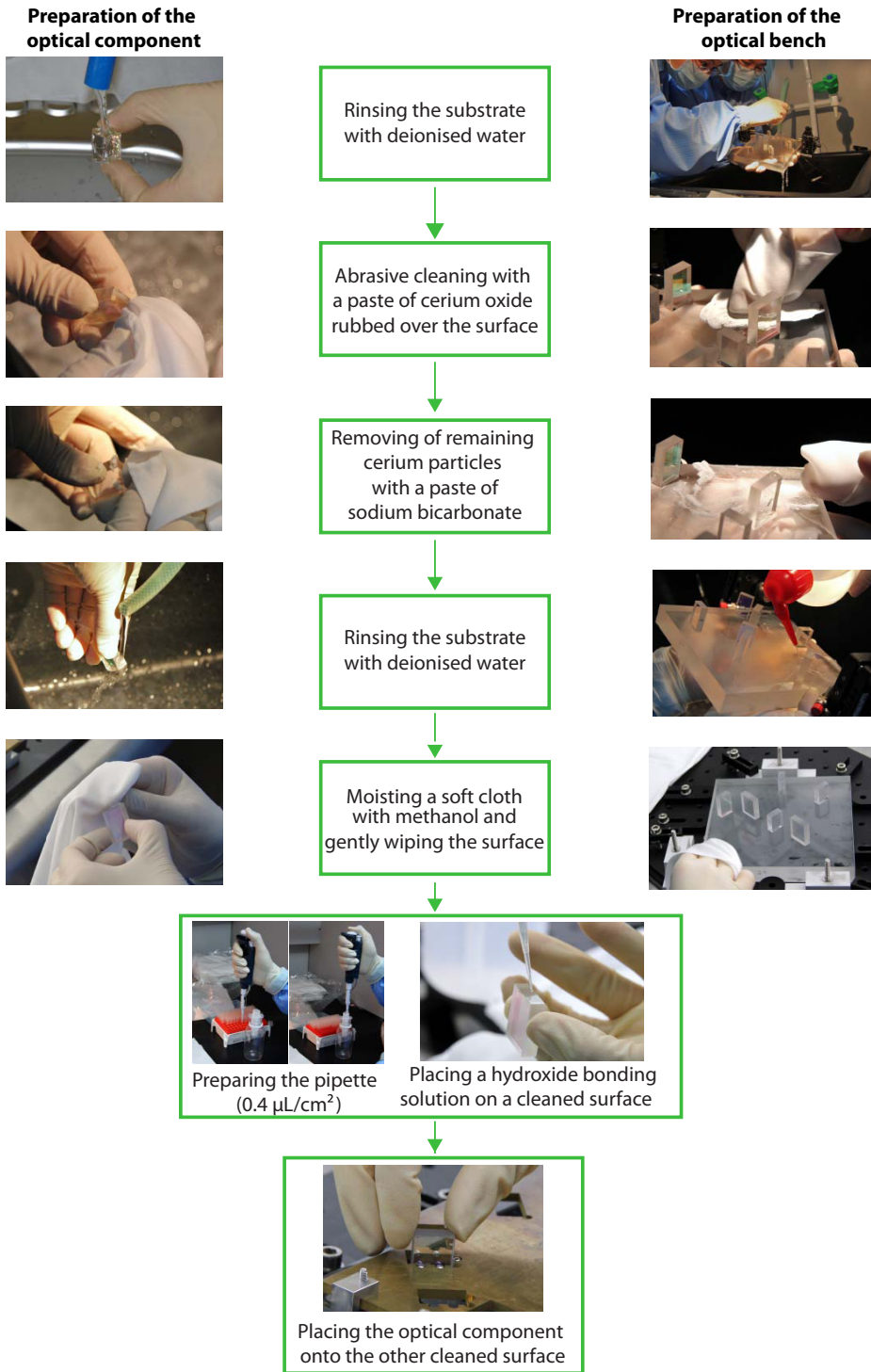


Figure 2.1.: Bonding procedure of a fused-silica component onto a low-expansion baseplate.

For further information the reader is kindly referred to other dedicated publications on this topic [46–48].

Silicate bonding is a technique which joins together two highly polished typically silicate-based materials, such as fused silica or Zerodur<sup>®</sup>, such that it forms one quasi-monolithic structure. By applying an alkaline bonding fluid, such as sodium hydroxide (NaOH), potassium hydroxide (KOH) or sodium silicate ( $\text{Na}_2\text{SiO}_3$ ) dissolved in water, and bringing the surfaces into contact, the free hydroxide ( $\text{OH}^-$ ) ions etch both surfaces. This results in chemical reactions, leading to siloxane chains rigidly connecting the two materials [47]. Due to this working process the silicate bonding is also known as *hydroxide-catalysis bonding*. Note that for convenience silicate or hydroxide-catalysis bonding is referred to as *bonding* throughout this thesis.

The period of time for bonding, also referred to as settling time, depends on the concentration of free hydroxide ions and on the temperature [48]. During the initial stage, when the etching takes place, an alignment of the two surfaces against each other is still possible, but the time period for doing this is a few tens of seconds. Once the bond is fully cured, which takes typically a few weeks, it is impossible to detach the component from the baseplate. Any attempt to remove the optic results in breaking it at its weakest location. This location is influenced by imperfection of the material and will typically not be the bonding surface. In contrast, it is possible to dismount a recently bonded component that is not yet fully cured. The glass assembly needs to be placed for 30 minutes or longer in a detergent solution inside an ultra sonic bath [34]. It is much simpler, if the bonding process has not yet started. In that case it might be possible to immediately add  $\text{OH}^-$  ions to significantly increase the settling time, which appears to stop the process. Depending on the quality and size of the bond the damage of the surface after detachment increases with the setting time.

It is preferable to conduct the delicate bonding procedure in a clean environment (optimally in a clean room  $\leq$  class 1000) to protect the surfaces from contamination with particles during the bonding process. In addition, the cleanliness of the surfaces is crucial to ensure that the substrates are free from chemical and particulate contaminants and to enable full hydration such that siloxane chains can be formed. To this end, a specific cleaning procedure has been developed at UGL. Figure 2.1 illustrates the cleaning procedure combined with the bonding process. The samples are rinsed with deionised water before the bonding surfaces undergo a light abrasive cleaning with a paste of cerium oxide rubbed over the surface. After again cleaning the surface with deionised water, any remaining cerium particles are removed with a paste of sodium bi-



carbonate  $\text{NaHCO}_3$ . After a final rinse with deionised water the samples are dried with a single wipe from a non-abrasive cloth moistened with methanol. The bonding solution is then placed on the surface of the optical component, in a scale of  $0.4$  to  $0.6 \mu\text{L cm}^{-2}$  (depending on the size of the footprint) [34]. The final step is to carefully place the optical component with the bonding solution onto the optical bench. This is very challenging and auxiliary tools are required to ensure quick and accurate alignment.

## Degrees of freedom of the alignment

Ideally, the alignment of the interferometer should cover four degrees of freedom (DoF): two angular (pitch / yaw) and two translational stages, where the translation in direction of the vertical axes is ignored (see Figure 2.2). Due to the fact that the components can be only aligned along the surface of the optical bench, the vertical degrees of freedom are predetermined by the components and baseplate surface. Both ‘out-of-plane’ degrees (yaw and height  $z$ ) must be controlled by an accurate machining of the components with stringent tolerances. These tolerances specify the flatness of a baseplate and the perpendicularity of a component. They are dependent on the layout of the interferometer and most notably on the required tolerances for the beam alignment. Typically, the perpendicularity of the optical surface to the bottom surface is required to be better than 2 arcseconds and the flatness of the baseplate needs to be  $\lambda/10$  over the whole surface. Thus, the beams in the interferometer will stay aligned in the ‘out-of-plane’ degrees at all points as long it was appropriately aligned in that plane from the beginning. The remaining ‘in-plane’ degrees ( $X - Y$  - plane) need to be adjusted manually, assuming all beams at constant height and parallel to the baseplate. This is described in the following.

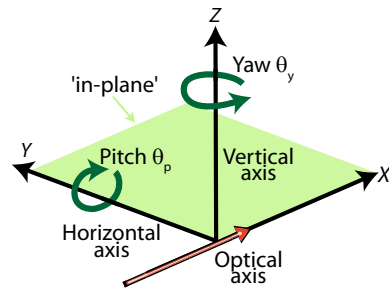


**Figure 2.2.:** Schematic of the coordinate frame including its degrees of freedom for beam alignment.

## 2.2. Template bonding

In the case of bonding non-critical components onto a baseplate, a metal template can be used to define the component’s position. This fast and less complicated procedure has the major advantage that one can bond several components in a single bonding session. However, after manufacturing the template the positions of all components relative to each other on the baseplate are fixed

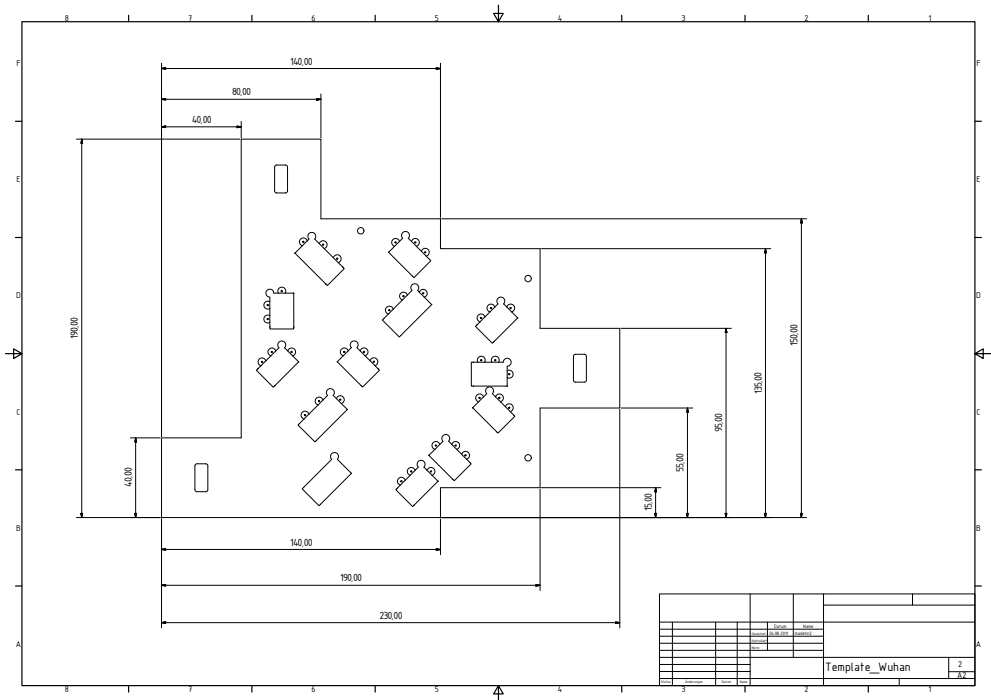


**Figure 2.3.:** CAD drawing for a template model created with the software **Autodesk Inventor Professional**. One sheet of the drawings with the outer dimensions of the template body is shown. This template was used for construction of the optical bench described in Chapter 9.

and no change of their position and angle is possible.

For producing an appropriate technical drawing of a template, the desired values are calculated with **IfoCad** [49], an in-house developed C-based 3D ray tracing program, and fed to CAD software (**Autodesk Inventor Professional** 2009). An example of such a drawing is depicted in Figure 2.3, where one sheet of the drawings for the dimensions of the template body is shown. Typically, such a template is made of brass and manufactured in the mechanical workshop of the AEI with an accuracy of  $100\ \mu\text{m}$ . Such a template is shown in Figure 2.4. The template provides a pocket for each component, where each pocket houses three spheres forming a reference frame (*cf.* enclosed photograph). Thus, this three-point-reference defines position and angle  $\theta_y$  of the component to be bonded. A distinction is drawn between non-critical and critical components. The pockets foreseen for the critical components, such as recombination beam splitters, do not include spheres, because they will be bonded with a different method (*cf.* Section 2.3.5). Therefore, these cut-outs can be categorised by one of three different categories:

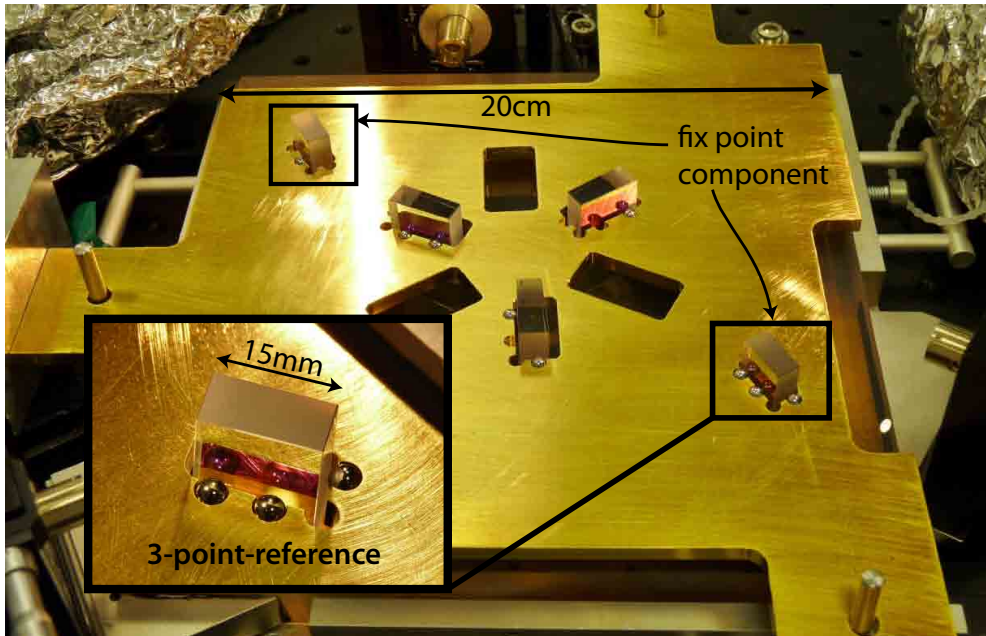


**Figure 2.4.:** Photograph of a bonding template used in the construction of the hexagon interferometer (see Chapter 8). The brass template includes two cut-outs for fixed-point components, three cut-outs housing spheres for bonding non-critical components and three larger cut-outs for critical components. *Enclosed picture:* Cut-out with its three spheres forming a well defined position for the component.

- **Cut-outs for fixed-point components.**

As the template has to be removed prior to every bonding session to clean the surface of the optical bench, reference points are required to relate the template to the baseplate. Therefore, fixed-point components are included in the layout defining the orientation and position of the template relative to the baseplate. They need to be bonded in the first bonding stage and can be seen in the enclosed photograph in Figure 2.4. During the whole bonding process three spheres need to be spatially distributed within the pockets. It is also possible to combine spheres from fixed-point components with those from a regular pocket for either beam splitters or mirrors. Since the risk of damaging the optical surface is higher in the latter case, special care has to be taken while the template is adjusted and removed.

- **Cut-outs for each component that will be bonded with the template.**

Only the spheres for the components bonded in the current stage need to

be inserted. In order to avoid misalignment of the template, the spheres of components that are already bonded (and those to be bonded later) have to be removed (except for the fixed-point components). The template remains in its position for a few hours until the component(s) has/have settled and the bond has started to harden. Afterwards, the template is removed to reuse it for the next bonding stage.

- **Cut-outs for all critical components on the baseplate.**

Critical components will be bonded separately with a different alignment method such as adjustable bonding. Therefore, these pockets do not house spheres and are usually larger.

The template is mounted slightly above the baseplate. In order to keep the component currently to be bonded in a well defined position, the baseplate is tilted by an angle of approximately  $5^\circ$ . Due to gravity the component will glide on the bonding fluid against the spheres and therefore has a well defined position.

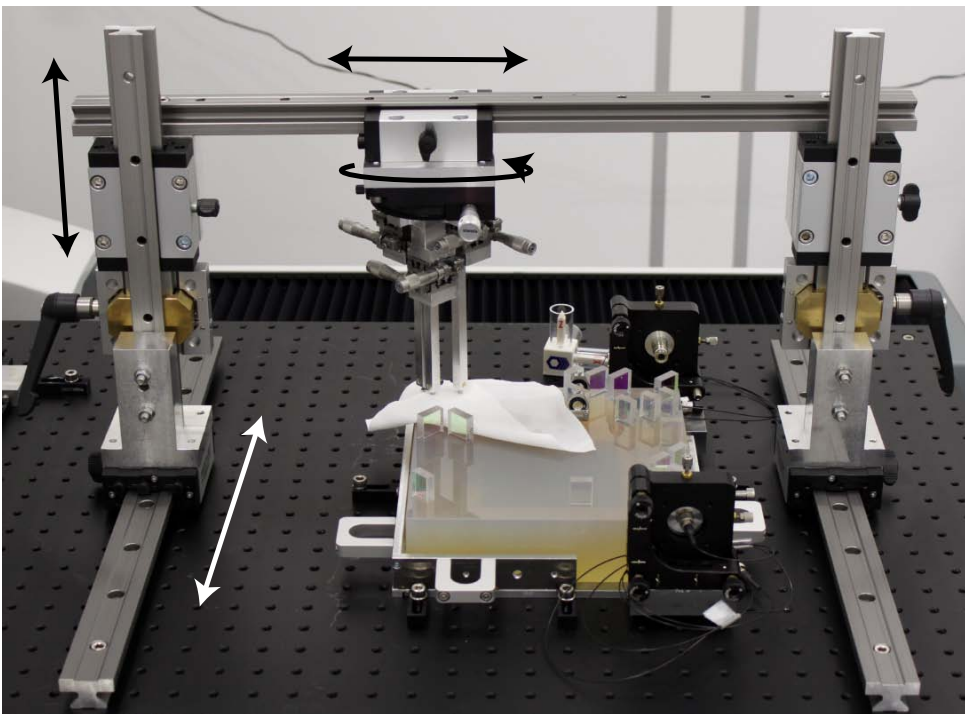


**Figure 2.5.:** The assembly of alignment tool and movable bridge, enclosing an optical bench. The arrows illustrate the four macroscopic DoF of the tool, which are used for a coarse adjustment.

## 2.3. Precision bonding

Since several components require a more precise position and angular alignment than can be obtained by template bonding, further techniques are needed. In addition, not all critical components can be placed by the template. They need to be aligned to an optical target (*cf.* Chapter 3) or to combine two beams by maximising their overlap in situ to achieve good interferometric contrast. This demands an auxiliary tool to ensure fast and precise alignment. In addition, it is desired to precisely measure the components' positions as well as several other features, such as the orientation of targets or the spheres of a template, with respect to an arbitrary coordinate frame (*cf.* Section 2.3.3). For this purpose a coordinate measuring machine is needed. Both tools are described below. Furthermore, the adapted techniques for bonding non-critical as well as critical components are described in the subsequent sections.

### 2.3.1. Alignment tool

The alignment tool consists of a movable bridge with a movable panel to which the main part is mounted. Thereby three degrees of freedom for a macroscopic alignment are served ( $x$ ,  $y$ , and  $z$ ), as shown in Figure 2.5. The main part is composed of four mechanical “fingers” equipped with tightly toleranced  $5\text{ mm} \pm 1.3\text{ }\mu\text{m}$  silicon nitride spheres [50], as shown in Figure 2.6. The permissible difference between the largest and smallest diameter measured on one sphere is specified to be better than  $0.13\text{ }\mu\text{m}$ . For the microscopic adjustment in both translational directions ( $X$  and  $Y$ ) of these spheres, two linear translation stages for each are attached to the panel, having a resolution of  $1\text{ }\mu\text{m}$  as well as a travel range of 10 mm. The translation stages (*M-SDS25*, Newport) are made of stainless steel with a  $25 \times 25 \times 12\text{ mm}^3$  footprint. A locking mechanism of the micrometer screw secures the stage position with negligible motion when the lock is engaged or disengaged. Throughout this thesis, these probes will be referred to as adjusters.

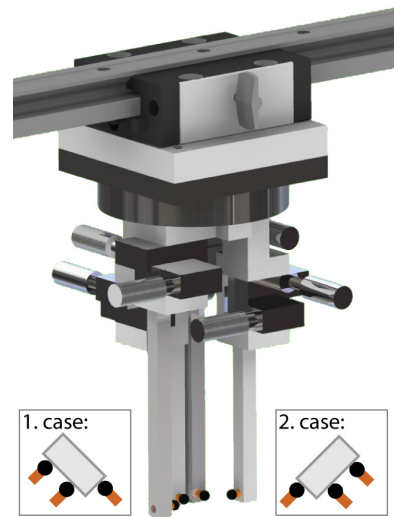


**Figure 2.6.:** CAD model of the alignment tool.

With the four adjusters it is possible to form two different types of three-point-reference for an optical component, omitting one adjuster. This can be seen in the enclosed pictures in Figure 2.6 for the two cases. Typically,

rectangular components are used. For both cases two adjusters are located on the same side touching the optical surface of the component. This defines its angle. The third adjuster is placed  $\pm 90^\circ$  rotated at the non-optical surface and controls the insensitive shift along the surface. The fourth adjuster has the same function and can be used instead of the third one, depending on the layout and the component orientation. In addition, the four adjusters are attached to a lockable rotation platform (*7R172-2*, Standa) actuated by a micrometer screw. Thus, the whole tool can be roughly prepositioned for any occurring orientation. Consequently, the alignment tool covers all desired DoF.

### 2.3.2. Coordinate measuring machine

As a versatile metrological instrument, a coordinate measuring machine (CMM) is best suited for flexible measuring with the ability to conform to exacting requirements. The CMM is a three-dimensional device for measuring the physical geometry of an object. To be precise, the CMM measures individual points in space and computes from them various geometrical parameters also referred to as *features*. There are two possibilities for controlling such a machine, either manually by an operator (by means of the portable terminal (*jogbox*)) or it may be directly computer controlled (DCC). To this end a specific software language for a *dimensional measurement interface specification* (DMIS) was developed and is supplied by the CMM manufacturer [51]. This neutral interchange format between dimensional measuring and CAD systems forms the basis of various commercially available CMM software languages such as PC-DMIS. Additionally, the measuring system consists of a control unit including the jogbox and a computer with appropriate software.

The CMM used for all measurements described throughout this thesis is a *DEA GLOBAL Advantage* from Hexagon Metrology GmbH [52]. The software used for programming and machine control is PC-DMIS 4.3 [53]. The CMM accuracy is specified by

$$\text{MPE}_E = 1.5 \mu\text{m} + \frac{L}{333000} \quad (\text{volumetric length measuring uncertainty}) \quad (2.1)$$

and

$$\text{MPE}_P = 1.7 \mu\text{m} \quad (\text{volumetric probing uncertainty}). \quad (2.2)$$

MPE is the acronym for *Maximum Permissible Error* [54]. Furthermore, the CMM has a measurement volume of  $0.7 \text{ m} \times 1 \text{ m} \times 0.5 \text{ m}$  ( $X \times Y \times Z$ ).

An annotated photograph of the used CMM operated in a clean room environment is shown in Figure 2.7. This device is based on a bridge architecture with Cartesian axes and a vertical spindle. For optimal rigidity a fixed granite



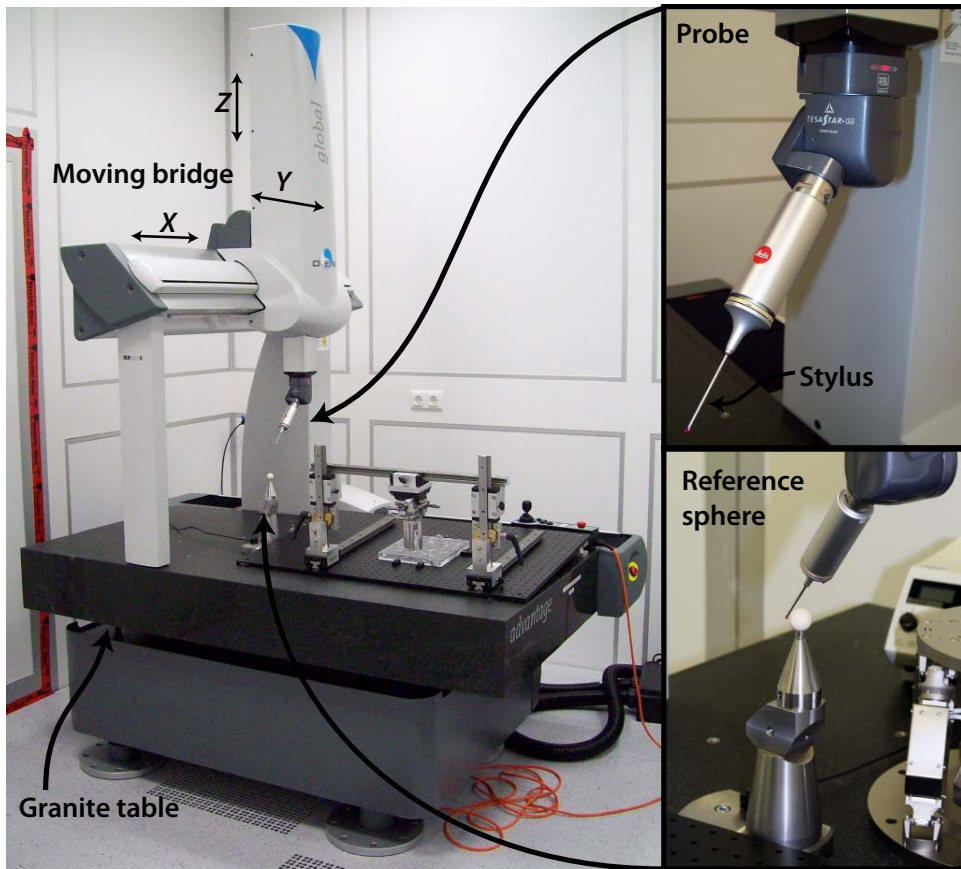


**Figure 2.7.:** Annotated photograph of the CMM used with its movable bridge architecture forming a Cartesian coordinate system. On the fixed granite table one can see the assembly of alignment tool and optical bench. The tactile probing head is presented in the upper right picture, whereby the bottom right picture shows the reference sphere for probe qualification.

work table is included. All three measurement axes are equipped with a motor and a sensor to determine the displacement along the axis. At one carriage of the gantry a probe head is attached carrying the sensor that actually measures the workpiece. One can assemble several types of probes and styli to it, resulting in more flexibility. However, it is preferable to measure one workpiece with a single probe-stylus combination to assure a high accuracy. Changing probes increases the uncertainty (*cf.* Appendix B). The CMM used offers the advantage of a choice between point-to-point measurement and continuous measurement (“scanning”) of the workpiece. Throughout the component alignment procedure the point-to-point measurement method is adopted. In doing so, the probe touches the workpiece with a defined static contact force. Its stylus gets deflected, whereas its position is determined from a combina-

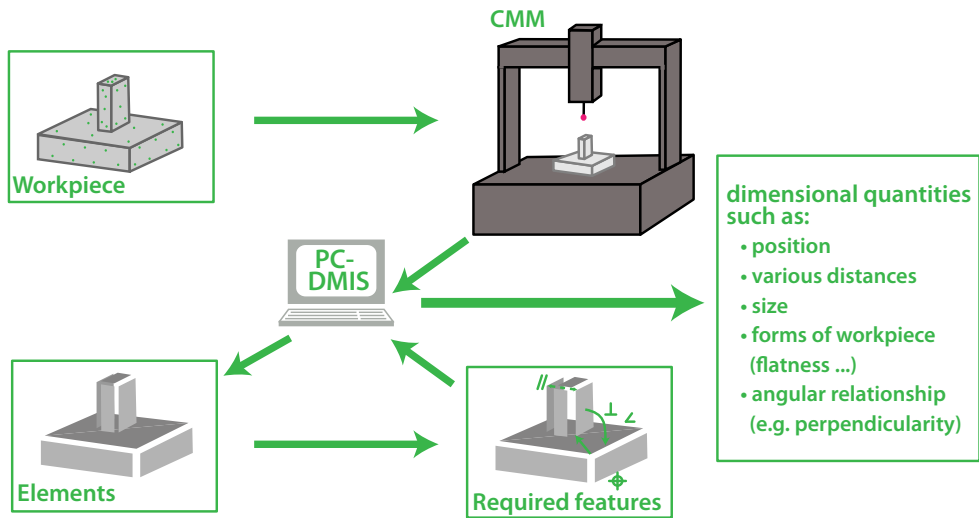


**Figure 2.8.:** Schematic of a coordinate metrology. A workpiece is measured by a CMM generating a set of data points. The software (PC-DMIS) is calculating the substitute geometric elements by applying an appropriate fit-algorithm to the data set. Doing so, the required features of the workpiece can be determined by combining the various elements. The calculated data are then processed either to a protocol or to a display.

tion of displacement transducer, measuring, for instance, the rotation of the spindle (tip displacement), and optical sensors attached on each of the three linear axes (probe displacement). The reflection scale of the optical sensor is made of steel with a hard gold graduation obtained by the Aurodur<sup>®</sup> process [55]. The tactile probing system used for all measurements throughout this thesis is a combination of *LSP-X1* from Leitz fitted to a *TESASTAR-m 5° M8* probe head, as can be seen in Figure 2.7 in the right upper corner. It consists of a probing element which ensures a mechanical interaction with the workpiece surface. This *tip ball* is made from ruby to benefit from its inherent high stiffness and low wear. The tip ball is attached at a steel stylus shaft for transferring the probe force to the sensor. The underlying principle of tactile probing is the force interaction between workpiece and tip ball. In case the probing force exceeds a mechanically (or electronic) controlled value, the contact is identified and the response is measured [56, 57]. The calculated data are then released in a protocol or on display.

Figure 2.8 presents the measurement process with the CMM. The shape of a workpiece along with its dimensional quantities can be obtained by probing several points on its surface. By applying an appropriate geometric element best-fit algorithm to the measured points, a mathematical model of the workpiece is determined. With the obtained geometric elements the desired features



can be calculated, such as its size and form; the angular relationship between different surfaces of the workpiece, as well as the position of the workpiece relative to a certain coordinate frame. This coordinate frame can be the machine coordinate system or an arbitrary coordinate frame from a workpiece. In Appendix A some CMM measurement strategies are described.

### 2.3.3. The coordinate frames

The need to define appropriate coordinate systems arises from using coordinate metrology. On the one hand, there is the machine's coordinate system in which the probing is performed and to which the probe qualification process is referred. On the other hand, there are some particular coordinate systems in which the features of interest are best expressed: especially the position of an adjuster as well as the orientation of a component relative to the optical bench. Therefore, several coordinate frames are used throughout this thesis. They are illustrated in Figure 2.9. All coordinate frames are right-handed as well as orthogonal, as defined in the subsequent paragraphs. The origin of a frame is denoted by  $O$  and a subscript (e.g.  $O_i$ ), whereas the axes of the frame are labelled  $X$ ,  $Y$ , and  $Z$  with an appropriate subscript. Only the reference frame has no subscript.

**MCS: Machine coordinate system** The three carriages of a CMM form a Cartesian coordinate system, see Figure 2.7. Whereas the main carriage, consisting of a beam and two shoulders, runs on the long side of the work table representing the  $Y_m$ -axis. The main carriage runs along the beam forming the  $X_m$ -axis, while the spindle attached to the main carriage moves perpendicular to the granite table along the  $Z_m$ -axis. The location of its origin is counter-intuitive, not being on the granite table, but rather 0.5 m shifted along the  $Z_m$ -axis. Thus, the measurement volume of the CMM spans a coordinate system with  $X_m$ ,  $Y_m$  and  $-Z_m$ . Note that all measurements performed with the CMM are related to this coordinate system and only transformed via the software PC-DMIS.

**OBF: Optical bench frame** This coordinate system is defined by the geometry of the optical bench. Its polished surface is by definition the  $X-Y$  plane, where the  $X$ -axis lies in the plane of one side surface. Thus, the  $Z$ -axis is orientated perpendicular to this plane completing a right-hand system. The origin is located at one of the four corners of the optical bench, depending on its orientation during the probing. It may be possible that several surfaces are blocked by e.g. the alignment tool and cannot be touched by the probe. Hence, three accessible surfaces are probed as required to determine a coordinate system. The OBF will be additionally referred to as the frame of reference within

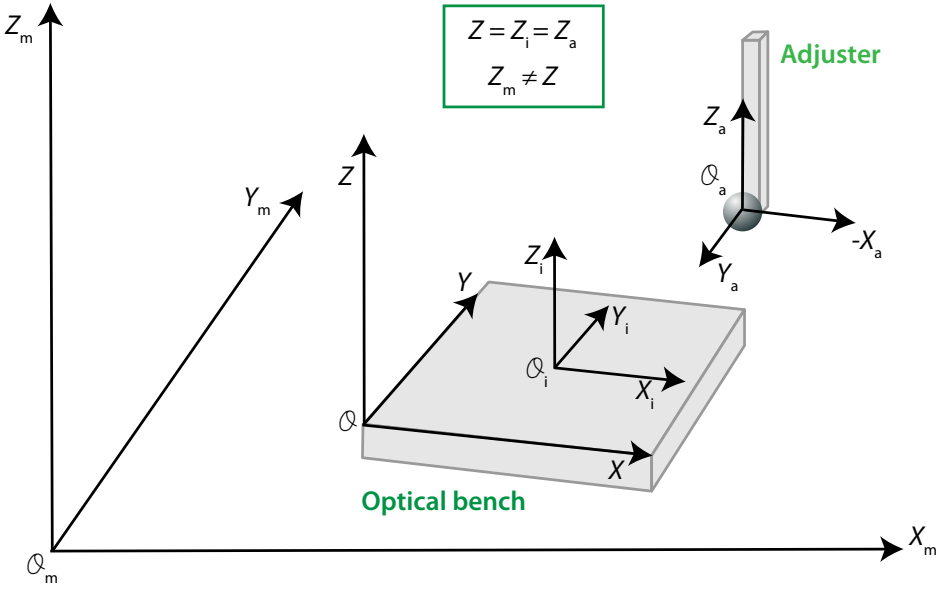


**Figure 2.9.:** Schematic of several coordinate systems used throughout this thesis. The machine coordinate system (subscript: m) is defining the measurement volume of the CMM. Within this frame all measurements are related to it and in the following, are transformed, for instance, to the optical bench frame representing the reference frame. This frame has no subscript, because it serves as a reference. The **IfoCad** frame (subscript: i) is the natural one within which the simulations and the designing are performed. Each adjuster used to align the component has its own frame (subscript: a), where its  $Z_a$ -direction is equal to  $Z$  and  $Z_i$ .

which, for instance, the measured properties of a workpiece like an optical component or the position of the tip ball are related.

**ICF: IfoCad frame** Since all discussed interferometers throughout this thesis are designed with **IfoCad**, this coordinate frame is the original one. Note that **OptoCad** is using the same coordinate frame as **IfoCad**. Because we assume no vertical misalignment of the beams, all beams are propagating in one plane. This plane is defined to be the  $X_i - Y_i$ -plane of the **IfoCad** frame with a  $X_i$ -direction parallel to one side surface of the bench. The  $Z_i$ -axis is perpendicular to the plane of the interferometer and thus pointing out of the optical bench. Its direction is the same as for  $Z$ . The origin  $O_i$  of the ICF is the centre of the optical bench.

**ACF: Adjuster coordinate frame** Since the adjusters are used to align a component on the optical bench, their coordinate systems are related to each other. Both share the same  $Z$ -direction, pointing out from the optical bench. This results in an  $X_a - Y_a$ -plane parallel to the  $X - Y$ -plane of the optical

bench. The  $Y_a$ -direction is defined to be perpendicular to the front surface of the stylus. Finally, the origin  $O_a$  is located in the centre of the sphere.

### 2.3.4. Adjustable bonding

Since one of the most sophisticated technologies to precisely measure points in space is a CMM, advantage will be taken of the flexibility and the high accuracy of such a coordinate metrology. Although the primary and most typical function of a CMM is to measure the actual shape of a workpiece, compare it to a reference shape and calculate geometrical characteristics, a procedure to align a three-point-reference relative to the optical bench frame has been developed. The resulting advantages are, on the one hand, a higher degree of precision than achieved by template bonding, and on the other hand the independence of the manufacturing time of such templates. This allows a redesign of the interferometer immediately after a determined misplacement of a component and continue bonding. However, it is very time consuming to adjust a single component and bond it in the desired position. This makes adjustable bonding very unattractive when complex interferometers have to be assembled quickly. Due to the fact that this bonding procedure requires the auxiliary tool presented in Section 2.3.1 in addition to the CMM, this method is referred to as *adjuster-aided / adjustable bonding* throughout this thesis.

In general, all non-critical components can be adjustably bonded onto the baseplate. In the same manner as for template bonding, the optical bench has to be

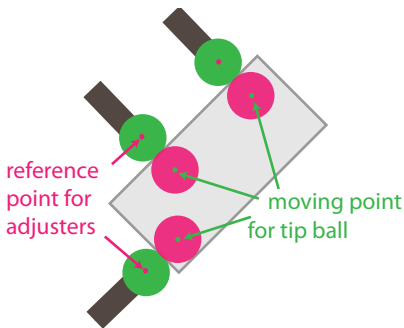


**Figure 2.10.:** Illustration of the reference point and moving point for adjustable bonding.

tilted by a small angle to ensure contact with the currently bonded component with the three spheres. The cleaning procedure described in Section 2.1 has to be performed and the cleaned surface should be kept wet. A measurement program has to be written including an automatic process for probing the desired features. For this reason the nominal positions, in the following referred to as *reference points*, for the three spheres attached to the adjusters as well as the three appropriate *moving points* have to be calculated by Ifocad. The desired position of the tip ball centre is referred to as the moving point. It is used to provide a reference for the adjusters, as illustrated in Figure 2.10. A typical measurement program for our purpose comprises the following steps:

1. Qualification of the touching probe with its various orientations that will

be used through the measurement program. Due to the fact that this process is referred to as *probe calibration* in the used software, the term *calibration* will be used instead of qualification [58]. The tip ball is calibrated with respect to its probe head reference point by measuring a (calibrated) reference sphere fixed to the granite table using 25 points on its surface [54]. In doing so, the probe tip's performance is estimated as well as the effective tip diameter. Although it is time consuming, the calibration of the probe head has to be repeated after each rotation of its probe head. This is the only way to ensure high accuracy in point measurements. The lower right photograph of Figure 2.7 shows a calibration procedure.

2. Determination of the optical bench position and orientation ( $\Rightarrow$  creation of OBF) in relation to the MCS. The term *alignment* will be used because the orientation of a workpiece is measured and a new coordinate system is constructed. This alignment procedure involves two steps:
  - Measuring manually several points distributed among three mutually orthogonal surfaces of the optical bench. Typically, the minimum number of points (six) are used to determine the initial rough coordinate system, as described in Section A.2.
  - Measuring in computer numerical control (cnc) mode the same three surfaces with more points. These points are more accurate than those measured in manual mode, because the machine motion parameters are controlled. Furthermore, the plane will be calculated with higher accuracy if more than three points are measured. The intersection point of these three planes defines the origin  $O$  of the redefined coordinate system OBF. Such an approach is illustrated in the left photograph in Figure 2.11 and described in detail in Section A.2.
3. Moving the tip ball to the moving point with an appropriate orientation of its probe head.
4. Positioning of the first adjuster by touching the tip ball. Its initial orientation is determined manually by touching the sphere as well as the front surface of the spindle using at least five points each. Once the rough alignment is established, the spindle and sphere are probed in cnc mode using more points yielding the ACF. This is illustrated in the upper right photograph of Figure 2.11.
5. In an iterative loop the sphere surface is remeasured in cnc mode, while the actual position is compared to the reference point. This deviation is

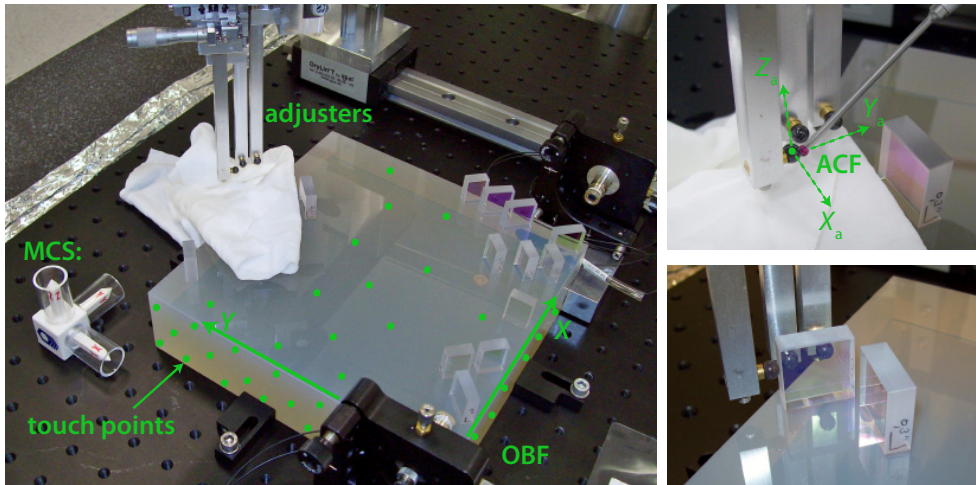


**Figure 2.11.:** *Left:* Alignment procedure of the optical bench in relation to the machine coordinate system (MCS). The green dots represent touch points for determining three planes in space yielding the auxiliary coordinate system of the optical bench (OBF). *Upper right:* Adjusters forming the three-point-reference with its appropriate coordinate system ACF. *Bottom right:* Bonded optical component enclosed by the adjusters.

computed and used to readjust the adjuster. Its coordinate frame is automatically adapted by feeding the performed translational displacement for the  $X_a$ - and  $Y_a$ -direction. This iterative procedure is completed when the reference point corresponds with the measured value to better than  $2\ \mu\text{m}$ .

6. Repeating steps 3.-5. for the two remaining adjusters.

Depending on the time period of the above described alignment process the optical bench has to be prepared again as described in Section 2.1. In that case all steps have to be repeated. Since the optical bench is adequately defined in the machine coordinate system by its mounting, the new orientation is close to the ideal one and the time period for readjusting the three-point-reference is shorter. Once the adjusters are aligned, the bonding fluid can be applied on the component surface and located against the three spheres. The alignment tool remains in its position for at least two hours until the component has settled and the bond has started to harden. Afterwards the alignment tool is removed to be reused for the next component. An adjuster-aided bonded component is shown in the bottom right picture of Figure 2.11.

### 2.3.5. Adjuster aided bonding to heterodyne signals

The most demanding stage in constructing precise interferometers is the alignment of critical components. Since non-critical components bonded previ-

ously can introduce position and angular errors, the beam combiners have to be aligned by injecting two interfering beams into the interferometer. Thus, they can compensate for previous errors and are identified as utmost critical.

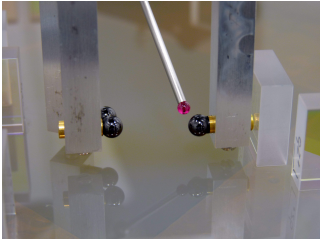


**Figure 2.12.:** Three-point-reference for a beam combiner.

As ‘out-of plane’ degree errors can be influenced only by optical component tolerances and by an appropriate alignment of the fibre injectors, the compensation through the recombiner is possible only for the two DoF of the ‘in-plane’ misalignment. In order to position components onto a baseplate, the principle of a three-point-reference system is used, as with template bonding or adjustable bonding. For this purpose, the alignment tool (*cf.* Section 2.3.1) is adapted by applying some minor modifications, such as a relocation of the adjusters to prevent blocking of the beams. This is depicted in Figure 2.12, where the probe is measuring the position of the adjusters. It is optional to realise a rough alignment of the three-point-reference frame by using the CMM. Nonetheless, it is also possible to orientate the adjusters by touching only the tip ball at each of its moving points.

By aligning the component in one lateral and one angular degree of freedom, the overlap of the two beams can be adjusted. The two interfering beams are measured by a photodetector and the heterodyne beat note is monitored by an oscilloscope. There is exactly one optimal position for a beam combiner, where the relative displacement and angle between the two beams is minimal yielding maximum contrast  $c$ . The contrast is calculated from the measured photocurrent  $I$  as

$$c = \frac{I_{\max} - I_{\min}}{I_{\max} + I_{\min}}, \quad (2.3)$$

where  $I_{\max}$  is the peak and  $I_{\min}$  the minimum of the measured beat note current. The attainable contrast depends on various beam parameters such as:

$$q = iz_R + z, \quad p = \frac{1}{q}, \quad k = \frac{2\pi}{\lambda}, \quad (2.4)$$

and the misalignment in angle  $\Delta\alpha$  and displacement  $\Delta x$  of the two combined beams, respectively. Note that the two misalignments have the same sign if the beams are divergent. For two beams with identical power, polarisation and beam parameter, the amplitude  $A$  obtained and thus the contrast can be

expressed by [59]

$$A = \exp\left(\frac{k[\Delta\alpha(\Delta\alpha - 2p\Delta x) + \Delta x^2 pp^*]}{4z_R}\right), \quad (2.5)$$

$$c = |A|. \quad (2.6)$$

Typically, the power of each beam ( $P_1$  and  $P_2$ ) is not identical. Therefore, a relationship between the contrast and heterodyne efficiency  $\gamma$  can be written as [60]

$$c = 2\frac{\sqrt{P_1 \cdot P_2}}{P_1 + P_2}\sqrt{\gamma}. \quad (2.7)$$

Therefore, the two beams have to be independently monitored by a second photodetector and, if possible, adjusted to equal power.

However, once the bonding fluid is applied to the component, the time period left for manipulating the component is less than one minute. This time is insufficient to complete the alignment procedure. Therefore, a buffer solution was used instead of the bonding fluid to allow alignment until maximum contrast was achieved. As a buffer liquid, an alkane such as n-Octane  $C_8H_{18}$  is suitable [61]. The initial amount of this buffer solution can be large but needs to be decreased before the final bonding process takes place. The procedure including a buffer solution was originally developed for construction of the prototype optical bench and for the engineering model of the LISA Pathfinder optical bench at UGL [44].

As long as the recombiner is gliding on the liquid, both the position and angle are iteratively varied in small steps until the contrast is optimised. Henceforth, the contrast is optimised by monitoring it on an oscilloscope. Once the optimum position is found, the bonding solution is applied and the optical component is relocated against the spheres. Again, the alignment tool remains in its position for a few hours until the bond has started to harden.

## 2.4. Appraisal of achievable accuracies

The central theme of this section is the evaluation of the achievable alignment accuracy and CMM measurement uncertainty. Previously, two different methods to locate components onto a baseplate were introduced. In order to adopt the applicable method with respect to required tolerances, the achievable accuracy has to be estimated. In the following, all assumptions are based on a worst case scenario.

### **Template bonding:**

Typically, the template is manufactured in the mechanical workshop at the AEI. Using a computer numerically controlled vertical milling machine, holes are machined in the (brass) template, into which the spheres were pushed. In doing so, a machining accuracy for the location of the spheres of less than  $100\ \mu\text{m}$  can be obtained. Note that the holes for the spheres are machined with respect to one corner of the template. Thus, any tolerance errors in the size of the template will appear as an offset error in the hole positions yielding possible systematic angular errors. The components used throughout this thesis were between 15 and 20 mm wide. This resulted in a baseline of two spheres located on the long side of 9 and 14 mm, respectively, due to mechanical restriction of the engineering. Assuming a baseline of 9 mm and a worst case deviation of  $200\ \mu\text{m}$  (each sphere shows opposite maximal deviation of  $100\ \mu\text{m}$ ), a component will be rotated by 22 mrad corresponding to a beam rotation of 44 mrad. With a baseline of 14 mm a component will be rotated by 14 mrad, associated with a beam rotation of 28 mrad. In order to illustrate the significant dimension of such large angular deviations, the resulting lateral beam deviation after a path length of 50 cm is calculated to be 2.2 cm (44 mrad over 50 cm).

By measuring the actual location of each sphere on the template using a CMM, the resulting position and angular deviations can be calculated by comparing them to the nominal values obtained from the IfoCad model. With the same software the beam propagation through the interferometer can be simulated and the errors evaluated. Several options exist to compensate for such errors:

1. *Compensation through a beam combiner:* As mentioned earlier, the recombination beam splitter can compensate angular deviations in the ‘in-plane’ degree of freedom by adjuster aided bonding. However, an arm length mismatch will occur.
2. *Alignment of the template:* By calculating how the template has to be rotated and shifted in the ‘in-plane’ degrees of freedom to fit to the ideal model, the occurred deviations can be partly minimised. The final alignment of the template has to be accomplished by adjusting a single three-point-reference with the CMM.
3. *Omitting critical components:* Once it is identified that a component might introduce a significant misplacement after bonding, it can be adjustably bonded. Thus, it will be rated as critical and the template bonding is continued.



**Adjustable bonding:**

Since the CMM is a complex system, the associated measurement uncertainty has to be estimated with care. An evaluation of the different uncertainty sources and their contribution to the total measurement uncertainty is described in Appendix B. In addition, an analysis of the uncertainty budget for an alignment process of one adjuster with maximum distance to the origin  $O$  (approximately 280 mm) is presented. Taking into account the contributions of CMM related sources, such as its structure, the probing system, thermal sources as well as the influence of measurement strategies to the total uncertainty, a combined uncertainty of  $2.43\ \mu\text{m}$  (expanded uncertainty:  $4.86\ \mu\text{m}$ ) for positioning one adjuster is calculated.

In contrast to template bonding, a slightly larger baseline for the two front located spheres could be chosen, namely 12 and 17 mm. By assuming an unmodified combined uncertainty of  $2.43\ \mu\text{m}$  for all three spheres of one reference frame, an angular accuracy for a component of  $416\ \mu\text{rad}$  ( $5\ \mu\text{m}$  over a baseline of 12 mm) and  $295\ \mu\text{rad}$  ( $5\ \mu\text{m}$  over a baseline of 17 mm) as well as a minimum positioning accuracy of  $\pm 4.86\ \mu\text{m}$  can be estimated.

**Adjustable bonding to heterodyne signals:**

The last critical step for building a precision interferometer is the alignment of the beam combiner. Typically, this is done by the adjuster aided bonding method, where the overlap of the two interfering beams is maximised in place. The resulting contrast depends on how well a component can be controlled during such a procedure. Throughout this thesis the presented alignment tool in Section 2.3.1 is used. The translation stages have a setting accuracy at the  $1\ \mu\text{m}$  level over a range of 10 mm. Since all beam combiners were 20 mm wide, the mean baseline between the two front locating spheres during this procedure was 16 mm. With a  $2\ \mu\text{m}$  differential translation of the two adjusters, the component can be rotated by  $125\ \mu\text{rad}$  corresponding to a beam rotation of  $250\ \mu\text{m}$ . In order to achieve alignment tolerances at a few  $10\ \mu\text{rad}$  level, the adjusters need to be controlled at the sub-micron level. This can be realised by using piezoelectric linear actuators with step sizes at the nm level.



## Chapter 3

# 3 Absolute metrology of beam propagation axis

Various alignment techniques for manufacturing precision interferometers have been discussed in Chapter 2. Since the ‘out-of-plane’ degrees of freedom cannot be controlled by these techniques, the beams must be aligned to the plane of the optical bench by other means. Typically, the interferometers set up at the AEI involved two beams injected through optical fibres onto the optical bench.

One method developed to precisely align these two beams with respect to each other and the plane of the optical bench requires that the associated fibre injectors face each other. In addition, an auxiliary optical component, such as a beam splitter at normal incidence or a partially reflecting glass plate, is needed to reflect a part of the beam back to the fibre as well as to let the beam propagate to the other fibre injector. A schematic of this alignment method is presented in Figure 3.1. For a detailed description see Section 4.5. Such an alignment method ensures a parallelism of the two beams relative to the bench at the level of the mirror’s perpendicularity: less than 2 arcseconds ( $\leq 10 \mu\text{rad}$ ). Clearly, this technique has significant limitations such as the number of fibre injectors as well as the restriction that two fibre injectors have to face each other<sup>[1]</sup>, entailing additional optics to be bonded.

In the case of complex interferometers and potentially more than two interfering beams, a different method to align beams with respect to the optical bench is demanded. Therefore it is required to precisely measure the absolute position and propagation axis of a beam in space. To be compatible with the current alignment technique, the accuracy of such a measurement needs to be at the  $\mu\text{m}$  level with a few tens of  $\mu\text{rad}$ . Due to the fact that it will be adopted

<sup>[1]</sup>It is not mandatory that both face each other in a direct line. The beams can be redirected with additional mirrors.

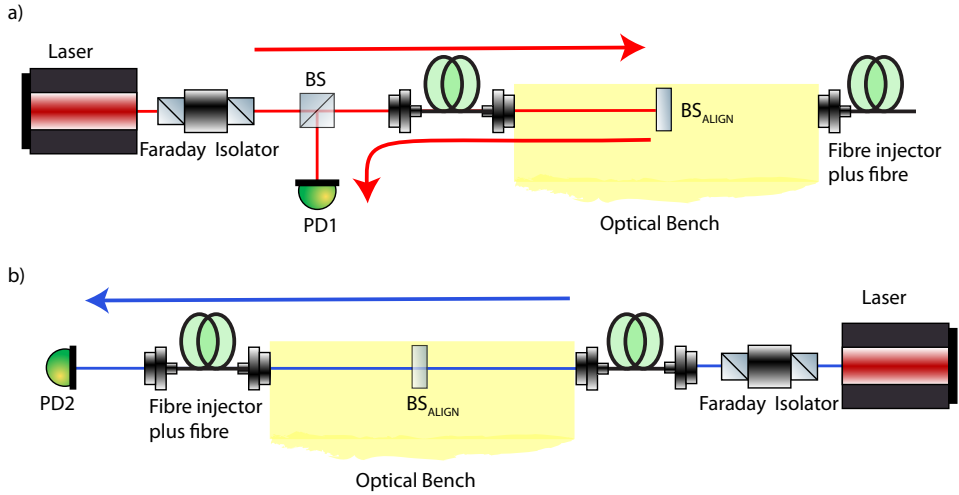


**Figure 3.1.:** Schematic of the alignment scheme of two fibre injectors: a) The ‘red’ beam is aligned parallel to the optical bench by coupling back the reflected part of the input beam; b) The ‘blue’ beam of the second fibre injector is aligned parallel with identical height as the ‘red’ beam, by coupling the transmitted part in the first fibre injector.

in connection with the bonding technique, the beam measurement has to be performed in real time with a quick readout.

In general, laser beam propagation can be approximated by assuming that the laser beam has an ideal Gaussian intensity profile, which corresponds to the  $TEM_{00}$  mode. Unfortunately, the output from a real laser is not truly Gaussian and contains some higher-order modes. However, the output of a single-mode fibre can be seen as a very close approximation to a Gaussian profile, since it acts as a spatial mode-cleaner. Therefore, a circular symmetric wavefront with a Gaussian transverse irradiance profile can be assumed, which can, however, become truncated at some diameter. Reasons can be limiting apertures in the optical path after the fibre coupler. In Figure 3.3 the changes in the wavefront dimensions along the distance travelled are shown. By assuming that the beam centroid after traveling a certain distance is still at the intensity peak, this *power centre* can be defined as the beam centre. One method for determining the beam’s centroid is to use a quadrant photodiode (QPD). The active area of such a photodiode is split into four quadrants with a gap (or slit) of width  $w_g$ , as illustrated in Figure 3.2. In balancing the powers in all four individual quadrants, the beam posi-

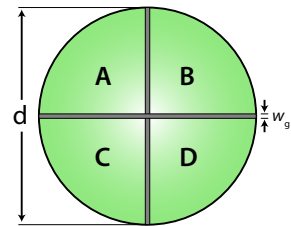


**Figure 3.2.:** Schematic of a quadrant photodiode.

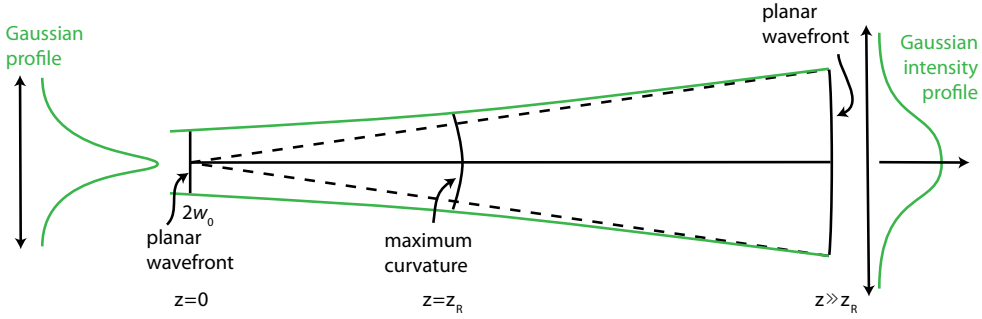


**Figure 3.3.:** Schematic of a Gaussian beam propagation. It begins with a planar wavefront with beam waist  $w_0$  and changes its wavefront along the distance travelled. After a distance  $z_R$  (Rayleigh range) the wavefront has attained its maximum curvature, while at  $z \gg z_R$  a planar wavefront is assumed again.

tion on the QPD can be obtained. The horizontal ( $\delta x$ ) and vertical ( $\delta y$ ) offsets of the beam centroid to the centre of the QPD are defined as

$$\delta x = \frac{P_{\text{left}} - P_{\text{right}}}{P_{\text{left}} + P_{\text{right}}}, \quad (3.1)$$

$$\delta y = \frac{P_{\text{top}} - P_{\text{bottom}}}{P_{\text{top}} + P_{\text{bottom}}}, \quad (3.2)$$

where the light power  $P_i$  is composed of the light power of each individual quadrant as follows

$$P_{\text{left}} = P_A + P_C, \quad P_{\text{right}} = P_B + P_D, \quad (3.3)$$

$$P_{\text{top}} = P_A + P_B, \quad P_{\text{bottom}} = P_C + P_D. \quad (3.4)$$

Note that if a beam is not circularly symmetric, the determined beam centroid will deviate from the true centre with an error bigger than tens of microns. Since beams injected from optical fibres are used with a sufficient circularity, no parasitic error contribution is expected.

By using Equations (3.1) and (3.2), the displacement of the beam centroid to the QPD centre can be calculated. If it would be possible to measure the exact position of the QPD, information about one single point of the beam related to the measurement coordinate system could be obtained. Using a CMM, the flexibility is given to relate the beam position to an arbitrary coordinate frame such as the MCS or the OBF (Section 2.3.3). In order to measure the physical position of a beam at a single point along its propagation axis, this propagation direction has to be additionally determined. This can be done by measuring the beam centroid in at least two spatially separated positions along the beam. This will give a line in space representing the beam's propagation direction.

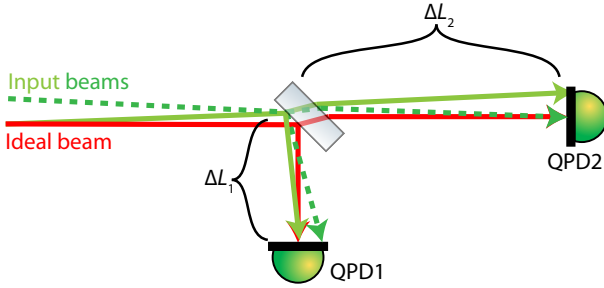


**Figure 3.4:** Principle of a CQP: The red line represents an ideal beam impinging on the two QPDs centred. Both green lines describe two different input beams deviating from the ideal beam by an angle and parallel offset, hitting only the centre of one QPD. The second QPD will not be hit simultaneously in the centre.

The drawback of such an approach is that only one position can be controlled at a time. Thus, the method is time consuming and the true position and direction cannot be precisely determined in real-time. In order to be applicable for constructing precision interferometers (*cf.* Chapter 2), two measurements need to be performed simultaneously. Within the framework of a master thesis [62] a device for determining a beam’s position and direction together with its calibration method (*cf.* Section 3.4) has been developed. Such a device will be referred to as *Calibrated Quadrant photodiode Pair* (CQP) throughout this thesis. The construction of our CQP is based on an existing CQP at the University of Glasgow [44].

### 3.1. Measurement principle of a CQP

A simultaneous measurement along the beam with two (or more) QPDs results in a baseline representing the beam axis. To realise such a measurement a beam needs to impinge on a beam splitter, of which both output ports are equipped with a QPD. The basic idea behind the CQP is to read out the photodiodes at different distances from the beam splitter. This distance is referred to as *effective distance*  $\delta_{\text{eff}}$  and describes the difference of the optical path lengths from the beam splitter to QPD1 ( $\Delta L_1$ ) and QPD2 ( $\Delta L_2$ ). The bigger the effective distance, the higher is the readout accuracy for the angle. This principle is illustrated in Figure 3.4. The red line represents an ideal beam impinging on the two QPDs centred. If a tilted beam (green) would impinge on one QPD surface centred, the other part of the input beam will hit the other QPD with an offset from its centre. Thus, one unique equation describing the beam position and propagation direction with respect to the CQP can be found for a specific assembly of beam splitter and QPDs. In order to obtain such an equation, the exact position of the beam centroid has to be known. Unfortunately, it is not feasible to measure the centre of a photodiode using a CMM. Hence, a stable

structure housing at least a beam splitter and two QPDs is desired. Aligning this housing to the beam by centring the beam on both QPDs ensures that the beam axis always follows the same path through the CQP. The position and orientation of the housing can be determined using the CMM. However, as long as the transformation between the optical beam and the structure is not known, the physical position of the beam in space cannot be determined. This transformation can be obtained by calibrating the CQP, which relates the QPD centres to their housing. Once the CQP is calibrated, it can be used not only for determining a beam's physical position but also act as a target. The use as a target can be realised by pre-positioning the CQP to a fixed position with a defined orientation and adjusting the beam to both QPD centres. Thus, any real beam can be aligned to the nominal beam of the CQP.

In order to take full advantage of such a device, positioning and manipulation at  $\mu\text{m}$  level is required. A hexapod is most suitable for an extreme fine control of the CQP's position. Throughout this thesis, a hexapod (*M-824.3VG*) from PI is used. It is a computer controlled 6-axis positioning platform, as shown in Figure 3.5 [63]. Two platforms are connected by six legs, where the minimum incremental motion is for the translation DoF at the sub-micron ( $0.3\ \mu\text{m}$ ) level with a travel range of  $\pm 22.5\ \text{mm}$  and  $\pm 12.5\ \text{mm}$  for the  $X$ - $Y$ -plane and  $Z$ , respectively. The resolution for rotation is  $3.5\ \mu\text{rad}$  with a travel range of  $\pm 7.5^\circ$  and  $\pm 12.5^\circ$  for  $\vartheta_x / \vartheta_y$  and  $\vartheta_z$ , respectively. The platform has a diameter of approximately 25 cm. For controlling the hexapod, the software PI Micromove

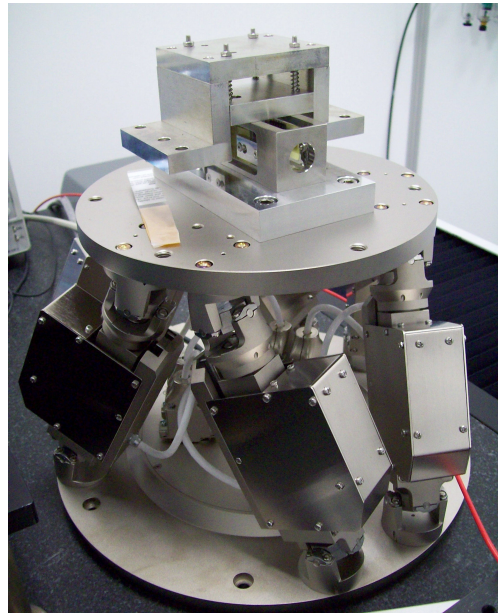


**Figure 3.5:** Photograph of the used hexapod along with the CQP. The CQP is attached on the upper platform via a mount based on a bridge architecture.

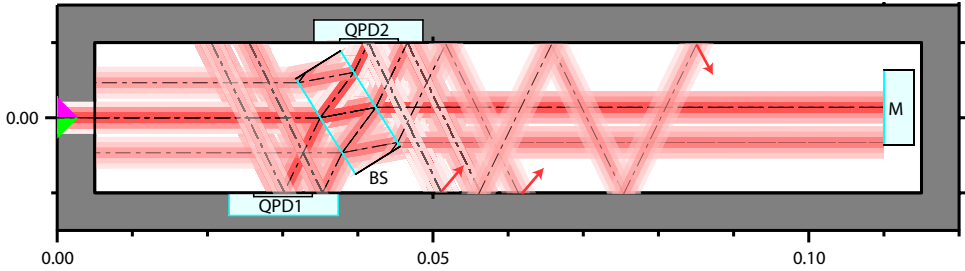


**Figure 3.6.:** OptoCad model of the CQP. The optical layout is done by IfoCad, whereas the stray light simulation is performed with OptoCad. The design provides a beam splitter rotated by  $30^\circ$ , a  $0^\circ$ -mirror at the rear side as well as two QPDs.

is used. The CQP is mounted on the hexapod to take full advantage. In order to minimise the possibility of mechanical deformations, a bridge construction was used to clamp the CQP onto the hexapod platform, as can be seen in Figure 3.5. In doing so, the same pressure is put each time onto the CQP. That ensures reliability of the determined calibration parameters. This necessity resulted from experience with the CQP at UGL [44].

## 3.2. CQP design

In order to use the CQP for alignment purposes in a bonding procedure, a stable and accurate device with a quick readout is required. Although the underlying principle of a CQP is very simple, various constraints have to be considered. Some of them arise due to the use of auxiliary tools such as the CMM and the hexapod and can be summarised as follows:

- The CQP needs to determine a beam with an accuracy at the  $\mu\text{m}$  and few  $10\ \mu\text{rad}$  level, or better.
- The effective distance has to be big enough to ensure a precise alignment of the CQP to the input beam.
- The size of the CQP needs to be small enough to fit in the measurement volume of the CMM alongside the optical bench and the hexapod. Furthermore, the weight of the CQP assembly is not allowed to exceed 5 kg.
- The housing of the CQP has to enable a reliable probing with the CMM.
- The CQP has to be symmetric under rotation to simplify the necessary calibration.



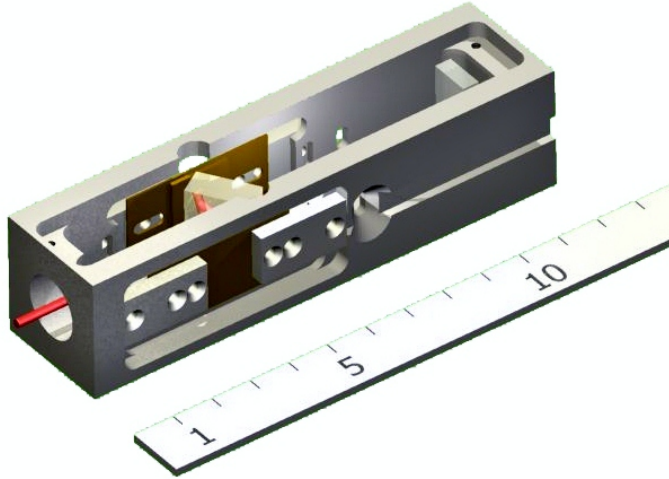


**Figure 3.7.:** CAD model of the CQP. With a footprint of  $30 \times 30 \times 120 \text{ mm}^3$  it houses a beam splitter, a mirror and two QPDs. For the input beam an aperture on the front side is foreseen. Apart from that, the inner life of the CQP is enclosed light-tight by an additional lid (not shown in the picture). In this way, background light and air fluctuations can be suppressed.

- Air fluctuations as well as background light hitting the QPD have to be minimised.

Using the software *IfoCad* in combination with *OptoCad* and the CAD program *Autodesk Inventor*, a device has been designed that satisfies the exacting constraints. In Figure 3.6 the optical layout is depicted. The number of components is kept small to mitigate angular deviations over long time periods due to moving components, which would lead to poor reliability. If a component moves, the nominal axis of the CQP changes and thus the corresponding calibration is no longer valid. A beam splitter located as close as possible to the front panel redirects the input beam to the first QPD, while the transmitted beam is propagating to the second QPD. To ensure an adequate resolution of the angular alignment, this optical path is folded. Thus, the effective distance is doubled to approximately 13 cm. Assuming a fluctuation of the beam centroid around the QPD centre by  $\pm 1 \mu\text{m}$ <sup>[2]</sup>, the effective distance leads to an angular uncertainty of centring the beam centroid on the QPD to approximately 15  $\mu\text{rad}$ .

<sup>[2]</sup>Due the stable housing, which suppresses background light and air fluctuations, in combination with an appropriate signal-to-noise ratio such a resolution is feasible. However, this assumes a stable beam and stably mounted QPDs.

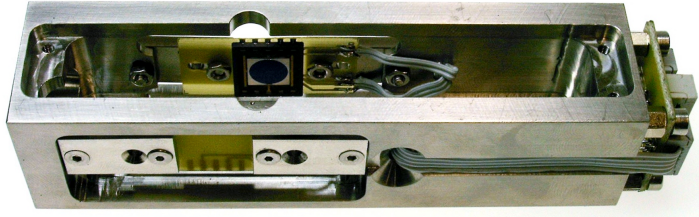


**Figure 3.8.:** Photograph of the final CQP housing. Both QPDs, soldered on small circuit boards, are attached to mounts, which enable adjusting to the nominal beam centre. The signals obtained are sent over a flat wire cable to another circuit board at the rear side (right), where they are sent to an electronic device for further processing.

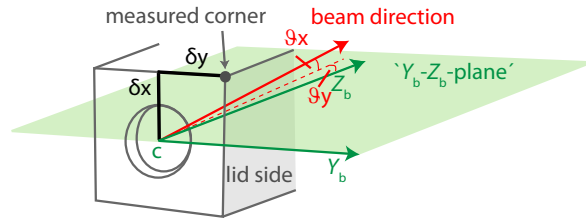
Figure 3.7 shows the CAD model of the CQP. To suppress background light as well as air fluctuations influencing the readout accuracy, the CQP is enclosed by a housing. This housing has dimensions of  $30 \times 30 \times 120 \text{ mm}^3$  with a centred hole in the front panel. The nominal axis of the housing has been designed to be co-aligned the rotation axis and later additionally the beam axis. Hence, the beam height with respect to its baseplate is 15 mm. Since investigations on the reflectivity of the photodiodes used revealed a backscattering of around 10% even though their windows were removed [62], a stray light analysis was performed. Simulations with `OptoCad` for several optical design alternatives were performed. The resulting design choice uses a beam splitter with an angle of incidence of  $30^\circ$ . For further suppression of stray light, the reflected beams from the photodiodes are blocked by mounting plates of anodised aluminium to the inside of the housing at beam height. In this way, the influence on the resolution by back-reflection occurring at the active area of the photodiode could be eliminated.

### 3.3. CQP architecture

After completing the design the construction process could begin. The manufacturing of the CQP is not described here for the sake of brevity, instead the reader is kindly referred to reference [62], where, in addition, a prototype based on aluminium and the construction process of both versions is described in detail. In this section the final CQP, its components and materials used will be only briefly described. A photograph of the final CQP assembly is shown in Figure 3.8.

To ensure high rigidity of the CQP the housing was made of Invar<sup>®</sup>, an iron nickel alloy. The inherent advantage of this material is a very low coefficient of thermal expansion of  $2 \times 10^{-6} \text{ K}^{-1}$ . This yields an estimated length expansion

**Figure 3.9:** The CQP with its angular and offset parameters, required to define the optical beam. For measuring a beam in space the CQP is placed in its initial position with the lid facing east. Its orientation and the upper right corner are determined.



of about  $0.24 \mu\text{m}/\text{K}$  for the CQP. The optical components, both made of fused silica, are glued with an epoxy resin (*ER2188*, Electrotube) onto the Invar<sup>®</sup> housing. The low thermal expansion coefficient of  $40 \text{ ppm}/\text{K}$  [64] yields negligible angular errors in the CQP length scale.

The silicon QPDs used have a large active area of  $4 \times 11.78 \text{ mm}^2$  and feature a very small separation between the four segments of  $18 \mu\text{m}$  (*QP50-6-18u-SM*, Pacific Silicon Sensor) [65]. Two advantages of this model are the very low dark current of  $\sim 2 \text{ nA}$  and a capacitance per segment of only  $25 \text{ pF}$  at  $10 \text{ V}$ . Both QPDs were reverse biased with  $9 \text{ V}$  and soldered each to a circuit board screwed with an auxiliary mount to the CQP. The mount was designed to allow alignment of  $5 \text{ mm}$  and  $9 \text{ mm}$  in vertical and horizontal direction, respectively. Each QPD is read out by a five-channel flat wire cable connected to a final circuit board at the rear side of the CQP. The bundled signals are sent to an electronic device, where the displacement signals  $\delta x$  and  $\delta y$  along with the DC value of each quadrant and their sum is calculated for both diodes. The signals obtained were displayed on an oscilloscope allowing simultaneous read-out of both QPDs.

An appropriate alignment of the two QPDs with respect to the nominal axes of the CQP is of crucial importance. By rotating the CQP around its nominal axis and iteratively aligning at each stage the centre of the QPD to comply with the beam centroid, we can ensure that the beam axis agrees well with the rotation axis. Once the optimum position for the QPDs is found, they are glued in place to minimise the possibility of movement.

### 3.4. Calibration

By using the CMM, the position and orientation of the CQP can be measured. However, the physical position of the CQP does not directly reveal the desired beam position and direction. A relationship between the measurable housing of the CQP and the beam vector needs to be established by calibrating the CQP. In Figure 3.9 four calibration factors are illustrated. In order to define

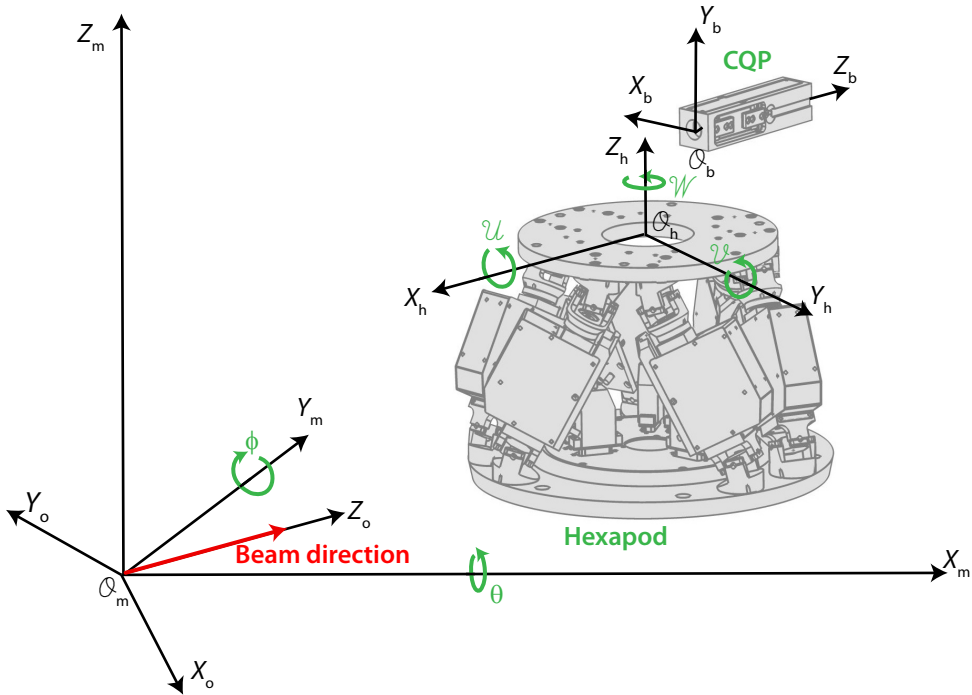


**Figure 3.10.:** Schematic of several coordinate frames (additional to Figure 2.9) used in combination with the CQP: machine coordinate system (subscript: m), optical beam coordinate frame (subscript: o), Hexapod coordinate frame (subscript: h) and CQP box coordinate frame (subscript: b).

the beam centroid in relation to the CQP, two offset parameters  $\delta x$  and  $\delta y$  define the distance of one certain corner with the beam incidence at the CQP. The remaining two parameters  $\vartheta x$ ,  $\vartheta y$  describe the angular deviation of the incident beam and the nominal axis of the CQP ( $Z_b$ , green).

Typically, a workpiece probed by a CMM is evaluated in the machine coordinate system (MCS), as introduced in Section 2.3.3. To be of any use, the parameters obtained defining the relation between CQP and beam vector have to be independent from the MCS but rather be directly related to the housing. Therefore, in addition to the coordinate frames introduced in the previous chapter (Figure 2.9), several auxiliary coordinate frames are defined. They are illustrated in Figure 3.10.

**BCF: CQP Box Coordinate Frame** This frame is defined by the geometry of the CQP and thus related to the axes of its CQP housing. The  $Z_b$  direction corresponds with the normal vector of the front panel, directing along the long side of the housing, while the  $X_b$ -axis points along the line of inter-

section between the front panel and the lid. The origin  $O_b$  is located at the front panel centre, where the aperture for the optical beam is. The calibration parameters describe the position and direction of the nominal beam within this reference frame.

**HCF: Hexapod Coordinate Frame** This frame is defined by the hexapod itself. Its origin  $O_h$  is the rotation point (pivot point) and can be shifted with a user command by any amount desired. In this particular frame the pivot point is located at the centre of the upper platform. The hexapod is placed in such a way that the  $X_h$ -axis points roughly along the opposite beam direction, while the  $Z_h$ -axis points out of the platform. The three rotations of the hexapod are defined as follows: a rotation around  $X_h$  defines the angle  $u$ , a rotation around  $Y_h$  defines the angle  $v$  whereby a rotation around the  $Z_h$ -axis defines the angle  $w$ . All six DoF have been calibrated and are related to the MCS such that the CQP can be placed in a defined position in the desired orientation.

**OCF: Optical Beam Coordinate Frame** A beam coordinate system is necessary to correct for movements along the beam direction during each calibration step. In this frame the optical beam points along the  $Z_o$  direction. The origin  $O_o$  coincides with the one in MCS. The knowledge of the exact direction either of  $X_o$  or  $Y_o$  is not important. They are defined by the coordinate transformation and will be invariant under all calibration steps.

An appropriate transformation from MCS to OCF is performed by two rotations, one around the  $X_m$ -axis by angle  $\theta$  and a second one about the  $Y_m$ -axis by  $\phi$ . Since the optical beam axis in the machine coordinate system is the  $Z_o$ -axis, a rotation around this axis can be ignored. Thus, the beam direction can be expressed in the MCS as

$$\begin{aligned} R_x \cdot R_y \cdot \begin{pmatrix} 0 \\ 0 \\ 1 \end{pmatrix} &= \begin{pmatrix} 1 & 0 & 0 \\ 0 & \cos(-\theta) & -\sin(-\theta) \\ 0 & \sin(-\theta) & \cos(-\theta) \end{pmatrix} \begin{pmatrix} \cos(-\phi) & 0 & \sin(-\phi) \\ 0 & 1 & 0 \\ -\sin(-\phi) & 0 & \cos(-\phi) \end{pmatrix} \begin{pmatrix} 0 \\ 0 \\ 1 \end{pmatrix} \\ &= \underbrace{\begin{pmatrix} \cos(\phi) & 0 & -\sin(\phi) \\ \sin(\theta) \sin(\phi) & \cos(\theta) & \sin(\theta) \cos(\phi) \\ \cos(\theta) \sin(\phi) & -\sin(\theta) & \cos(\theta) \cos(\phi) \end{pmatrix}}_R \begin{pmatrix} 0 \\ 0 \\ 1 \end{pmatrix} \end{aligned} \quad (3.5)$$

$$= \begin{pmatrix} -\sin(\phi) \\ \sin(\theta) \cos(\phi) \\ \cos(\theta) \cos(\phi) \end{pmatrix} =: \begin{pmatrix} \alpha \\ \beta \\ \gamma \end{pmatrix}^{\text{MCS}}. \quad (3.6)$$

In order to transform any vector from MCS to OCF, the transpose of the matrix

$R$  was used. Rotation matrices are unitary, thus  $R^{-1} = R^T$ . Since a beam direction can be directly determined in MCS, the Euler angles  $\theta$  and  $\phi$  can be described by the coordinates of the beam direction as

$$\sin(\phi) = -\alpha, \quad \cos(\phi) = \sqrt{\beta^2 + \gamma^2}, \quad (3.7)$$

$$\sin(\theta) = \frac{\beta}{\sqrt{\beta^2 + \gamma^2}}, \quad \cos(\theta) = \frac{\gamma}{\sqrt{\beta^2 + \gamma^2}}. \quad (3.8)$$

Hence, the necessary rotation matrix for an OCF transformation can be written as

$$R^{-1} = \begin{pmatrix} \sqrt{\beta^2 + \gamma^2} & -\frac{\alpha\beta}{\sqrt{\beta^2 + \gamma^2}} & -\frac{\alpha\gamma}{\sqrt{\beta^2 + \gamma^2}} \\ 0 & \frac{\gamma}{\sqrt{\beta^2 + \gamma^2}} & \frac{\beta}{\sqrt{\beta^2 + \gamma^2}} \\ \alpha & \beta & \gamma \end{pmatrix}. \quad (3.9)$$

As the first calibration stage the alignment of the two QPDs to a stable beam by rotating about the beam axis can be considered. In doing so one ensures that the rotation axis agrees with the optical beam axis. The accuracy is limited by the angle resolution defined by the baseline of the two QPDs.

The next stage can be split into three steps, all of which involve the use of the CMM. By probing several features of the housing with an appropriate number of points, the alignment in the BCF can be established. Since the Invar<sup>®</sup> housing has a rough surface finish, the same points should be probed each time to improve the repeatability of the BCF and all desired features, such as the beam vector or the calibration vectors. In order to avoid systematic errors in the CQP calibration due a poor probe calibration, the same orientation of the probe head is used for all steps. Furthermore, the incident beam needs to be stable at the  $\mu\text{m}$  (and a few  $\mu\text{rad}$ ) level over the duration of the calibration procedure (approximately 1 hour).

The three consecutively steps representing the calibration procedure can be described as follows:

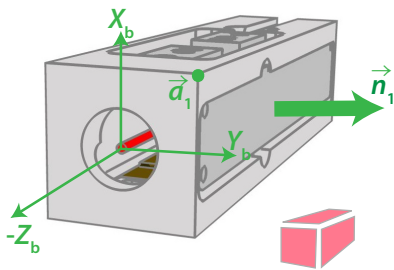


**Figure 3.11.:** Step 1 of the calibration.

**Step 1:** In the initial position of the CQP (lid is facing east) several points on the CQP front panel, lid surface and aperture are measured manually to establish a rough alignment of the BCF. This will be denoted as  $\text{BCF}_{\text{man}}$ . Henceforth, all individual steps for calibration will be related initially to that frame. Thus, it is ensured to probe identical points on the CQP at all stages. However, an alignment with high precision has to be established to enhance the calibration reliability.

Therefore, the same features are probed in cnc-mode with numerous points. The  $\text{BCF}_{\text{cnc}}$  is depicted in Figure 3.11 with its origin in the centre of the aperture. Next, three planes (the scaled-down illustration at the bottom right in Figure 3.11 represents the probed planes in red) are measured to determine the desired vector  $\vec{a}_1$ . This can be obtained by calculating the point where the intersection line between upper and lid plane intersects the front plane (piercing point). In addition, the normalised normal vector  $\vec{n}_1$  of the lid plane is obtained. In total, the first calibration step yields

$$\Rightarrow \vec{n}_1 \text{ and } \vec{a}_1.$$

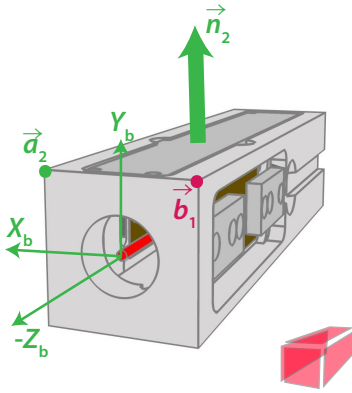


Figure 3.12.: Step 2 of the calibration.

**Step 2:** The CQP is rotated about the beam axis by  $\approx 90^\circ$  ( $\vartheta$ ) and both QPDs are aligned to the optical beam by moving the hexapod. The  $\text{BCF}_{\text{cnc}}$  is established by probing the same features as in step 1. In this configuration four planes are measured (as depicted in the Figure 3.12) to determine the position of the two upper corners ( $\vec{a}_2$ ,  $\vec{b}_1$ ) on the CQP and the normal vector  $\vec{n}_2$  of the lid side. Since the related coordinate frame is in approximation the same as in step 1, point  $\vec{a}_1$  is consistent with point  $\vec{a}_2$  as well as  $\vec{n}_1$  with  $\vec{n}_2$ . The second calibration step yields

$$\Rightarrow \vec{n}_2, \vec{a}_2 \text{ and } \vec{b}_1.$$

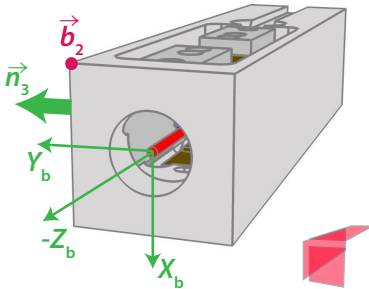
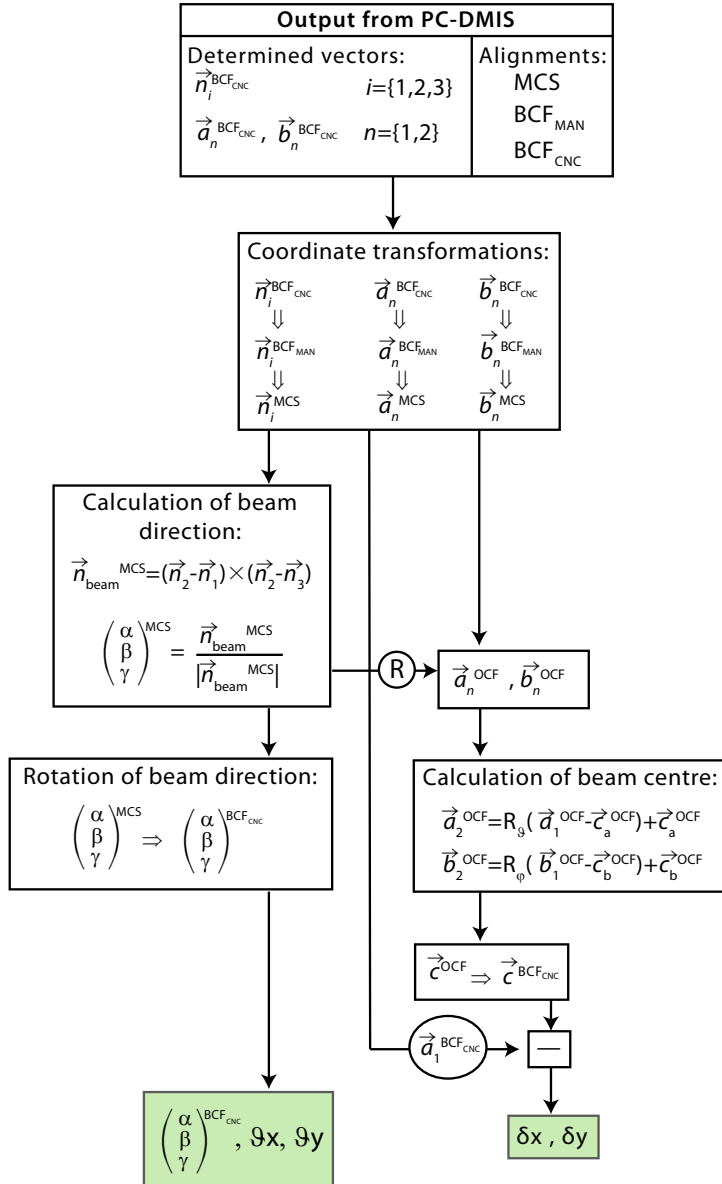


Figure 3.13.: 3. step of the calibration.

**Step 3:** The CQP is rolled about the the beam axis by another  $\approx 90^\circ$  ( $\varphi$ ) and aligned to the optical beam. After determining the alignment BCF in cnc-mode, three planes, as illustrated in red in Figure 3.13, are probed to calculate the position of the upper left corner  $\vec{b}_2$  and once again the normal vector of the lid  $\vec{n}_3$ . Due to the fact that all measurements are related to the same coordinate frame, the two vectors describing corner b are identical in a first approximation. Thus, the third calibration step yields

$$\Rightarrow \vec{n}_3 \text{ and } \vec{b}_2.$$



**Figure 3.14.:** Flow chart of the calibration algorithm: The parameters obtained from the workpiece's program such as the normal vectors  $\vec{n}_i$ , the four corners  $\vec{a}_n$  and  $\vec{b}_n$  as well as several alignments (MCS, BCF) are processed using a computer program written in C. The beam direction and the beam centroid are computed. Finally, the required offset parameters  $\vartheta x, \vartheta y, \delta x$  and  $\delta y$  are transformed into the CQP box coordinate system BCF (in cnc-mode).



The output of the part program from PC-DMIS includes the two measured alignments  $BCF_{\text{MAN}}$  and  $BCF_{\text{CNC}}$  as well as the position of the two front corners and the normal vector of the lid for the three different configurations. In order to derive the beam equation, various calculations, such as to retrieve the beam direction and the offset parameters of the beam centroid with respect to one certain corner on the CQP, have been implemented in a program written in the C language. In the following sections, a summary is given of how the direction and position is derived. For a detailed derivation the reader is kindly referred to [62]. The corresponding calibration algorithm is illustrated in a flow chart in Figure 3.14.

### 3.4.1. Calculation of the beam direction

The normal vectors  $\vec{n}_i$  ( $i=\{1,2,3\}$ ) change their direction within the machine coordinate system through the calibration procedure, but in BCF they remain the same except for measurement errors. In MCS their relation to each other can be expressed by rotation around the beam axis as

$$\vec{n}_2 = \begin{pmatrix} \cos(\vartheta) & -\sin(\vartheta) & 0 \\ \sin(\vartheta) & \cos(\vartheta) & 0 \\ 0 & 0 & 1 \end{pmatrix} \vec{n}_1 \quad \text{and} \quad \vec{n}_3 = \begin{pmatrix} \cos(\varphi) & -\sin(\varphi) & 0 \\ \sin(\varphi) & \cos(\varphi) & 0 \\ 0 & 0 & 1 \end{pmatrix} \vec{n}_2. \quad (3.10)$$

Due to the fact that only vectors approximately perpendicular to the beam axis are transformed, it is reasonable to divide the normal vector into a part perpendicular to and one parallel to the beam axis. Since vectors parallel to the rotation axis do not change under rotation, these parts of each normal vector are identical. Hence, two vectors perpendicular to the beam axis can be calculated by differencing two of  $\vec{n}_1$ ,  $\vec{n}_2$ ,  $\vec{n}_3$ . In order to determine the beam direction, the cross product of these two vectors has been formed, while considering the right-hand rule. The calculated beam direction  $\vec{n}_{\text{beam}}$  points along the rotation axis and can be expressed by

$$\begin{aligned} \vec{n}_{\text{beam}} &= (\vec{n}_2 - \vec{n}_1) \times (\vec{n}_2 - \vec{n}_3) & (3.11) \\ &= (\vec{n}_2^\perp - \vec{n}_1^\perp) \times (\vec{n}_2^\perp - \vec{n}_3^\perp) \quad \text{and} \quad \begin{pmatrix} \alpha \\ \beta \\ \gamma \end{pmatrix}^{\text{MCS}} = \frac{\vec{n}_{\text{beam}}}{|\vec{n}_{\text{beam}}|}. \end{aligned}$$

Since the part program (PC-DMIS) yields the used coordinate axis in relation to the foregone coordinate systems such as the MCS or the  $BCF_{\text{MAN}}$ , the transformation of the beam direction denoted in MCS to the desired  $BCS_{\text{CNC}}$  can be performed as

$$\begin{pmatrix} \alpha \\ \beta \\ \gamma \end{pmatrix}^{\text{BCF}_{\text{MAN}}} = \begin{pmatrix} \cdot & \cdot & \cdot \\ \vec{X}_b^{\text{MCS}} & \vec{Y}_b^{\text{MCS}} & \vec{Z}_b^{\text{MCS}} \\ \cdot & \cdot & \cdot \end{pmatrix} \begin{pmatrix} \alpha \\ \beta \\ \gamma \end{pmatrix}^{\text{MCS}}, \quad (3.12)$$

followed by the final transformation

$$\begin{pmatrix} \alpha \\ \beta \\ \gamma \end{pmatrix}^{\text{BCF}_{\text{MAN}}} \Rightarrow \begin{pmatrix} \alpha \\ \beta \\ \gamma \end{pmatrix}^{\text{BCF}_{\text{CNC}}}. \quad (3.13)$$

Thus, the relationship between the beam direction and the CQP housing is determined.

### 3.4.2. Calculation of the beam centroid

In order to calculate the incidence of the optical beam onto the CQP housing and thus the beam centroid, the four determined vectors ( $\vec{a}_n, \vec{b}_n, n=\{1,2\}$ ) are used. In the machine coordinate system they appear to be four individual corners of the CQP, but essentially two corners are measured, each in two different orientations. By transforming these position vectors into the optical beam coordinate frame using Equation (3.4), each corner is projected in a plane being perpendicular to the beam axis. Since it is assumed that the  $Z_o$ -component lies on the beam axis and is the same for all points in that plane, the calculation of the beam centroid can be simplified from a three-dimensional to a two dimensional function. To make use of the beam centroid in that particular frame it needs to be transformed back into the CQP box coordinate frame, where the final offset parameters  $\delta x$  and  $\delta y$  can be determined.

By using Equation (3.10), the measured corners  $\vec{a}_1^{\text{OCF}}$  as well as  $\vec{b}_1^{\text{OCF}}$  could be rotated in the  $X_o - Y_o$ -plane anticlockwise by an angle  $\vartheta$  and  $\varphi$  about the beam axis, respectively. In doing so, the beam centre could be determined twice. Since such a rotation has to be performed about the origin of the corresponding coordinate system (here the  $Z_o$ -axis with  $O_o$ ), the actual rotation point has to be shifted to the origin. This can be done by translating the four corners parallel in the  $X_o - Y_o$ -plane by the beam centroid  $\vec{c}_n$ . Such a transformation from a vector  $\vec{a}$  by a vector  $\vec{c}$  can be expressed with a translation matrix  $T$  as follows [66]

$$\begin{pmatrix} a'_x \\ a'_y \\ 1 \end{pmatrix} = \underbrace{\begin{pmatrix} 1 & 0 & c_x \\ 0 & 1 & c_y \\ 0 & 0 & 1 \end{pmatrix}}_T \begin{pmatrix} a_x \\ a_y \\ 1 \end{pmatrix}. \quad (3.14)$$

Hence, the transformation for the first corner  $\vec{a}$  in OCF, which is composed of a translation and a rotation about the beam axis by an angle  $\vartheta$ , can be written as

$$\begin{pmatrix} a_{2,x} - c_{a,x} \\ a_{2,y} - c_{a,y} \end{pmatrix}^{\text{OCF}} = \begin{pmatrix} \cos(\vartheta) & -\sin(\vartheta) \\ \sin(\vartheta) & \cos(\vartheta) \end{pmatrix} \begin{pmatrix} a_{1,x} - c_{a,x} \\ a_{1,y} - c_{a,y} \end{pmatrix}^{\text{OCF}}. \quad (3.15)$$

In same manner, the relation between the two measurements for the second corner  $\vec{b}$  can be expressed by

$$\begin{pmatrix} b_{2,x} - c_{b,x} \\ b_{2,y} - c_{b,y} \end{pmatrix}^{\text{OCF}} = \begin{pmatrix} \cos(\varphi) & -\sin(\varphi) \\ \sin(\varphi) & \cos(\varphi) \end{pmatrix} \begin{pmatrix} b_{1,x} - c_{b,x} \\ b_{1,y} - c_{b,y} \end{pmatrix}^{\text{OCF}}. \quad (3.16)$$

By utilising the scalar product of the two measured normal vectors of the lid  $\vec{n}_i$ , both angles of rotation  $\vartheta$  and  $\varphi$  can be calculated. The first angle of rotation is given by [66]

$$\cos(\vartheta) = \frac{\vec{n}_1 \cdot \vec{n}_2}{|\vec{n}_1| |\vec{n}_2|}. \quad (3.17)$$

Since the only unknown parameter is the beam centroid, Equation (3.15) can be solved for [62]

$$c_{a,x_o} = \frac{a_{2,x_o} + a_{1,x_o}}{2} + \frac{(a_{1,y_o} - a_{2,y_o}) \sin(\vartheta)}{2(1 - \cos(\vartheta))}, \quad (3.18)$$

$$c_{a,y_o} = \frac{a_{2,y_o} + a_{1,y_o}}{2} - \frac{(a_{1,x_o} - a_{2,x_o}) \sin(\vartheta)}{2(1 - \cos(\vartheta))}, \quad (3.19)$$

and Equation 3.16 to

$$c_{b,x_o} = \frac{b_{2,x_o} + b_{1,x_o}}{2} + \frac{(b_{1,y_o} - b_{2,y_o}) \sin(\varphi)}{2(1 - \cos(\varphi))}, \quad (3.20)$$

$$c_{b,y_o} = \frac{b_{2,y_o} + b_{1,y_o}}{2} - \frac{(b_{1,x_o} - b_{2,x_o}) \sin(\varphi)}{2(1 - \cos(\varphi))}. \quad (3.21)$$

Thus, the beam centroid has been computed twice and could be averaged. Since both transformations were performed in the OCF, the averaged beam centroid  $\vec{c}^{\text{OCF}}$  needs to be transformed to the  $\text{BCF}_{\text{CNC}}$ . This can be done by using the rotation matrix  $R$  (see Equation (3.5)) to transform the beam centroid back to the MCS. From there it is easy to transform  $\vec{c}^{\text{MCS}}$  via the  $\text{BCF}_{\text{MAN}}$  to the required  $\text{BCF}_{\text{CNC}}$ . Note that the beam centroid had the same  $Z_o$ -component as the corner vectors, since they have been brought in the same  $X_o - Y_o$ -plane.

However, the basic idea behind the calibration is to relate the position and orientation of the CQP to the physical position of the beam. Therefore, the

beam centroid needs to be related to a certain feature on the CQP for each application. A suitable choice for this purpose is one front corner of the CQP. In our case the corner measured first during the calibration procedure  $\vec{a}_1$  serves as reference. In order to retrieve the beam incidence onto the CQP front panel, the offset parameters of the computed beam centroid to the reference are derived and computed in the CQP box coordinate frame. For reasons of simplicity they are stored together with the beam direction in a `.txt`-file, which can be used for any application. With the beam direction calculated in Section 3.4.1 sufficient parameters were calculated to retrieve the physical position of a beam in space.

#### 3.4.3. Repeatability of the calibration

Typically, several measurements per day were taken, each representing one calibration [3]. By each calibration the beam direction and the offset parameters from one corner to the beam centroid was derived. By averaging the individual results and calculating the residuals, the accuracy of the calibration procedure can be evaluated. Representative residuals for a set of calibration can be found in Figure 3.15.

The presented set of calibration comprises eight calibrations performed during one day, where each consists of three measurements. It is apparent that the CQP calibration is accurate to around  $\pm 4 \mu\text{m}$  (beam centroid) and  $\pm 30 \mu\text{rad}$  (beam direction). The inaccuracy of the calibration process has two major sources: the inherent errors of the coordinate measuring machine (*cf.* Appendix B) and the angular uncertainty of centring the beam on the two QPDs. The latter is for each calibration step about  $15 \mu\text{rad}$ . However, the accuracy of the CQP calibration depends largely on how well the features such as the various CQP alignments, the three normal vectors of the lid as well as the four corners can be either measured or fitted.

As shown in the plot, there are indications of systematic errors between the two angular parameters. It is noticeable that the inaccuracy for  $\vartheta x$  is a bit higher than for  $\vartheta y$ . This is mainly caused by the probing uncertainty of the CMM. Since the normal vectors of the lid are needed to calculate the beam direction and thus the angular parameters, any error induced by the measurement of the required planes will contribute to the uncertainty. With the maximum permissible error for volumetric probing given by Equation (2.2), an uncertainty of about  $100 \mu\text{rad}$  ( $\pm 3.4 \mu\text{m}$  over 30 mm) and  $30 \mu\text{rad}$  ( $\pm 3.4 \mu\text{m}$  over 120 mm) may occur for  $\vartheta x$  and  $\vartheta z$  of a normal vector, respectively. Thus, the probing of

---

[3]The author was solely responsible for all measurements performed throughout this Chapter. In addition, refinement of the calibration procedure has been realised.

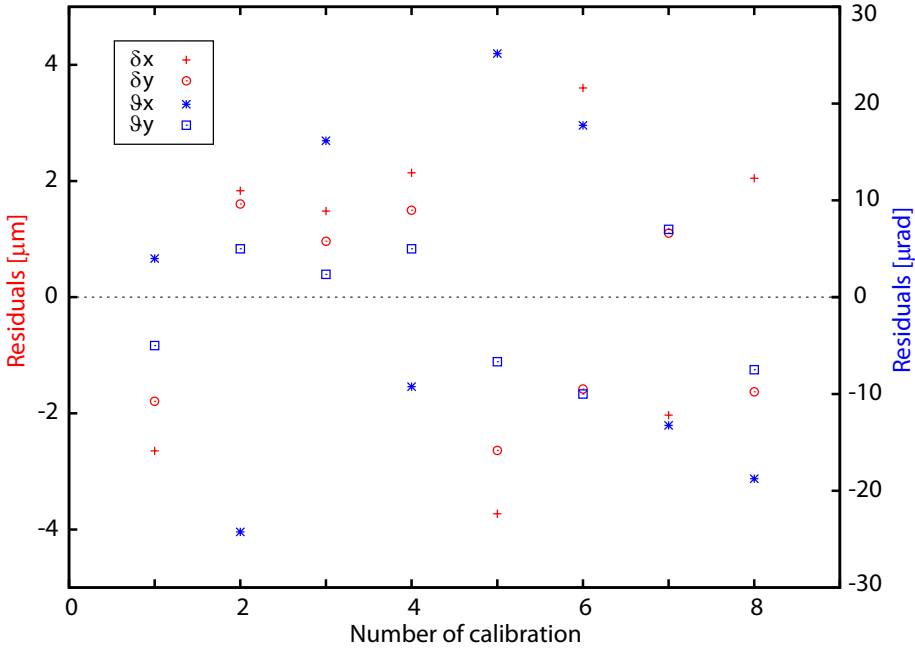


**Figure 3.15.:** Residuals of a representative set of calibrations. Eight individual calibrations were performed during one day. The deviation of the two offset parameters ( $\delta x$ ,  $\delta y$ ) and the angular parameters ( $\vartheta x$ ,  $\vartheta y$ ) to the calculated daily mean are plotted in red and blue, respectively.

the plane associated with the normal vector can be identified as error source. By assuming that the normal vectors of the lid experience a maximum error in both angles ( $\vartheta x$  and  $\vartheta z$ ; direction of  $\vec{n}_i$  is almost the  $Y_b$ -axis) for all three CQP orientations:  $-90^\circ$ ,  $0^\circ$  and  $+90^\circ$ , an error for both angular parameters of about  $30 \mu\text{rad}$  can be estimated. Notice that essentially the maximum uncertainty cannot be obtained simultaneously for both angles, but is used for an estimation of the minimum accuracy for both angles. In practice, the inaccuracy of features being probed in vertical direction to the probe spindle is higher than for probing them parallel. Taking this into account and reducing the errors for  $\vec{n}_1$  and  $\vec{n}_3$ , the error for  $\vartheta x$  will remain the same but the error for  $\vartheta y$  will shrink.

The translation of probing errors into the angular parameters can be also identified by comparing the obtained normal vectors  $\vec{n}_i^{\text{BCF}}$  from the PC-DMIS program. In Table 3.1 measured normal vectors of a representative calibration process are listed. These vectors belong to the third calibration of Figure 3.15. Ideally, they would agree with each other. Hence, their deviations of the mean

$$\xi_i = \vec{n}_i - \frac{\sum_{i=1}^3 \vec{n}_i}{3} \quad (3.22)$$

**Table 3.1.:** Computation of beam direction during a CQP calibration. A representative example is shown of the three normal vectors of the lid  $\vec{n}_i$  (which serve for determining the beam direction) with their deviation of the mean. The impact of this inequality on the beam direction is denoted with  $\epsilon(\vartheta x)$  and  $\epsilon(\vartheta y)$ .

Normal vector $\vec{n}_i$ and $\xi_i$ [ $\mu\text{m}$ ]	Orientation of the CQP		
	$+90^\circ$	$0^\circ$	$-90^\circ$
$\vec{n}_1$	(2.1, $10^6$ , 108.1)		
$\xi_1$	(18, 0, -10)		
$\vec{n}_2$		(-58.7, $10^6$ , 127.9)	
$\xi_2$		(-42.8, 0, 9.8)	
$\vec{n}_3$			(8.9, $10^6$ , 118.2)
$\xi_3$			(24.8, 0, 0.1)
$\epsilon(\vartheta x) / \epsilon(\vartheta y)$ [ $\mu\text{rad}$ ]	14.88 / 4.92		

can be used to evaluate the error propagation to the beam direction and are additionally tabulated. By performing the calculations described in Section 3.4.1, angular errors of about  $15 \mu\text{rad}$  and  $5 \mu\text{rad}$  for  $\vartheta x$  and  $\vartheta y$ , respectively, can be roughly estimated for this specific calibration. Doing this error estimation for all performed calibrations presented in the figure, a good agreement with the residuals can be found.

The two offset parameters defining the beam centroid are calculated using the measured corners of the CQP. Figure 3.15 shows slightly bigger residuals for the  $\delta x$  offset parameter. In order to show the implication of the CMM accuracy with which it assumes a new feature such as a piercing point (defining a corner) from a measured set of features like planes, the required four measured corner points are listed in Table 3.2. In an ideal situation both respective corner pairs would be identical in the BCF. Their deviation from each other ( $\Delta x$  and  $\Delta y$ ) shows a slightly higher disagreement in the  $Y$  variable of the first corner  $\vec{a}_n$ . Comparing this case to the other calibrations, all indications are that a small systematic error arises between the  $0^\circ$  and  $-90^\circ$  orientation of the CQP for  $\vec{a}_{n,y}^{\text{BCF}}$ . The exact source of this specific error is unknown. Since the piercing points are constructed by intersecting the front plane with an intersection line between the lid plane and a respective second plane, the probing uncertainty for these two planes dominates the calculation of the beam centroid in the  $X_o - Y_o$ -plane. The direction of the intersection line with its origin can be constructed with an accuracy of  $\pm 30 \mu\text{rad}$  ( $3.4 \mu\text{m}$  over  $120 \text{mm}$ ) and  $\pm 1.8 \mu\text{m}$

**Table 3.2.:** Computation of beam centroid during a CQP calibration. A representative example is shown of the four obtained vectors  $\vec{a}_n$  and  $\vec{b}_n$  with their deviation from each other ( $\Delta x, \Delta y$ ) and their impact on the resulting beam centroid  $\vec{c}_i$ . All  $Z$ -components can be considered as negligibly small.

	+ 90 ° [mm]	0 ° [mm]	- 90 ° [mm]	$\Delta x / \Delta y$ [ $\mu\text{m}$ ]
$\vec{a}_1$	(15.0394, 14.9478)	(15.0448, 14.9369)		-5.45/+10.84
$\vec{a}_2$				
$\vec{b}_1$		(-14.947, 14.9377)	(-14.941, 14.9440)	+6.16/-6.45
$\vec{b}_2$				
$\vec{c}_a$	(0.033831, 0.005153)			+7.82/+2.36
$\vec{c}_b$	(0.041647, 0.00751)			

(Equation (2.2)) for both axes. This results in an error of  $\pm 3.8 \mu\text{m}$  for the corner points. Moreover, by considering that the probing accuracy is higher for features not being probed vertical to the probe spindle, the systematic error cannot be explained by this, due to the fact that it should influence the  $X$ -deviation as well as the  $Y$ -deviation in the BCF in the same manner. However, in the OCF a higher accuracy for  $a_{1,y_b}$ ,  $a_{2,x_b}$ ,  $b_{1,x_b}$  and  $b_{2,y_b}$  translates to a reduced error for the  $Y_o$  parameters. Taking Equations (3.18) – (3.21) the error propagation to the beam centroid can be roughly estimated to be  $\pm 4 \mu\text{m}$  for  $\delta x$  and something less than  $\pm 4 \mu\text{m}$  for  $\delta y$  (in OCF as well as in BCF).

Besides the calibration accuracy, the long-term stability of the CQP is of importance. If the calibration parameters would drift over time, a re-calibration would be necessary. However, this would improve the CQP performance only temporarily, leading to subsequent calibrations. Due to the fact that a calibration process is very time consuming, this option is very undesirable. In order to avoid drifts in the parameters, some effort was done to provide a stable CQP, as described in Section 3.3, as well as to minimise errors occurring through inappropriate use of the CMM. For instance, Invar<sup>®</sup> was chosen as material for the support structure of the CQP as well as a low-expansion epoxy resin to fix the components made of Suprasil<sup>®</sup>. To be independent of different calibration parameters of the probe head, only one orientation was used to probe the various features during the calibration steps. Further investigations were performed on how to mount the QPDs as well as the CQP housing on the hexapod itself. In the course of time several calibration sets were carried out to investigate the long-term stability of the calibration parameters. Figure 3.16 presents seven calibration sets over a time period of three months, each

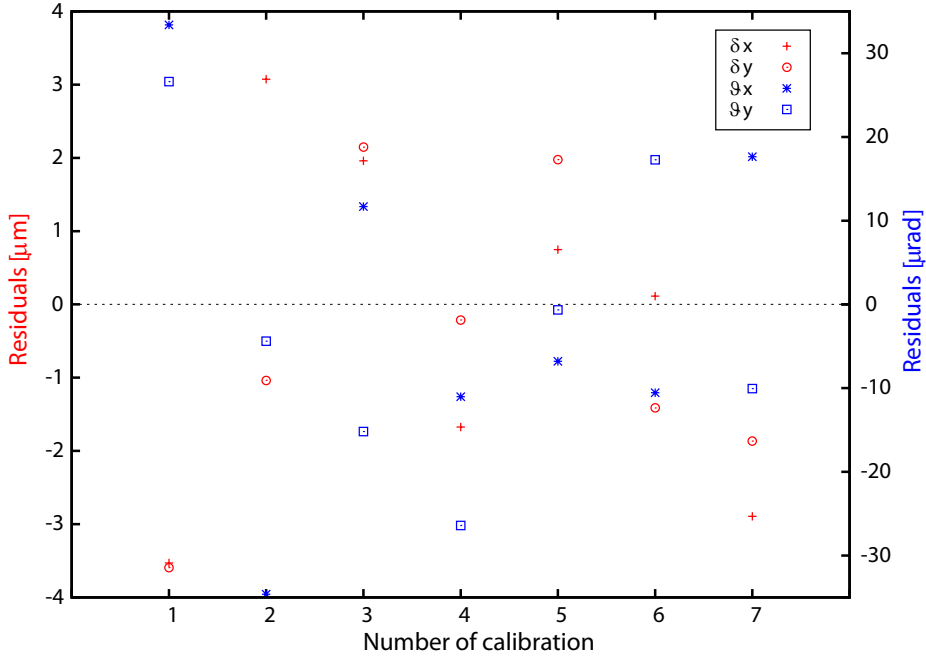


**Figure 3.16.:** Verification of the repeatability of the calibration procedure. Shown are the residuals with respect to the mean calibration parameters of seven calibration sets over a time period of three months. Left axis (red) shows the residuals of the offset parameters, while the right axis (blue) presents the residuals of the angular parameters.

set resulting of at least four calibration procedures performed within one day. Shown are the residuals of the two angular and two offset parameters with respect to the mean calibration parameters. It can be seen that the repeatability of the calibration parameters are of the order of  $\pm 4 \mu\text{m}$  and  $\pm 30 \mu\text{rad}$ , which is comparable with the estimated calibration accuracy.

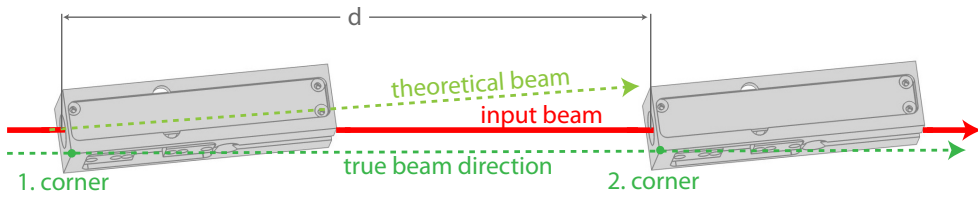
### 3.5. Reliability of the CQP

The determined calibration accuracy does not imply automatically that the CQP is performing as expected. Therefore, it is important to verify its accuracy. However, it is necessary to distinguish between the angular and the offset parameters of the calibration. The two can be checked in different ways. The underlying principle to show the reliability of the CQP is to make at least two measurements of a stable beam at different positions along its optical axis.

In order to check the angular parameters, it is sufficient to measure the stable beam at two positions with an appropriate distance along its length. The prin-



## Verifying angular parameters:



## Verifying offset parameters:

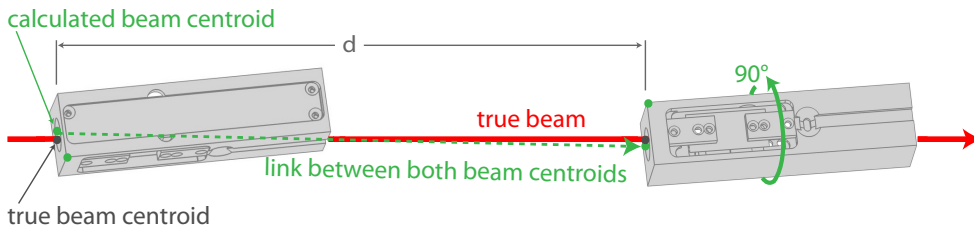


**Figure 3.17.:** Principle of detecting calibration errors and verifying the CQP accuracy by making multiple measurements along a stable beam. *Upper figure:* The link between the two corners gives the true direction of the input beam. By comparing the true beam with the theoretical beam, incorrect angular parameters of the calibration procedure can be detected. *Lower figure:* By making at least two measurements rotated about the stable beam, incorrect offset parameters can be identified. For this the line between the two calculated beam centroids yields a vector, which is compared to the true beam.

principle is illustrated in Figure 3.17. At each point along the beam the position and orientation of the CQP is measured by the CMM. In the same manner as for calibrating the CQP, the output data from the PC-DMIS part program is processed by a program written in C, which computes the beam direction and its centroid in the desired coordinate frame by using the calibration parameters  $\delta x$ ,  $\delta y$ ,  $\vartheta x$  and  $\vartheta y$ . In addition, a vector for one corner on the CQP is obtained. For this reliability check the MCS is chosen but in principle any other frame can be selected. For instance, the OCF is the preferred reference frame for using the CQP in combination with the optical bench and its fibre injectors.

Joining two corner points along the beam will reveal the true direction of the input beam. Ideally, the theoretical beam will agree with the measured true beam. Since the moved distance  $d$  can be exactly calculated from this vector, the incident point on the CQP at the second measurement position can be predicted. For this, the theoretical beam is used. By comparing the predicted beam centroid with the calculated one, the accuracy of the angular parameters can be checked. Analogous to this, the true beam can be directly compared to

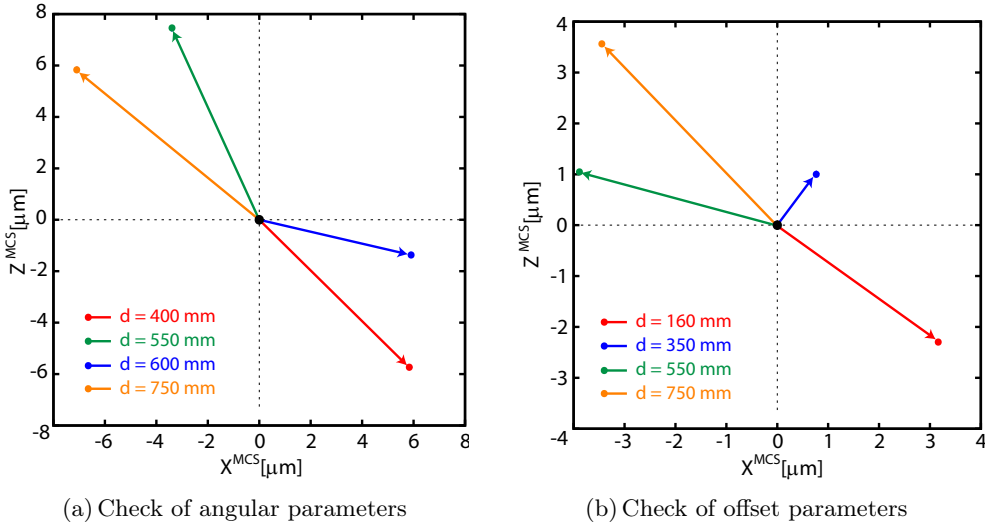


**Figure 3.18.:** Verifying the CQP accuracy by making several measurements of the physical position of a stable beam along its optical axis (pointing into the page). (a) Shown is the deviation of the true beam with the theoretical one for several distances. The CQP orientation stayed the same. (b) Shown is the deviation of the true beam with the vector linking both calculated beam centroids, while the beam is measured in two orientations.

the theoretical beam, yielding the same results.

According to the scheme described, multiple measurements were performed with a baseline (from front to front) of 400 mm up to the maximum permissible distance of 750 mm<sup>[4]</sup>. The resulting deviations of the nominal values are shown in Figure 3.18(a). The starting point of the beam lies in the origin of the frame. The calculated incident point on the CQP shifted along the optical axis is depicted with a dot. In contrast, the predicted beam centroid is intended to lie in the origin. Both points can be best imagined in a three dimensional frame, where the beam axis points into the page; shifted about  $d$  along the beam. Consequently, the arrows represents the pointing deviation of each measurement. The resulting angular errors in the MCS are given in Table 3.3.

The accuracy is partly limited by the baseline over which the measurements are performed. For instance, the minimum resolution for a baseline of 750 mm is  $10 \mu\text{rad}$  ( $\pm 3.8 \mu\text{m}$  for each corner point). From these results no systematic errors in the angular parameters are visible. The deviations that had occurred are most likely caused by the CMM inaccuracy and the limited stability of the

<sup>[4]</sup>The measurement baseline was limited by the measurement volume of the CMM.

**Table 3.3.:** Angular errors (given in MCS) of measurements of a beam at several points along a beam propagation axis.

d [mm]	$\vartheta x$ [ $\mu\text{rad}$ ]	$\vartheta z$ [ $\mu\text{rad}$ ]
400	15	-15
550	-6	13
600	10	-2
750	-10	8

beam. Since the drift of the hexapod has been measured to be about  $\pm 100$  nm for one hour [67], a potential significant movement of the CQP caused by the hexapod can be excluded.

Potentially systematic errors in the two offset parameters cannot be identified yet. Hence, a more sophisticated method is needed. A suitable approach is to make several measurements of a stable beam in at least two different CQP orientations with a sufficient separation. Figure 3.17 shows in the bottom illustration the adopted method. The initial measurement is identical to the previous method, which yields the calculated beam centroid on the CQP front and a theoretical beam. The information of the corner point is not needed. For the second measurement the CQP is rotated about the beam by an angle of  $-90^\circ$ , where the beam centroid and direction is again calculated. Since errors in the CQP due to an incorrect calibration will rotate along with it, it is possible to identify them. Joining the two calculated beam centroids will form a vector, in ideal case being identical to the true beam. The deviation of both of them as well as of the calculated beam centroid with the true one reveals possible errors in the offset parameters. The results obtained are shown in Figure 3.18(b). The beam axis is pointing into the page just like for 3.18(a). The plotted vectors represents the connection line between the two theoretical beam centroids, where the true ones are subtracted. One can see that they agree well with the true incident points on the CQP within the ascertained accuracies of  $\pm 4 \mu\text{m}$ . Both theoretical beams agree with the true beam as well as with the link between both calculated beam centroids with a variation of  $\pm 20 \mu\text{rad}$  and  $\pm 10 \mu\text{rad}$  for  $\vartheta x$  and  $\vartheta z$ , respectively. Furthermore, there are no obvious indications for incorrect offset parameters.

### 3.6. Conclusion

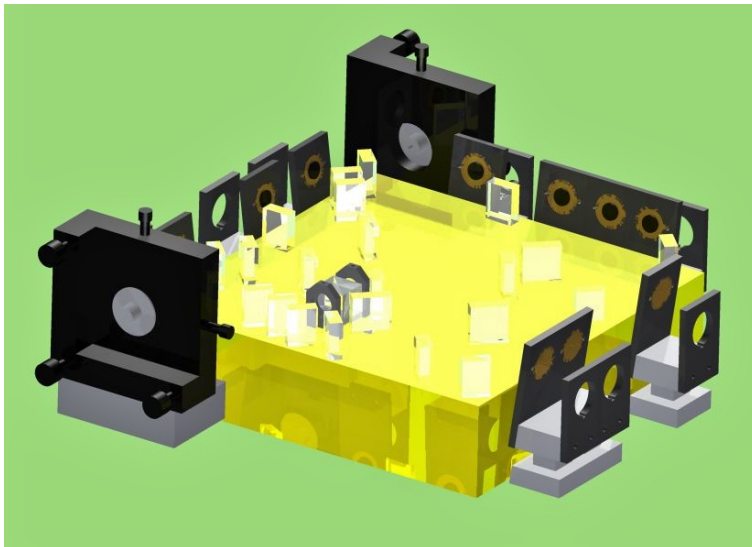
A device was needed for precisely measuring a beam's physical position in space. For this purpose a so-called calibrated quadrant photodiode has been developed consisting of two QPDs. Its housing was probed with a CMM to

determine its position and orientation within the CMM measurement volume. However, this did not directly reveal the desired beam position and propagation direction. A relationship between the CQP housing and the beam vector needed to be established by calibrating the CQP. With an angular uncertainty of centring the beam on the two QPDs (baseline accuracy) of  $15\ \mu\text{rad}$ , a calibration accuracy of around  $4\ \mu\text{m}$  (beam centroid) and  $30\ \mu\text{rad}$  (propagation axis) could be achieved. Furthermore, it was shown that the repeatability of the calibration is comparable with the estimated calibration accuracy.

Once the CQP was calibrated, it could be used on the one hand for determining a beam's physical position and on the other hand for serving as a target. In order to evaluate the reliability of calibration parameters and thus the accuracy of determining a beam's physical position, measurements along the beam propagation axis were performed. They agreed well with the true values within the ascertained accuracies of  $4\ \mu\text{m}$  and  $20\ \mu\text{rad}$ . The use as a target has been realised by pre-positioning the CQP using a hexapod to a fixed position with a defined orientation and adjusting the beam to both QPD centres. With this approach three beams have been aligned with respect to the plane of the optical bench consisting of the hexagonal interferometer within the ESA project *LISA metrology system*. A detailed characterisation of the experiment and the use of the CQP is described in Chapter 8.

## Part II

# Verification of polarising optics for heterodyne interferometry





## Chapter 4

# 4 Design, analysis and construction of the test bed

In order to meet the many technological challenges of LISA, the ESA precursor mission LISA Pathfinder (LPF) will test key technologies for LISA. However, some elements will not be tested in space. One of these elements is the use of polarising components in laser interferometry. In the current LISA elegant breadboard (EBB) baseline design they are favoured to separate incoming and outgoing beams in the telescope interface and test mass interferometer [68]. The optical bench will contain a combination of non-polarising and polarising Mach-Zehnder interferometers, as shown in Figure 4.1. In contrast, the optical bench of the LISA technology package (LTP) aboard LPF will only use non-polarising optics. For a detailed description of the LISA EBB, the reader is referred to references [44, 69].

In order to read out the position and angle of a test mass, at least two options are possible:

- Use a non-polarising interferometer with a non-normal incidence on the test mass as in LPF.
- Use a polarising interferometer with normal incidence on the test mass.

Both possibilities are illustrated in Figure 4.2. The left side shows the non-polarising layout, where the angle of incidence on the test mass is a few degrees. Thus, the beam sent to the test mass and the reflected one are spatially separated. The polarising layout can be seen on the right hand side, where the beams sent to and reflected from the test mass are separated by a polarising beam splitter (PBS). The s-polarised light is converted to p-polarisation by a half-wave plate. Hence, the beam sent to the test mass can be transmitted through the PBS. After passing the quarter-wave plate twice the polarisation

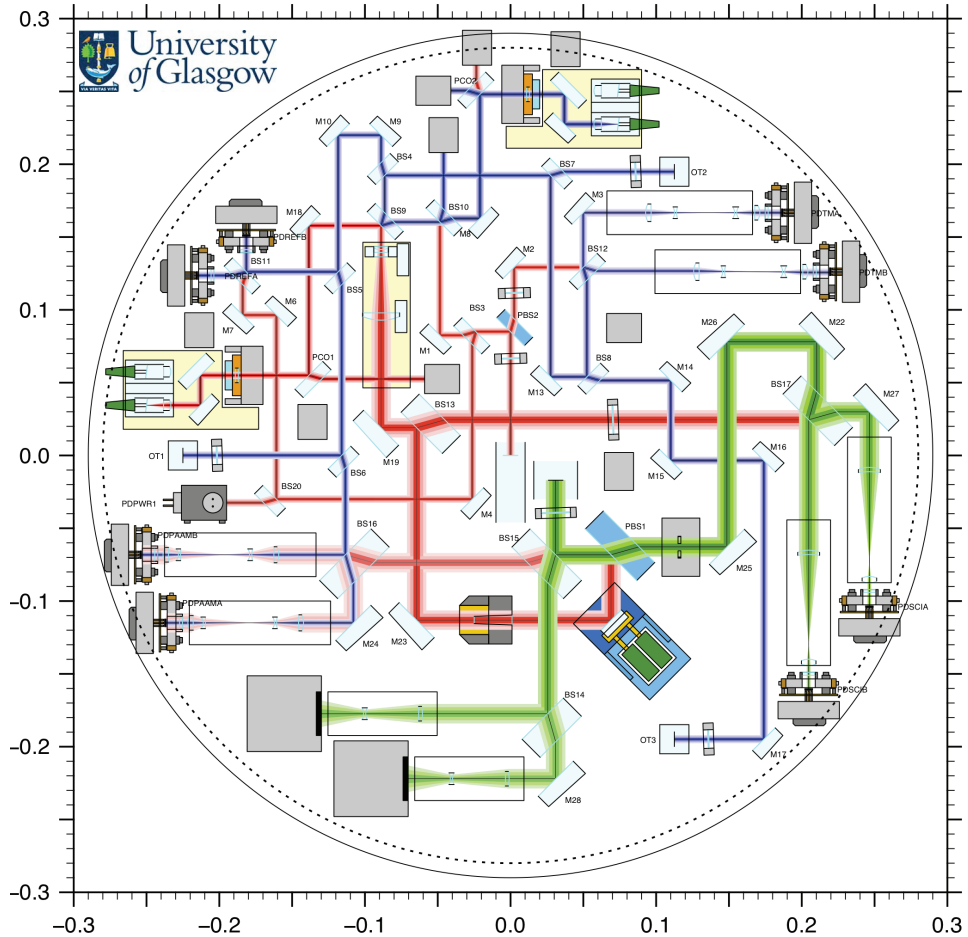


**Figure 4.1.:** Current design of the LISA elegant breadboard (EBB). Image courtesy of University of Glasgow (UGL).

is rotated by  $90^\circ$  and is reflected from the PBS. For the test mass readout both layouts seem to be equally possible with the advantage on the side of the polarising scheme due to the normal incidence.

For the science interferometer it is inevitable to separate the incoming and outgoing beam, because they are using the same telescope for sending and receiving light to and from the remote spacecraft and thus sharing the same beam path. Broadly, there are two ways to realise this:

- Use a non-polarising layout, where a non-polarising beam splitter serves the dual function of sampling a fraction of the outgoing light as local oscillator and separating the incoming from the outgoing light.



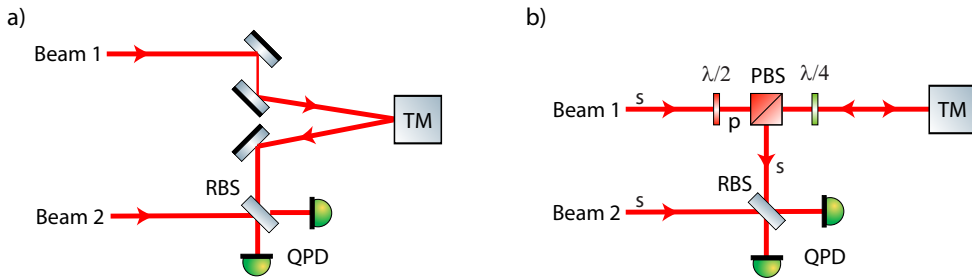


**Figure 4.2.:** Two possibilities for test mass readout: a) non-polarising layout with a non-normal incidence and b) polarising layout with normal incidence on the test mass.

- Use a polarising layout, where a polarising beam splitter is separating the two beams.

Again, both layouts are schematically shown in Figure 4.3. In the non-polarising layout (left side) the major component is the beam splitter. It has to send a small fraction of the outgoing beam to the beam combiner (RBS), where it serves as local oscillator (LO), but also to separate the incoming from the outgoing beam. Therefore, it is desirable to have a small reflectivity while the outgoing beam is transmitted. However, this would be disastrous for the incoming beam, where the opposite is required. As a result, the main disadvantage is a significant loss of the incoming light, which travels towards the laser, where it must be removed with a Faraday isolator in order to avoid laser instabilities. With a polarising layout (right side) one has the freedom to select the optimal local oscillator level via the reflectivity of the first beam splitter and to utilise all the light power from the remote spacecraft.

Possible concerns are the thermal stability of the polarising components used

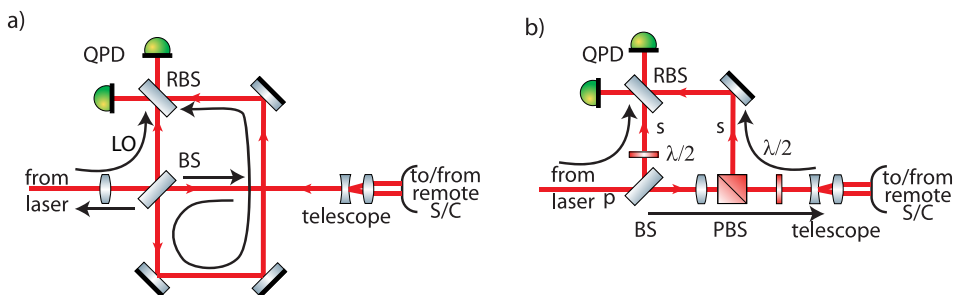


**Figure 4.3.:** Two possibilities for beam separation in the science interferometer: a) non-polarising and b) polarising layout.

in transmission and periodic phase errors. The latter can be caused, e.g., by imperfect polarising beam splitters and is described in the following section. Thermal influences are able to modify the optical path length, the polarising plane and the extinction ratio. Due to the advantages named, the polarising layout was selected as baseline for the science interferometer and the test mass readout.

Transferring these concepts into the LISA optical bench requires that a  $\text{pm}/\sqrt{\text{Hz}}$  stability of polarising optics in the mHz region has been validated. For this purpose, a test bench has been designed. It is desired that the optical bench for investigating the influence of polarising optics onto the interferometer sensitivity is built in a LISA-like setup, to be as representative as possible. This includes that the interferometers are constructed on a low-expansion baseplate and the hydroxide-catalysis bonding technique (*cf.* Section 2.1) is used. Length measurements of polarising and non-polarising interferometers will be compared. When the length measurement performed with the non-polarising interferometer complies with ([70], R<220-030>)

$$\tilde{\delta}_s = 1.42 \cdot 10^{-12} \frac{\text{m}}{\sqrt{\text{Hz}}} \times \sqrt{1 + \left(2.8 \frac{\text{mHz}}{f}\right)^4} \quad (4.1)$$

end-to-end displacement noise in the frequency band from 0.1 mHz to 1 Hz, it is shown that the test bed has sufficient sensitivity. Next, it has to be shown whether the same noise level can be achieved when performing the length measurement with the polarising interferometer. Additionally, the difference between the two interferometers has to agree with the required length stability.

### Benefit for future GRACE-like missions

In general, polarising optics are most useful whenever a single optical path has to be multiplexed. For instance, a possible GRACE-like mission (*cf.* Chapter 1) with an on-axis optical design, which consists of a laser-link between the two spacecraft, requires polarising optics to separate the beams coming from and being sent to the other spacecraft. A sketch of a symmetric active heterodyne layout is depicted in Figure 4.4. The round-trip Doppler shift introduces variations in the interferometer beat note up to a few MHz. Therefore, a suitable heterodyne frequency is between MHz and a few 10 MHz, with the lower limit given by the maximal Doppler shift and the required control bandwidth of the offset phase lock. The upper limit is given by technical considerations concerning the photodiodes and the phasemeter. A heterodyne bandwidth from 1 MHz to 20 MHz is reasonable for the photodiodes and the phase measurement system. The frequency band of interest from 1 to 100 mHz for the length

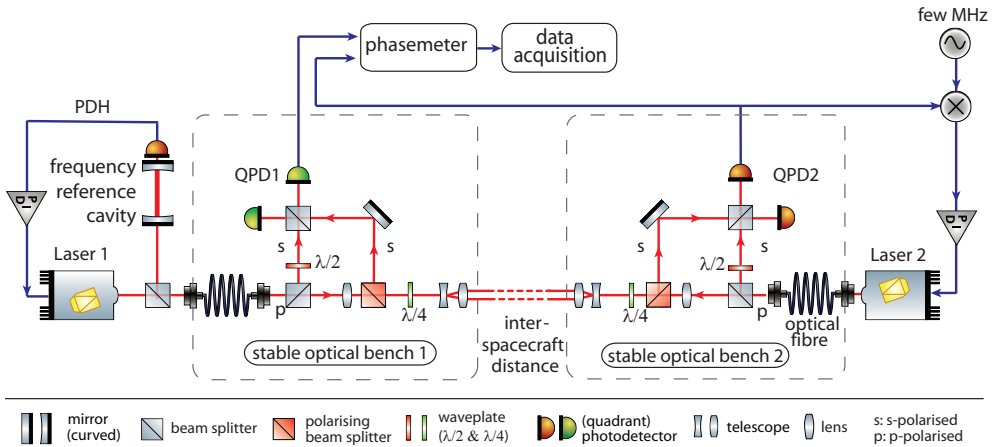


**Figure 4.4.:** Baseline design for a future GRACE follow-on mission: a symmetric system of two on-axis heterodyne Mach-Zehnder interferometers with lasers and detectors on both spacecraft.

measurement agrees with the one for LISA or LPF. The requirements on the length stability for this system are considerably relaxed compared to the requirements for the LISA mission. A nanometre/ $\sqrt{\text{Hz}}$  precision would improve the sensitivity significantly for frequencies above a few mHz, whereas under a few mHz the accelerometer noise would still limit the sensitivity. A validation of a displacement noise around  $10 \text{ nm}/\sqrt{\text{Hz}}$  in the low frequency range would be sufficient to give confidence for the use of polarising optics in such a mission. Hence, investigations concerning an influence of polarising components on the phase read-out confirm a significant advantage for a future on-axis GRACE-like mission.

## 4.1. Periodic non-linearities

By using polarising optics in heterodyne interferometry additional sources for periodical phase errors may emerge depending on the setup. The first prediction of non-linearity was done by Quenelle [71]. He predicted the periodic error of displacement measurements performed by Hewlett Packard laser interferometers to be in the range of 1–5 nm with a periodicity of one cycle per fringe change (equivalent to  $2\pi$ ) in optical path. This could be demonstrated experimentally by Sutton [72]. In addition, he observed a smaller non-linear effect with a periodicity of two cycles per fringe. Ever since, these periodic phase errors are referred to as first-harmonic and second-harmonic non-linearity, respectively. In Figure 4.5 the dependence of measured phase on length change is shown. For an interferometer without non-linearities the dependence would



**Figure 4.5:** Plot of measured phase versus travelled distance. Comparison of an ideal interferometer (blue trace) and one including non-linearity of the first order (red/solid) as well as second order (green/-dashed).

be linear. In contrast, in presence of disturbances the behaviour of the measured phase becomes non-linear with first and second order phase errors (or a combination of the two). Both, theoretical discussions and experimental investigations using different techniques can be found in many publications [73–84].

For a description of the analytical model of such a non-linearity, a typical configuration of a Michelson interferometer is considered, as shown in Figure 4.6. The input beam from a laser source consists of two polarised beams having a slightly different frequency ( $f_1, f_2$ ), which are normally linearly polarised in orthogonal axes. This is typically achieved by using a Zeeman-stabilised laser [85] or two longitudinal modes laser [86], or a single frequency laser with an acousto-optic modulator (AOM). The laser light is split at a non-polarising beam splitter into two beams. The reflected beam passes a polariser, which is oriented with its axis at  $45^\circ$  to the two polarisation axes. The resulting interference signal is acting as reference signal  $I_{\text{ref}}$  and measured by a photodetector as

$$I_{\text{ref}} \propto AB \cos(2\pi(f_1 - f_2)t), \quad (4.2)$$

with real amplitudes  $A$  and  $B$ .

On the other hand the transmitted beam is divided by a PBS in a measurement arm ( $L_1$ ) and a reference arm ( $L_2$ ) with real amplitudes  $A$  and  $B$ , respectively. In an ideal case each beam has its own purified single frequency ( $f_1$  and  $f_2$ ) and polarisation direction. The reference beam is reflected at a fixed corner cube acting as mirror. In contrast, the measurement beam is experiencing a Doppler shift due to the moving corner cube. This results in a phase shift of the measurement signal compared to the reference signal of

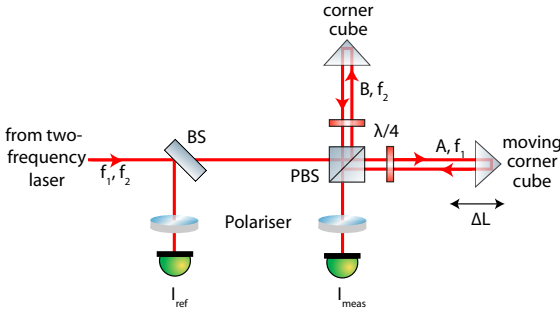


**Figure 4.6.:** A conventional setup of a polarising heterodyne interferometer to discuss periodic phase errors according to reference [80].

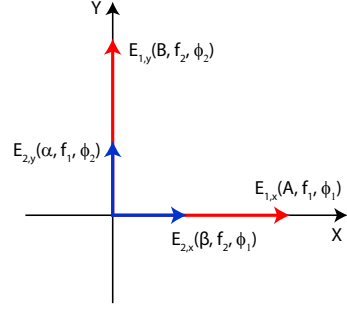


**Figure 4.7.:** Beam components according to [80].

$$\Delta\phi = \frac{4\pi}{\lambda}\Delta L, \quad (4.3)$$

where  $\lambda$  is the mean laser wavelength and  $\Delta L = L_1 - L_2$  the mirror's displacement. After passing twice through a quarter wave plate the polarisation directions of both beams are rotated by  $90^\circ$  and recombined at the PBS. The detected signal of the interference after passing a polariser can be expressed by

$$I_{\text{meas}} \propto AB \cos(2\pi(f_1 - f_2)t + \Delta\phi). \quad (4.4)$$

By combining the reference signal  $I_{\text{ref}}$  and measuring signal  $I_{\text{meas}}$  the phase difference  $\Delta\phi$  is obtained.

In practise, the situation is more complicated. A small part of the “measurement beam” with frequency  $f_1$  enters the reference arm, and also a fraction of the “reference beam” with  $f_2$  enters the measurement arm, see Figure 4.7. The latter experiences the same Doppler shift as the main measurement beam resulting in an extra phase term  $\Delta\phi_{\text{NL}}$  in the measurement signal

$$I_{\text{meas,NL}} \propto AB \cos(\Delta\omega t + \Delta\phi + \Delta\phi_{\text{NL}}), \quad (4.5)$$

where  $\Delta\omega = 2\pi(f_1 - f_2) = 2\pi f_{\text{het}}$  is the heterodyne frequency.

These non-linearities can be caused by various factors, such as

- Elliptical polarisation of the input beams
- Non-orthogonality of the polarisation direction of the beams

- Rotational misalignment of the polarisation states of the laser and the polarising beam splitter
- Rotational error in the alignment of the polariser or retarders
- Imperfection of the polarising beam splitter
- Polarisation modification due to the corner cube or wave plate
- Residual reflections
- or a combination of the different factors

Note that only non-linearities caused by the setup or the optics, in particular polarising optics, are considered in this discussion and that errors induced by e.g. the phase measuring electronics are not included in the following calculations.

The source of the induced cross talk terms can be divided into two terms: frequency mixing and polarisation mixing. In some publications, e.g. [77], a third term called polarisation-frequency mixing is introduced. It represents a combination of polarisation and frequency mixing and is caused by the ellipticity of the polarisation states. In this thesis this factor is classified as frequency mixing. Frequency mixing results from non-ideal polarisation modes associated with the two optical frequencies. Thus, it arises from ellipticity of the polarisation states, non-orthogonality of the two frequencies emitted from the laser source and an azimuthal misalignment of the PBS or retarders. Assuming an incomplete separation of the interfering beams in the interferometer depicted in Figure 4.6, frequency mixed states will be present in both arms, as shown in Figure 4.9. The amplitudes of these cross talk terms are represented by  $\alpha$  and  $\beta$ . The resulting intensity at the photodetector is then given by

$$\begin{aligned}
 I_{\text{meas,NL}} \propto & \underbrace{AB \cos(\Delta\omega t + \Delta\phi)}_{\text{Main signal}} \\
 & + \underbrace{(A\beta + B\alpha) \cos(\Delta\omega t) + \alpha\beta \cos(\Delta\omega t - \Delta\phi)}_{\text{Periodic error terms}}. \quad (4.6)
 \end{aligned}$$

Please note that the author has purposefully left out the contamination into the beams that are due to ellipticity. This would be beyond the scope of this section, as it is preferred to give a basic overview of the problem.

So far, only imperfections of the laser source have been assumed in Equation (4.6). If imperfect optics are additionally considered, in particular a non-ideal PBS, mixed polarisation states will be present in both beams. Figure

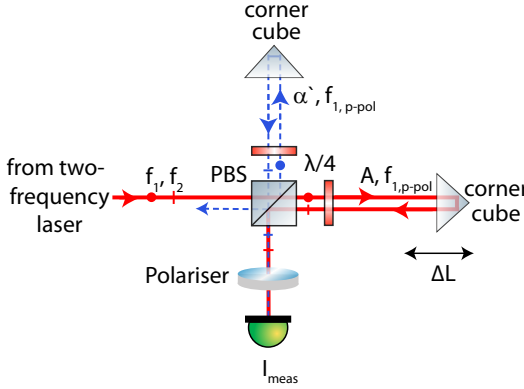


**Figure 4.8.:** Schematic of a heterodyne interferometer containing one PBS to explain polarisation mixing.

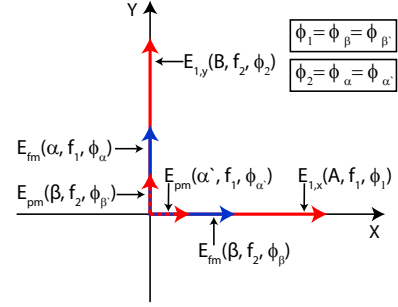


**Figure 4.9.:** Beam components: frequency and polarisation mixing.

4.8 shows the effect of an imperfect PBS for the measurement beam with frequency  $f_1$ . The reference beam will suffer in the same manner. For simplicity the influence of frequency mixing is omitted in both figures. In an ideal case all light power is transmitted or reflected by the PBS for the measurement and reference beam, respectively. However, in reality the PBS will reflect a small fraction of the measurement beam. After the beam is reflected at the stationary corner cube and passed twice through the quarter-wave plate the residual beam will mostly be reflected by the PBS. Due to the same imperfection, a small part will be transmitted and contaminate the initial measurement beam. Note that polarisation mixing can be seen as a second-order effect, because the contamination results from two successive leakages of the PBS. Thus, it is much smaller than the influence resulting from rotational misalignment. By considering the effect of polarisation mixing into the calculation of non-linearities the measurement signal can be expressed by

$$\begin{aligned}
 I_{\text{meas,NL}} \propto & \underbrace{\cos(\Delta\omega t + \Delta\phi)}_{\text{Main signal}} \\
 & + \underbrace{\gamma_1 \cdot \cos(\Delta\omega t)}_{\text{1st harmonic error}} \\
 & + \underbrace{\gamma_2 \cdot \cos(\Delta\omega t - \Delta\phi)}_{\text{2nd harmonic error}}, \quad (4.7)
 \end{aligned}$$

where  $\gamma_1$  and  $\gamma_2$  are given by

$$\begin{aligned}
 \gamma_1 &= \frac{A\beta + A\beta' + B\alpha + B\alpha'}{AB} \\
 \gamma_2 &= \frac{\alpha\beta + \alpha\beta' + \alpha'\beta + \alpha'\beta'}{AB}. \quad (4.8)
 \end{aligned}$$

Both are far smaller than 1. For reasons of simplicity and clarity in terms of understanding the phase error, Equation (4.8) can be expressed in a more general form as

$$I_{\text{meas,NL}} = \cos(\Delta\omega t + \Delta\phi) + \sum_n \gamma_n \cos(\Delta\omega t - \varphi_n + \phi_{\gamma_n}). \quad (4.9)$$

The first term is the ideal signal without the presence of non-linearities. The second term contains the periodic phase errors resulting from frequency and polarising mixing. For the special case described in this section the index can have the two values  $n = 1, 2$  and the phase variable  $\varphi_n$  is zero or  $\Delta\phi$ , respectively. The initial phase relative to the ideal measurement signal is  $\phi_{\gamma_n}$ . Although it is assumed that the initial phases of each contamination are equal to  $\phi_1$  or  $\phi_2$  and thus  $\Delta\phi$  or zero, it is included in Equation (4.9) by reason of generality.

In order to obtain the required phase, usually a phase measuring system is used: the heterodyne component of the measurement signal is decomposed into a real and an imaginary part by projection onto the basis vectors  $\sin(\Delta\omega t)$  and  $\cos(\Delta\omega t)$ . Thus, the complex vector of the measurement signal is [87]

$$Z = C + iS, \quad (4.10)$$

with the low-pass filtered results

$$C = I_{\text{meas,NL}} \cdot \cos(\Delta\omega t) \quad \text{and} \quad S = I_{\text{meas,NL}} \cdot \sin(\Delta\omega t). \quad (4.11)$$

The obtained phase can be written as

$$\begin{aligned} \Delta\phi_m &= \arctan\left(\frac{S(t)}{C(t)}\right) \\ &= \arctan\left(\frac{\sin \Delta\phi + \sum_n \gamma_n \sin(\phi_{\gamma_n} - \varphi_n)}{\cos \Delta\phi + \sum_n \gamma_n \cos(\phi_{\gamma_n} - \varphi_n)}\right) \end{aligned} \quad (4.12)$$

In order to understand how the residual terms in Equation (4.8) influence the measurement of the displacement  $\Delta\phi_m$ , it is convenient to visualise the cross talk between these terms and the main beat signal in terms of a phasor diagram. The length of the phasor represents the amplitude of that term, while it is rotating about the origin with  $\Delta\phi$ . Note that an equation of the form  $\cos(\Delta\omega t + \Delta\phi)$  can be expanded through trigonometric functions into  $\cos(\Delta\phi) \cos(\Delta\omega t) - \sin(\Delta\phi) \sin(\Delta\omega t)$ . By associating each quadrature  $\cos(\Delta\omega t)$  and  $\sin(\Delta\omega t)$  with the horizontal and vertical axes of a Cartesian coordinate system respectively, the cosinusoidal oscillation of the measurement signal can be depicted in such a phasor diagram. By the absence of non-linearity, Equation (4.8) will be reduced to the first term representing the ideal



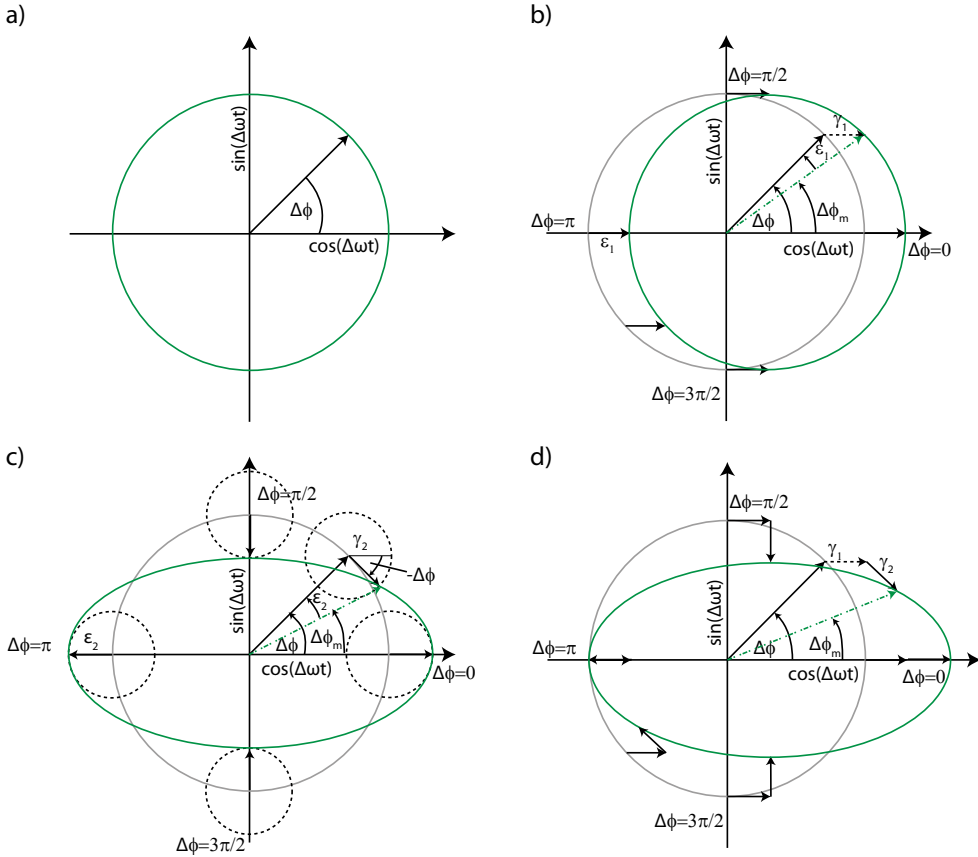


**Figure 4.10.:** Phasor representation of the first and second harmonic non-linearity. a) The full circle stands for the ideal measurement signal (in absence of non-linearity) which rotates with  $\Delta\phi$ . b) and c) show the first and second order of non-linearity, respectively. While d) illustrates the combination of both error terms.

beat signal. This corresponds to an ideal circle in the phasor diagram, as sketched in Figure 4.10 a). The measurement vector with amplitude 1 rotates around its origin with  $\Delta\phi$  ( $\hat{=} \Delta\phi_m$ ). The influence of the second term on the main signal is shown in b). This contribution is independent of  $\Delta\phi$  and thus adding a phasor with constant magnitude  $\gamma_1$  and direction to the main phasor. The measurement signal of the first two terms can be represented again by a circle but with a constant shift of  $\gamma_1$  on the  $\cos(\Delta\omega t)$  axis. By tracking the resultant phasor, the periodic phase error  $\epsilon_1 = \Delta\phi_m - \Delta\phi$  can be obtained. It can be seen that the non-linearity introduced by the first term is a periodic phase error of one cycle per fringe ( $\hat{=} 2\pi$ ), which is zero at  $\Delta\phi = 0$  or  $\pi$  and maximal at  $\Delta\phi = \pi/2$  or  $3\pi/2$ . The non-linearity of the first order with  $\gamma_1 \ll 1$  can be expressed as

$$\epsilon_1 = \gamma_1 \sin(\Delta\phi). \quad (4.13)$$

In a similar way the contribution of the third term on the main (first) term can be analysed. In contrast to the first time this term has a dependence of  $-\Delta\phi$ , resulting in an additional phasor rotating in the opposite direction as the main (ideal) signal. In Figure 4.10 c) this residual phasor rotating with radius (amplitude)  $\gamma_2$  is depicted with a dashed circle. The resulting phasor of the main signal and the third term is tracking an ellipse. Again, by comparing this ellipse with the ideal circle produced by the ideal signal the phase error of the third term is obtained. There is no phase error at  $\Delta\phi = 0, \pi/2, \pi, 3\pi/2$  and  $2\pi$  but a maximum error occurs at  $\Delta\phi = \pi/4, 3\pi/4, 5\pi/4$  and  $7\pi/4$ . Obviously due to the reverse rotation of the main phasor and error phasor, the third term contributes a non-linearity with two cycles per fringe (because there are two peaks and valleys of phase error within  $2\pi$ ). This second order non-linear phase error can be expressed by

$$\epsilon_2 = \gamma_2 \sin(2\Delta\phi), \quad (4.14)$$

with  $\gamma_2 \ll 1$ . The combination of the ideal signal with the two error terms produces an elliptic phasor, as depicted in Figure 4.10 d), which is shifted by  $\gamma_1$  on the  $\cos(\Delta\omega t)$  axis.

The phasor approach enables us to simplify Equation (4.12) to

$$\Delta\phi_m = \Delta\phi + \sum_n \gamma_n \sin(-\varphi_n - \Delta\phi). \quad (4.15)$$

The outcome of this is that the non-linearity in the setup shown in Figure 4.6 is mixed with phase errors of one or two cycles per fringe.

As additional source of non-linearity, spurious reflections also known as ghost reflections have been identified. The interface of each optical component generates residual reflections (multiple reflections as well as diffusely scattered light), which can impinge upon the receiver. The resulting effect is similar to the contaminations caused by frequency and polarisation mixing and can be modelled in an analogue way. Due to the independence of ghost beams from polarising components, this effect will not be discussed here, but can rather be found in [76], where the periodic non-linearities resulting from ghost reflections of a very similar setup as in Figure 4.6 are discussed in detail. Ghost beams resulting from the optical bench will be discussed in the following Section 4.2 as well as in Section 6.1, where a subtraction algorithm for eliminating these periodic phase errors is presented.

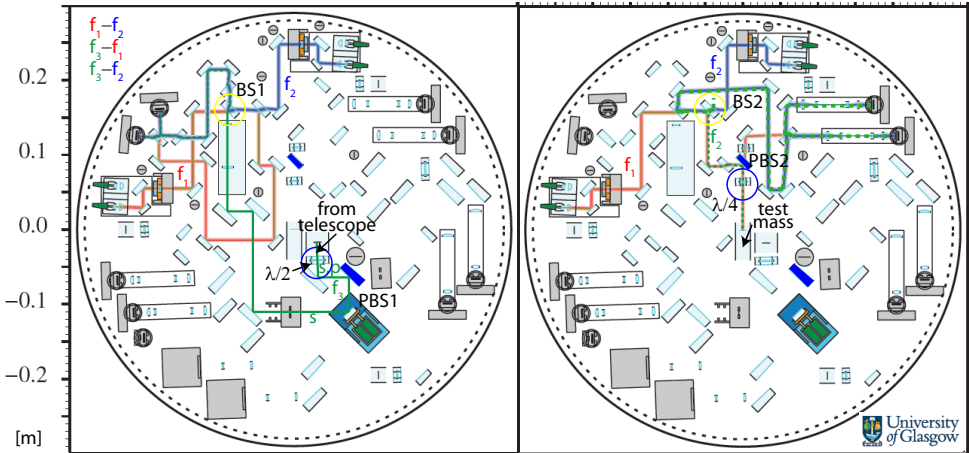


**Figure 4.11.:** Analysis of non-linearity induced by polarising optics on the LISA EBB. *Left:* Reference interferometer with a parasitic beam coming from the far spacecraft via the telescope. *Right:* Test mass interferometer with a parasitic beam induced by the quarter wave plate after reflection at the test mass. Image source: [16] (The image has been modified by the author).

Finally, it is of importance how large the contribution of periodic non-linearities will be in the LISA EBB design. Figure 4.1 showed the complete layout of the LISA EBB, in which the polarising beam splitters are illustrated in blue. By ray tracing, it can be seen that, on the one hand, the input beams with different frequencies as well as different polarisation states can overlap. Thus, contamination due to frequency and polarisation mixing could occur. The origin of these contaminations is discussed in the following section.

Polarisation mixing as well as frequency mixing can arise due to the imperfection of the PBS or a rotational misalignment of the wave plates. In order to specify both noise sources, both interferometers potentially affected are shown in detail in Figure 4.11. The two polarising beam splitters PBS1 and PBS2 are shown in blue colour, and both wave plates of interest are highlighted by a circle in blue. The left picture illustrates the reference interferometer. Assuming a rotational misalignment of the half-wave plate, a small part of the incoming light from the far spacecraft and entering the optical bench through the telescope with frequency  $f_3$  will be reflected at PBS1 and be redirected to the reference readout via BS1, highlighted in yellow, and interfere there with the second beam with frequency  $f_2$ . At the virtual beam combiner the parasitic beam will interfere also with the first beam, which has the frequency  $f_1$ . Thus, the phase measurement system will sense the main signal at the correct beat note frequency  $f_1 - f_2$  and two spurious signals with  $f_3 - f_1$  and  $f_3 - f_2$ . If the frequencies are well separated and the phasemeter works well, then the two

spurious signals will have no effect on the readout.

The test mass interferometer is shown in the right picture in Figure 4.11. The beam reflected by the test mass will re-enter its original optical path due to an imperfect alignment of the half-wave plate. Consequently, the parasitic beam with frequency  $f_1$  will be redirected over different components to BS2. At this component it will interfere with the second beam and introduce an extra beat note at the correct heterodyne frequency. As long as no other noise sources contribute to a phase change in the green optical path length, the parasitic signal will not influence the phase readout. However, as such ideal conditions are not realistic, the contribution of a periodic phase error to the interferometer sensitivity needs to be simulated and a requirement of the rotational alignment for both wave plates needs to be defined.

The third contribution is introduced by the imperfection of both PBSs and thus caused by polarisation mixing. Assuming an imperfect PBS1, a small fraction of the p-polarised incoming light through the telescope simulator will be reflected towards BS1. If, in addition, an imperfect PBS2 is assumed, the beam reflected at the test mass will impinge on the PBS and a fraction of the beam will be re-directed to BS1. Thus, this residual beam will have frequency  $f_1$  and p-polarisation state. At the beam splitter BS1 these two beams will interfere and generate a beat note signal at  $f_3 - f_1$  at the output of the reference interferometer. However, the phasemeter for the reference interferometer is sensitive for beat notes with  $f_1 - f_2$ . Consequently it should not be influenced by the residual periodic phase error. This needs to be verified in the future.

As a result the layout of our optical bench for testing the influence of polarising optics to the interferometer sensitivity will not necessarily show potential for frequency and polarisation mixing. Nevertheless, it has to be shown that periodic phase errors do not exist or do not affect the length measurements.

## 4.2. Design

For reasons of compatibility with the later flight hardware the optical test bench was set up on a low-expansion baseplate by applying the hydroxide-catalysis bonding technique. Another reason is that otherwise the picometre sensitivity required would be very hard (or impossible) to achieve at mHz frequencies. However, this building technique results in some constraints, which have to be considered. One of them is to ensure that the layout is compatible with the alignment technique developed for bonding the bench with a CMM (*cf.* Chapter 2). But also the manufacturability of the bench has to be considered. The

design of the optical bench had further requirements to fulfil, such as

- Using a baseplate with a footprint of  $200 \times 200 \text{ mm}^2$ .
- Hosting three Mach-Zehnder interferometers with no arm length imbalances.
- Including one interferometer with a possible big arm length mismatch.
- The beams have to be alignable to each other.
- The number of transmissions should be equal for both interferometer arms.
- It should have rotatable and replaceable wave plates.
- The two beams have to impinge upon a  $0^\circ$ -mirror (representing a test mass dummy) ideally at the same spot. The angles of incidence of the measurement beam have to be kept zero and as small as possible, respectively.
- Non-linearity caused by polarising optics has to be avoided.

Under these constraints and requirements a layout was designed. This was done by using the software `IfoCad` and `OptoCad`. The resulting test bench design for investigating polarising optics consists of four separate heterodyne Mach-Zehnder interferometers on a single stable baseplate, as depicted in Figures 4.12 and 4.13. They can be described as follows:

- a) The *non-polarising interferometer* uses only non-polarising elements for relative length measurements, using non-normal incidence as in LPF.
- b) The *polarising interferometer* senses the position fluctuations of the same mirror as the non-polarising interferometer, but additionally uses polarising optics. The two outputs were compared for relative length measurements.

The beam paths of these two measurement interferometers have been designed to occupy roughly identical parts of the test bench, in order to reduce effects from thermal gradients in the length measurement. Furthermore the angle of incidence on M3 is kept as small as possible in order to preserve the light power, while it is still big enough to mitigate any scattering and bending on the polarising components.

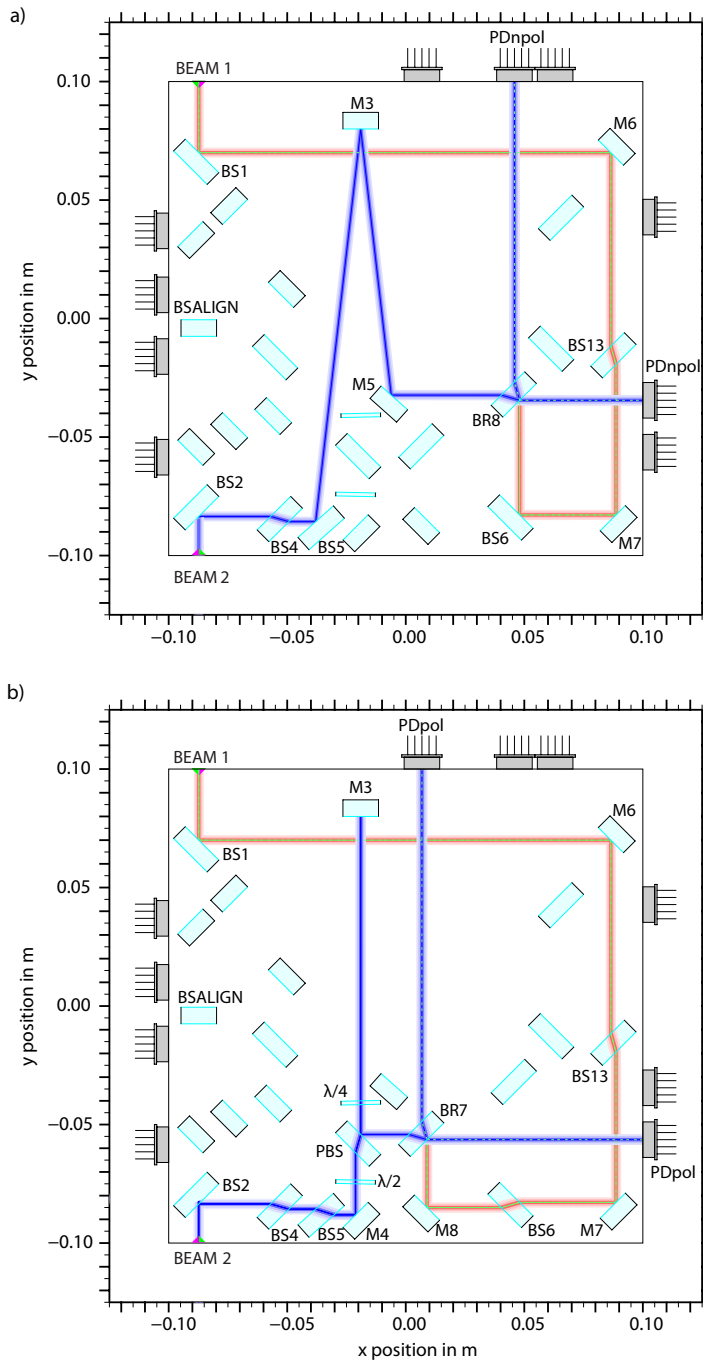


**Figure 4.12.:** OptoCad models of the laser interferometer for a comparison between polarising and non-polarising optics: a) non-polarising interferometer; b) polarising interferometer.

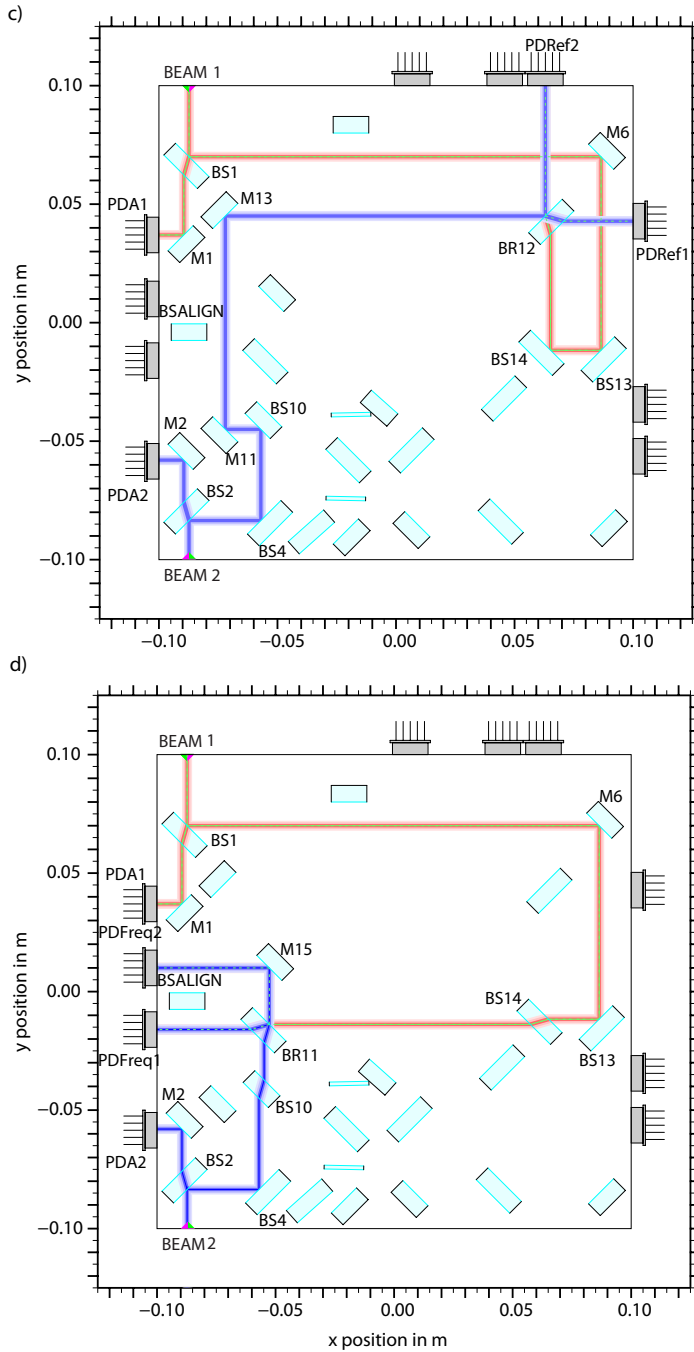


**Figure 4.13.:** OptoCad models of the laser interferometer for a comparison between polarising and non-polarising optics: c) reference interferometer; d) frequency noise interferometer (unequal arm lengths).

- c) The *reference interferometer* yields a reference phase containing all those environmental noise contributions that were external to the stable optical bench and common mode in all four interferometers. These fluctuations were subtracted from the polarising and non-polarising interferometers in data post-processing.
- d) The *frequency noise interferometer* has an intentional arm length mismatch of about 27 cm and is included for sensing the laser frequency noise. Its output signal might be used to actively stabilise the laser's frequency or to remove the effect of frequency noise in post processing.

In each interferometer the number of transmissions through optical components such as beam splitters was equal for both laser beams being used, except for the polarising interferometer. This minimised the dependence of optical path length on temperature.

In order to align the two beams to each other the component BS<sub>ALIGN</sub> was used. The alignment method is described in detail in Section 4.5. Additionally to the two auxiliary interferometers, two outputs were included in each beam path for a laser intensity stabilisation. Broadly, most suitable for this purpose is to use a beam splitter with a reflectivity of more than 90%. However, in the baseline layout these two beam splitters are involved in the beam alignment process. Although the two beams were aligned to each other before placing any component, except BS<sub>ALIGN</sub>, the components M1 and BS1 as well as M2 and BS2 are used during construction to align the fibre injectors, if necessary. Thus, it is convenient to have more light power in this optical path. Instead of mirrors we have used beam splitters as redirectors to the photodiodes.

##### 4.2.1. Stray light analysis

Since spurious beat note signals can significantly impair the phase readout, a careful design concerning stray light is mandatory. Parallel beam splitter surfaces are known to be the main source of spurious reflections in the optical path of the first beam. Although the rear (transmissive) side is anti-reflective (AR) coated, approximately 0.2% of the light power still gets reflected by this surface. A high potential source for ghost beams in the second beam path are the polarising components, especially the wave plates and the 0°-mirror M3. Usually, these components are placed normal to the beam leading to reflections into the main beam path. These reflections can lead to a spurious beat note signal which can disturb the interferometric phase readout. For this reason OptoCad is used to simulate the occurring ghost beams on the optical bench and to identify the parasitic reflections coupling into the main measurement path (*cf.* Figure 4.14). Note that stray light induced by the wave plates or



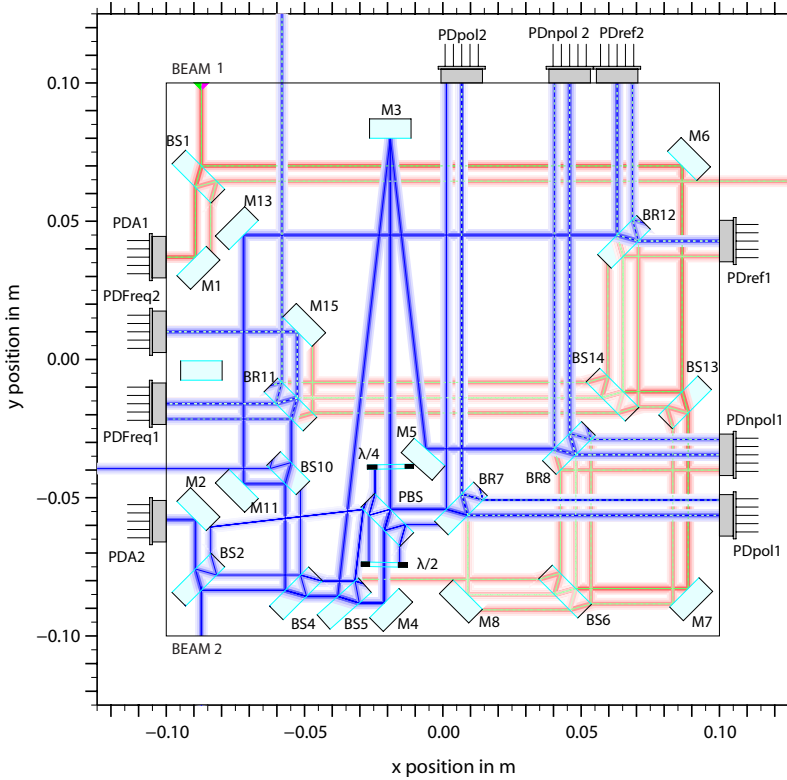


**Figure 4.14.:** Stray light analysis of the optical bench made with OptoCad.

mirror M3 are on the main path and thus not visible on the figure.

In order to evaluate the signal power of the different ghost beams, the ratio  $A_{dB}$  of each ghost beam's power  $b_{i,SLn}$  to the main beam's power  $b_{i,M}$  was calculated by

$$A_{dB} = 10 \times \log_{10} \left( \frac{P(b_{i,SLn})}{P(b_{i,M})} \right), \quad (4.16)$$

where  $i = 1, 2$  is the beam id and  $n$  is an index. In Figure 4.15 and 4.16 these ratios are plotted for both measurement interferometers against the corresponding beam position on the photodiode surface. The active area of 10 mm width is highlighted in black. Since the minimum separation of two beams is around  $\pm 5.5$  mm and thus outside the active area of the photodiodes used, they would not contribute to the main beat note signal. In case of the non-polarising interferometer a power attenuation down to less than  $1/10^6$  ( $-60$  dB) would occur for ghost beams on the same path as the main beam corresponding to  $1/10^3$  of the interfering amplitude. In contrast, a considerably smaller power attenu-

**Table 4.1.:** Influence of ghost beams to the main beat note signal of the non-polarising interferometer. The interfering amplitude (normalised to 1 V), the associated contrast, the signal to be detected for each interference as well as the corresponding two beams are listed.

Non-Polarising interferometer, PD <sub>NonPol1</sub>				
Distance to centre	Amplitude [V]	Contrast	Signal [V]	Interfering beams
0 mm	1	1	1	$b_{1,M}$ , $b_{2,M}$
	0.00098	1	0.00098	$b_{1,SL1}$ , $b_{2,M}$
	0.00098	1	0.00098	$b_{1,SL2}$ , $b_{2,M}$
5.5 mm	0.00098	1	0.00098	$b_{1,SL3}$ , $b_{2,SL1}$
	0.00098	1	0.00098	$b_{1,SL4}$ , $b_{2,SL1}$
0 and 5.5 mm	0.000045	0.293255	0.000013	$b_{1,M}$ , $b_{2,SL2}$
0 and 5.5 mm	0.031305	2.76956e-14	8.6701e-16	$b_{1,M}$ , $b_{2,SL1}$
	0.031305	2.76954e-14	8.67003e-16	$b_{1,SL7}$ , $b_{2,M}$
	0.031305	2.76954e-14	8.67003e-16	$b_{1,SL3}$ , $b_{2,M}$
	0.031305	2.76954e-14	8.67003e-16	$b_{1,SL4}$ , $b_{2,M}$

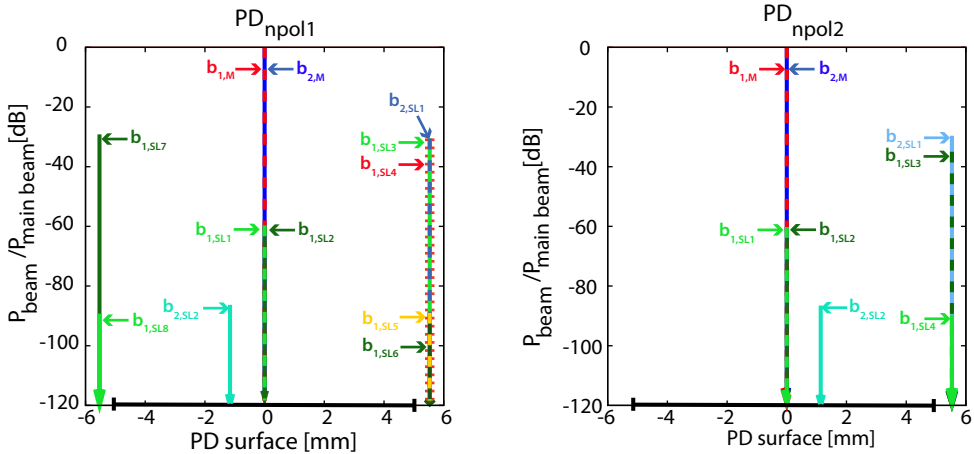


**Figure 4.15.:** Ratio of ghost beam to main beam detected at the two photodiodes for the non-polarising interferometer; The active area of 10 mm width is highlighted in black.

**Table 4.2.:** Influence of ghost beams to the main beat note signal of the polarising interferometer. The interfering amplitude (normalised to 1 V), the associated contrast, the signal to be detected for each interference as well as the corresponding two beams are listed.

Polarising interferometer, PD <sub>Pol1</sub>				
Distance to centre	Amplitude [V]	Contrast	Signal [V]	Interfering beams
0 mm	1	1	1	$b_{1,M}, b_{2,M}$
	0.0448334	1	0.0448334	$b_{1,M}, b_{2,SL2}$
	0.044699	1	0.044699	$b_{1,M}, b_{2,SL3}$
	0.0446096	1	0.0446096	$b_{1,M}, b_{2,SL4}$
	0.002	1	0.002	$b_{1,M}, b_{2,SL5}$
	0.002	1	0.002	$b_{1,M}, b_{2,SL6}$
	0.001998	1	0.001998	$b_{1,M}, b_{2,SL7}$
	0.001994	1	0.001994	$b_{1,M}, b_{2,SL8}$
	0.001994	1	0.001994	$b_{1,M}, b_{2,SL9}$
	0.00199002	1	0.00199002	$b_{1,M}, b_{2,SL10}$
	0.00098	1	0.00098	$b_{1,SL1}, b_{2,M}$
	0.000089	1	0.000089	$b_{1,M}, b_{2,SL14}$
	0.000045	1	0.000045	$b_{1,M}, b_{2,SL1}$
	5.5 mm	0.00098	1	0.00098
0.000044		1	0.000044	$b_{1,SL2}, b_{2,SL12}$
0.000044		1	0.000044	$b_{1,SL2}, b_{2,SL13}$
0 and 5.5 mm	0.031305	$2.76973e-14$	$8.67063e-16$	$b_{1,M}, b_{2,SL11}$
	0.031305	$2.76921e-14$	$8.66899e-16$	$b_{1,SL2}, b_{2,M}$

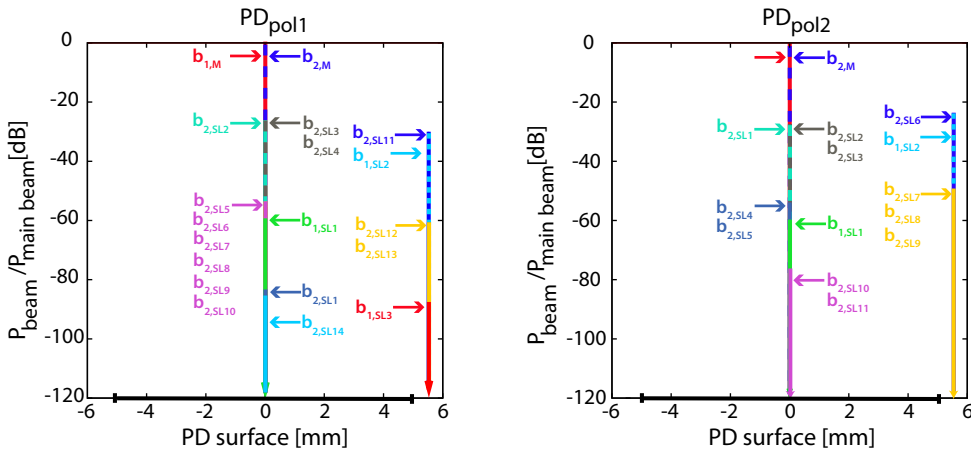


**Figure 4.16.:** Ratio of ghost beam to main beam detected at the two photodiodes for the polarising interferometer; The active area of 10 mm width is highlighted in black.

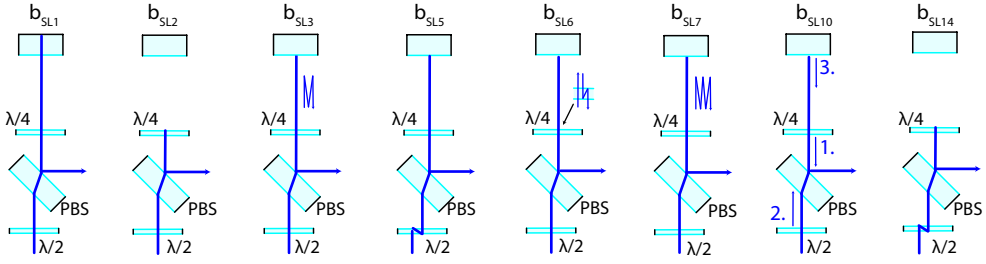


**Figure 4.17.:** Possible stray light sources for the second beam of the polarising interferometer.

ation only down to 1/500 (-27 dB) would emerge for ghost beams on the main optical path in the polarising interferometer, which corresponds to 1/22 of the interfering amplitude.

In order to assess the influence of each occurring ghost beam to the main beat note signal, the interfering amplitude (normalised to 1 V), the contrast and the additional detected signal for each interference have been calculated. In Table 4.1 and 4.2 the results for the two measurement interferometers are listed, divided in the main beat note signal at the centre of the photodiode, in an additional beat note signal shifted by 5.5 mm on the photodiodes's surface and in a beat note between beams of the two locations. The results for the two auxiliary interferometers are comparable to the non-polarising interferometer. The interferometric signal between beams on the main optical path and displaced by 5.5 mm do not lead to serious disturbances and can be neglected.

Since the beat note signal displaced from the centre is comparable to the main signal, the placement of the photodiode has to be handled with care to not accidentally detect the parasitic signal. Stray light occurring in the non-polarising interferometer would have no important impact on the interferometric performance. Since as source the parallel beam splitter surfaces are identified, aperture plates can be placed in the optical path of the first beam to eliminate the spurious beams, if desired. However, the situation in the polarising interferometer is more complex. The induced ghost beams would significantly influence the phase readout and produce an additional signal of approximately 0.165 V (main beat note signal is normalised to 1 V). The different sources of ghost beams induced by the polarising optics are presented in Figure 4.17. The two main sources are on the one hand the poor anti-reflection coating of the wave plates leading to spurious back reflections into the main optical path. These ghost beams, in turn, can experience multiple reflections due to the wave plate and the plain mirror M3 yielding cavity effects, such as illustrated in the third

and sixth picture of Figure 4.17. On the other hand, a small part of the main beam will be transmitted by the mirror M3 and reflected back at the rear side of that mirror into the main optical path. This possibility is sketched in the first picture. However, the resulting beat note signal with respect to the main signal is of the order of  $1/20000$  and thus negligible. Due to the fact that the ghost beams share the same optical path with the main beam, they cannot be eliminated by aperture plates. Consequently, the design has to be readjusted to finally guarantee a stray light reduced layout. Since the reflection at the rear side of a mirror causes a negligible contribution to the beat note signal, it will not be considered in the following.

There are different ways to mitigate beams re-entering the main optical path and thus creating parasitic interferometers:

- Choose thicker parallel components, such that the centre of the ghost beam is separated by a minimum of  $6w_0$  from the main beam.
- Use components with a wedge in in-plane direction. Thus, parallel reflections are suppressed and the risk of recoupling into the main path is minimised. Note that an in-plane wedge is necessary lest the transmitted beam is not travelling out of plane.
- Have all surfaces nominal to the beam, such as the wave plates and the  $0^\circ$ -mirror, tilted by a small angle. Cavity effects between these components will be avoided and residual reflections will not interfere with the main beam.

These modifications have been carried out in Figure 4.18. One can see that the first and second order reflected beams are separated by an angle, minimising the risk of stray light re-entering the main beam path. Furthermore, the analysis showed that there are no significant disturbances caused by reflections from the second beam.

Apparently, the wedged components are providing the best solution for minimising spurious reflections resulting in parasitic interferometers. However, there are two problems with this approach. The minor one is the challenging manufacturing, the involved high costs and the longer production time. The major drawback is the risk of adding path length noise due to beam jitter across the wedge. While the beam jitters it will scan across the component's surface by a small amount and experience a variable thickness of the substrate. The resulting change in optical path of the beam will couple into the measurement as a direct source of path length noise. This coupling was calculated first for the LISA OB by the University of Glasgow and can be found in [44, 88].

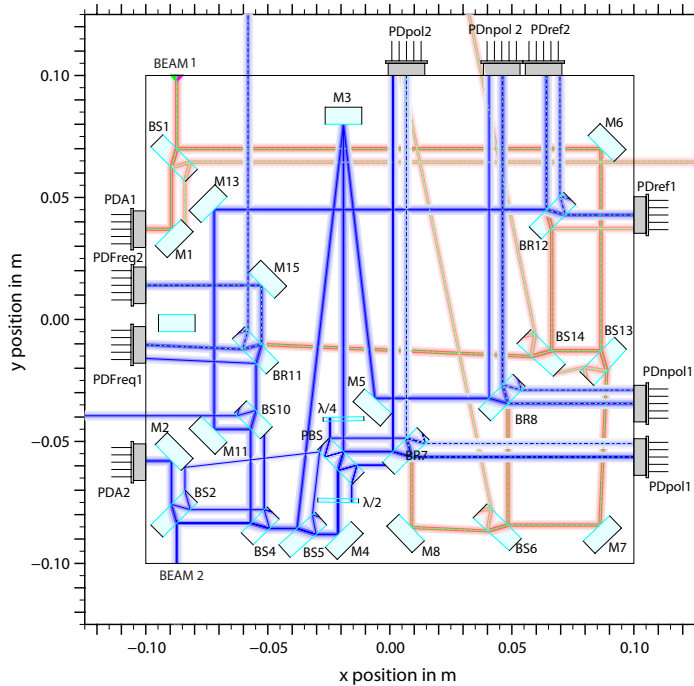


**Figure 4.18.:** Stray light analysis of the optical bench after implementing wedged components performed with OptoCad.

The simulation of path length noise induced inside an optical component in dependence on its wedge angle has been adopted for the optical bench testing polarising components. Assumed is a polarising beam splitter with a wedge of  $3^\circ$ . The beam propagates 170 mm to the wedged component and another 390 mm to the photodiode. The fibre coupler assembly will cause the beam to jitter with approximately  $10 \text{ nrad}/\sqrt{\text{Hz}}$ . This beam jitter will introduce path length noise of around  $500 \text{ pm}/\sqrt{\text{Hz}}$  at the PBS, which has centre thickness of 7.5 mm.

The potential for adding displacement noise to the system is significant and cannot be neglected. As a consequence, the use of parallel components for all optics has been decided as baseline. Furthermore, we avoided to use wedged components for mirrors due to the long lead time and the minor influence on stray light. Even though a sufficient thickness for the parallel components was chosen, the second order reflected beam is still re-entering the main beam due to the poor configuration. It is not possible to avoid such a configuration due to limited space, the required equal transmission count and equal arm lengths. However, stray light interfering with the main beam before passing the recombiner can be subtracted with balanced detection from the measurement signal in data post-processing. This has the effect that the measurement is depending

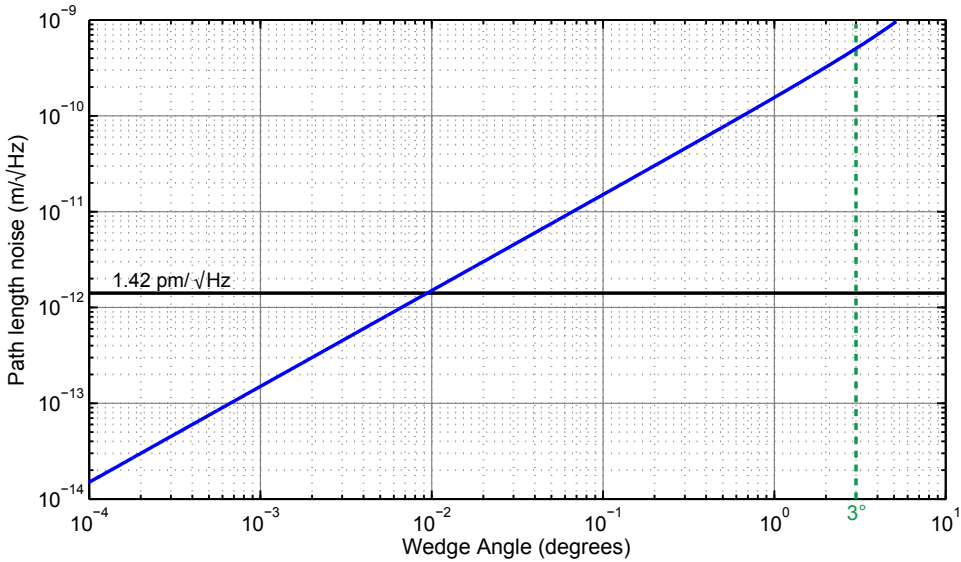


**Figure 4.19.:** Plot showing the influence of wedged optics onto the interferometer performance. *Blue:* Path length noise induced by an optical component as a function of its wedge angle for an  $45^\circ$ -angled incident beam with a jitter of about  $10 \text{ nrad}/\sqrt{\text{Hz}}$ ; *Black:* LISA requirement.

on both output ports of the beam splitter and the required redundancy of the photodiode is gone. In the case that the two beams have the same frequency, an aperture plate can be installed in the optical path suppressing spurious beams re-entering the optical path. Thus, it was decided to go ahead with this plan. The only change in design foresees to rotate both wave plates and the  $0^\circ$ -angle of incidence mirror by a small angle.

#### 4.2.2. Properties of the optical components

The baseplate is made of Clearceram<sup>®</sup>-Z HS. Clearceram<sup>®</sup> is a material with very low coefficient of thermal expansion of about  $2 \times 10^{-8} \text{K}^{-1}$  at room temperature [89]. The width and length of the baseplate are both 200 mm with a height of 50 mm. Its surface has been polished to an optical surface quality of  $\lambda/10$ .

In order to be aware of a possible deformation of the baseplate due to gravity, a numerical computation with MATLAB<sup>®</sup> has been performed to compute the magnitude of the bending [90, 91]. The calculation included the following parameters of Clearceram<sup>®</sup>-Z: density of  $2.55 \text{ g/cm}^3$ , Young's modulus of 90 GPa and Poisson's ratio of 0.25 [92]. A simple mounting of the bench only by its four edges is assumed. Thus, a symmetrical bending around its centre is expected. Figure 4.20 shows a 3D plot of the simulated deformation for a 50 mm thick

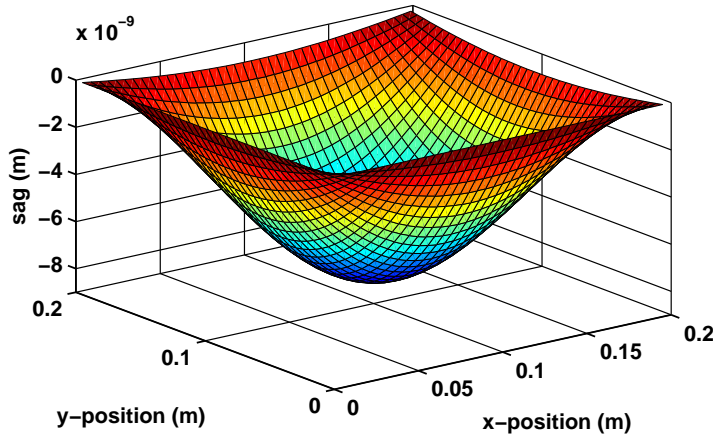


**Figure 4.20.:** Deformation analysis of a 50 mm thick Clearceram<sup>®</sup> bench under gravitational load. Shown is the deviation (vertical axis) from the nominal position without gravitational load for each position (horizontal axes) on the optical bench, while the baseplate is hold at its four edges.

optical bench under gravitational load. One can see the deviation (vertical axis) from the nominal position without gravitational load for each position (horizontal axes). The maximum sag is located in the middle of the plate and is about 8 nm. This deformation is more than two orders of magnitude below the angular tolerances of the optical components and more than one order of magnitude below the stringent requirement of its optical surface quality.

Parasitic length noise can also be due to thermal expansion of the substrate material and thermally driven changes in the refractive index induce fluctuations in the optical path of transmissive components. In order to suppress these path fluctuations, the components are made of a low-expansion material, such as fused silica. The inherent advantage of fused silica is the low coefficient of thermal expansion combined with an appropriate mechanical stability. In addition, fused silica exhibits a sufficient radiation hardness which was tested at UGL [93]. Due to strict constraints on the component's quality, *Suprasil*<sup>®</sup> 1 was chosen as baseline material. A high homogeneity was required along with a low absorption. *Suprasil*<sup>®</sup> 1 has a very low transmitted wavefront distortion due the fact that its has no striations in all three dimensions. The refractive index of *Suprasil*<sup>®</sup> 1 at 1064 nm is 1.44963 [94]. Furthermore, its thermal expansion coefficient  $\alpha$  is  $0.51 \times 10^{-6}/\text{K}$  and its temperature dependency on the index of refraction  $dn/dT$  is approximately  $9.8 \times 10^{-6}/\text{K}$  @ 632 nm. The relevant coefficients for transmissive components is

$$\frac{dn}{dT} + (n - 1) \cdot \alpha. \quad (4.17)$$



Special “athermal” glasses (e.g. Ohara S-PHM52, Schott N-FK51 and Schott N-FK56) are superior to fused silica in this criterion and are therefore used, e.g., as optical window in LTP, but are difficult to handle and it is unknown if they can be bonded [95]. Even though both coefficients are very low, transmission through the optics could still induce path length fluctuations of the level of a few picometre. To avoid this, the number of transmission for both optical paths had been designed to be identical.

The dimensions of the mirrors and the (polarising) beam splitters are  $15 \times 20 \times 7 \text{ mm}^3$  and  $20 \times 20 \times 7 \text{ mm}^3$ , respectively. Anti-reflection coatings are on all secondary surfaces. They serve to limit residual reflections, as well as for reducing stress. All front surfaces have a dielectric coating from an ion-beam-sputtered (IBS) coating process. This technique leads to dense layers with very low optical absorption. The mirror and beam splitter coatings are designed to provide 99.9% and 50% reflection, respectively, for an incoming angle of incidence of  $45^\circ$ . The polarising beam splitter has been specified to have a reflectivity of 99.9% for s-polarised light and only 2% for p-polarised light.

The zero-order wave plates are made from two plates of crystalline quartz, optically contacted with the direction of retardation opposed. As a result, the final retardation between the two polarisation axes is the difference of the thickness of the two plates,  $\lambda/2$  or  $\lambda/4$ . The thickness of each plate is around 0.8 mm, resulting in a total thickness of approximately 1.6 mm. The outer diameter of the wave plates is 12.7 mm. Both surfaces are anti-reflection coated to minimise residual reflections. On the one hand the optical path in a zero-order wave plate is less temperature sensitive. But on the other hand the optical path difference is more sensitive to tilts. Therefore, it has to be taken care that the tilt is smaller than  $1.5^\circ$  resulting in a deviation of the nominal path length difference smaller than the production tolerance.

The specified wavefront distortion for all optical components is  $\lambda/10 @ \lambda = 550 \text{ nm}$  and the parallelism of the front and rear surface is better than  $2''$ .

### 4.3. Description of the experimental setup

The interferometric readout was done in a LISA Pathfinder configuration [96]. An LTP based readout has been demonstrated to have sufficient sensitivity to measure picometre stability in the milli-Hertz region [87]. Therefore, an LTP-like phasemeter and modulation scheme was used to assess and compare the path length noise performance of the test bench. Although the metrology system of the LISA mission is based on heterodyne measurement at MHz

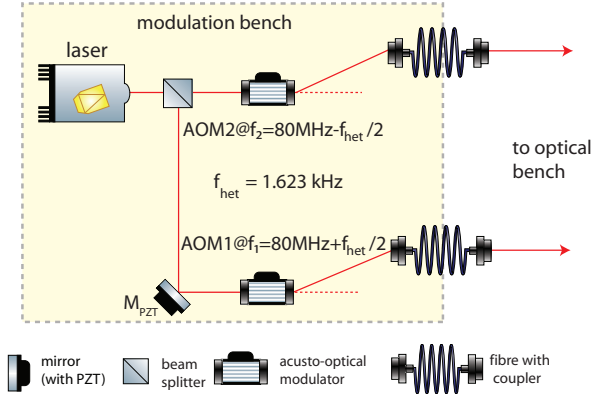


**Figure 4.21:** The modulation bench is in charge of the beam preparation and consists of the laser source and two acousto-optic modulators (AOMs). For an optical path length stabilisation a mirror  $M_{PZT}$  is mounted on a piezoelectric element.

frequencies it is expected that the LTP-style measurement at kHz is representative for MHz frequencies regarding the influence of polarising components to the interferometer sensitivity.

In the LTP scheme only one laser source was needed. As laser source a diode-pumped, monolithic Nd:YAG non-planar ring laser (*Innolight Mephisto*, 500 mW @ 1064 nm) has been used. This laser generates single frequency light with low intrinsic noise [97]. Furthermore, the interferometers are divided into two functional parts: the *modulation bench* and the *optical bench*. The modulation bench, which can be seen in Figure 4.21, provides the beam preparation and consists of the laser source and two acousto-optic modulators (AOMs). The linearly polarised single-frequency laser beam was split into two equal parts by a beam splitter. Notice that the initial beam was coupled into an optical fibre and injected onto the same modulation bench again. Consequently, the use of different lasers, in particular a frequency stabilised laser, was possible. Each beam was then shifted in frequency by an AOM driven at approximately 80 MHz, with a frequency difference  $f_{\text{het}}$  between the two driving signals. A phase-locked loop stabilised the difference frequency between the two AOM drivers to the heterodyne frequency of  $f_{\text{het}} = 1.623$  kHz. The two frequency shifted beams were coupled into single mode polarisation-maintaining optical fibres. These fibres acted as spatial mode-cleaners, which was necessary to achieve high interferometer contrast [98, 99]. In one beam path an auxiliary mirror  $M_{PZT}$  between AOM and fibre was installed, which could be moved by a piezoelectric transducer to compensate fluctuating optical path length differences (*cf.* Section 5.4). The two beams with almost equal optical path length and power were injected into the optical bench. The optical bench contained the four beam combiners and photodiodes, and thus formed the designed interferometers.

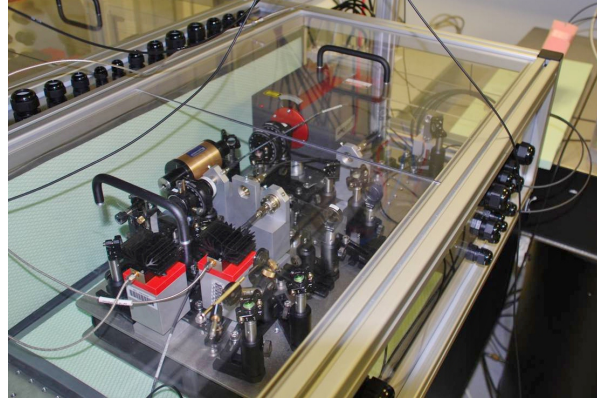


**Figure 4.22:** Modulation bench enclosed by a plexiglass and Styrodur<sup>®</sup> box to increase thermal stability and to reduce air movements.

The modulation bench was assembled on a double-plated steel Honeycomb-core ( $600 \times 300 \times 60 \text{ mm}^3$ , Thorlabs). This made it feasible to transport the whole experimental setup and to use different laser systems as well as vacuum chambers. In order to reduce air movements and enhance the thermal stability, the modulation bench was enclosed by a plexiglass box and by an additional box made of Styrodur<sup>®</sup>. Figure 4.22 shows the modulation bench in its laboratory environment.

#### 4.4. First experimental setup based on an aluminium baseplate

Due to the complexity of the design and the number of components, it was desired firstly to verify the general principle of the measurement scheme and to identify the difficulties in the design before implementing it on a low-expansion baseplate having long delivery times. To this end the experiment was set up on a  $45 \times 45 \text{ cm}^2$  aluminium baseplate. Other benefits arose due to the obtained experience and knowledge with the phase measurement system, the data post-processing chain, the polarising optics as well as the electronic devices, such as photodiodes and various control loops. Additionally, the time used for the initial experiment could be used to bridge the long lead time for the procurement of the vacuum chamber, the coordinate measurement machine (*cf.* Section 2.3.2) as well as the optical components including the optical baseplate and to prepare the required alignment techniques for the bonding process (*cf.* Chapter 2).

From the beginning it was clear that a picometre stability as required in Equation (4.1) cannot be validated for length measurements including polarising components set up on a metal breadboard. Such a sensitivity level can be

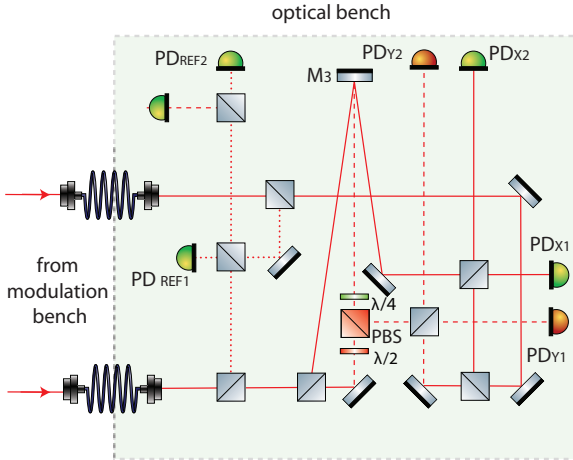


**Figure 4.23:** Schematic of the optical bench based on aluminium. It consists of two measurement interferometers (one with polarising components) and one reference interferometer.

reached only when the experiment would be assembled on a thermally and mechanically ultra-stable setup. However, the initial setup was already sufficient to demonstrate a performance on a future GRACE-like mission sensitivity level (*cf.* Section 4). The requirements for such a future mission are considerably relaxed compared to the LISA requirements, a few  $\text{nm}/\sqrt{\text{Hz}}$  as opposed to picometre.

For setting up the optical bench on a metal plate, some modifications in the design presented in Figure 4.12 and 4.13 were carried out. The major one was to abandon the frequency interferometer. Instead, a frequency stabilised laser was used. For reason of simplicity the fibre injectors were replaced, and unused components, such as  $\text{BS}_{\text{ALIGN}}$ , M1, M2, BS1 and BS2, were omitted from the setup. The schematic of the optical bench based on aluminium can be found in Figure 4.23. All non-polarising components used in the setup were made of fused silica, and all secondary surfaces had an anti-reflective coating to suppress ghost beams re-entering the optical path. The polarising components were all manufactured by Bernhard & Halle Nachfolger GmbH. As polarising beam splitter a cube type made of flint glass with a ceramic filler was used. Figure 4.24 shows the whole experiment including the modulation and optical bench.

In order to obtain the desired phases  $\phi_i$ , a software-based phase measurement system (PMS) was used. The heterodyne signals measured at the photodiodes were digitised by a computer at discrete intervals resulting in the vector  $I_k$  which contained several intensity samples that were then multiplied by a set of complex coefficients  $c_k$  that represents the sinusoidal modulation frequency. This yielded two series of coefficients  $b_k \propto \sin(k\Delta\phi)$  and  $a_k \propto \cos(k\Delta\phi)$  in

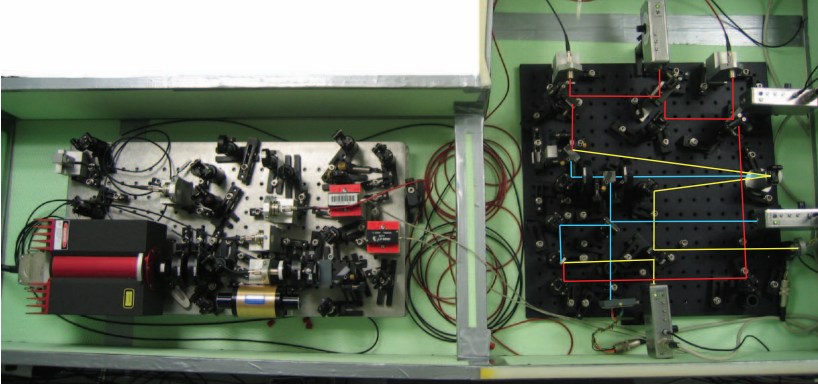


**Figure 4.24.:** Photograph of the initial setup based on an aluminium breadboard. *Left:* the modulation bench; *Right:* the optical bench containing three Mach-Zehnder-Interferometers, namely reference (red), non-polarising (yellow) and polarising (blue) interferometer.

orthogonal quadratures. The  $\Delta\phi$  inside the cosine and sine arguments was the phase shift representing the phase step between two consecutive intensity samples  $I_k$ . Finally summing over  $M$  samples of the discrete Fourier transform (DFT) led to:

$$\Im(\phi) = \sum_{k=0}^{M-1} a_k I_k \quad ; \quad \Re(\phi) = \sum_{k=0}^{M-1} b_k I_k, \quad (4.18)$$

where  $\Im(\phi)$  and  $\Re(\phi)$  represented the imaginary and real part of the Fourier Transform, respectively. The phase could be recovered by the arctangent operation over the sum of  $M$  samples of the DFT as

$$\phi = \arctan \sum_{k=0}^{M-1} c_k I_k. \quad (4.19)$$

Moreover, a phase tracking algorithm had to be included in order to avoid phase wrapping [100].

The displacement noise of this experimental setup is shown in Figure 4.25. The initial measurement (red trace) was performed in air, while it was enclosed by a plexiglass box. The dominant noise sources were non-linearities introduced by the two AOMs [101] and thermal instabilities. Consequently, some effort was made to improve the noise performance. Among these were successful attempts, such as to operate the optical bench in a vacuum environment as well as to implement an optical path length stabilisation (Section 5.4). Furthermore, it turned out that the arm length imbalances for the polarising and non-polarising interferometer were about 10 cm and 4 cm, respectively. A

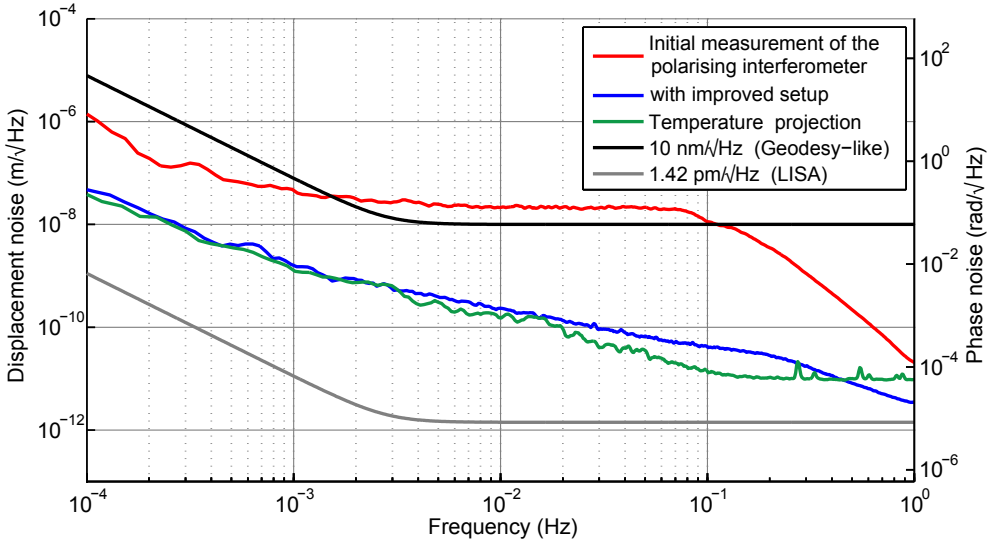


**Figure 4.25.:** Noise performance of the setup based on aluminium along with the temperature stability in its vacuum chamber (right axis) and the requirements of a future GRACE-like mission as well as the LISA mission. The initial measurement (red trace) was performed in air, while the blue trace represents the measurement conducted in a vacuum environment with an improved setup.

frequency stabilised laser was used to prevent frequency fluctuations from coupling into path length noise. In addition, the input polarisation state of the two beams on the modulation bench was adjusted to the two fibres injecting to the optical bench, and their output polarisation direction on the optical bench was readjusted (*cf.* Section 5.5). In order to mitigate stray light induced by the cubic PBS, this component was replaced by a rectangular one, analogue to the baseline design in Figure 4.12. Much effort was gone to reduce electronic and digitisation noise. As a consequence, the phase measurement system was replaced by a hardware phasemeter using field-programmable gate arrays (FPGAs), namely *PM3* [102, 103]. The last attempt towards an enhancement of the phase readout included the implementation of different algorithms in the `MATLAB`<sup>®</sup>-code used for noise subtraction in the data post-processing chain (*cf.* Chapter 6). In order to do so, various coupling coefficients were determined and used additionally for projecting the noise source into the length measurement. Thus, the resulting displacement noise reached a sensitivity of  $4 \times 10^{-11} \text{ m}/\sqrt{\text{Hz}}$  @ 100 mHz increasing with  $1/f$  towards lower frequencies, as presented by the blue trace in Figure 4.25. One can see that the length stability fulfilled already the requirement for a geodesy mission such as an on-axis GRACE follow-on mission [104], but had to be significantly improved for a picometre sensitivity as required for the LISA mission.

Despite all this effort, the phase readout could not be significantly reduced. Moreover, it turned out through several noise projections that these noise sources did not really limit the phase readout. Rather the thermal instability of the setup was identified as the limitation of the performance. This can be seen by the projection of the thermal noise to the displacement noise (green trace in Figure 4.25). The temperature measurement was limited by sensor noise for frequencies above 200 mHz. The linear coefficient of thermal expansion (CTE) of the aluminium baseplate is about  $23.7 \times 10^{-6}/\text{K}$  [105]. This yields thermal expansions of about  $11 \mu\text{m}/\text{K}$  for the 45 cm square metal breadboard. A temperature stability of a  $10^{-4} \text{K}/\sqrt{\text{Hz}}$  @ 1 mHz was obtained leading to a length stability of approximately  $1 \text{nm}/\sqrt{\text{Hz}}$  @ 1 mHz. In addition, all mounts for the components were made of aluminium further affecting the length measurement due to beam pointing instability. In order to improve the long-term path length and short-term beam jitter stability, the originally designed four interferometers were set up on a low-expansion glass-ceramic baseplate as described in the following.

## 4.5. Quasi-monolithic setup

One significant limiting noise source of the setup based on aluminium is the non-homogeneous thermal expansion of the metal baseplate. In order to overcome this limit, the hydroxide-catalysis bonding technique was used to assemble the originally designed four interferometers onto a low-expansion glass-ceramic baseplate made of Clearceram<sup>®</sup>-HS. The inherent advantage of such a material is the very low coefficient of thermal expansion. With a temperature stability better than  $10^{-4} \text{K}/\sqrt{\text{Hz}}$  no additional noise will be induced from expansion of the baseplate. By applying the bonding technique (*cf.* Section 2.1), ultra stable quasi-monolithic interferometers can be built performing on a picometre level, which has been demonstrated in various publication, e.g. [87, 106].

In contrast to the previous setup, the assembling of a quasi-monolithic bench is significantly more difficult. Challenging constraints had to be taken care of, where the antecedent design process tried to serve already some of them, such as the manufacturability or the ability to align the beams to each other. The main drawback of such stable interferometers is that there is no possibility to realign a component once the bond has settled. A typically settling time for the components used was about 30 seconds. Therefore, a precise positioning of each optical component was necessary. As described in detail in Chapter 2, there were mainly two options to do so. On the one hand a template could be used, where the component's position accuracy is limited by its manufacturing accuracy (*cf.* Section 2.2). Typically, this approach yields position accuracies of



about 100  $\mu\text{m}$  and an angular accuracy of few mrad [107]. On the other hand a coordinate measuring machine in combination with an alignment tool could be employed (*cf.* Section 2.3). This approach would allow to precisely manipulate every component to a level of a few microns. However, the precise placement of each component is very time consuming, but the resulting advantages prevailed over this drawback. One main advantage is the possibility to verify the final position of the component bonded and if needed, to correct for an occurred misplacement by adjusting other components. In addition, a minor factor at that time was a possible early delivery of the wedged components, which could be used instead of the rectangular mirrors. Using the CMM, a new component could immediately be implemented in the layout without losing time at the long manufacturing time for a template. Typically, the templates were produced at the mechanical workshop of the AEI. The manufacturing time of a template of such complexity was two to four weeks depending on the plant utilisation. Therefore, it was decided to adopt the CMM procedure for the precise alignment of the whole optical bench.

Depending on the layout, an alignment plan had to be developed to ensure that

- the CMM in combination with its alignment tool had sufficient space on the optical bench
- the sequencing of the construction proceeded from left to right (or backwards) or from the centre outwards; the recombination beam splitters were excluded from this constraint
- the two beams were aligned to each other from the beginning

The alignment plan developed can be found in detail in Appendix D. It can be summarised in three main stages: the first stage involved the glueing of the two fibre injectors onto the optical bench as well as the bonding of the auxiliary component  $\text{BS}_{\text{ALIGN}}$  for aligning the two beams to each other. Once both beams were parallel with respect to the baseplate and at the same height, all non-critical components could be bonded, representing the second stage. Optical components are classified as non-critical if they only split or reflect light without the need to hit a particular spot to very high precision. Apart from the recombination beam splitter all the components on the optical bench were categorised as non-critical in terms of alignment. That also included the two wave plates, although their polarisation direction had to be adjusted as precisely as possible. In addition, the tilt of the assembly of retarder and mount had to be kept below  $1.5^\circ$ , while transmitting it in the centre. After finalising this stage, all critical components, in particular the four beam combiners, had



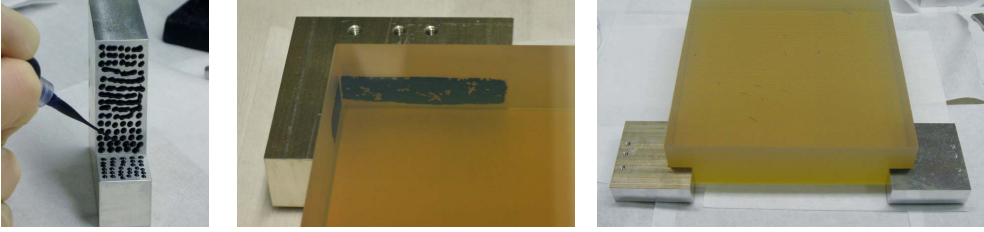


**Figure 4.26.:** Gluing process of the auxiliary plates (left picture) for mounting the fibre injector assemblies on the optical bench (both right pictures).

to be aligned in real-time and bonded to the baseplate. With this third stage the assembling of the optical bench had been completed. In the following paragraphs these three stages are described in more detail.

### Input beam alignment

One of the critical alignment processes was the precise alignment of the two fibre injectors ( *60FC-4-A11-03*, Schäfer & Kirchhoff) and the input beams involved. For the alignment of the fibre injectors, a mount with six degrees of freedom was used (*K6X*, Thorlabs): tip, tilt, rotation and three translational stages. Note that the  $Z$ -axis translation requires the combined use of the three adjusters (pitch, yaw and pivot) and was not needed. This mount had a  $4^\circ$  control of the pitch/yaw angles and a  $\pm 1.5$  mm dynamical range for the  $X/Y$  translation. Since the input beams define the position of the optical components and in particular the precise position of the recombination beam splitter, it is advisable to link them rigidly to the optical bench. Therefore, the assembly of fibre injector and mount was screwed on a plate made of Invar<sup>®</sup>. This material was chosen due the inherent low index of thermal expansion of  $2 \times 10^{-6} \text{ K}^{-1}$ . Prior to this, both plates were glued with an an epoxy resin (*ER 2188*, Electrotube) to the optical baseplate, as shown in Figure 4.26.

Because the vertical angle between the beams and the plane of the optical bench cannot be adjusted by the optical components on the baseplate, it is mandatory that both input beams are as parallel to the bench as possible. Therefore, the first component to be bonded on the baseplate was the auxiliary one, namely  $\text{BS}_{\text{ALIGN}}$ . It was used to align the two input beams parallel at identical height to the baseplate and to each other. Initially, the position and height of one fibre injector was aligned by measuring the centre of the fibre collimator with the CMM, which is shown in Figure 4.27. By using a polarimeter, the polarisation states of the two beams were adjusted. The preferred polarisation state was perpendicular to the plane of the baseplate (s-polarised). In order to align the first beam parallel with respect to the plane of the base-

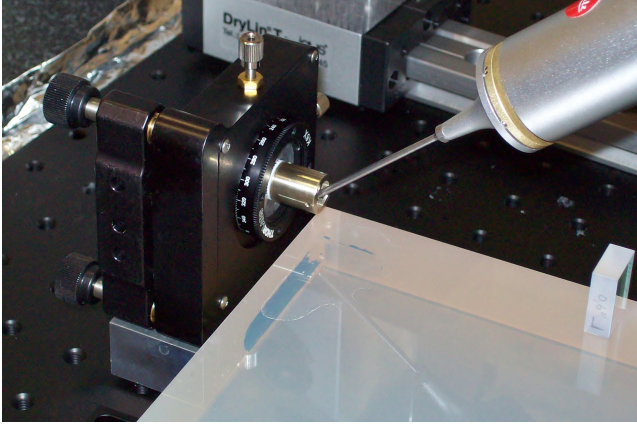


**Figure 4.27:** Photograph of the fibre injector assembly glued at the baseplate. The CMM is measuring its height and position. On the right side one can see the auxiliary component BSALIGN, with which the two beams have been collimated.

plate, the mirror BS<sub>align</sub>, used under 0°, reflected one part of the first input beam back to the fibre injector and transmitted the remaining light through the component to the second fibre injector. Figure 3.1 a) shows this first stage of the alignment process. By maximising the detected signal detected on PD1, the coupling efficiency was optimised. After coupling back the reflected part of the first input beam, the transmitted part was used to align the second fibre injector parallel with identical height to the baseplate. As an alternative, the input beam from the second fibre injector could be used. For this purpose, the transmitted part of the beam was coupled into the first fibre injector. Again, the detected signal on PD2 was maximised, as shown in Figure 3.1 b). This ensured the parallelism of both beams relative to the plane of the bench to a level of the mirror's perpendicularity of less than 2 arcseconds ( $\leq 10 \mu\text{rad}$ ). To conclude the beam alignment the lenses of both fibre injectors were coarsely adjusted to be collimated.

The two beam splitters BS1 and BS2 were bonded subsequently to redirect the input beams to the desired direction. For implementing an amplitude stabilisation readout, the components M1 and M2 were bonded. Using beam splitters instead of mirrors allowed a realigning of the two beams in case that one fibre coupler (or both) were misaligned before bonding the first recombination beam splitter.

### Alignment of non-critical components

In order to place all mirrors as well as all non-critical beam splitters on the baseplate, the adjustable bonding technique was adopted. For a detailed description of this process the reader is kindly referred to Section 2.3.4. In general, the baseplate as well as the optical component to be bonded had to undergo a cleaning procedure, as shown in Figure 4.28. Using the CMM, a three-point-



**Figure 4.28.:** Several cleaning steps during the bonding process: *Left:* describes the cleaning of the baseplate; *Middle:* describes the rinsing of the optical component with deionised water; *Right* describes the cleaning of an optical component.

reference (alignment tool) had been aligned for each component. An example of a program used for PC-DMIS is listed in Appendix C. Once the adjusters were aligned, the component, with the bonding fluid applied to its surface, was positioned against the three spheres, as shown in Figure 4.29. The used bonding solution had a 1:6 ratio of an aqueous sodium silicate solution ( $\text{Na}_2\text{Si}_3\text{O}_7$ ; 27% of  $\text{SiO}_2$  and 14%  $\text{NaOH}$  in  $\text{H}_2\text{O}$ ) to deionised water and was filtered with a  $0.2\ \mu\text{m}$  pore size filter. Figure 4.29 shows three examples of a component located against its three-point-reference, while its bond was settling. The alignment tool remained in its position for at least two hours until the component had settled and the bond had started to harden. Afterwards the alignment tool was removed to reuse it for the next component.

All non-critical optical components have been positioned with the adjustable bonding technique except the two wave plates. The zero-order wave plates (Bernhard Halle Nachfl. GmbH) have been mounted in a construction made of Invar<sup>®</sup>. Due to its low index of thermal expansion it is well suited for such a purpose. Finally, both wave plates were glued on the optical bench with an epoxy resin (*ER 2188*, Electrotube). In order to rotate the retarder

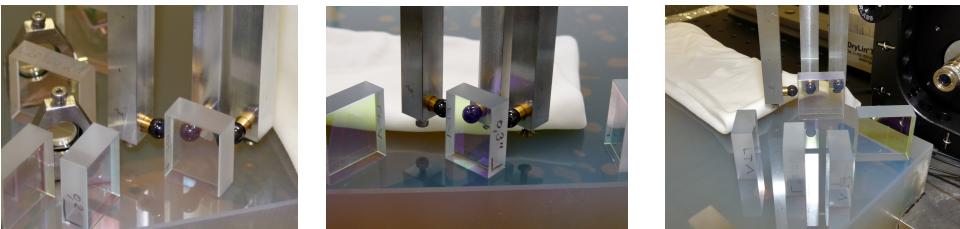


**Figure 4.29.:** A selection of adjustable bonded optical components in their three-point-reference frame.

after installation a small pin was glued to its mount. Thus, they were still rotatable and exchangeable. Initially, the  $\lambda/2$  wave plate was adjusted to maximum transmission through the polarising beam splitter by monitoring the transmitted light behind the polarising beam splitter ( $\Rightarrow$  p-polarised).

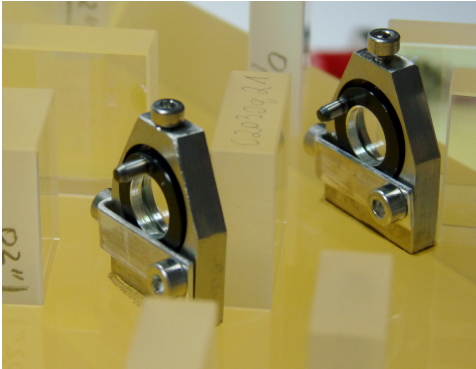


**Figure 4.30.:** Photograph of the polarising components on the optical bench.

For adjusting the  $\lambda/4$  wave plate the mirror M3 had to be bonded in place. This time the reflected beam at the polarising beam splitter was monitored by a photodetector and the orientation of the retarder was adjusted to maximum reflection. Note that after a double pass through a  $\lambda/4$ -plate the polarisation is rotated by  $90^\circ$  and thus s-polarised. A photograph of both glued wave plates is shown in Figure 4.30. In between them the bonded polarising beam splitter can be seen.

through a  $\lambda/4$ -plate the polarisation is rotated by  $90^\circ$  and thus s-polarised. A photograph of both glued wave plates is shown in Figure 4.30. In between them the bonded polarising beam splitter can be seen.

### Alignment of the beam combiners

In contrast to all non-critical components, the beam combiners for the four interferometers had to be aligned to the two beams to maximise the interferometric contrast at the photodetector. Resulting position and angular errors arising from the previously bonded non-critical components could thus be compensated with the recombination beam splitters. Therefore, they are classified as critical and the adjuster-aided bonding technique to heterodyne signals has been adopted.

The coarse alignment was done by using the CMM (Figure 4.31; upper left corner). Since the combiners had to be aligned during the bonding process, two beams with a heterodyne frequency of 1.6 kHz were injected onto the optical bench. For the precise alignment a buffer solution was used to allow adjustment until achieving maximum contrast. As a buffer liquid an alkane, such as n-Octane  $C_8H_{18}$ , was used. The initial amount of this buffer solution was high but would be decreased till the final bonding process took place. As long as the recombiner was gliding on the liquid, the position and the angle were iteratively varied in small steps until the contrast was optimised (main photograph in Figure 4.31). Once the optimum position was found the real bonding solution was applied in a scale of 0.8 micro litre per  $cm^2$ . For a detailed description of the adopted alignment process the reader is kindly referred to Section 2.3.5.

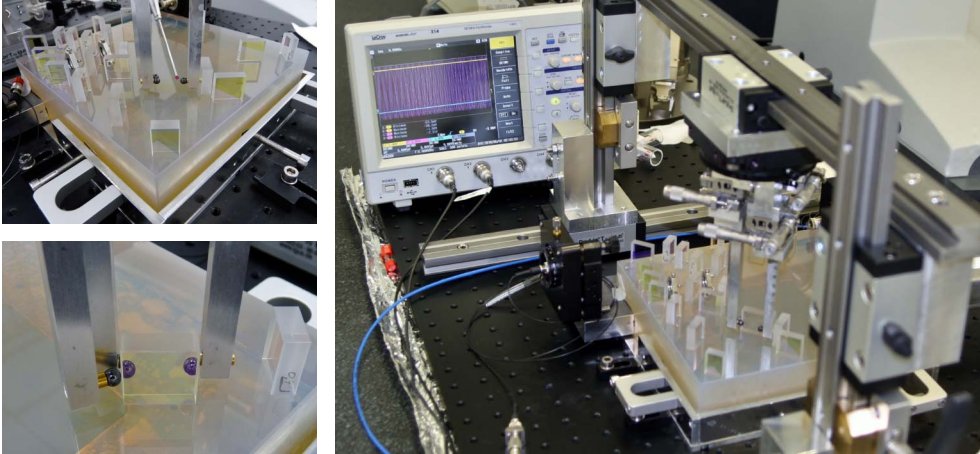


**Figure 4.31.:** Photographs of the interferometer before/during/after the alignment of a beam combiner.

## 4.6. Characterisation of the optical bench

One of the main advantages of using a CMM is the possibility to verify the final component positions after they were bonded and therefore being able to redesign the optical bench to correct for an unwanted misplacement of the component, if needed. Hence, the position and orientation of the components bonded have been determined step by step. The resulting values were fed to the IfoCad-file and the optical layout was updated.

The determined positioning accuracy of each component is listed in Table 4.3. Due to imperfection of the component dimensions, each component is well defined by only one corner point and its angle with respect to the coordinate frame of the optical bench (OCF). With the used software PC-DMIS the position of the corner point lying in the three-point-reference frame, the angle of the optical surface with respect to the  $X$ -axis of the optical bench and the thickness of each component were calculated. The deviation of the designed position,  $\Delta x$  and  $\Delta y$ , as well as the angular deviation are tabulated. A deviation  $\epsilon_d$  from the nominal thickness of 7 mm causes arm length imbalances on the optical bench. Since this yields a stronger coupling of frequency noise in the length noise this error is not negligible and therefore listed additionally in the table.

The resulting position accuracy is in average about  $\pm 10 \mu\text{m}$ , where the two uppermost and lowermost values are not taken into account. The uncertainty of a component's position is made up of the measurement uncertainty of its position and the positioning uncertainty of a single adjuster. A detailed evaluation



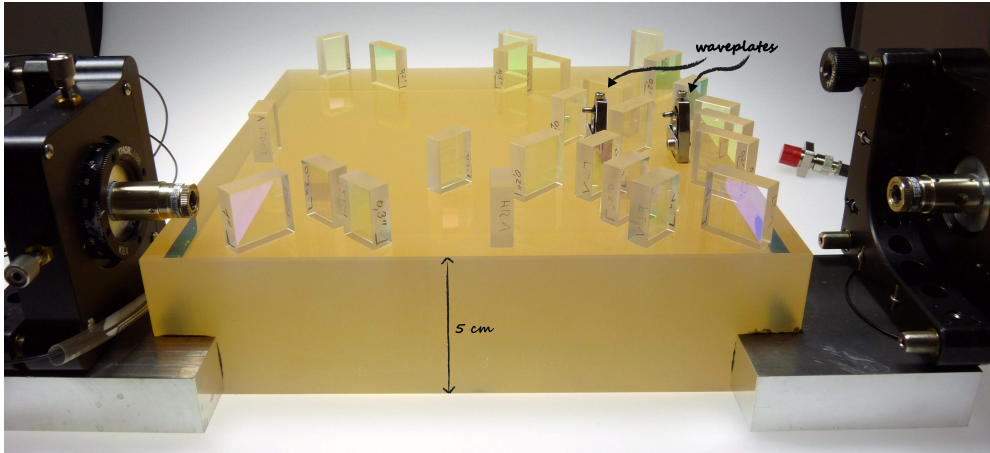


**Figure 4.32.:** Final bonded optical bench including the glued wave plates and fibre injectors.

of both uncertainty contributors are described in Appendix B.2. As a result, the expanded uncertainty of positioning a single adjuster is  $4.86 \mu\text{m}$  and the expanded uncertainty for measuring the component's position located in the centre of the optical bench is estimated to be  $5.38$ . Thus, a total uncertainty of  $10.24 \mu\text{m}$  is expected. This agrees with the determined position accuracy. Another important specification is the orientation of each component with respect to the optical bench frame. The measured orientation accuracy is for small components in average  $400 \mu\text{rad}$  (the uppermost and lowermost values have been excluded) and for bigger components  $170 \mu\text{rad}$ . Since the angular accuracy depends on the baseline of the measurement, a bigger variation of the angular deviation for small components ( $15 \times 7 \times 20 \text{ mm}^3$ ) was expected. Including the sampling uncertainty of the optical surface ( $20 \times 20 \text{ mm}^2$  or  $20 \times 15 \text{ mm}^2$ ), a measurement uncertainty of a component's orientation can be calculated for small components to be  $400 \mu\text{rad}$  and for bigger components to be  $280 \mu\text{m}$ . In addition, one has to consider the accuracy with which the angular orientation of a component can be defined (Section 2.4). This has been determined to be for small components  $510 \mu\text{rad}$  corresponding in an error of about  $105 \text{ arcseconds}$  and for the bigger ones about  $360 \mu\text{m}$ , which corresponds to an angular deviation of  $74 \text{ arcseconds}$ . Consequently, the determined angular accuracy for both types of components would be better than  $900 \mu\text{rad}$  ( $\sim 185 \text{ arcseconds}$ ) and  $640 \mu\text{rad}$  ( $\sim 130 \text{ arcseconds}$ ), respectively. Hence, the resulting orientations are confirming the model except for one component. The mirror M4 shows a relatively big deviation from its nominal orientation. This was probably due to too high positioning pressure in the bonding process.

Table 4.4 shows the characterisation of the four beam combiners and the

**Table 4.3.:** Accuracy characterisation of the bonded optical bench: deviation of the nominal position of the corner  $\Delta x/\Delta y$ , angular error and deviation of the nominal component thickness  $\epsilon_d$ .

Component	$\Delta x$ [ $\mu\text{m}$ ]	$\Delta y$ [ $\mu\text{m}$ ]	Angular deviation	$\epsilon_d$ [ $\mu\text{m}$ ]
BS1	-15	-53	03"	-43
BS2	-6	-20	-52"	143
M1	+1	+42	01'43"	174
M2	-10	+9	07"	174
BS4	-8	+12	44"	-43
BS5	+1	-9	36"	-42
M4	-4	-5	10'40"	184
M11	+3	+12	1'19"	70
BS10	-4	+29	-3'43"	146
M13	-3	-101	40"	43
M6	-15	-3	02'24"	182
BS13	-3	+9	01'23"	55
BS14	-22	0	11"	186
M7	-14	+10	29"	180
BS6	-1	0	00'00"	182
M8	-2	+8	-4"	182
PBS	-5	0	12"	192
M5	-16	+29	-4'0.5"	-36
M3	+7	-13	-35"	173

achieved contrast for each interferometer. Since they were adjustably bonded to optimise the heterodyne signals, a deviation of the nominal position and orientation was expected. The measured orientations deviate from the nominal orientation of  $45^\circ$ , caused by the previous misalignment of the non-critical optical components as well as a possible misalignment of the two input beams. Especially the misalignment of both measurement interferometers can be traced back to mirror M4. As a consequence, the alignment of subsequent components (*cf.* the alignment plan in Appendix D), in particular M3 and M5, had been redesigned. Furthermore, the measured position deviations indicate bigger arm length difference in the frequency and non-polarising interferometers. The achieved contrast for the frequency interferometer was 76%, while for the reference interferometer a contrast of 83% was achieved. For the polarising and non-polarising interferometers a contrast of 85% and 82% was attained, respectively.

**Table 4.4.:** Characterisation of the four interferometers by comparing the recombination beam splitters: deviation of the nominal position of the corner  $\Delta x/\Delta y$ , angular alignment of the component's optical surface to the  $X$ -axis, deviation of the nominal component thickness  $\epsilon_d$  and achieved contrast.

Interferometer	$X / Y$	$\Delta x / \Delta y$ [ $\mu\text{m}$ ]	Angle	$\epsilon_d$ [ $\mu\text{m}$ ]	Contrast
Polarising RBS7	x	324	-44°54'03"	186	85 %
	y	-858			
Non-polarising RBS8	x	$2.197 \cdot 10^3$	-45°10'50"	186	82 %
	y	72			
Frequency RBS11	x	$-1.245 \cdot 10^3$	44°52'12"	-42	76 %
	y	422			
Reference RBS12	x	404	44°58'02"	-44	83 %
	y	-286			

## 4.7. Summary

In the current baseline design for the LISA optical bench, the use of polarising optics is foreseen to separate optical beams. Therefore it is important to investigate the influence of polarising components on the interferometer sensitivity. For this purpose a quasi-monolithic optical bench has been designed consisting of two measurement interferometers (one including polarising optics). Additionally a frequency and reference interferometer were included. Stray light on the optical bench was simulated and reduced by modifying the layout. In addition, the layout was analysed with respect to periodic non-linearities. As a result periodic phase errors should have no effect on the phase readout. First, a modified layout was set up on an aluminium breadboard. Noise performances reached a length stability on the order of  $50 \text{ pm}/\sqrt{\text{Hz}}$  at 100 MHz increasing as  $1/f$  at lower frequencies. The significant limiting noise sources were non-homogenous thermal expansion of the metal baseplate and mechanical stability of the setup. To improve the thermal and mechanical stability, a Clearceram<sup>®</sup> baseplate was used and the silicate bonding technique was applied. A CMM was used to align the positions of the optical components, which yielded a positioning accuracy of  $10 \mu\text{m}$  and an angular accuracy of about  $400 \mu\text{rad}$  and  $170 \mu\text{rad}$  for the small and big components, respectively. The measurement uncertainty of the CMM could be identified as limiting source. Furthermore, the arm length differences were determined to be on the order of 1 mm.

In order to validate that the required picometre/ $\sqrt{\text{Hz}}$  path length stability is achievable, several experimental investigations have been performed, which are presented in the following chapter.



# 5 Experimental investigations

*For the sake of clear reference, a set of abbreviations (subscripts) is introduced, a measurement code (m-code), to specify the measures and stabilisations performed as well as the applied noise subtraction models in post-processing. It is applied to all displacement measurements shown in Chapters 5 and 6.*

Reduction of external influences		Data post-processing	
Vacuum	V	Stray light	s
Thermal shield	T	Laser intensity noise	a
Polarisation control:	P	DWS	d
only on modulation bench	P <sub>M</sub>	Frequency noise	f
only on optical bench	P <sub>OB</sub>	Temperature noise	t
Active stabilisation		<i>Example: m-code: VFs</i>	
OPD	O	Measurement conducted in vacuum and actively frequency stabilised. The balance detection is applied in post-processing.	
Frequency fluctuations	F		
Intensity fluctuations	A		

A quasi-monolithic optical bench consisting of four heterodyne Mach-Zehnder interferometers was built to investigate the influence of polarising optics on interferometer sensitivity. The design and the characterisation of the optical bench, as well as the basic experimental setup, are described in Chapter 4. In this chapter the experimental investigations of the optical bench are de-

scribed, including the verification of the functional operation and noise levels of the phase measurement system, the reduction of external influences such as thermal and air fluctuations, and the investigation on residual noise sources such as frequency and amplitude fluctuations of the laser system used. Since polarising optics can introduce non-linear errors, the interferometric sensitivity can potentially be limited by these phase errors. Therefore, the behaviour of polarising optics concerning periodic phase errors was also investigated and the results of these investigations are presented in this chapter.

### 5.1. Characterisation of phase measurement noise

Since the phase read-out noise is potentially limited by the phase measurement system (PMS) used, a characterisation of the PMS is mandatory. For the initial measurements based on an aluminium baseplate, a software-based phasemeter called *PM2* implemented on a PC was used. Before sending the detected beat note signals to the data acquisition (DAQ) system, they were low-pass filtered to prevent aliasing. The DAQ system consisted of a sampling card from National Instruments (*NI6014*) featuring 16 input channels with a combined sampling rate of up to 200 kHz. Since it was desired to simultaneously read out several channels, the single 16 bit analogue-to-digital converter (ADC) was used with a 16-channel sample-and-hold circuit and a multiplexer to digitise the input signals. Thus, 10 channels with a sampling frequency of 20 kHz could be read out and processed in the software. A DFT algorithm, as described in Section 4.4, has been applied and the resulting phase was stored on the PC. Verification of the phase measurement noise revealed a lowest achievable noise of about  $1 \text{ pm}/\sqrt{\text{Hz}}$  with ideal signals [91]. Such a noise level was sufficiently low for the experiments initially performed on the aluminium baseplate and did not limit the phase readout. However, for reaching the required noise level of  $1.42 \text{ pm}/\sqrt{\text{Hz}}$  the noise of the *PM2* system was insufficient, since even small disturbances increased the phase noise considerably above the requirement. Therefore, this phase measurement system was replaced by a digital hardware-based phasemeter, called *PM3* [87], using field-programmable gate arrays (FPGAs) [102].

A picture of the LPF based phasemeter *PM3*, developed at AEI, is shown in Figure 5.1. The underlying principle is based on a single-bin discrete Fourier transform (SBDF) [103] at the heterodyne frequency. The core processing of the SBDF is implemented in field-programmable gate arrays. The signal from each of the 20 input channels is sampled by a dedicated ADC and split into sequential data sets. Then the data are processed in FPGA chips. For in-

**Figure 5.1:** Photograph of the hardware-based phase measurement system (PM3) implemented using field-programmable gate arrays with an analogue front-end (20 input channels).



In this system, a single input channel consists of a low-noise transimpedance amplifier, a dedicated ADC with an 18 bit resolution running with a sampling frequency of 800 kHz, and one FPGA unit for the SBDFT computation. In order to enable synchronous sampling in all channels, all ADCs are triggered by the same reference clock. This clock is additionally used for synchronising the PLL for both AOMs and the data acquisition of the temperature measurement system. The computed data can be read out by the host PC with a parallel port interface. The final phase computation and further processing are performed by a C program running on the PC and stored on the PC. The gathered data were evaluated using the LISA technology package data analysis (LTPDA) toolbox for MATLAB<sup>®</sup>, which is the software toolbox developed for the data analysis of the LISA Pathfinder mission, but also for reproducible laboratory data analysis.

In order to measure the phase measurement noise, electrical signals from a single function generator were used. The electrical sinusoidal signal was split into 20 identical signals, which were connected to all input channels of the phasemeter. The amplitude of the input signal was varied from 25 mV<sub>pp</sub> to 1.5 V<sub>pp</sub> and the influence on the measurement noise was computed. The difference between two channels of the phasemeter, with nominally identical phases, was calculated. Figure 5.2 shows the phasemeter noise of two channels used for the polarising as well as the non-polarising interferometer. When digitisation noise or electronic noise within the phasemeter analogue front end is the limiting noise source, the phasemeter noise would depend on the input signal amplitude: with decreasing signal amplitude the phase noise is increasing. This is caused by a reduction in signal-to-noise ratio and therefore a lower number of effective bits [100]. Typically, input signals with an amplitude of approximately 0.75 V<sub>pp</sub> were used yielding phasemeter noise approximately one order of magnitude below the requirement. Note that this can be seen only as a lower limit on phasemeter noise, since the real signals detected by the photodiodes

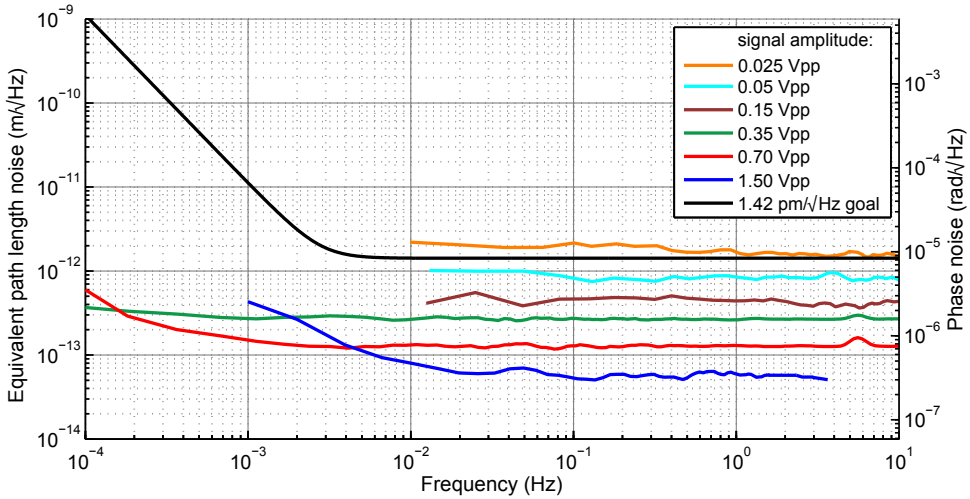


**Figure 5.2.:** Comparison between phasemeter noise of two channels used for the polarising and non-polarising interferometer, while the input signal levels generated by a single function generator have been varied. The phase measurement system used, is an FPGA-based phasemeter developed for LPF at AEI: PM3

are likely to have higher phase and amplitude noise than the ideal signal from the function generator.

## 5.2. Reduction of environmental influences

Fluctuations in air pressure as well as temperature lead to fluctuations in the refractive index of air and appear as path length changes [108]. One possibility towards minimising this noise source is to enclose the experiment in a box. An initial measurement of the quasi-monolithic setup enclosed by a box made of plexiglass with an additional layer of Styrodur<sup>®</sup> is indicated in Figure 5.4 by the red trace. Although the experiment is protected from external airflows, parasitic airflows in the enclosed volume, caused by convection from heated surfaces, as well as acoustical and thermal coupling are still limiting the phase readout.

In order to avoid any coupling of noise induced by variations of the refractive index of air into the phase readout, the measurement was henceforth conducted in vacuum. The vacuum chamber used throughout this experiment is made of steel with outer dimensions of  $80 \times 80 \times 80 \text{ cm}^3$ , as shown in Figure 5.3 a). Typically, pressure levels between  $10^{-5}$  and  $10^{-6}$  mbar have been achieved using a turbo-molecular pump in combination with a scroll pump. Length measurements of the polarising interferometer – in fact any measurements performed

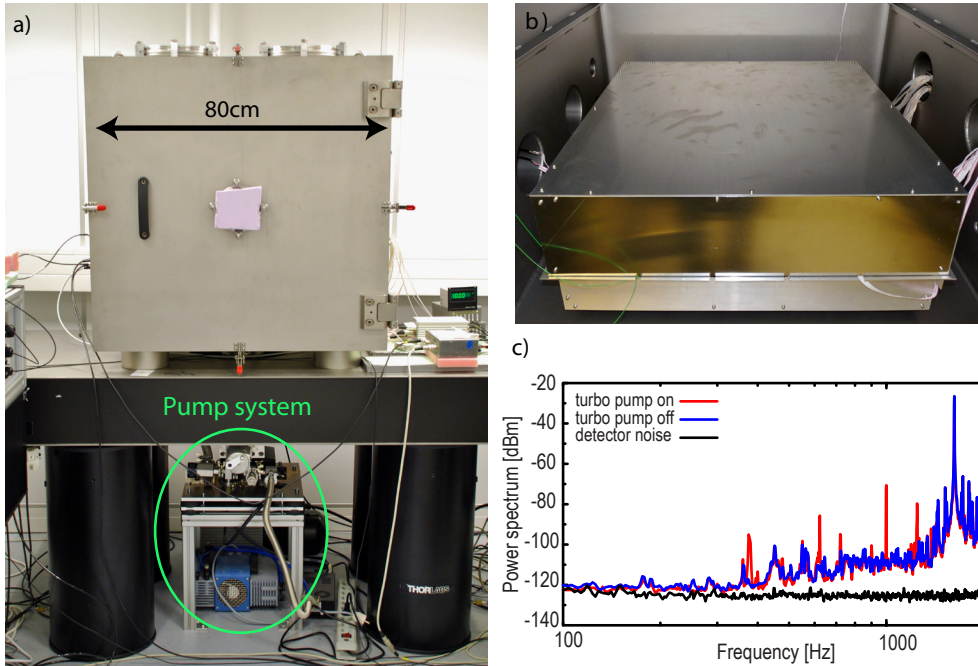


**Figure 5.3.:** *a)*: Photograph of the vacuum chamber and its pump system (circled in green) located on an optical table. A passive vibration isolation avoids the rotational frequency of the pump system from coupling into the beat note signal. The pump system is additionally isolated via a diaphragm bellows; *b)*: Thermal shield made of polished aluminium sheet metal; *c)*: Power spectrum of the beat note signal with running turbo pump and without.

with one of the four interferometers—show an improvement in sensitivity of about two orders of magnitude for frequencies above 1 mHz, as reflected in Figure 5.4 by the green trace.

The limiting noise source in the low-frequency range, in particular below 10 mHz, is temperature instability. In general, the measurements are conducted at room temperature. Although the temperature fluctuations in the laboratory are controlled to be less than 1°C and the vacuum chamber served as a reasonable low-pass filter for temperature fluctuations, thermal variations still affected the length measurements. For a further reduction of temperature noise a passive thermal shield (TS) was installed inside the chamber, which consisted of an aluminium baseplate on ceramic spacers made of Macor<sup>®</sup> with a cover made of polished aluminium sheet metal. It acted as a thermal low-pass and reduced the heat radiation, whilst the ceramic spacer reduced heat conduction. Figure 5.3 b) shows the TS used, which is split in the middle such that an experimental alignment is easy accessible. In order to verify the impact

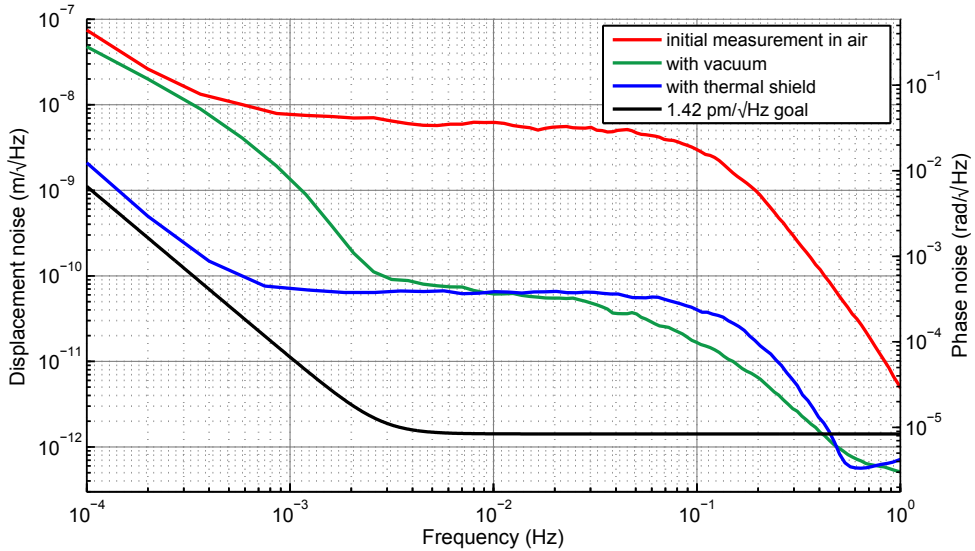


**Figure 5.4.:** Polarising interferometer performance: *Red trace:* Initial measurement in air but enclosed by a box made of plexiglass with an additional layer of Styrodur<sup>®</sup>; *Green trace:* [m-code:V] measurement is conducted in vacuum; *Blue trace:* [m-code:VT] enclosed by a thermal shield in vacuum.

of the thermal shield on the temperature noise, the temperature was measured at different locations outside and inside the vacuum chamber as well as inside the thermal shield. This was done by an eight-channel thermometer, developed at AEI, based on a Wheatstone bridge where one resistor is a platinum resistance thermometer (PRT) [109]. Throughout this thesis platinum sensors (PT10K) with resistance of  $10\text{ K } \Omega @ 25^\circ\text{C}$  were used. The bridge is excited with an AC voltage and the differential voltage of the bridge is measured with a 28-bit sigma-delta ADC front end with subsequent processing performed by an FPGA. The measured data were read out by the host PC with a serial port interface. The resulting noise estimates of temperature measured inside the thermal shield (blue trace) indicated a suppression of more than four orders of magnitude compared to room temperature (grey trace) as depicted in Figure 5.5. The lpsd (linear frequency axes power spectral density) algorithm [110, 111] was used for this and all other spectral estimates throughout this thesis. Measurements conducted inside the thermal shield were limited by the PT10K sensor noise for frequencies above 2 mHz. This can be concluded by considering the difference of two sensors, representing the uncorrelated noise between the two channels. The read-out limit determined for the PT10K sensors is shown in Figure 5.5 by the dashed grey trace labelled ‘read-out limit’. In contrast, the estimates for the temperature stability inside the vacuum chamber (red trace) were improved by one order of magnitude with respect to the

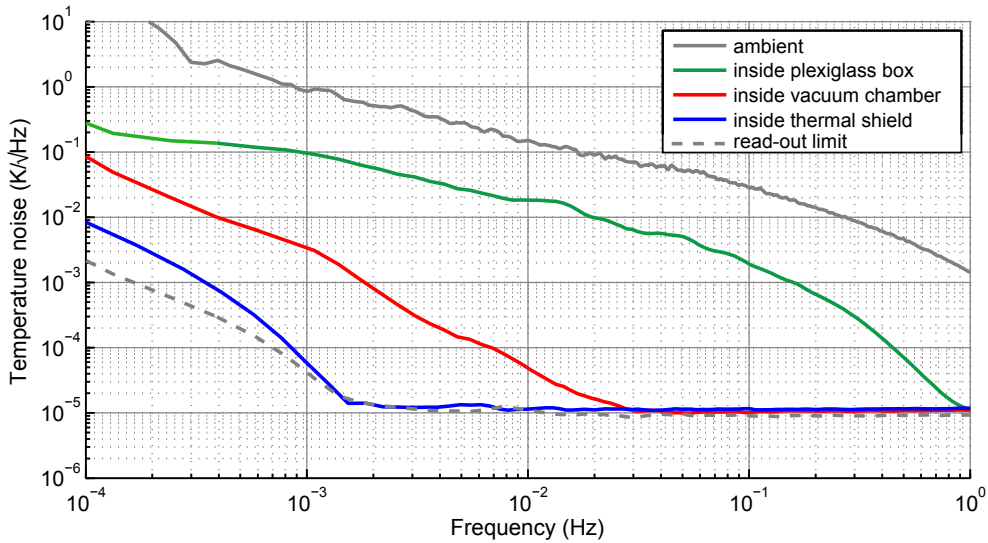


**Figure 5.5.:** Measured temperature noise in- and outside the vacuum chamber to verify the effect of the thermal shield.

obtained stability without TS for frequencies below 20 mHz. The stability obtained was also limited by sensor noise for frequencies higher than 20 mHz.

Consequently, the length measurements performed under such a thermally stable environment has been significantly improved for frequencies  $\leq 3$  mHz (Figure 5.4, blue trace).

In order to reduce vibrations induced by the pump system a passive vibration isolation of the optical table with the vacuum chamber on it was used. The pump system is located beneath the chamber and isolated via a diaphragm bellows, as depicted in Figure 5.3 a) by the green circle. This minimised the rotational frequency of the turbo-molecular pump coupling into the beat note signal at 1.623 kHz. The noise power spectrum of the beat note signal obtained with and without the turbo pump running is shown in Figure 5.3 c). Furthermore, a valve was installed between pump system and chamber enabling a switching off of the turbo pump. Vacuum compatible dampers were installed beneath the thermal shield. This led to a vibration isolation for excitation frequencies above 10 mHz.

Due to the significant improvements of the length performance and the excellent temperature isolation obtained by the thermal shield, all further measurements have been conducted in the described improved environment. The implementation of the optical bench in that environment along with the photodiodes



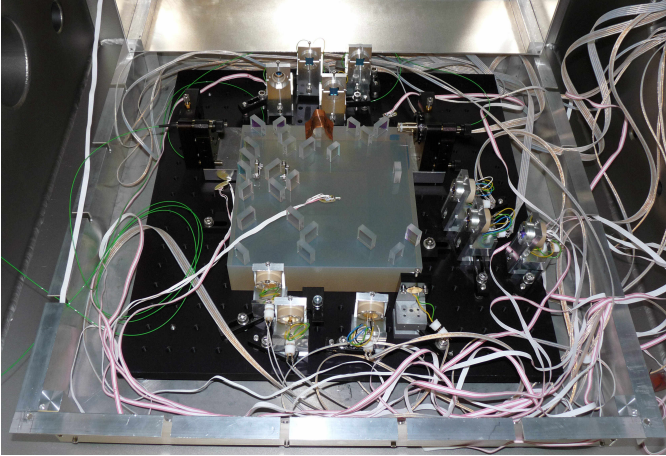


**Figure 5.6:** Implementation of the optical bench in its vacuum environment including thermal shield, photodiodes and temperature sensors.

and temperature sensors used is shown in Figure 5.6.

### 5.3. Beam pointing fluctuations

In order to inject light from a laser to an optical bench in space applications, it is desirable to use quasi-monolithic, bonded fibre coupler assemblies. Such fibre injector optical sub-assemblies (FIOS) will be used on the final LISA optical bench [112]. However, at the time of manufacturing the optical bench described in this thesis, these ultra-stable fibre injectors were not available, nor for the subsequent bonded optical bench (*cf.* Chapter 8). Consequently, commercial off-the-shelf adjustable fibre couplers produced by Schäfter & Kirchoff were used instead, as described in Section 4.5. For mounting as well as adjusting these injectors, commercial mounts produced by Thorlabs were purchased. Although the type of mount selected provided lockable adjustment screws as well as a compact and solid body, a significant beam pointing jitter was expected and also eventually observed. Pointing jitter can couple into the detected phase and significantly disturb the phase readout [113].

In order to assess this noise source, the relative angle between the two beams impinging onto the photodiode was measured. Using quadrant photodiodes instead of single element photodiodes ( $PD_{\text{pol}2}$ ,  $PD_{\text{npol}2}$  and  $PD_{\text{ref}2}$ ), the technique of differential wavefront sensing (DWS) could be applied [114, 115]. It starts with a separate phase measurement on each segment of the quadrant photodiode. The horizontal DWS signal  $\varphi$  was calculated from the phase difference between the left and the right side of one QPD:

$$\varphi_{\text{dws}} = \kappa_{\text{dws}} (\phi_{\text{left}} - \phi_{\text{right}}) \quad (5.1)$$



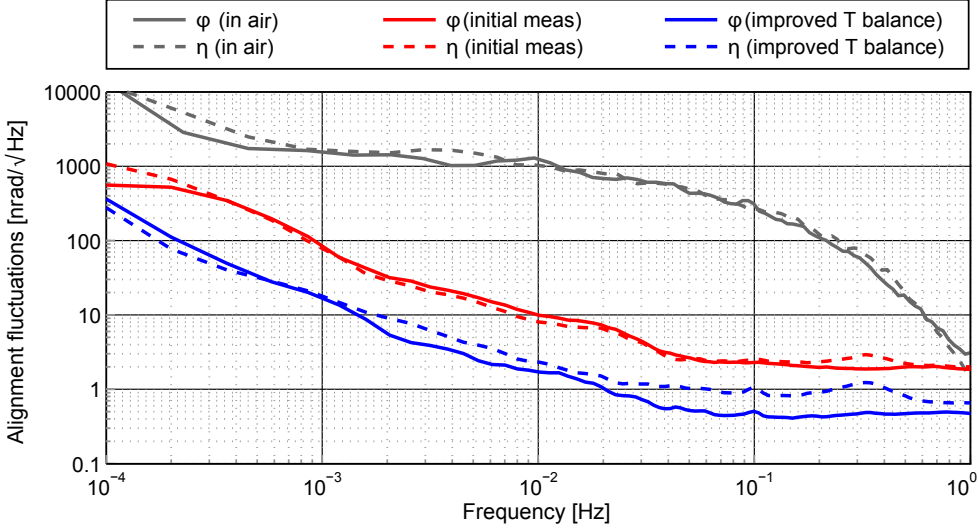


**Figure 5.7.:** Angular noise of a measurement in air but enclosed by the vacuum chamber (grey) along with one conducted after a few days in the evacuated chamber (blue) and then at reaching a state close to thermal equilibrium (red).

with<sup>[1]</sup>

$$\phi_{\text{left}} = \phi_A + \phi_C, \quad \phi_{\text{right}} = \phi_B + \phi_D, \quad (5.2)$$

where  $\phi_i$  is the phase measured at quadrant  $i$  (*cf.* Figure 3.2) and  $\kappa_{\text{dws}}$  is the coupling factor of DWS signal [phase change in rad] to beam angle change. Thus, a signal is generated that depends on the relative angle between the wavefronts of the two interfering beams. In the same manner, the vertical wavefront tilt  $\eta$  was obtained from the phase difference between the upper and the lower quadrants of the same QPD:

$$\eta_{\text{dws}} = \kappa_{\text{dws}} (\phi_{\text{top}} - \phi_{\text{bottom}}) \quad (5.3)$$

with

$$\phi_{\text{top}} = \phi_A + \phi_B, \quad \phi_{\text{bottom}} = \phi_C + \phi_D. \quad (5.4)$$

To convert the DWS signals to beam tilt the coupling factor  $\kappa_{\text{dws}}$  was determined. This was done by tilting the fibre couplers in the horizontal and vertical plane by a certain angle and measuring the resulting response in the DWS signals. Figure 5.8 shows the recorded time series of the vertical and horizontal DWS signals of the two measurement and reference interferometers for the two beams. The fibre mounts were vertically and horizontally tilted by

<sup>[1]</sup>Often alternative definitions are used as  $\phi_{\text{left}} = (\phi_A + \phi_C)/2$  etc.

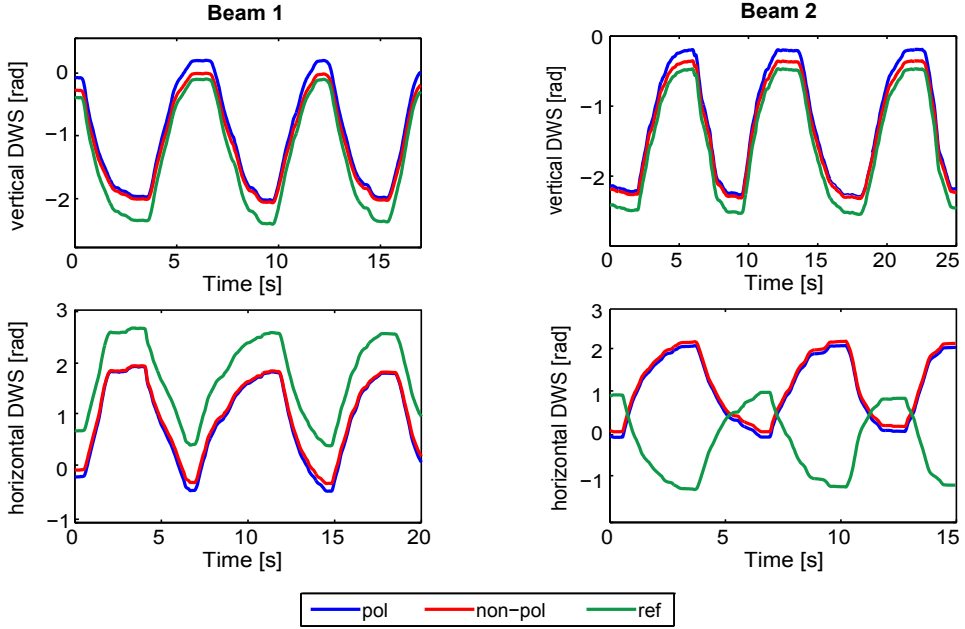


**Figure 5.8.:** Recorded time series of the vertical and horizontal DWS signals of the polarising, non-polarising and reference interferometer, whilst the fibre mounts of both input beams were tilted by approximately  $625 \mu\text{rad}$ , consecutively.

about  $1/8$  revolution of the fine motion screw, consecutively. This corresponds to approximately  $625 \mu\text{rad}$  [116]. The peak-to-peak variation in DWS signal is for all interferometers approximately  $2.3 \text{ rad}_{\text{dws}}$ . Thus, the coupling coefficient determined is

$$\kappa_{\text{dws}} = \frac{2.38 \text{ rad}_{\text{dws}}}{625 \mu\text{rad}} \approx 3800 \frac{\text{rad}_{\text{dws}}}{\text{rad}}. \quad (5.5)$$

Using this coupling coefficient the angular noise was determined and is presented for three different measurement runs in Figure 5.7. The grey traces show the angular fluctuations for measurements in the non-evacuated vacuum chamber. It becomes apparent that angular noise is increased by temperature and air fluctuations. By suppressing air and thermal fluctuations a significant improvement was obtained. The blue traces represent a measurement taken a few days after the chamber was closed and evacuated, whereas the red traces show the measurement taken two weeks after the chamber was closed and evacuated. The temperature stability had reached an equilibrium while the pressure stayed at a constant level.

Although the angular noise could be greatly reduced, it remains a potentially limiting noise source. Therefore, residual alignment fluctuations have been subtracted from the interferometric signals in data post-processing. For a de-

tailed description of the subtraction algorithm the reader is kindly referred to Section 6.4.

## 5.4. Reduction of sideband-induced noise

The interferometer concept included a reference interferometer that sensed common-mode phase fluctuations caused by environmental noise, such as fluctuations in the modulation bench which was outside the chamber. By subtracting this reference phase from the measurement phases, these fluctuations were sufficiently suppressed for frequencies below 1 Hz.

Electrically induced sidebands on the light, which give rise to non-linearities in the interferometer output, can reduce this common mode noise rejection and disturb the interferometer sensitivity [117]. The noise shoulder being present in Figure 5.10 (red trace) is a sign of such periodic phase errors. Electrical sidebands were introduced by the RF driving signals of both AOMs used for the generation of the heterodyne signal (*cf.* Section 4.3). These electrical sidebands in the AOMs caused optical sidebands in the modulated light and subsequently also in the beat note signals measured at the photodiodes. As a result, these optical sidebands produced a spurious beat note signal: the sideband-induced noise. A detailed description of the conversion of electrical into optical sidebands as well as the influence of these sidebands on the phase readout is given in [101]. One way to suppress optical sidebands was to reduce electronic cross-talk. By separating as well as shielding the two AOM drivers from each other the amplitude of electronic side bands could be reduced. In order to measure this effect, the optical path length difference (OPD) was scanned using a mirror mounted on a piezoelectric element (piezo) on the modulation bench

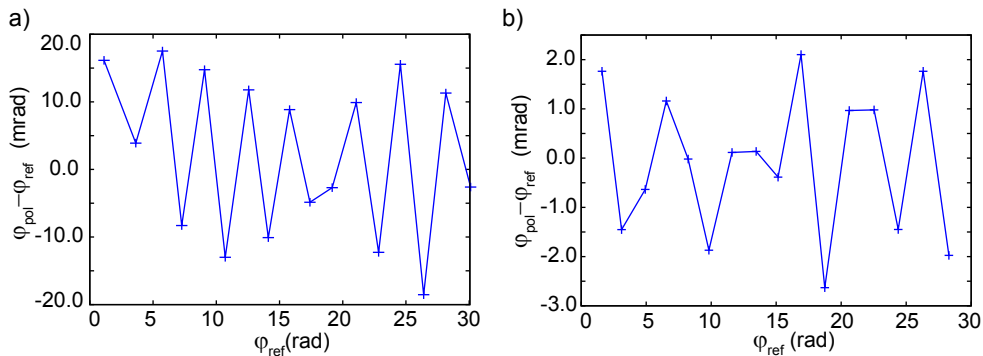


**Figure 5.9.:** Effect of sideband-induced noise into the interferometric phase of the polarising interferometer with reduced electronic cross-talk (b) and without (a). (Note the difference in scales.)

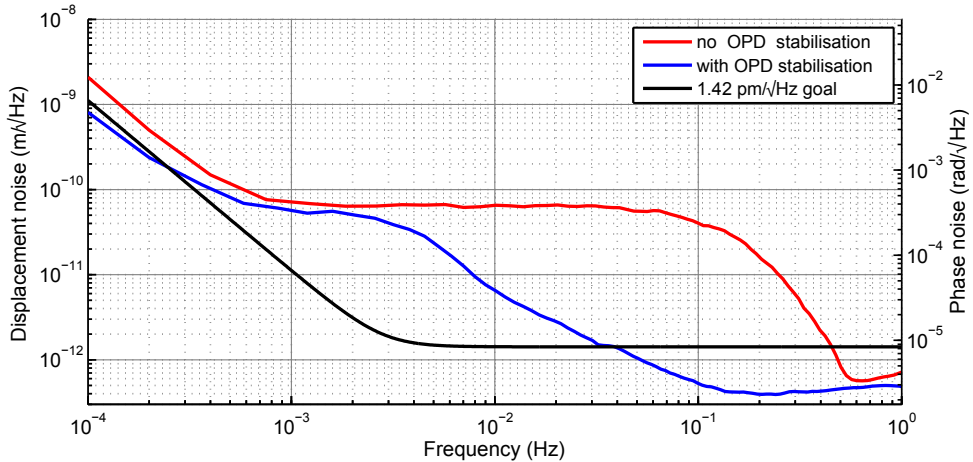


**Figure 5.10.:** Comparison between noise performance of the polarising interferometer observed with an active optical path length difference (OPD) stabilisation and without [m-code:VTO].

$M_{PZT}$ <sup>[2]</sup>. A triangular scanning signal with a frequency of 1 Hz and amplitude of  $500 \text{ mV}_{pp}$  generated by a function generator was injected via a high voltage amplifier to the piezo. However, due to the Doppler effect, fast OPD changes can also introduce an additional error. As described in Section 5.1, the core process of the phasemeter is based on a SBDFT, which in turn relies on the heterodyne frequency to remain exactly centred in one output bin of the DFT. Fast phase shifts, such as caused by fast OPD fluctuations, lead to spurious fluctuations of the heterodyne frequency within the chosen bin. This residual error term, resembling a Doppler shift and therefore called *Doppler-induced errors*, have to be subtracted from the measurement before further analyses on the sideband-induced error can be carried out. The method of subtracting has been discussed in reference [87] and [101] and is omitted here for the sake of brevity. The Doppler-corrected initial measurement of the phase difference between the polarising and reference interferometer versus the reference phase is depicted in Figure 5.9 a). Measuring the same phase difference with the focus on minimising electrical cross-talk by separating and shielding the AOM drivers as well as cables, the induced electrical sidebands could be reduced by one order of magnitude to be about 3 mrad. This is reflected in Figure 5.9 b).

### Stabilisation of optical path length difference

In order to further mitigate these periodic phase errors emerging from optical sidebands, a stabilisation of the OPD has been integrated into the modulation

<sup>[2]</sup>This work was done together with Malte Vogt.

bench by comparing the reference phase  $\phi_{\text{ref}}$  to the electronic phase  $\phi_{\text{het}}$  of the reference oscillator [95]. The phase difference was held constant in closed-loop control by actuating mirror  $M_{\text{PZT}}$  that was mounted on a piezo on the modulation bench (*cf.* Figure 5.20). In contrast to reducing the amplitude of electrical sidebands, this method does not minimise this noise source, but converts the error term into a constant and relative small offset in the differential phase measurement.

Figures 5.11 and 5.12 represent time series and spectral densities, respectively, of OPD fluctuations with stabilisation (blue trace) and without (red trace). Comparing the free-running and stabilised case it becomes apparent that a significant noise suppression of up to three orders of magnitude had been reached. Note that the comparison is based on an “in-loop” measurement, which can be seen as upper limit on the suppression. However, the adoption of an OPD stabilisation does indeed result in a significant improvement of the displacement noise for frequencies above 3 mHz (Figure 5.10; blue trace). Since the induced phase fluctuations have been significantly reduced, all further measurements were performed with an active OPD stabilisation.

## 5.5. Control of the polarisation state stability

For injecting laser light into the optical bench placed in a vacuum chamber, polarisation-maintaining optical fibres of the PANDA-type (PANDA stands for polarisation-maintaining and absorption-reducing) were used. In the worst case, a non-matched polarisation state of the beam with respect to the fibre

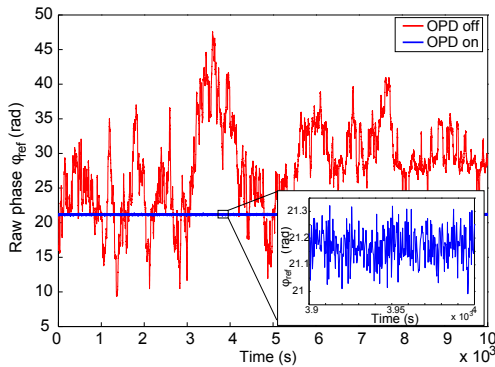


**Figure 5.11.:** Comparison between free-running (red trace) and stabilised (blue trace) OPD fluctuations in the time domain. The insert shows a section (100 sec) of the time series for stabilised OPD fluctuations.

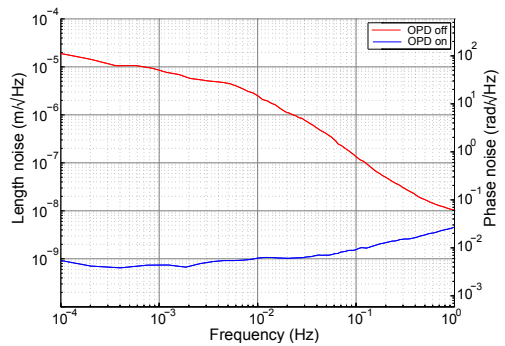


**Figure 5.12.:** Linear spectral densities of OPD fluctuations with stabilisation (blue trace) and without (red trace), both measured as the raw phase  $\Phi_{\text{ref}}$  of the reference interferometer.

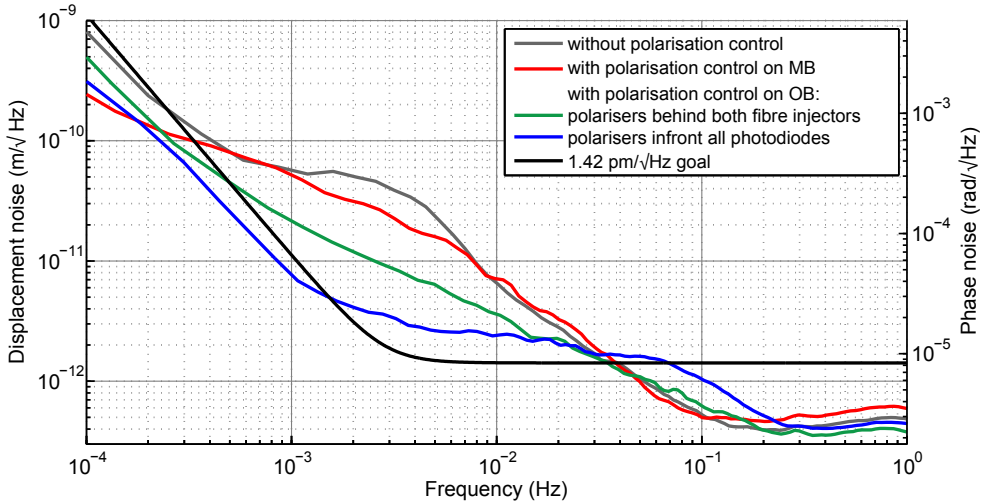


**Figure 5.13.:** Comparison between noise performance of the polarising interferometer observed with polarisation control and without.

[m-code: VTO (grey), VTP<sub>M</sub>O (red), VTPO (green/blue)]

axis would lead to elliptically polarised light. Which, in turn, would change in response to external influences on the fibre, resulting in laser power fluctuations [118]. Temperature fluctuation as well as mechanical perturbations are the most severe problems in the optical fibres used [119]. Thus, the exact polarisation will be sensitive to variations in temperature and mechanical stress. In addition, residual interference with the wrong polarisation can induce parasitic noise in the phase readout. By enhancing the polarisation state stability such noise sources were suppressed.

In order to align the polarisation of the input light with respect to the stress direction in the fibre, two retardation plates ( $\lambda/2$  and  $\lambda/4$ ) were placed in front of the fibre inputs on the modulation bench. By monitoring the output polarisation with a polarimeter (*SK9782-NIR*, Schäfter & Kirchhoff), the input polarisation state was matched to the polarisation-maintaining axes of the two fibres. For the period of the measurement procedure for the extinction ratio the fibre was put under stressed, e.g., by manually pushing the fibre. The corresponding software computed the polarisation state on the Poincaré sphere. In real-time both wave plates were aligned to maximise the polarisation extinction ratio which is equivalent to minimising the radius of the Poincaré sphere, as shown in Figure 5.14. Typically, extinction ratios of the order of 30 dB have been obtained. Figure 5.13 shows the result obtained after aligning both wave plates, depicted in red. In the frequency band of 1 mHz to 8 mHz one can observe a slight enhancement of the phase readout.

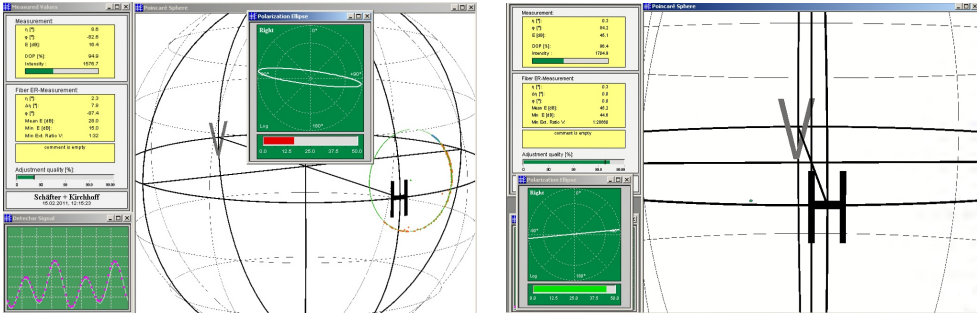


**Figure 5.14.:** Adjusting the polarisation state of one input beam using a polarimeter: *Left:* Initial condition of the polarisation state *Right:* Maximising the polarisation extinction ratio, which is equal to minimise the radius of the Poincaré sphere

To ensure a stable s-polarisation state on the optical bench, Glan-Thompson polarisers by Bernhard Halle Nachfolger GmbH with a high extinction ratio and an excellent wavefront quality were installed at both fibre outputs on the optical bench. With a well defined polarisation state for both beams, a significant reduction of phase readout noise for frequencies between 0.3 and 30 mHz was achieved (Figure 5.13; green trace). In addition, thin-film polarisers (*colorPol<sup>®</sup> VISIR CW02*, Codixx) with an extinction ratio of  $10^6$  were placed directly in front of each photodiode. This enabled suppression of parasitic signals leading to a spurious interferometric signal. To avoid ghost reflections back into the optical setup, the photodiodes were tilted by a few degrees. The resulting displacement noise of the polarising interferometer is presented in Figure 5.13 by the blue trace. It is evident that the noise could be reduced for frequencies below 20 mHz by up to a factor of two. Taking all three steps for enhancing the polarisation state stability into account, a significant improvement of the measurement sensitivity of up to one order of magnitude is reached.

## 5.6. Impact of frequency noise on longitudinal phase noise

In a heterodyne interferometer the path length difference  $\Delta L$  between the two interfering beams translates laser frequency changes into phase fluctuations  $\widetilde{\delta\phi}$  at the heterodyne frequency. The translation of frequency noise  $\widetilde{\delta\nu}$  into phase noise is given by the differential time delay  $\Delta L/c$  as [103]

$$\widetilde{\delta\phi} = \frac{\Delta L}{c} 2\pi \widetilde{\delta\nu}, \quad (5.6)$$

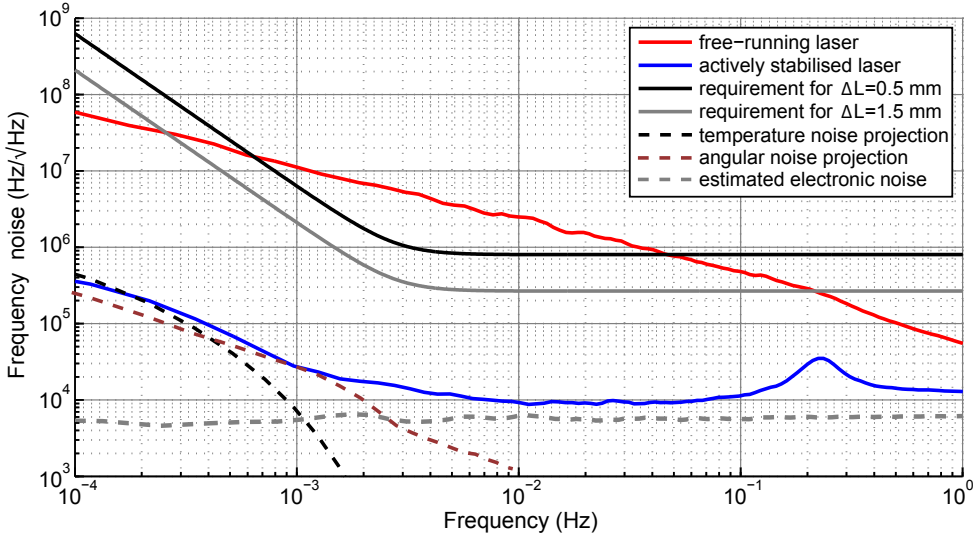


**Figure 5.15.:** Comparison between measured free-running frequency stability (red trace) and frequency stability reached with active stabilisation (blue trace). The required frequency stability for path length fluctuations of the two measurement interferometers to remain below  $1.42 \mu\text{m}/\sqrt{\text{Hz}}$  is depicted in black and grey. The three limiting noise sources are projected into the frequency stability and presented dashed.

where  $c$  is the speed of light.

Path length differences before the optical bench are cancelled by referring all measurements to the reference interferometer, thus that only those on the optical bench couple into the phase measurement. By intentionally modulating the laser frequency, as described in Section 6.2, arm length differences of 1.5 mm and  $500 \mu\text{m}$  for the non-polarising and polarising interferometer, respectively, were measured. For the phase fluctuations to remain below  $8.4 \mu\text{rad}/\sqrt{\text{Hz}}$  corresponding to path length fluctuations of  $1.42 \mu\text{m}/\sqrt{\text{Hz}}$ , the required frequency stability for the two measurement interferometers can be calculated to:

$$\widetilde{\delta\nu}_{\text{np}} = 267 \frac{\text{kHz}}{\sqrt{\text{Hz}}} \left[ \frac{1.5 \text{ mm}}{\Delta L} \right] \quad \widetilde{\delta\nu}_{\text{p}} = 802 \frac{\text{kHz}}{\sqrt{\text{Hz}}} \left[ \frac{0.5 \text{ mm}}{\Delta L} \right]. \quad (5.7)$$

The measured free-running frequency noise of the unstabilised Nd:YAG NPRO laser (used in the experimental setup) at 10 mHz is about  $2 \times 10^6 \text{ Hz}/\sqrt{\text{Hz}}$  and is depicted in Figure 5.15 by the red trace. This has been determined by using Equation (5.6) together with the longitudinal signal measured using the auxiliary interferometer with an intentionally arm length mismatch of  $\Delta L = 27.4 \text{ cm}$ . The investigation has shown the necessity of the frequency stabilisation, as the laser's free running frequency fluctuations would be a significant noise source



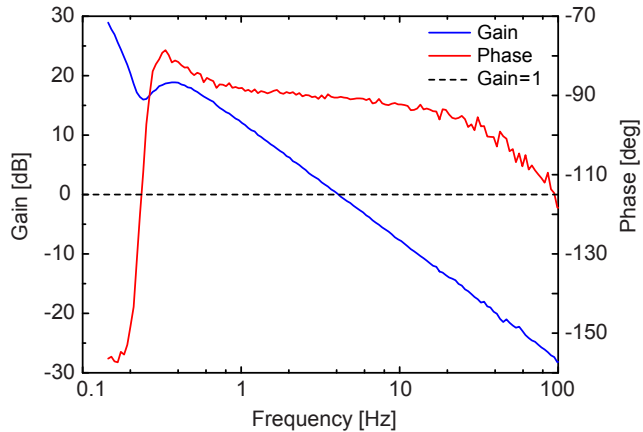


**Figure 5.16:** Measured open loop gain (OLG) of the frequency stabilisation.

in the two measurement interferometers.

The auxiliary interferometer with an intentional arm imbalance was used to sense the laser frequency fluctuations. Using a feedback loop the laser frequency was actively stabilised [95]. An analogue servo containing two input channels for the photodiode signals of the reference and frequency interferometers was used. With an analogue multiplier the phase difference between the two signals was determined. In order to suppress the harmonics of the heterodyne frequency the signal was low-pass filtered. This error signal was converted into two different feedback signals of different frequency ranges. The first one was fed to the piezoelectric fast laser frequency actuator and the second feedback signal to the slower laser's crystal temperature tuning. The achieved bandwidth of the control loop was about 3 Hz (increasing with  $1/f$  towards lower frequencies with an additional integrator at a few hundred millihertz resulting in a  $1/f^2$  increase), as shown in Figure 5.16. The measured unity gain frequency indicates a potential frequency noise suppression of more than three orders of magnitude at 1 mHz. However, such a noise suppression can be expected only if other noise sources, such as beam jitter or readout noise, are negligible and an adequate thermal equilibrium is obtained, which is typically not the case. Since the beam jitter and the thermal expansion of the baseplate both couple into the path length noise proportional to the length difference, a compromise between achievable frequency stability and arm length mismatch in the auxiliary interferometer has to be made.

As illustrated in Figure 5.15, a laser frequency stability of  $28 \text{ kHz}/\sqrt{\text{Hz}} @ 1 \text{ mHz}$  was achieved. In addition, the stability required for the two measurement interferometers (Equation (5.7)) is shown. Equation (5.6) was used for estimating the stability achieved using the signal measured with the auxiliary interferom-

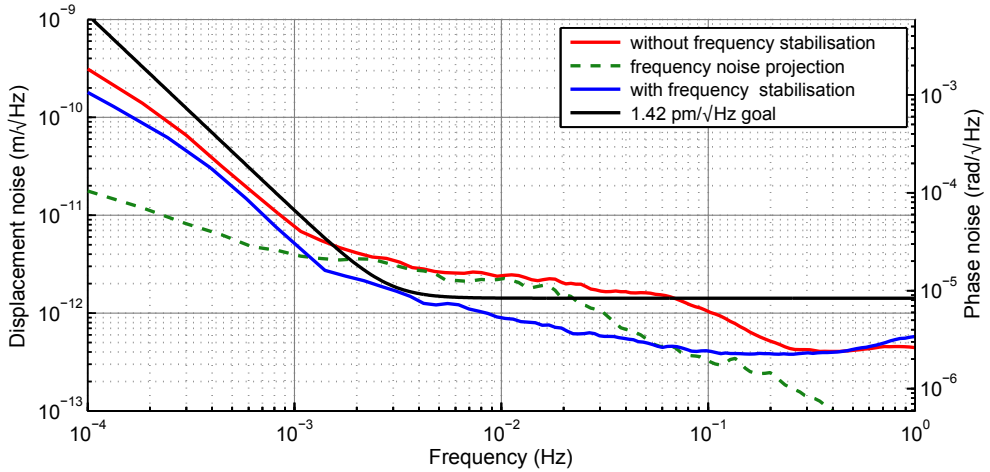


**Figure 5.17.:** Comparison between noise performance of the polarising interferometer observed with frequency stabilisation and without. [m-code: VTPO (red), VTPOF (blue)]

eter and the determined arm length difference. The red trace shows the free running laser while the blue trace shows the actively stabilised laser. A stability improvement in frequency noise of more than two orders of magnitude for frequencies below 100 mHz has been achieved. That is one order of magnitude poorer than theoretically expected from the loop gain used. On the one hand, the stability was limited in the low frequency range (less than 1 mHz) by temperature-driven path length fluctuations. This effect is reflected with the black dashed trace. On the other hand, beam jitter induced by the metal fibre injector assemblies prevent a successful suppression of frequency fluctuations of three orders of magnitude in the mid-frequency band. In addition, the stability in the frequency range of 10 mHz to 1 Hz is limited by electronic noise such as the phase readout noise, differential noise of photodiodes as well as noise introduced by the analogue electronics. Assuming a phase readout noise of  $10^{-6}$  rad/ $\sqrt{\text{Hz}}$ , a lower limit for electronic noise has been estimated (grey dashed trace). The shown “in-loop” measurement can give only a lower limit for the real frequency noise. However, the later results confirm that the frequency noise suppression was sufficient for this experiment.

Figure 5.17 shows the displacement noise of the polarising interferometer with actively stabilising the laser’s frequency and without. It is evident by the green dashed trace that the initial measurement was limited by frequency instabilities between 2 mHz and 20 mHz. After applying a stabilisation loop to the laser’s frequency, an improvement in that frequency range has been obtained (blue trace).

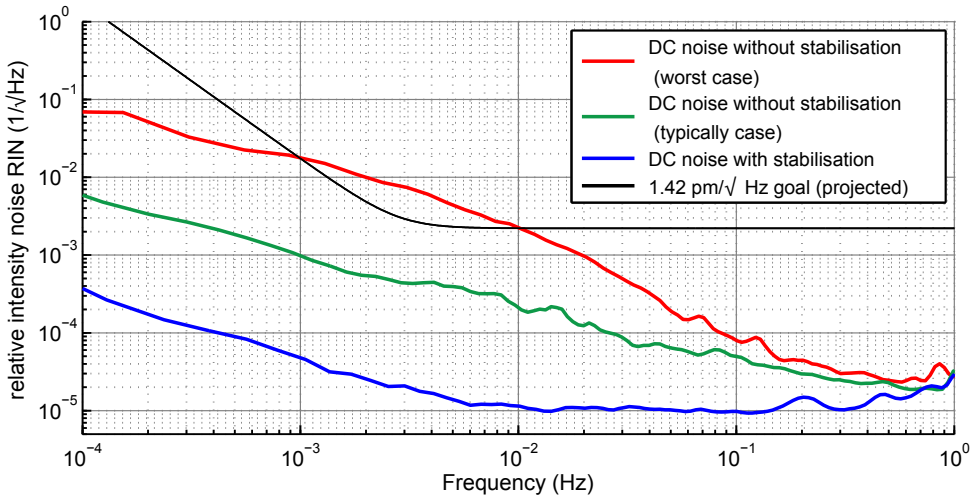


**Figure 5.18.:** Comparison between relative intensity noise (RIN) observed with DC noise stabilisation and without.

## 5.7. Impact of laser intensity noise

Laser intensity noise causes radiation pressure noise resulting in an acceleration of movable surfaces, e.g. test masses on LISA. In addition, it can introduce slow changes in the photodiode capacitance due to the variation in absorbed light power [91]. In general, any laser power fluctuation couples into the assigned photo current, which in turn is read out with the phase measurement system and thus contributes to phase noise.

The two photodiodes, PDA1 and PDA2, were integrated on the optical bench to measure such fluctuations in laser power. These signals were used in two separate feedback loops to stabilise the power of both input beams. For this purpose the signal of each single element photodiode was compared to a voltage reference yielding the error signal for the feedback loop. The RF-signals driving the AOMs have been used as actuators.

In order to evaluate the influence of laser intensity noise into the phase readout, knowledge of the corresponding amplitude coupling coefficient was required. Therefore, several measurements (without amplitude stabilisation) were performed, while the amplitude of the RF-signal driving the AOMs has been varied, resulting in a modulation of the light power. By monitoring the modulation of the amplitude and the phase response for each interferometer, the coupling coefficient could be calculated. With this amplitude coupling coefficient of 3.8 mrad/V, the contribution of laser power noise to phase noise could be estimated. In addition, using the coupling coefficient, a requirement for the

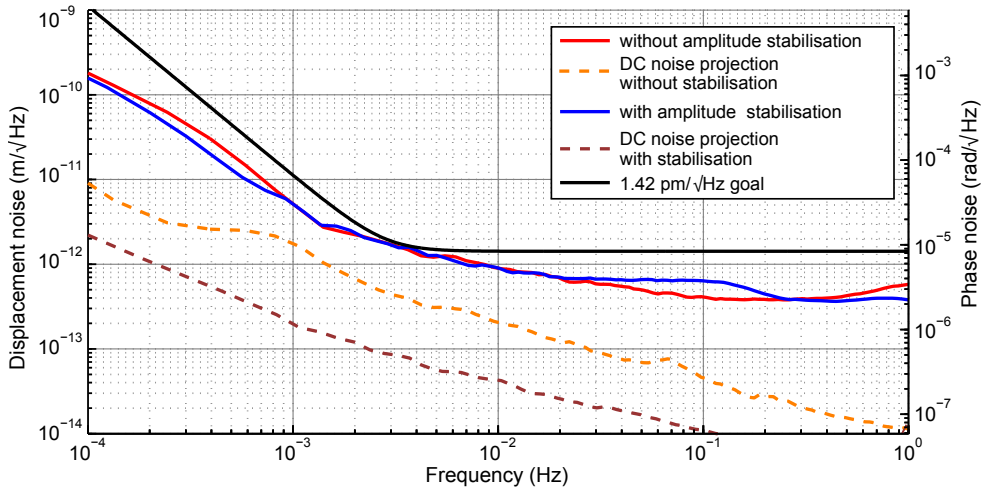


**Figure 5.19.:** Comparison between noise performance of the polarising interferometer observed with laser intensity stabilisation and without. [m-code: VTPOF (red), VTPOFA (blue)]

relative amplitude stability of better than  $2 \times 10^{-3} / \sqrt{\text{Hz}}$  could be estimated to ensure a displacement noise below  $1.42 \text{ pm} / \sqrt{\text{Hz}}$ .

Figure 5.18 compares the relative intensity noise of the laser (RIN) of three measurement runs: one with stabilising the laser’s amplitude and two without. The two measurements performed without an amplitude stabilisation represent an upper and lower limit of occurred relative intensity noise levels<sup>[3]</sup>. Note that typically amplitude noise of the order of the lower limit were present. Nevertheless, in case of the upper limit (red trace) an amplitude stabilisation was required. With active amplitude stabilisation, the amplitude noise was suppressed by up to two orders of magnitudes for frequencies below 1 Hz (blue trace).

Using the amplitude coupling coefficient, the influence of amplitude noise could be projected to the phase noise, as shown in Figure 5.19 with the orange dashed trace. The projection indicates that amplitude noise was not the limiting noise source for the measurement represented by the red trace. Stabilising the amplitude leads, on the one hand, to a mitigation of the noise source, as the noise projection (brown dashed trace) reveals, but on the other hand not to an improvement of the phase readout (blue trace).

<sup>[3]</sup>The RIN of the laser was influenced by external factors.

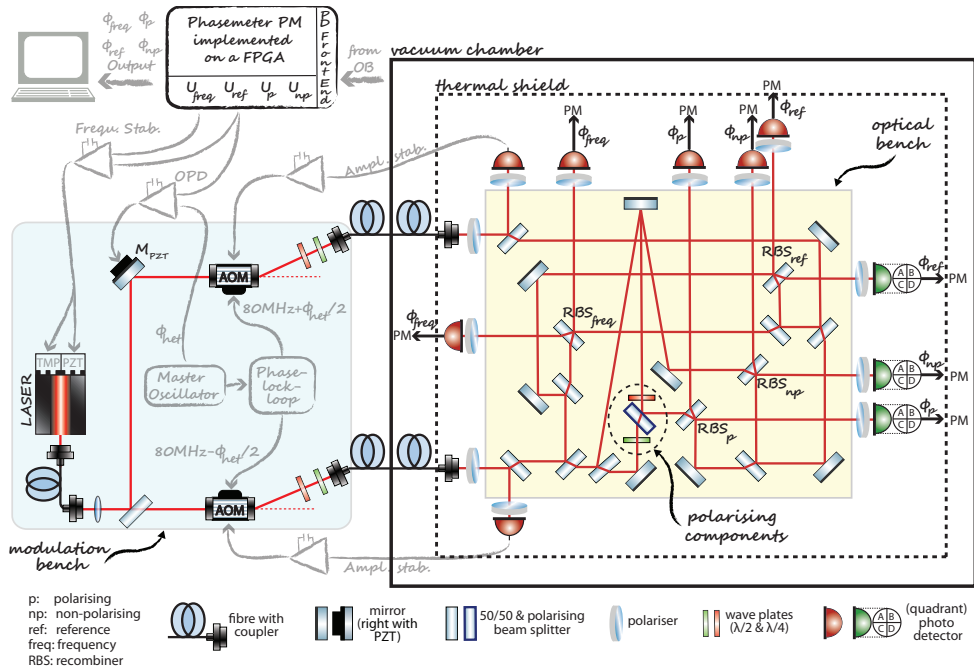


**Figure 5.20.:** Schematic of the experimental setup. *Left:* the modulation bench provides the beam preparation. *Right:* the optical bench containing the interferometers enclosed by a thermal shield inside a vacuum chamber. The implemented stabilisation loops are greyed out.

## 5.8. Noise performance

For the sake of visualisation, the experimental setup with the various stabilisation loops used is sketched in Figure 5.20. An OPD stabilisation was used to reduce non-linear errors induced by the AOMs on the modulation bench. Laser frequency fluctuations were suppressed by using a feedback loop controlling the laser resonator length and the temperature of the crystal, and also the laser intensity fluctuations were actively stabilised. Using polarising components on the modulation bench as well on the optical bench, the polarisation state of the two interfering beams could be controlled.

The interferometric performance after the implementation of all these stabilisation loops is shown in Figure 5.21. The red trace displays the displacement noise of the polarising interferometer conducted in a vacuum environment ( $\approx 10^{-6}$  mbar) and enclosed within a thermal shield. One can see that the noise performance fulfils the requirement over the whole frequency range. However, it is important to know what is actually limiting the noise performance. Therefore, the projection of several noise sources are additionally plotted. For this

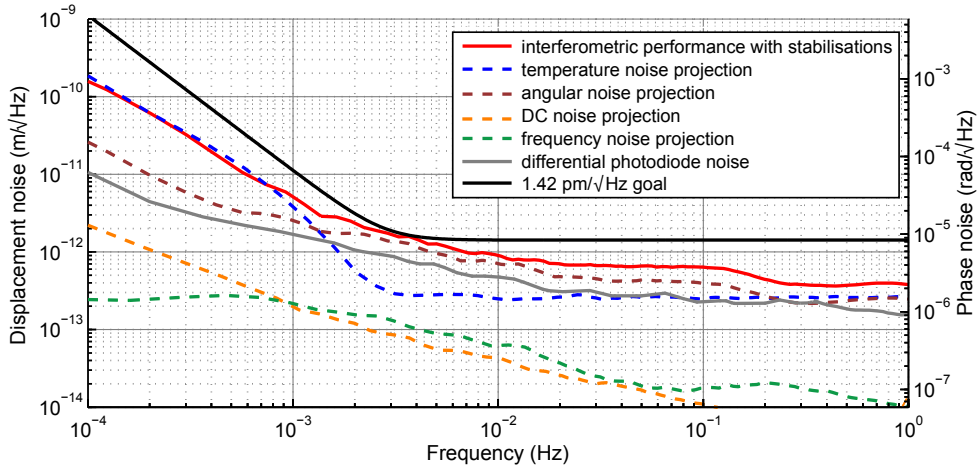


**Figure 5.21.:** Noise performance of the polarising interferometer with active laser frequency and intensity stabilisation, whilst the optical bench is enclosed within a thermal shield in vacuum. In addition, projections of several noise sources are plotted (dashed).

[m-code: VTPOFA (red)]

purpose the measured coupling coefficients (*cf.* Chapter 6) in combination with the associated computed data were used. On the other hand, the influence of angular noise on length change was estimated by using the least squares fit method built into MATLAB<sup>®</sup>. Band-pass filtered angular and longitudinal interferometric signals were fed to the fit algorithm [120]. The obtained coefficients were used to project the residual angular noise in the frequency band of interest.

For the low-frequency range below 1 mHz temperature driven path length fluctuations on the optical bench cause the dominant noise contribution. As arm length imbalances could not be avoided and the desired equality in number of transmissions through optics could not be realised for each interferometer, expansion of the optical components and baseplate caused by temperature fluctuations induced path length fluctuations. In order to minimise the contribution of thermal noise, one has to ensure a higher thermal stability. A first step towards an improved thermal stability could be to enclose the experiment by a second thermal shield.

The interferometric performance in the frequency band of 1 mHz to 100 mHz is apparently limited by beam pointing fluctuations caused by the commercial off-the-shelf fibre injector assemblies. One way to mitigate this noise source is to use quasi-monolithic fibre injector assemblies rigidly connected to the optical bench. They have a thermal drift of approximately  $3.5 \mu\text{rad}/\text{K}$  [121], resulting

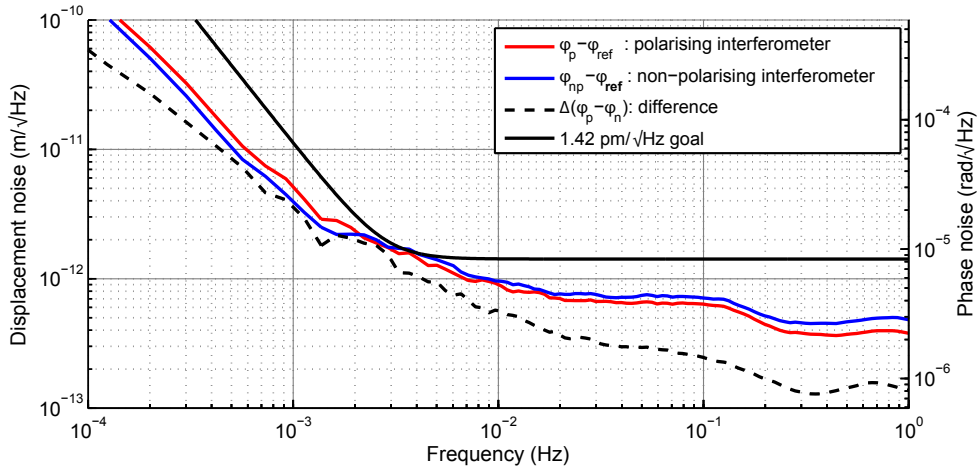


**Figure 5.22.:** Comparison between noise performance of the polarising and non-polarising interferometer with all stabilisations. In dashed black the difference between the two is shown.

[m-code: VTPOFA (red/blue)]

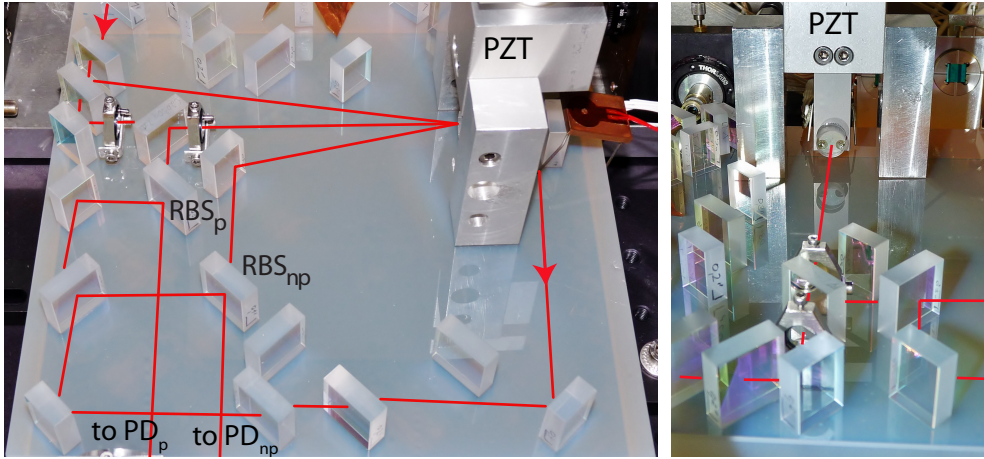
in phase noise of less than  $10^{-10}$  rad/ $\sqrt{\text{Hz}}$ . However, another possible limiting noise source can be the limited ability of the phase measurement system including photodiodes to measure the phase. By equipping one output port of a beam combiner with an additional beam splitter and photodiode, the difference of two in principal exactly matching signals can be determined. This *differential photodiode noise* is also plotted in Figure 5.21 (grey trace). Thus it appears that the angular noise as well as the total noise performance is limited by electronic noise. Both projections for the laser's frequency and intensity noise show a margin of one order of magnitude to the requirement. Thus, they do not significantly limit the performance as long as they are stabilised.

Figure 5.22 compares the performance of the two measurement interferometers as well as their difference. Both obtained noise performances follow the same trace and fulfil the requirement within the whole frequency band. Furthermore the noise of the difference between polarising and non-polarising interferometer complies with the  $1.42 \text{ pm}/\sqrt{\text{Hz}}$  level. Hence, it is shown that polarising optics do not limit the interferometer sensitivity on a picometre/ $\sqrt{\text{Hz}}$  level.

## 5.9. Periodic phase errors

In heterodyne interferometry the sensitivity can be limited by non-linearity errors. These periodic phase errors have a cyclic behaviour with first- and second-order harmonics [72]. They are mainly induced by the phase measure-





**Figure 5.23.:** Photographs of the non-linearity experiment: *Left:* The shared plain mirror (for a  $0^\circ$  angle of incidence) is replaced by a piezo-actuated mirror, which induced path length variations of about  $5\ \mu\text{m}$  for both measurement interferometers. The coupling of this modulation is measured and compared. The beam propagation of the two interferometers is highlighted in red. *Right:* Frontal view of the piezo-actuated mirror with a part of the polarising interferometer.

ment system and in our LTP-like setup by spurious sidebands on the AOM radio frequency driving signal (*cf.* Section 5.4). For both sources the induced noise can be suppressed to a level not affecting the picometre measurements. In particular the sideband-induced non-linearity can be mitigated to a few milliradian through an optical path length stabilisation as shown in Figure 5.12.

By using polarising optics in heterodyne interferometry additional sources for periodic phase errors can emerge depending on the setup. These errors can be due to elliptically polarized laser beams, beam splitter leakage and rotational errors in the alignment of laser and polarisation beam splitter or retardation plates [122]. Through frequency or polarisation mixing they can induce a spurious beat note signal. Therefore the heterodyne scheme used has been analysed with respect to non-linear effects (*cf.* Section 4.1). As a result, no cross-talk between the two main beams and residual beams was apparent. Hence, it is assumed that periodic phase errors caused by polarising components are not significant in these experiments.

In order to verify this assumption, the setup has been modified to be able to induce path length changes in one arm of the two measurement interferometers. Figure 5.23 shows the modification carried out. By “replacing” the plain mirror for angle of incidence of  $0^\circ$  with a PZT-actuated mirror the path length



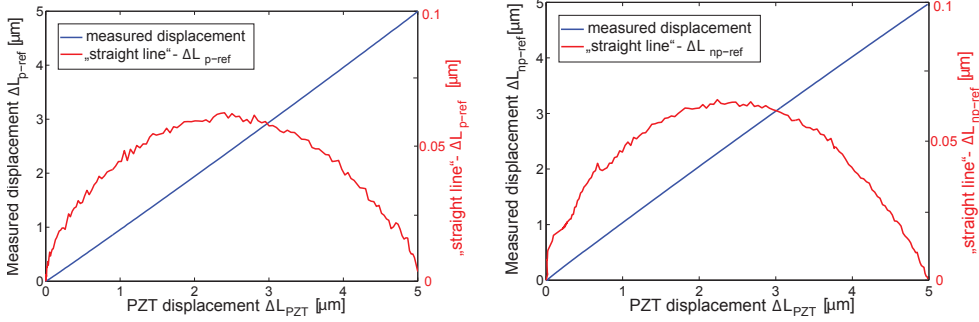


**Figure 5.24.:** The measured displacement of both measurement interferometers  $\Delta L_{m-ref}$  versus the displacement of the piezoelectric element (PZT). The solid red line represents the deviation of measured data to a straight line. *Left:* Displacement measured in the polarising interferometer; *Right:* Displacement measured in the non-polarising interferometer.

was changed by about  $5 \mu\text{m}$  for both, polarising and non-polarising interferometer, consecutively, by using a function generator. The phase responses in the various interferometers were read out by the phasemeter. In addition, the signal for actuating the PZT was fed to the phase measurement system and processed. The displacement induced by the PZT was determined by using the measured coupling coefficient of  $1.9 \mu\text{m}/\text{V}$ . The measured displacement in the two interferometers were compared with the displacement induced. The displacements in the polarising and non-polarising interferometer are plotted in Figure 5.24 (blue trace). To ensure that the displayed displacement is caused by the PZT, the reference phase was subtracted. The red trace shows the deviation of the measured displacement and the desired one. In an ideal case the PZT modulation would result in a linear length variation. However, if the polarising components induce a non-linear effect, one would expect to see five cycles for first-harmonic non-linearity and ten cycles for second-harmonic non-linearity, as five fringes were scanned. Consequently, non-linearities caused by polarising optics are not present but rather the curve shape can be interpreted as the non-linearity of the PZT mirror. This is also confirmed by the difference of measured and theoretic displacement deviating from zero.

## 5.10. Summary

Using the quasi-monolithic interferometer, the influence of polarising optics into the length measurement was investigated. The experiment can be divided into the modulation bench, providing the beam preparation, and the stable optical bench. The investigations were performed at a heterodyne frequency of  $1.623 \text{ kHz}$  and used a hardware-based phase measurement system. In or-

der to suppress fluctuations in the refractive index of air the experiment was conducted in vacuum. For reducing thermal fluctuations the bench was additionally enclosed by a thermal shield. Two main noise sources were identified and actively stabilised. One is the effect of non-linear optical path length difference: due to electromagnetic cross-talk between the AOM drivers, spurious sidebands are generated, resulting in residual beat notes but of unstable phase. The second noise source is fluctuations of the laser frequency that proportionally translate to interferometer phase noise. By suppressing these noise sources, a significant improvement of the phase readout is obtained. Furthermore, by equipping the optical bench with polarisers and taking care of the incoming polarisation state of the two beams, the phase readout noise was reduced in the frequency band between 0.3 and 30 mHz

Readout sensitivities for both non-polarising and polarising interferometers of better than  $3 \times 10^{-5}$  rad/ $\sqrt{\text{Hz}}$  and 5 pm/ $\sqrt{\text{Hz}}$  at 1 mHz were obtained, respectively. The interferometer performance complies with the requirement stated in Equation (4.1) for the whole frequency range from 1 Hz to 0.1 mHz.

In order to investigate the occurrence of non-linearity induced by polarising components on the optical bench, several measurements were conducted. One common arm length of the two measurement interferometers was intentionally modulated and the response in phase was observed. By comparing the displacement in the polarising interferometer with either the displacement measured in the non-polarising interferometer or the determined displacement of the piezo, no evidence was found for periodic phase errors induced by polarising optics.

## Performance investigations in data post-processing

In the previous chapter a series of experimental investigations has been carried out to identify noise sources impairing the interferometer performance. Initially, the three main limiting noise sources were fluctuations in laser frequency and temperature as well as residual non-linear noise of the OPD. To suppress these noise sources, different stabilisation schemes were presented. For instance, the laser frequency and OPD has been actively stabilised to a level not effecting the phase readout. Currently, the interferometer performance is limited by temperature fluctuations and either by beam pointing or readout noise.

As an alternative to active stabilisations, all these noise sources can be subtracted in data post-processing. Thus, under non-ideal conditions it is still possible to reach the required noise performance, which leads to an improved robustness for the LISA mission. In the following the subtraction models used to reduce noise sources are presented. Noise sources were parasitic beams due to ghost reflections and coupling of noise into the displacement measurement such as beam pointing and laser intensity fluctuations, as well as temperature and laser frequency noise.

### 6.1. Subtraction of spurious beat note signals

Since spurious beat note signals can significantly impair the phase readout a careful design concerning ghost beams was mandatory. The rear side of each optical component, even if equipped with an anti-reflective coating, generates ghost beams, which may eventually reach the detector. Although the bench has been designed such as to minimise their effect (*cf.* Section 4.2.1), some

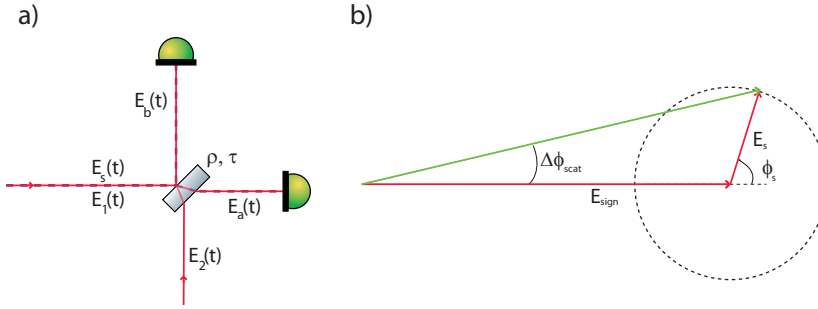


**Figure 6.1.:** a) Recombination of light fields at a beam splitter in an interferometer; b) Phasor diagram illustrating the effect of a small amount of scattered light ( $E_s$ ,  $\Phi_s$ ) interfering with the main signal ( $E_{\text{sign}}$ ).

ghost beams can not be avoided.

They are sharing the same optical path and beam parameters as the main laser beam. Two kinds of spurious beat note signals can be distinguished: *i*) those where a ghost beam interferes with a main beam at the recombination beam splitter and *ii*) those where a ghost beam interferes prior to the recombination beam splitter. The nominal beat signal will leave the two recombiner ports with a phase difference of  $180^\circ$  due the conservation of energy. In case *i*) the interference signal between ghost beam and main beam also show  $180^\circ$  phase difference. Hence, they cannot be distinguished from the nominal signal. In case *ii*) however the phase difference between ghost beam and nominal beam is  $0^\circ$ . This parasitic signal cancels if the difference of both interference signals is taken, which at the same time doubles the main signal. On the other hand, laser power fluctuations at the heterodyne frequency causes residual phase error terms. Another possibility is that a spurious beat note signal is introduced in the electronic modulation process.

The two main incoming light fields  $E_1(t)$ ,  $E_2(t)$  and the scattered light field  $E_s(t)$  (case *ii*:  $f_2 = f_s$ ) can be described by:

$$E_i(t) = A_i \cdot \exp [i(\omega_i t + \phi_i)] \quad (6.1)$$

where  $\omega_i = 2\pi \cdot f_i$  is the angular frequency and  $\phi_i$  is the phase of the light field. The recombination and detection of these three light fields are shown in Figure 6.1. Their combined amplitude at the two output ports of the beam splitter can be calculated by:

$$\begin{pmatrix} E_a(t) \\ E_b(t) \end{pmatrix} = \begin{pmatrix} i\tau & \rho \\ \rho & i\tau \end{pmatrix} \cdot \begin{pmatrix} E_1(t) + E_s(t) \\ E_2(t) \end{pmatrix}, \quad (6.2)$$

where  $\rho$  is the amplitude reflectivity and  $\tau$  the amplitude transmittance of a partially reflecting surface. Throughout this thesis, a recombination beam splitter with an approximately 50:50 coating was used. Thus, both reflectivity and transmittance can be assumed as identical:  $\rho = \tau = 1/\sqrt{2}$ .

The AC component of the signal at the photodetector is proportional to the square of the electric field  $|E_i(t)|^2$ :

$$I_a(t) \propto \underbrace{A_1 A_s \cos [(\omega_1 - \omega_s)t + (\phi_1 - \phi_s)]}_{\text{Periodic error term}} - \underbrace{A_1 A_2 \sin [\Delta\omega t + \Delta\phi]}_{\text{Main signal}}, \quad (6.3)$$

whilst the phase of the interferometric signal at the remaining output port is shifted by  $\pi$ :

$$I_b(t) \propto \underbrace{A_1 A_s \cos [(\omega_1 - \omega_s)t + (\phi_1 - \phi_s)]}_{\text{Periodic error term}} + \underbrace{A_1 A_2 \sin [\Delta\omega t + \Delta\phi]}_{\text{Main signal}}, \quad (6.4)$$

where  $\Delta\omega = \omega_1 - \omega_2 = \omega_{\text{het}}$  is the frequency difference between the two interfering beams, in our case  $f_{\text{het}} = 2\pi\omega_{\text{het}} = 1.623$  kHz, and  $\Delta\phi = \phi_1 - \phi_2 = \Phi_{\text{sign}}$  is the interferometric measured phase if no stray light would be present. This ideally measured phase is related to the path length changes  $\Delta L$  by

$$\Delta\Phi_{\text{sign}} = \frac{2\pi\Delta L}{\lambda}, \quad (6.5)$$

where  $\lambda$  is the wavelength of the light used ( $\lambda = 1064$  nm). Hence, Equations (6.3) and (6.4) can be rearranged and combined:

$$I \propto \pm \cos(2\pi f_{\text{het}} t + \Delta\Phi_{\text{sign}}) + \frac{A_s}{A_2} \cos(2\pi f_{\text{het}} t + \Delta\phi_{\text{scat}}), \quad (6.6)$$

where  $\Delta\phi_{\text{scat}}$  is the phase difference between the main beam and the ghost beam, as illustrated in Figure 6.1 b).

Similar to Section 4.1 it is convenient to visualise the cross talk between the periodic error term induced by stray light and the main beat signal in terms of a phasor diagram, where the measured phase  $\Phi_{\text{meas } i}$  for both output ports ( $i = \{a, b\}$ ) is the phasor sum of the three electric light fields arriving at the recombination beam splitter:

$$\Phi_{\text{meas } a} = \Delta\Phi_{\text{sign}} + \epsilon_{\text{scat}} \quad (6.7)$$

$$\Phi_{\text{meas } b} = -\Delta\Phi_{\text{sign}} + \epsilon_{\text{scat}}, \quad (6.8)$$

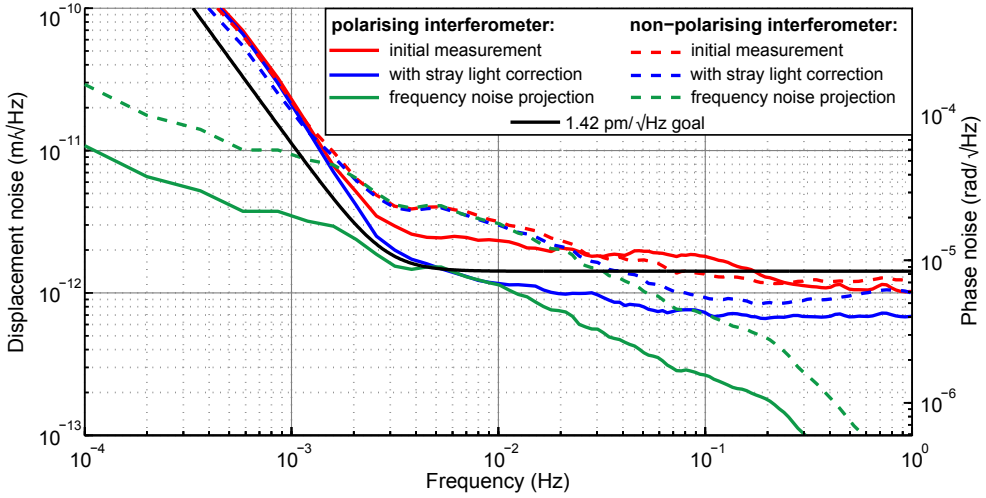


**Figure 6.2.:** Comparison of noise levels of both measurement interferometers observed in raw data (“initial measurement”) and after the applied stray light correction. The projection of laser frequency noise for both interferometers is additionally plotted. [m-code: VTPO (red), VTPOs (blue)]

where  $\epsilon_{\text{scat}}$  is the periodic phase error. This residual term has a dependency of  $\Delta\phi_{\text{scat}}$ , resulting in an additional phasor rotating at the end of the nominal signal with amplitude  $A_s/A_1$ . With the assumption  $A_s \ll 1$  the induced phase error due to scattered light can be expressed by

$$\epsilon_{\text{scat}} = \frac{A_s}{A_1} \cdot \sin \phi_{\text{scat}}. \quad (6.9)$$

By subtracting the two measured phases, a cancellation of the residual stray light signal results:

$$\Phi_{\text{meas a}} - \Phi_{\text{meas b}} = 2\Delta\Phi_{\text{sign}}. \quad (6.10)$$

Since the amplitudes in both detectors were not matched closely, a restricted impact of the applied subtraction would result. Thus, the beat note signals had to be normalised [123]. Please note that errors caused by non-ideal reflectivity and transmittance can not be corrected by the normalisation. However, to ensure a complete stray light elimination both values have to be known for each component and be included in the balanced detection method.

The results obtained using the balanced detection scheme to remove spurious beat note signals is presented in Figure 6.2. The corrected noise spectral densities for both measurement interferometers are represented by the blue trace (solid: polarising interferometer; dashed: non-polarising interferometer) along with their initial noise performances, depicted in red, and the corresponding

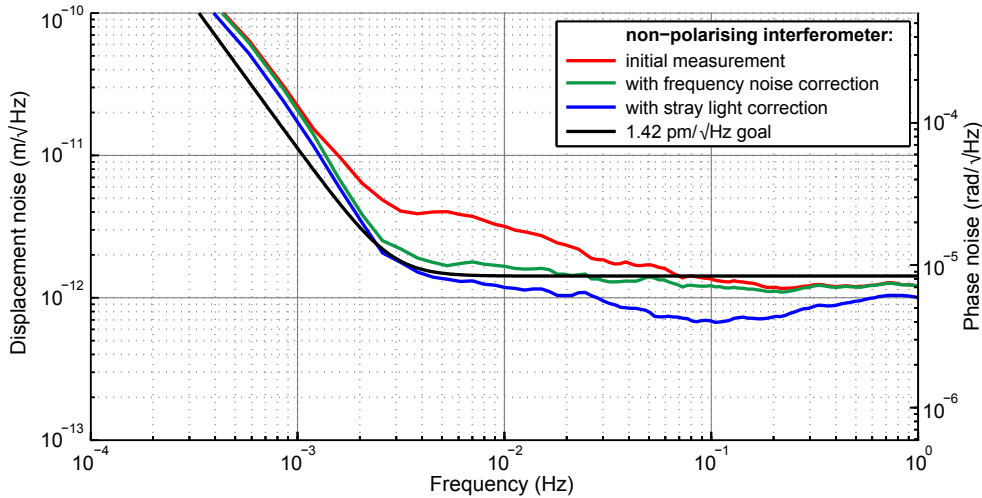


**Figure 6.3.:** Comparison of noise levels of the non-polarising interferometer observed in raw data (“initial measurement”) and by applying first a laser frequency noise subtraction (green trace) with a subsequent stray light correction (blue trace). [m-code: VTPO (red), VTPOf (green), VTPOfs (blue)]

frequency noise projection (green). On the one hand the applied correction leads to a reduction by about a factor of two of the observed noise in case of the polarising interferometer for frequencies greater than 2 mHz. On the other hand, the elimination of stray light in the non-polarising interferometer is considerably less and efficient for frequencies greater than 20 mHz. The associated frequency noise projection indicates a limitation due to frequency fluctuations. Therefore, a frequency noise correction has been applied before using balanced detection. The principle of a frequency noise correction is described in Section 6.2. In the case of the polarising interferometer there is no difference by applying first a frequency noise correction. In contrast, the stray light subtraction applied to the non-polarising interferometer shows a significantly higher efficiency after removing the noise contribution due to frequency fluctuations. This is reflected in Figure 6.3.

Apparently, both measurement interferometers show the same efficiency in stray light subtraction. This indicates that polarising optics do not induce spurious beat note signals effecting a noise performance at a picometre level. This has been proved by the fact, that the amount of removable stray light is not constant or even disappeared by applying an amplitude stabilisation.

## 6.2. Laser frequency noise subtraction

The second auxiliary interferometer with unequal arm length provides a frequency fluctuation signal  $\phi_{\text{freq}}$ . This signal was used in an active stabilisation loop as described in Section 5.6. Alternatively it can be used in a post-measurement correction. For this reason the frequency coupling coefficients corresponding to the arm length imbalances were determined. This was done by modulating the laser frequency, while observing the resulting coupling to the interferometric phase, where they appear scaled by the arm length difference of each interferometer, as given by Equation (5.6).

One way to modulate the laser frequency is to tune the temperature of the monolithic laser crystal of the Nd:YAG laser used by applying a sinusoidal signal from the function generator (*TMP-M*). Thus, the length of the laser's crystal is changing, leading to a change in the resonator length and thereby to a modulation of the laser frequency. The coefficient of laser frequency tuning per temperature change was determined to be  $\eta_{\text{TMP}} = 3.1 \text{ GHz/K} \pm 0.2 \text{ GHz/K}$  [124]. By observing this modulation in the corresponding phase-meter outputs the coupling coefficients can be obtained. The resulting ratios of the measured peak amplitude  $\delta(\phi_i - \phi_r)$  to the modulation are:

$$\frac{\delta(\phi_i - \phi_{\text{ref}})}{U_{\text{pp}} \cdot \eta_{\text{TMP}}} = \frac{2\pi}{c} \cdot \Delta L_i, \quad (6.11)$$

where  $U_{\text{pp}}$  is the input voltage and  $i$  is a place holder for *freq* (frequency), *np* (non-polarising) and *p* (polarising), respectively. The resulting frequency

**Table 6.1.:** Frequency coupling coefficients with the corresponding arm length imbalances by applying two different methods for frequency tuning: temperature modulation *TMP-M* and resonator length modulation *PZT-M*. For clarity the design constraints are listed.

Interferometer		TMP-M	PZT-M	Design
non-polarising	$c_{\text{np}}$	$25 \frac{\mu\text{rad}}{\text{MHz}}$	$32 \frac{\mu\text{rad}}{\text{MHz}}$	0
	$\Delta L$	$1.2 \pm 0.1 \text{ mm}$	$1.5 \pm 0.3 \text{ mm}$	
polarising	$c_{\text{p}}$	$5 \frac{\mu\text{rad}}{\text{MHz}}$	$11 \frac{\mu\text{rad}}{\text{MHz}}$	0
	$\Delta L$	$290 \pm 15 \mu\text{m}$	$500 \pm 50 \mu\text{m}$	
frequency	$c_{\text{f}}$	$5 \frac{\text{mrad}}{\text{MHz}}$	$6 \frac{\text{mrad}}{\text{MHz}}$	27.1 cm
	$\Delta L$	$24 \pm 1.5 \text{ cm}$	$27.4 \text{ cm}$	



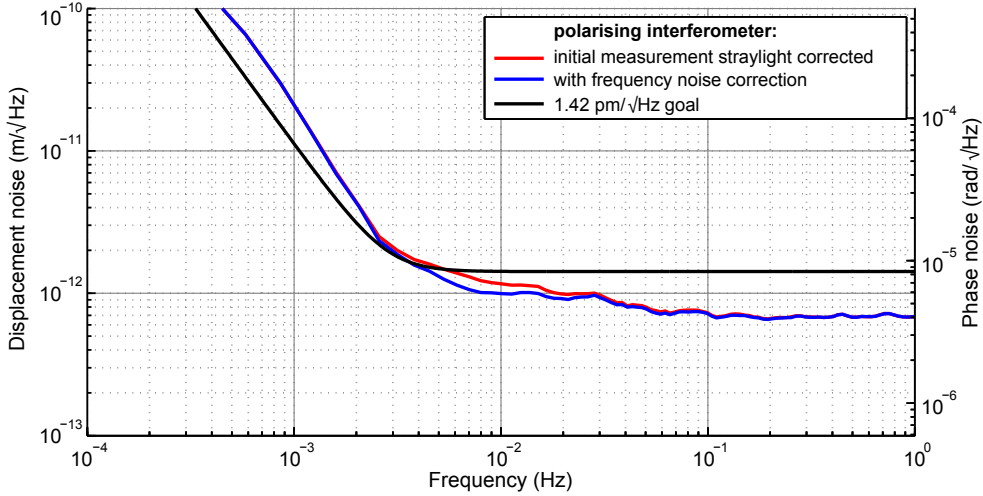


**Figure 6.4.:** Comparison of noise levels of the polarising interferometer observed in the initial measurement after using balance detection and after applying a laser frequency noise subtraction (blue trace). [m-code: VTPOs (red), VTPOsf (blue) ]

coupling coefficients with the corresponding arm length mismatch are summarised in Table 6.1.

Another possibility to determine the frequency coupling coefficients is to modulate the length of the laser resonator directly over the piezo electrical actuator. The piezo tuning coefficient is determined to be about  $\eta_{PZT} = 1.7 \text{ MHz/V} \pm 0.1 \text{ MHz}$ . This fast laser frequency tuning can be achieved by applying a high voltage sinusoidal signal to the piezo on the laser crystal. Thus, the length is varied with a frequency of 1 Hz. The observed modulation of the three phasemeter outputs can be used to calculate the frequency coupling coefficients. The ratio of resulting phase modulation to frequency change can be written as

$$\frac{\delta(\phi_i - \phi_{\text{ref}})}{U_{\text{pp}} \cdot \eta_{\text{PZT}}} = \frac{2\pi}{c} \cdot \Delta L_i. \quad (6.12)$$

The resulting coefficients with the associated arm length mismatch is listed in Table 6.1. Both approaches (temperature modulation *TMP-M* vs. resonator length modulation *PZT-M*) yield frequency coupling coefficients  $c_i$  of the same order of magnitude. Since the frequency interferometer has been designed with an intentional arm length imbalance of 27.1 cm, the obtained result of 27.4 cm has been rated as reliable. Thus, the coefficients obtained with the second method, modulation of the resonator length, have been used throughout this Chapter.

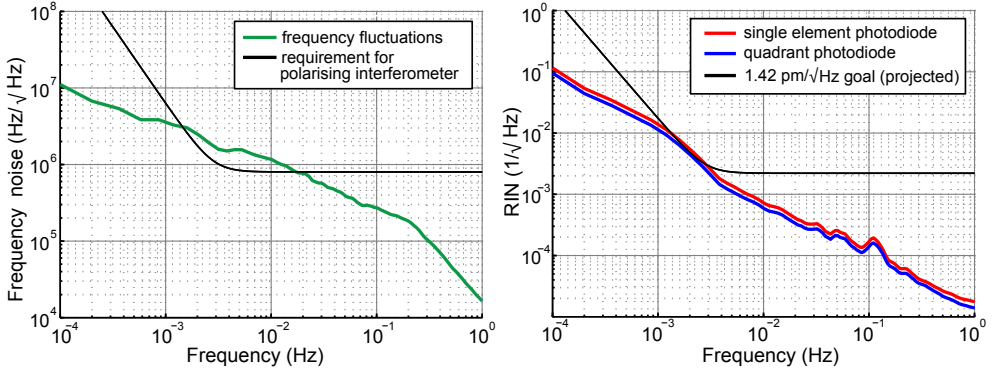


**Figure 6.5.:** *Left:* Laser frequency stability during the measurement run discussed in this Chapter. *Right:* Relative intensity noise of the performed measurement used for this Chapter. The red trace represents the RIN for a single element photodiode, whilst the blue trace denotes intensity fluctuations of the quadrant photodiode of the polarising interferometer.

The resulting ratio  $c_m$  ( $m=\{p, np\}$ ) of the modulation peak height  $\delta$ , expressed by

$$c_m = \frac{\delta(\phi_m - \phi_{\text{ref}})}{\delta(\phi_{\text{freq}} - \phi_{\text{ref}})}, \quad (6.13)$$

were used for long-term measurements to obtain a frequency noise corrected interferometric phase as

$$\Phi_{\text{cor}} = (\phi_m - \phi_{\text{ref}}) - c_m \cdot (\phi_{\text{freq}} - \phi_{\text{ref}}). \quad (6.14)$$

Depending on which noise source is the actual limiting one, a stray light or an angular noise subtraction had to be adopted prior to the frequency noise correction.

By implementing this subtraction algorithm, an improvement in displacement sensitivity for both measurement interferometers were obtained, as shown in Figure 6.3 for the non-polarising interferometer and in Figure 6.4 for the polarising interferometer. The noise curve lies well below the requirement for frequencies greater than 3 mHz. Since the arm length of the polarising interferometer is closely matched, the influence of frequency noise to phase noise is relatively small compared to the non-polarising interferometer with a three times larger arm length imbalance. This is reflected in both figures. The frequency stability of the laser used during the measurements is shown in Figure 6.5 along with the required stability of the polarising interferometer. Thus it appears that the effect of the frequency noise reduction is expected to be smaller. The limiting noise source for frequencies below 2 mHz is attributed

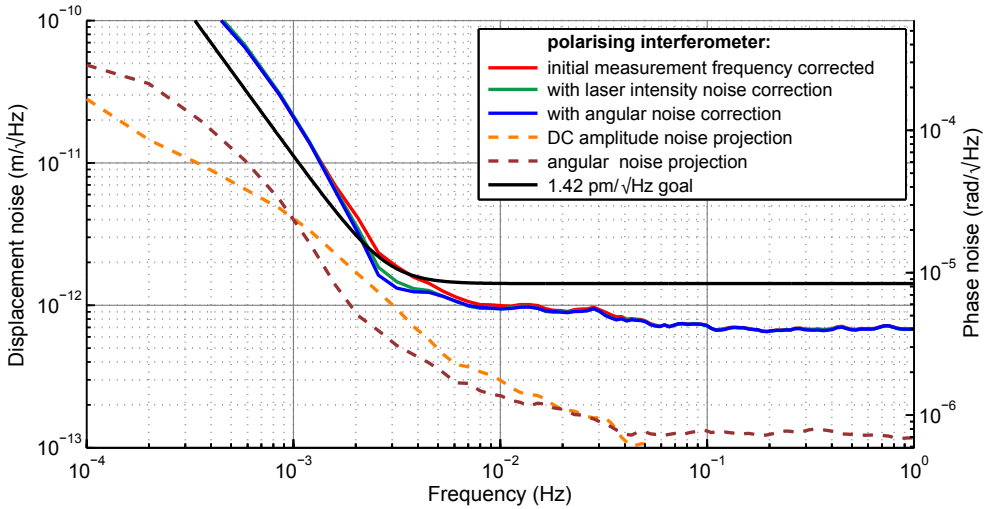


**Figure 6.6.:** Comparison of noise levels of the polarising interferometer observed in stray light and frequency corrected longitudinal signal (“initial measurement”) and by applying a laser intensity noise subtraction (green trace) as well as an angular noise correction (blue trace). [m-code: VTPOsf (red), VTPOsfa (green), VTPOsfad (blue)]

to temperature fluctuations. Angular noise as well as laser power fluctuations can be considered to limit the sensitivity for frequencies around 3 mHz.

### 6.3. Amplitude noise subtraction

The DC signals of the interferometer have been used to verify the relative laser noise and, if required, to correct for this noise source. It can be seen in Figure 6.5 that for the example discussed in this chapter the RIN was on the level of the requirement for frequencies between 1 mHz to 3 mHz. As the measurement of amplitude noise was not limited by the phase readout, it was estimated that the length measurements were affected by this noise source. Using a linear fitting algorithm implemented in MATLAB<sup>®</sup>, the influence on length change in the appropriated frequency band of 1 mHz to 10 mHz was estimated. For this purpose, the filtered DC signals have been linearly fitted to the equally filtered length measurement of both measurement interferometers. The estimated coefficients were used to subtract the spurious noise from the unfiltered longitudinal signal. It is worth mentioning that the estimated and measured coupling coefficients are in good agreement (*cf.* Section 5.7).

Figure 6.6 shows on the one hand the fitted laser intensity noise projection on the length measurement of the polarising interferometer, displayed by the orange dashed trace, and on the other hand the corrected one, represented by

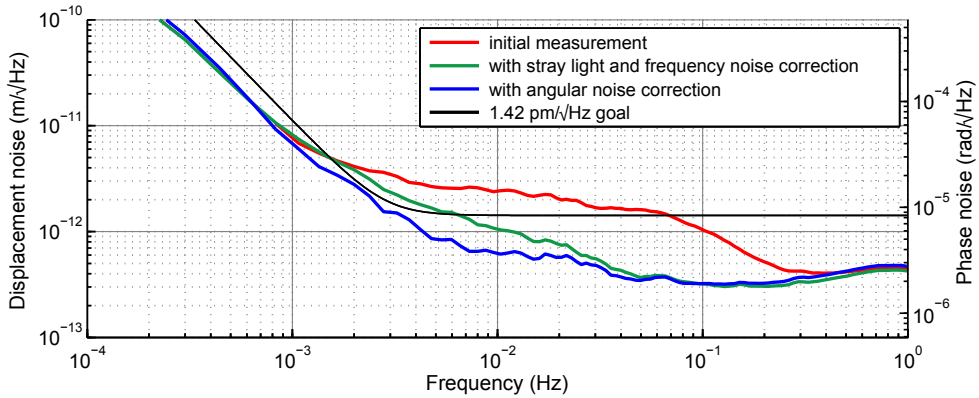


**Figure 6.7.:** Comparison of noise in the polarising interferometer after using the balance detection and applying the frequency noise corrections and after adopting the differential wave front signal subtraction. [m-code: VTPO (red), VTPOsf (green), VTPOsfd (blue)]

the green trace. It is apparent, that the length measurement has been slightly improved by this correction for frequencies between 1 and 10 mHz.

## 6.4. Angular noise subtraction

It is necessary to monitor the fibre injectors attitude jitter in order to characterise a cross-coupling between angular and displacement degrees of freedom. For this reason, the optical bench included quadrant photodiodes (QPD) at the three main interferometer outputs. In the data post-processing the differential wavefront sensing (*DWS*) correction technique has been applied [114]. For specifying the angular noise, initially, the coupling factor of *DWS* signal to beam angle change has been determined by introducing well defined beam angles and monitoring the resulting *DWS* variations. This led to a calibration factor of approximately  $3800 \text{ rad}_{\text{dws}}/\text{rad}$ . A detailed description of this procedure can be found in Section 5.3. Figure 6.8 represents on the left side the angular noise (scaled with the determined coupling coefficient) of the measurement run discussed throughout this Chapter.

To estimate the influence of angular noise on length change MATLAB<sup>®</sup>'s built-in least squares fit method was used. In the same manner as for the laser intensity noise subtraction, band-pass filtered angular and longitudinal interferometric signals were fed to the fit algorithm [120]. Typically corner frequencies were 1 mHz and 100 mHz, between which the longitudinal and angular signals were influenced by the assigned noise source. The coefficients obtained from this fit were used to subtract the spurious noise from the unfiltered longitudinal signal.

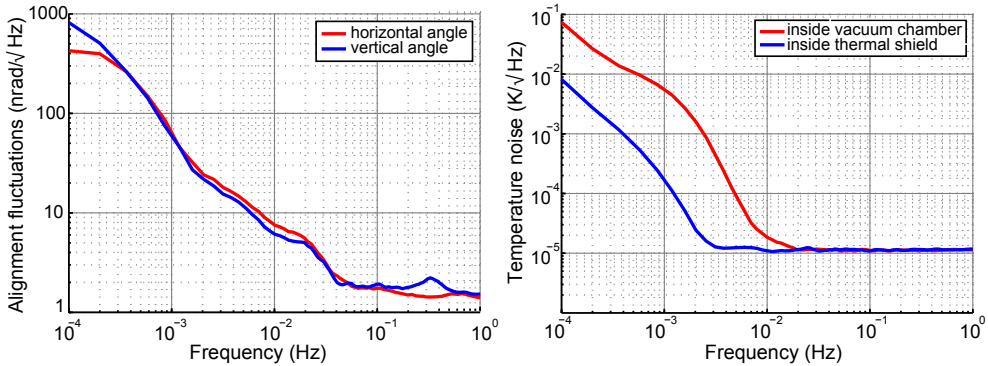


**Figure 6.8.:** *Left:* Angular noise of the performed measurement used for this Chapter. *Right:* Temperature stability during the measurement run discussed in this Chapter.

Using the computed coefficients the influence of angular noise into the longitudinal signal could be fitted. This is reflected in Figure 6.6 by the brown dashed trace. Applying the described subtraction algorithm to this particular measurement led to a slightly improvement of the sensitivity. However, depending on external factors and on how good the DWS signal of both beams has been aligned as well as centred on the QPDs, it was possible to significantly improve the phase readout. One example for this is shown in Figure 6.7. The initial noise level of the polarising interferometer is shown in solid red, whilst the noise level achieved after using balance detection and applying a frequency noise correction is plotted in solid green. The blue trace represents the angular noise corrected noise level. It is evident, that the fitting algorithm yielded an improvement in sensitivity by a factor of about 2 for frequencies between 1 mHz and 50 mHz.

## 6.5. Impact of temperature fluctuations

The noise performance in the low frequency range ( $\leq 1$  mHz) was dominated by temperature noise. Although the optical bench has been placed in a vacuum environment, enclosed by a thermal shield and used low-expansion ceramic as material for the optical bench, the temperature influenced the stability at the  $\text{pm}/\sqrt{\text{Hz}}$  level. Hence, a temperature noise correction in data post-processing was performed. In order to allocate the impact of temperature variations conducted at the PBS on the phase readout, the associated coupling coefficient was measured.

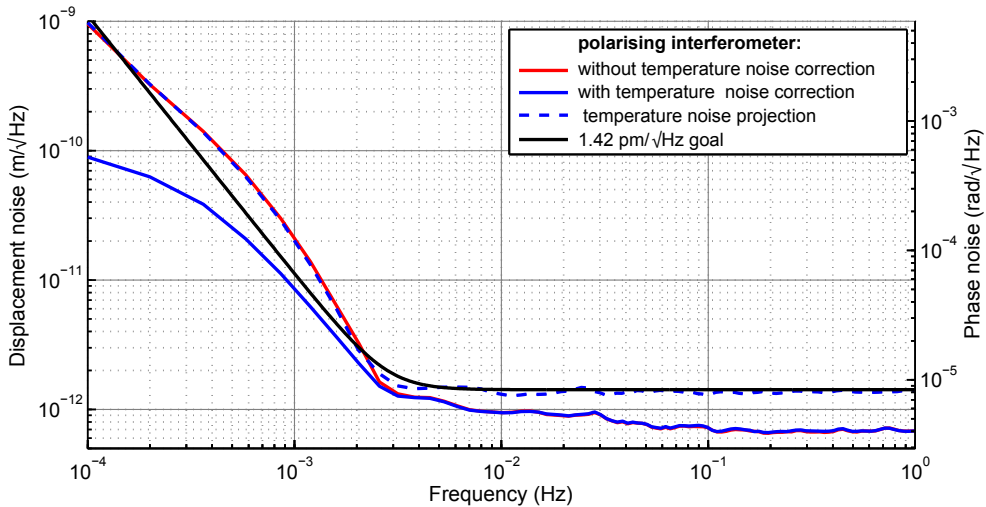


**Figure 6.9.:** Comparison of noise levels of the polarising interferometer observed in longitudinal signal with all previously discussed corrections applied (red trace) and after applying the temperature noise subtraction (blue trace). The temperature noise projection into the longitudinal signal is shown in dashed blue. [m-code: VTPOsfad (red), VTPOsfadt (blue)]

### 6.5.1. Temperature noise subtraction

In order to assess the impact of temperature fluctuations on the longitudinal signal, the thermal stability was measured at different locations during all measurements performed. Thus, the measured temperature inside the thermal shield was used in a linear fit for estimating a coefficient between temperature and measured phase. By using again a least squares fit method implemented in MATLAB<sup>®</sup> the coupling factor was determined to be about 1.3 rad/K corresponding to 220 nm/K. This is in good agreement with the expected value, when assuming an optical path length of 60 cm with three transmissions through optical components for one arm of the polarising interferometer. A coarse estimation yields a coupling coefficient of 0.4 rad/K, which includes the major contribution of three transmissions of 0.4 rad/K each (*cf.* Equation 6.25) and the minor one due to the optical bench of less than 0.1 rad/K. Using the determined coefficient the temperature induced phase changes were subtracted from the main measurement. Note that the measurement was not limited by temperature variations if the optical bench was enclosed for more than one week by its thermal shield in vacuum. An adequate state close to the thermal equilibrium ( $\widehat{\delta T} \leq 0.1 \text{ mK}/\sqrt{\text{Hz}} @ 1 \text{ mHz}$ ) was reached after one week, further improving with longer setting time.

The right side in Figure 6.8 shows a comparison between the thermal stability

achieved inside the vacuum chamber and inside the additional thermal shield. Using the coupling coefficients calculated with the fitting routine the influence of temperature fluctuations into the longitudinal signal has been determined, as shown in dashed blue in Figure 6.9. The solid red trace represents the longitudinal signal with all previous corrections applied. Hence, temperature fluctuations have been confirmed to be the limiting noise source for frequencies below 2 mHz. The solid blue trace shows the noise level after applying the temperature noise subtraction. A significant reduction of noise for frequencies below 2 mHz has been observed. Thus, the noise performance fulfils the requirement in the whole frequency range.

### 6.5.2. Coupling factor between temperature of PBS and longitudinal phase signal

The influence of temperature fluctuations at the polarising components, in particular the PBS, to the longitudinal phase has been investigated. The used PBS was made of fused silica with a dielectric coating. Any modifications of the extinction ratio or polarisation plane result in power fluctuations, which couple to the longitudinal measurement. Therefore, the PBS was heated up while the temperature at the beam splitter and the corresponding phase was monitored. In order to measure only induced phase changes of the PBS, the phase difference of the two main interferometers was used.

To heat the PBS a Kapton<sup>TM</sup> heater (*HK 5186*, MINCO) with a radius of 12.7 mm, including a cut-out of 2.4 mm radius, was used. As the heater would not have occupied the whole contact area of the PBS if glued on top, it was attached with an adhesive to a thin copper plate, as shown in Figure 6.10. The copper plate, in turn, was located 1 mm above the PBS. Thus, a nearly homogeneous heat dissipation was realised. In addition, this protected the PBS from damage and contamination resulting from the adhesive. A PT10K sensor was attached at the PBS, measuring the temperature change.

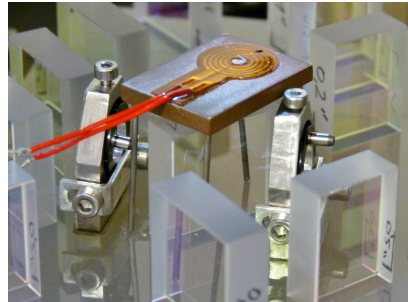


**Figure 6.10.:** Photograph of the polarising components on the optical bench.

Considering only a single optical component, the PBS, being in the path, the detected length difference at the interferometer output is given by:

$$s = s_0 + s_{\text{sub}}(n - 1), \quad (6.15)$$

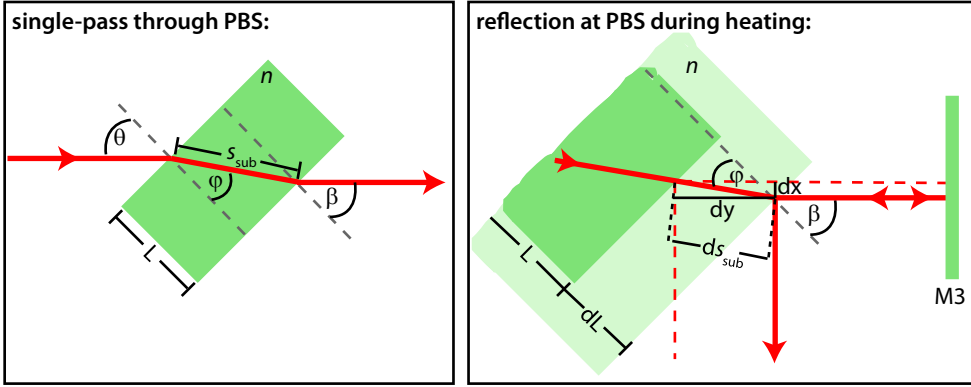


**Figure 6.11.:** Determining the coupling factor between temperature of PBS and longitudinal phase signal: *Left:* Single-pass through a PBS with thickness  $L = 7\text{ mm}$  and an angle of incidence of  $\theta = 45^\circ$ ; *Right:* While the PBS is heated it expands by  $2 \cdot dL$  and the beam coming from mirror M3 impinges with an angle of incidence of  $\beta = \theta$  on a different spot as without temperature influence. This results in a shortened optical path length.

where  $s_0$  expresses the geometrical path length of the interferometer. The path length within the substrate is denoted by  $s_{\text{sub}}$ . The refractive index  $n$  of Suprasil<sup>®</sup> 1 at 1064 nm is 1.44963 [94]. Using Snell's law together with geometrical considerations, the path length within the substrate with thickness  $L$  can be written as:

$$s_{\text{sub}} = \frac{L}{\cos \varphi} = \frac{L}{\sqrt{1 - \left(\frac{\sin \theta}{n}\right)^2}}, \quad (6.16)$$

for an incoming beam with incidence angle  $\theta$ .

The coupling of temperature into the path length for single-pass through the PBS is calculated by the derivative

$$\frac{ds}{dT} = \frac{ds_0}{dT} + (n-1) \frac{d}{dT} \left[ \frac{L}{\sqrt{1 - \left(\frac{\sin \theta}{n}\right)^2}} \right] + \frac{L}{\sqrt{1 - \left(\frac{\sin \theta}{n}\right)^2}} \frac{dn}{dT}. \quad (6.17)$$

Assuming that the initial interferometric path length is not affected by temperature and that the linear thermal expansion coefficient is given by  $\alpha = \frac{dL}{LdT}$ , Equation (6.17) can be derived with respect to temperature:

$$\frac{ds}{dT} = \frac{L}{\sqrt{1 - \left(\frac{\sin \theta}{n}\right)^2}} \left[ \alpha(n-1) + \frac{dn}{dT} \left( 1 - \frac{\sin^2 \theta (n-1)}{n(n^2 - \sin^2 \theta)} \right) \right]. \quad (6.18)$$

As the PBS is (homogeneously) expanded, the beam coming back from M3 and reflected towards the beam combiner experiences a shortened path length. This



effect is reflected in Figure 6.11. The geometric length of beam propagation within the expanded part of the PBS can be expressed by:

$$ds_{\text{sub}} = \frac{dL}{\cos \varphi} = \frac{\alpha L}{2 \cdot \cos \varphi}. \quad (6.19)$$

Carrying out some geometrical consideration on Figure 6.11, the additional path length difference  $s_r$  due to reflection at an expanded PBS can be written as

$$s_r = dx + dy \quad (6.20)$$

with  $dx = ds_{\text{sub}} \sin(\beta - \varphi)$  and  $dy = ds_{\text{sub}} \cos(\beta - \varphi)$ .

In this expression is  $\beta$  the exit angle as well as the angle of incidence of the impinging beam coming from the plain mirror M3. Since the exit angle is not affected by temperature driven changes, it can be equated with the incidence angle  $\theta$ :

$$\theta = \arcsin(n \sin \varphi) = \arcsin\left(n \cdot \frac{\sin \beta}{n}\right) = \beta. \quad (6.21)$$

Thus, Equation (6.20) can be re-written as

$$s_r = \frac{\alpha L}{2} \left[ \cos \theta + \sin \theta + \frac{\sin \theta - \cos \theta}{\sqrt{1 - \left(\frac{\sin \theta}{n}\right)^2}} \cdot \frac{\sin \theta}{n} \right] \quad (6.22)$$

Taking into account a single pass through the PBS and the influence of the reflection at the return path, the coupling of temperature change  $dT$  to the optical path length change  $ds$  by the PBS for an angle of incidence  $\theta = 45^\circ$  can be expressed by

$$\frac{ds}{dT} = \underbrace{\frac{L}{\sqrt{1 - \frac{1}{2n^2}}} \left[ \frac{dn}{dT} \left( 1 - \frac{n-1}{2n^3 - n} \right) + \alpha(n-1) \right]}_{\text{single pass through PBS}} - \underbrace{\frac{\alpha L}{\sqrt{2}}}_{\text{reflection}}. \quad (6.23)$$

Introducing the temperature coefficient of the refractive index  $dn/dT$  of 9.8 ppm/K together with the thermal expansion coefficient  $\alpha$  of 0.51 ppm/K [94] a coupling coefficient proportional to the geometric thickness  $L$  ( $\approx 7$  mm) of the PBS can be estimated:

$$\frac{1}{L} \frac{ds}{dT} = 10 \text{ ppm/K}. \quad (6.24)$$

To compare the results obtained from heating the PBS we can express the coupling of temperature to the optical path length in terms of phase in single pass (including the reflection on the optical surface of the PBS) by

$$\frac{d\Phi}{dT} = \frac{2\pi}{\lambda} \frac{ds}{dT} \approx 0.4 \frac{\text{rad}}{\text{K}}. \quad (6.25)$$

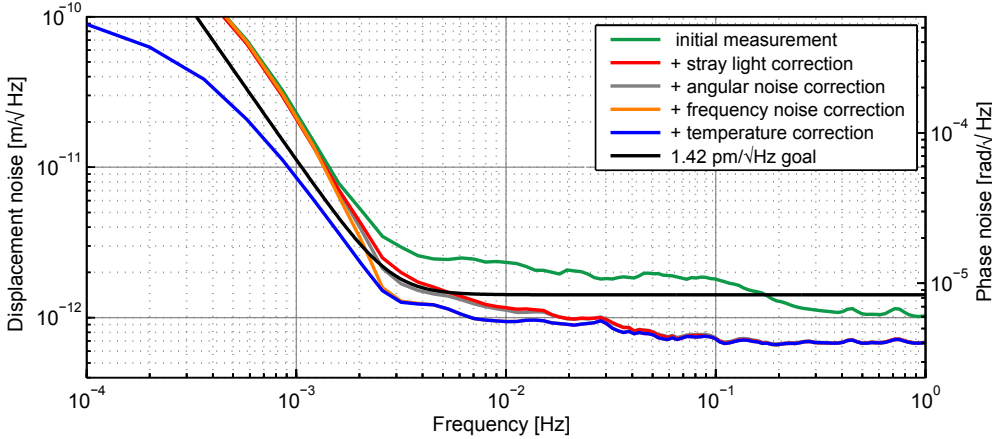


**Figure 6.12.:** Final noise performance with corrections applied in data post-processing. [m-code: VTPO (green), VTPOs (red), VTPOsd (grey), VTPOsdf (orange), VTPOsdf (blue)]

The experimentally determined coupling coefficient of 0.3 rad/K roughly agrees to the theoretical value. The discrepancy can be caused by having not measured the temperature inside the PBS, but on the optic's surface. One way to improve the measurement would be to measure the temperature on both optical surfaces each with at least two sensors as far as possible separated, and taking the mean value as the temperature change. However, a temperature stability in the polarising beam splitter required to detect path length fluctuations of  $1 \text{ pm}/\sqrt{\text{Hz}}$  is thus approximately  $2 \cdot 10^{-5} \text{ K}/\sqrt{\text{Hz}}$ . Using the determined coupling coefficient of 1.3 rad/K for the interferometer including all components an over all temperature stability requirement of  $4.5 \text{ } \mu\text{K}/\sqrt{\text{Hz}}$  for frequencies smaller than 2 mHz can be deduced.

## 6.6. Resulting noise performance

This section is discussing the final results of both measurement interferometers after adopting the actively stabilisation loops described in Chapter 5 and after all subtractions introduced in this chapter have been additionally applied in data post-processing. For the sake of completeness the difference between the two main longitudinal signals  $\Delta(\phi_p - \phi_{np})$  is additionally considered.

The displacement noise with implemented noise subtraction models are presented in Figure 6.12. The initial measurement is a length measurement of the polarising interferometer conducted for a few days in a vacuum environment while it was enclosed by a TS (green trace). The OPD stabilisation was used and the polarisation state of both beams injected to the bench were controlled.

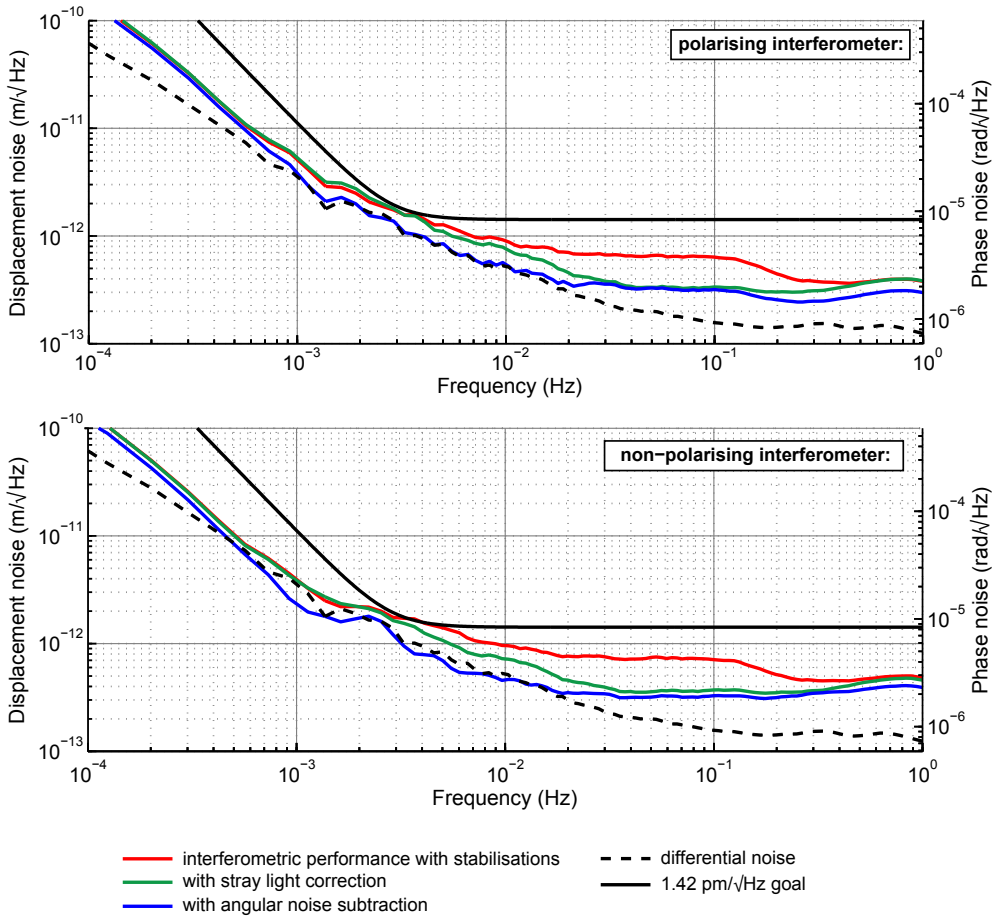


**Figure 6.13.:** Final noise performance with actively stabilisations, such as laser frequency and intensity stabilisation, together with two noise subtractions applied in data post-processing. One was the balanced detection method and the other one adopted the DWS technique to subtract angular noise. [m-code: VTPOFA (red), VTPOFAs (green), VTPOFAsd (blue)]

Residual noise induced by stray light was eliminated by balanced detection. The applied correction led to a considerable reduction of the observed displacement noise for frequencies bigger than 2 mHz (red trace). The grey trace illustrates the displacement noise with an additional angular noise subtraction. This subtraction method had a minor efficiency and only slightly improved the phase readout in the small frequency band from 2 mHz to 10 mHz. By implementing the frequency noise subtraction algorithm a displacement sensitivity well below the requirements for frequencies bigger than 2 mHz (orange trace) was obtained. For frequencies smaller than 2 mHz the length measurement was limited by temperature noise. However, it was possible to notably enhance the

phase readout sensitivity by applying a temperature noise subtraction. Thus, the blue trace represents the final displacement sensitivity, where all the presented noise subtractions were applied. One can see that the noise performance fulfils the requirement in the whole frequency range. Hence, under non-ideal conditions it was still possible to reach the required noise performance, which leads to an improved robustness for a LISA mission.

By combining the subtraction algorithms with the stabilisation loops described in Chapter 5 the performance could be further enhanced. Figure 6.13 shows the noise performance for both measurement interferometers ( $\phi_p, \phi_{np}$ ) along with the difference between these two signals  $\Delta(\phi_p - \phi_{np})$ . For this measurement run the OPD stabilisation as well as the laser frequency and intensity stabilisation were used. Furthermore, the polarisation state of both beams was matched with respect to the axis of the optical fibre. A stray light correction as well as an angular noise subtraction were implemented in data post-processing. The obtained noise traces fulfil the requirement within the whole frequency band. Moreover, it is shown that the displacement noise has still a margin of more than a factor two. Length measurements for the polarising and non-polarising interferometer were compared and found to comply with the  $1.42 \text{ pm}/\sqrt{\text{Hz}}$  level.

# 7 Conclusion

In the current baseline design for the LISA optical bench, the use of polarising optics is foreseen to separate optical beams. Therefore it is important to investigate the influence of polarising components on the interferometer sensitivity. For this purpose a quasi-monolithic optical bench has been designed and built consisting of two measurement interferometers (one including polarising optics). Additionally, a frequency and reference interferometer were included. The frequency interferometer had unequal arm lengths and was used to actively stabilise the laser's frequency to  $10 \text{ kHz}/\sqrt{\text{Hz}} @ 10 \text{ mHz}$ . Stray light on the optical bench was analysed and, by modifying the layout, reduced. In addition, the layout was analysed with respect to periodic non-linearities. As a result periodic phase errors potentially have no effect on the phase readout. First, a modified layout was set up on an aluminium breadboard. Noise performances reached a length stability on the order of  $50 \text{ pm}/\sqrt{\text{Hz}}$  at  $100 \text{ mHz}$  increasing as  $1/f$  at lower frequencies. The significant limiting noise sources were non-homogeneous thermal expansion of the metal baseplate and mechanical stability of the setup. To improve the thermal and insufficient mechanical stability, the silicate bonding technique was applied. A CMM was used to align the positions of the optical components, which yielded a positioning accuracy of  $10 \mu\text{m}$  and an angular accuracy of a few hundred  $\mu\text{rad}$ . The measurement uncertainty of the CMM could be identified as limiting source. Furthermore, the arm length differences of the two measurement interferometers were determined to be on the order of  $1 \text{ mm}$ .

Displacement noise better than  $1 \text{ pm}/\sqrt{\text{Hz}}$  for frequencies between  $3 \text{ mHz}$  and  $1 \text{ Hz}$  was demonstrated in a heterodyne interferometer using polarising components. Length measurements for the polarising and non-polarising interferometer were compared and found to be below the given requirement of  $1.42 \text{ pm}/\sqrt{\text{Hz}}$  in the frequency band from  $3 \text{ mHz}$  to  $1 \text{ Hz}$ , increasing towards

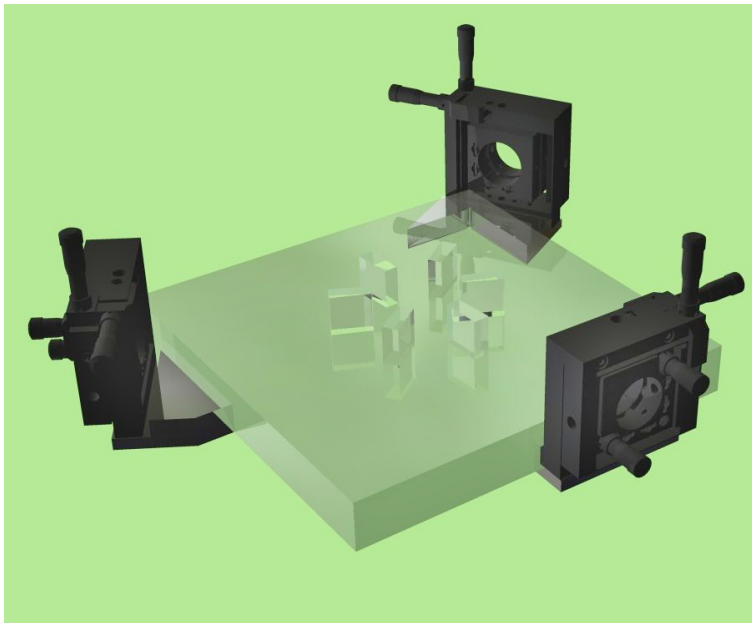
lower frequencies. In order to reach that noise level different noise sources were identified and suppressed. Two main noise sources were identified and mitigated by active stabilisations. One is the effect of non-linear optical path length difference: due to electromagnetic cross-talk between the AOM drivers, spurious sidebands are generated, resulting in residual beat notes but of unstable phase. The second noise source is fluctuations of the laser frequency that proportionally translate into interferometer phase noise. Furthermore it has been shown that the polarisation state of the incoming light plays a major role. By equipping the optical bench with polarisers and optimising the incoming polarisation state of the two beams, the phase readout noise was significantly reduced in the frequency band between 0.3 and 30 mHz.

Alternatively, several noise sources were subtracted in data post-processing. These noise sources were caused by parasitic beams due to ghost reflections (stray light) and coupling of noise into the displacement measurement such as beam angle noise, temperature noise, as well as laser frequency and intensity noise. Thus, under non-ideal conditions it was still possible to reach the required noise performance, which leads to an improved robustness for a LISA mission.

The measured coupling from the temperature of the polarising optics to the displacement measurement was as expected. Thus, no additional requirement for the temperature stability is needed. In order to investigate the occurrence of non-linearity induced by polarising components on the optical bench, several measurements were conducted. One arm length of the two measurement interferometers was intentionally varied and the response in phase was observed. By comparing the displacement in the polarising interferometer with either the displacement measured in the non-polarising interferometer or the determined displacement of the piezo, no evidence was found for periodic phase errors induced by polarising optics.

## Part III

# The way towards an ultimate phasemeter test







# 8 Assembly of a hexagonal interferometer for optically testing a phase measurement system

One of the key systems in a precision differential length metrology is the phase measurement system (PMS). It needs to be capable of measuring the phase of beat note frequencies up to 20 MHz with microcycle accuracy over 100 ... 1000s time scales in the presence of continuous frequency drifts and laser noise, which will be the case in e.g. LISA or GRACE follow-on. In the case of LISA this readout is based on a tracking phasemeter implemented on FPGAs. The actual readout is performed using a digital phase-locked loop (DPPL) for processing the digitised signals [125].

This readout scheme has been chosen after various investigations have been carried out at different research centres such as NASA/JPL [126, 127], the University of Florida in Gainesville [128] and AEI [129]. The ongoing investigations at AEI are being performed within the framework of an ESA technology project: *LISA Metrology System*. To this end, an elegant breadboard model of the LISA PMS has been developed and manufactured under a scientific collaboration with the National Space Institute of the Danish Technical University (DTU Space) and the Danish industry partner Axcon ApS. Before building the final system various requirements had to be validated in advance. For this purpose, several phasemeter prototypes were built. One of them has been used throughout this Chapter.

In the course of the ESA project the basic functionality of the phasemeter prototype has been demonstrated [130]. It was shown that the prototype PMS is

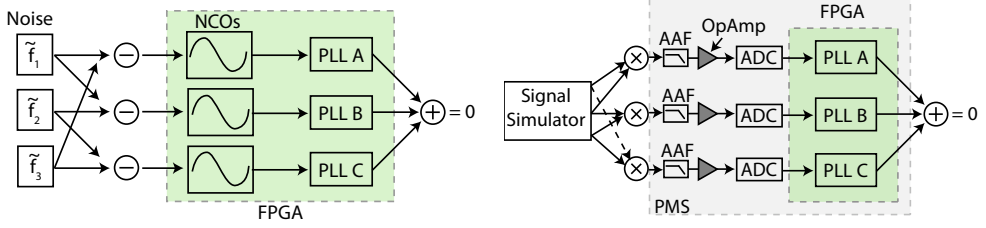


**Figure 8.1.:** Schematics of electrical linearity test of PMS. *Left:* digital linearity test *Right:* analogue linearity test using a signal simulator and the analogue front end.

capable of tracking a generated input signal of known frequency, but also being able to track multi-signals. That means that the PLLs can simultaneously track the main beat note frequency as well as the frequencies of the upper and lower sideband beat note signal [130]. Furthermore, the required phase noise performance of [16]

$$\widetilde{\delta\phi} = 6 \frac{\mu\text{rad}}{\sqrt{\text{Hz}}} \times \sqrt{1 + \left(\frac{2.8 \text{ mHz}}{f}\right)^4} \quad (8.1)$$

in the measurement bandwidth down to  $3 \times 10^{-5}$  Hz under laboratory conditions has been demonstrated [130]. As real input signals are not ideal but rather contain additional noise sources, the core process inside the PLL and its stability are influenced. Furthermore, the PLL has intrinsic non-linear behaviour. This can result in a worse phase performance, cycle slips in the PLL tracking [131–133], and in a loss of the phase lock. However, by controlling various parameters such as the loop gain to keep the error between incoming frequency and LO frequency small enough, the output can be forced to be proportional to the error in phase and thus the PLL operates in a linear regime. As non-linearity would lead to an insufficient noise performance of the PMS, high requirements are necessary. For instance, the occurrence of cycle slips has to be kept at virtually zero, and a stable linear operation has to be ensured. In order to verify the required PMS linearity, three different approaches are used: digital, analogue electrical, and optically testing the linear behaviour of the PMS. The underlying principle for both approaches is based on the fact that if three phase difference outputs are linearly combined, the noise should add to zero [134].

For given noise sources the digital phasemeter linearity test has been successfully performed [135]. Three independent noise sources were generated, representing three laser systems, appropriately combined and fed to three independent numerically controlled oscillators (NCO), as shown in Figure 8.1(a). The

PLL tracked the signals with frequencies  $(f_1 - f_2)$ ,  $(f_2 - f_3)$ , and  $(f_1 - f_3)$  and phases  $\phi_a$ ,  $\phi_b$ , and  $\phi_c$ , respectively. If the system works linearly the combination of these signals results in

$$(f_1 - f_2) + (f_2 - f_3) + (f_3 - f_1) = 0. \quad (8.2)$$

Any residual noise is caused by non-linearity in the PLL. In the case of the analogue electrical test three signals have been generated using a signal simulator [130]. The setup used is depicted in Figure 8.1(b). One main difference to the setup sketched in Figure 8.1(a) is that the analogue front end and ADC are included in the measurement chain. Using the signals from the signal simulator three analogue beat note signals were generated by appropriately combining GHz signals. The MHz signals were then fed to the PLL cores where the corresponding frequencies were tracked. As the mixers showed excess phase noise at low frequencies, the LISA performance stated in Equation (8.1) could not yet be reached [135].

It is, however, an actual optical test that is needed for the ultimate linearity test. In an optical setup all PMS functionalities can be combined and real laser noise is present, thus allowing a test and characterisation of the PMS under conditions that are as representative for the real application as possible on ground.

## 8.1. Design of the prototype optical bench

The considerations towards a prototype optical bench for optically testing of PMSs at a picometre/ $\sqrt{\text{Hz}}$  level together with the final design is presented in this section. Analyses concerning stray light and beam jitter were performed and described in detail.

### 8.1.1. Design considerations

For optically testing the LISA phasemeter as well as any arbitrary phasemeter down to picometre/ $\sqrt{\text{Hz}}$ , several constraints had to be taken into account. The design had to cope with the following problems:

- Use an optical bench made from a material with a low coefficient of thermal expansion, such as Zerodur<sup>®</sup> or ULE<sup>®</sup>.
- The optical components need to be rigidly joined with the optical bench.
- Combine three symmetric and identical heterodyne interferometers on one single bench.

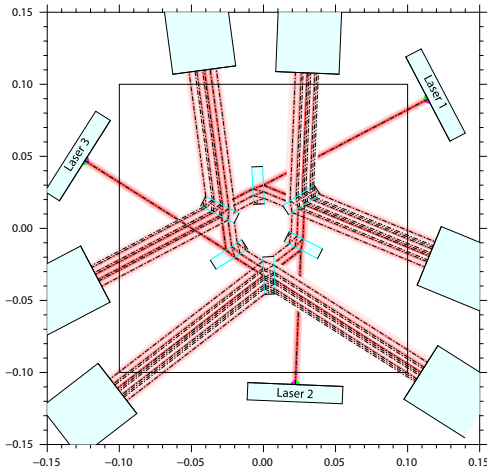


**Figure 8.2:** Simulation of stray light occurring in a hexagonal layout with three input beams and three beam combiners involved when using rectangular beam splitters.

- Have three laser light beams coupled via fibre injectors onto the optical bench.
- The number of components shall be kept small.
- Minimise residual ghost beams.
- The design and choice of materials have to be compatible with the bonding techniques described in Chapter 2.

Considering all these constraints, the following layout has been developed together with Gerhard Heinzl.

### 8.1.2. Layout of a hexagonal optical bench

The basic layout of the interferometer consists of three beams forming three recombination points via six beam splitters. In general, one has the choice between multiple possibilities. Restrictive constraints were, on the one hand, to form a symmetric interferometer with nearly no ghost beams that would couple into the phase readout and, on the other hand, to optimise the floor planning under the constraint that the six photodiodes and three fibre injectors do not intersect with each other. Moreover, we tried to minimise the path lengths, at the same time being compatible with bonding techniques described in Chapter 2. To satisfy these criteria, the optimum layout was developed with IfoCad. This stage included the simulation of ghost beams occurring on the optical bench, which has been performed using in addition the software OptoCad. Initial simulations on an interferometer layout consists of rectangular beam splitters revealed a high contribution of spurious beat note signals into

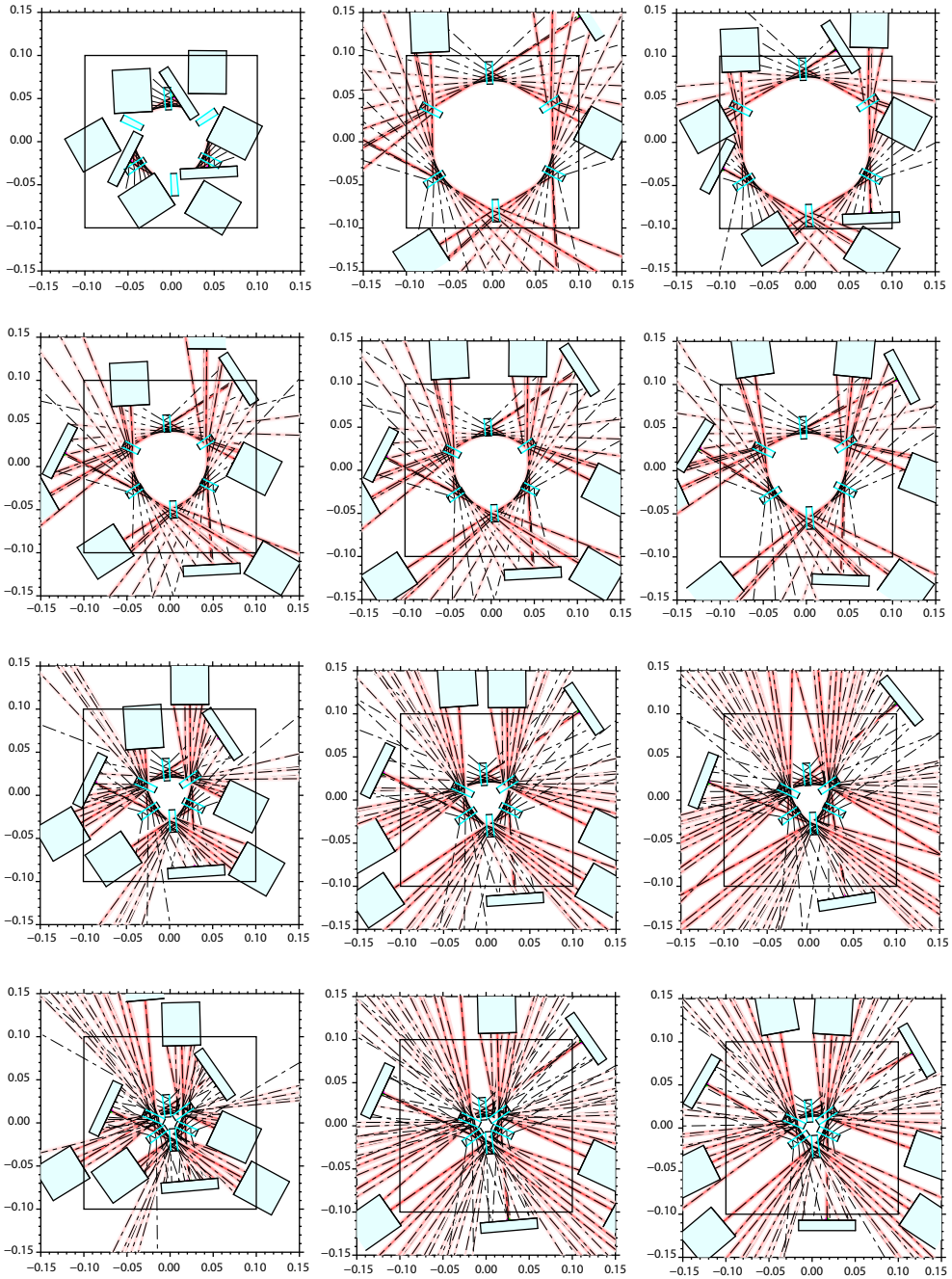
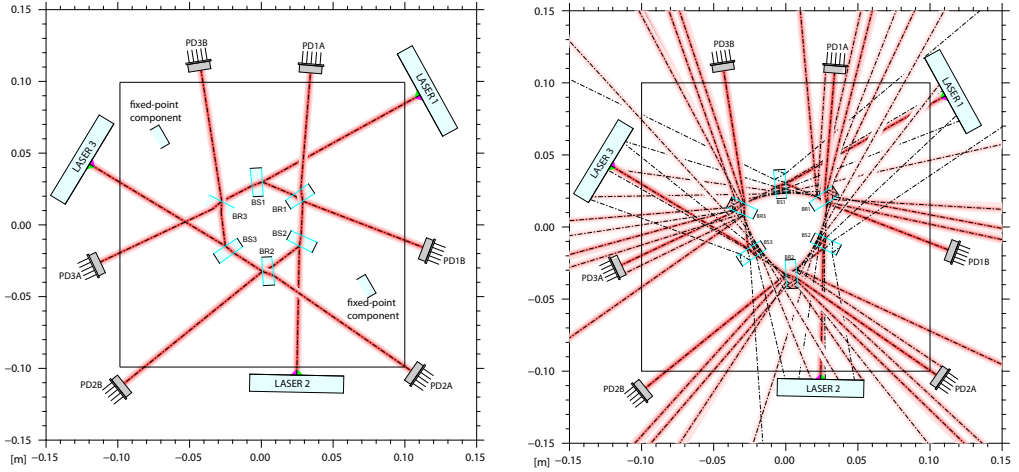


**Figure 8.3.:** Iterative procedure towards an optimum hexagonal layout: The radius of the polygon as well as the angle of incidence of the first beam impinging on BS1 and thus RB1 were varied, while the stray light was analysed. By adopting a polygonal floor planning algorithm the photodiodes and fibre injector assemblies were shifted out of the optical bench until the assigned bounding box did not intersect with a nearby bounding box.

## 8. Assembly of a hexagonal interferometer for optically testing a phase measurement system



(a) Layout of the optical path on the optical bench made with IfoCad.

(b) Simulation of ghost beams made with OptoCad.

**Figure 8.4.:** Final design and stray light analysis of the hexagonal interferometer being used to test the functionality of a phase measurement system.

the main signal, as shown in Figure 8.2. In contrast, using optical components with a wedge angle most of the ghost beams can be prevented from re-entering the main optical path. In an automated iterative procedure the “radius” of the polygon and/or the incidence angles of the beam impinging on the first wedged beam splitter BS1 were varied, while a stray light analysis was simultaneously performed. Meanwhile, the differential path length of a single interferometer has been kept zero and the difference of the two angles of incidence has been controlled, e.g. in the range between  $-10^\circ$  and  $+10^\circ$ . Using a polygonal collision avoidance floor planning algorithm [136, 137], the three fibre injector assemblies (represented by a bounding box) and the six photodiodes (also represented by a bounding box) were shifted outside the optical bench along the beam direction until the polygonal bounding box did not intersect with any other polygon including polygons representing beams. Such a procedure is shown in Figure 8.3, where the radius of the hexagon has been varied along the columns and the differential angle of incidence along a single row.

As several layout choices existed that all conform to reduced stray light impinging on the photodiode, the layout with the shortest possible radius was chosen as baseline. Figure 8.4(a) shows the final layout, while Figure 8.4(b) displays the ghost beams occurring on the optical bench. It consists of three identical interferometers in a hexagonal configuration with an inner radius of approximately 3 cm. The stray light simulation performed indicated, on the

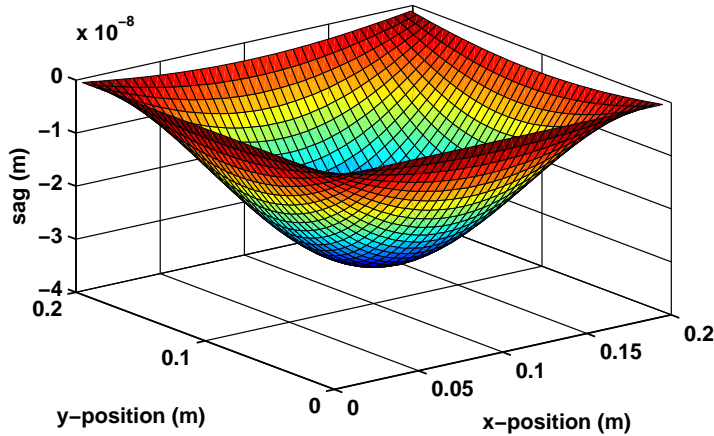


**Figure 8.5.:** Deformation analysis of a 25 mm thick Zerodur<sup>®</sup> bench under gravitational load. Shown is the deviation (vertical axis) from the nominal position without gravitational load for each position (horizontal axes) on the optical bench, while the baseplate is hold at its four edges.

one hand, no presence of ghost beams on the main optical path and, on the other hand, ghost beams only impinging at least 2 mm away from the main beam's centre. Their contribution to the main signal is less than 0.05 %. Thus, parasitic noise due to spurious beat note signals was avoided. For constructing the bench, it was decided to adopt the template bonding technique for the initial beam splitters, while the three beam combiners should be positioned and bonded with the method of adjuster aided bonding by using heterodyne signals (*cf.* Sections 2.2 and 2.3.5). In order to relate the template to a reference position, two fixed-point components have been included. Furthermore, this layout enabled us to install quasi-monolithic FIOS at a later stage, but also provided sufficient space for commercially available fibre injector assemblies.

As all the beam splitters and beam combiners nominally are used at  $25.85^\circ$  and  $35.85^\circ$  incidence angle to the beams, respectively, and each beam experienced only one transmittance prior to interfering with the other beam, moreover each pair of arms has a balanced path length in the interferometer. Thus, path length changes due to thermally driven changes in refractive index ( $dn/dT$ ) and bulk expansion ( $L^{-1} \cdot dL/dT$ ) were made as “common mode” as possible.

### 8.1.3. Properties of components used

The baseplate used for the hexagonal optical bench is made of Zerodur<sup>®</sup>. Similar to Clearceram<sup>®</sup> used for the optical bench to investigate the influence of polarising optics into the phase readout, Zerodur<sup>®</sup> has a low coefficient



## 8. Assembly of a hexagonal interferometer for optically testing a phase measurement system

---

of thermal expansion of  $2 \times 10^{-8} \text{ K}^{-1}$  at room temperature [138]. A square plate of Zerodur<sup>®</sup> of side length 200 mm and thickness 25 mm was used. Its surface has been polished to an optical surface quality of  $\lambda/10$ . In order to assess the baseplate's deformation due to gravity load, a numerical computation with MATLAB<sup>®</sup> has been performed to compute the magnitude of the bending [91]. The calculation included the following parameters of Zerodur<sup>®</sup>: density =  $2.53 \text{ g/cm}^3$ , Young's modulus = 90 GPa and Poisson's ratio = 0.243 [138]. In the same manner as described in Section 4.2.2, a mounting of the bench by its four edges is assumed. Figure 8.5 shows a 3D plot of the simulated bending for a 25 mm thick optical bench under gravitational load. The vertical axes represents the deviation from the nominal position without gravitational load for each position, which is defined by the horizontal axes. The maximum sag is located in the middle of the plate and is about 30 nm. This deformation is more than one order of magnitude below the angular tolerances of the optical components.

The choice of optical component material and dimension is important both for mechanical and optical properties of the beam splitters. One potential noise source in the interferometer comes from thermally driven changes in the refractive index as well as in the component's dimensions (via  $\alpha$ ), resulting in optical path length changes in the material of the transmissive components. Fused silica is chosen as material due to its very low thermal expansion coefficient, temperature dependence on the index of refraction of a few  $10^{-6}/\text{K}$  @ 632 nm and its previous successful application in similar interferometers. Suprasil<sup>®</sup>

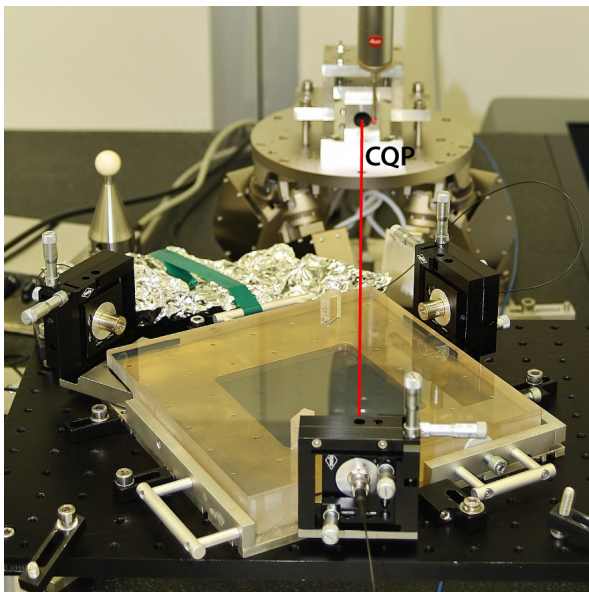


**Figure 8.6:** Experimental setup for input beam alignment: The CQP was used as target and was precisely pre-positioned with a hexapod, while its position was measured by a CMM. The fibre injector assembly of the hexagonal interferometer (in front) were aligned so that the input beam agreed well with the nominal beam.



1 has a refractive index of 1.44963 at 1064 nm, a  $dn/dT$  of  $9.8 \times 10^{-6} \text{K}^{-1}$  at 632 nm and a coefficient of thermal expansion equal to 0.51 ppm/K [94].

Another significant noise source is due to spurious reflections at the rear side of beam splitters re-entering into the main optical path, as shown in Figure 8.2. If these ghost beams impinge on the photodiode, spurious beat note signals result. Thus, as discussed above, components with a wedge in in-plane direction were preferred. However, wedged components entail the risk of adding path length noise due to beam jitter across the wedge. While the beam jitters it will scan across the component's surface by a small amount and experience a variable thickness of the substrate. The resulting change in optical path will couple into the measurement. Ongoing investigations of the influence of wedged optics into the length measurements seem to indicate a coupling of a few tens  $\mu\text{m}/\text{mrad}$ . However, further analyses and simulations are required.

In order to inject light from the three lasers to the optical bench, commercial off-the-shelf adjustable fibre couplers produced by Schäfter & Kirchoff (*60FC-4-A11-03*) were used. For mounting as well as adjusting these injectors, commercial mounts produced by OWIS (*TRANS 40-D25-MS* in combination with *FV 65-XY-MS*) were chosen. Although the type of mount selected consisted of a compact and solid body, a significant alignment jitter of the order of 10 to 100  $\text{mrad}/\sqrt{\text{Hz}}$  was expected. Thus, it is desirable to use quasi-monolithic fibre coupler assemblies instead. At the time of manufacturing the optical bench these FIOS were not available.

## 8.2. Construction

The manufacture of the optical bench can be divided into four stages. The first stage consisted of the alignment of the three input beams with respect to the baseplate. This has been realised by using the CQP described in Chapter 3. Thereafter, the fixed-point components were aligned using a CMM and were optically contacted to provide a reference for the template. The third stage included the template-assisted bonding of the three beam splitters, all rated as non-critical. Finally, the three beam combiners were aligned to heterodyne signals by optimising the contrast monitored. In the following sections these stages are described in detail.

### 8.2.1. Input beam alignment

One of the critical alignment processes was the precise alignment of the three fibre injectors that emit the input beams. As these input beams define the precise position of the recombination beam splitters, it was required to link them rigidly to the optical bench. For this purpose, each assembly of fibre

injector and mount was screwed on a metal plate, which was glued with an epoxy resin (*ER 2188*, Electrotube) to the optical baseplate.

The alignment of the three input beams has been realised by adopting the CQP. In this case the CQP was used as a target to which the beam was aligned. In order to allow an extremely fine control of the CQP position, a hexapod was used. Its six degrees of freedom were calibrated with respect to the machine coordinate system MCS, enabling a fast and accurate pre-positioning. Probing the structure of the CQP with the CMM, its position and orientation within the MCS was defined. By additionally measuring the physical position of the optical bench, the CQP's position with respect to the optical bench was known. The first step consisted of the precise positioning of the CQP. Therefore, a program written in the C language was used to calculate the input parameters of the three translations and the three rotations for the hexapod software PI Micromove. The C-program required as input the calibration parameters for the hexapod as well as the CQP, the measured CQP position at the initial hexapod position, and the desired beam propagation axis with a point along its axis. After the determined parameters have been processed, the new position and orientation was measured by the CMM. The theoretical beam propagation axis and position were determined and compared to the nominal ones. If necessary, the hexapod and consequently the CQP was slightly moved to optimise the desired position. Finally the beam could be aligned by centring it on both QPDs, as shown in Figure 8.6. This procedure has been repeated twice until all three beams were on the same height and parallel with respect to the baseplate's surface, and each had the required propagation axis. The achievable accuracy was restricted by the accuracy of the CQP itself, being of the order of 30  $\mu\text{rad}$  and 4  $\mu\text{m}$ .

### 8.2.2. Alignment of the template

Though both fixed-point components were not used optically, they were still rated as critical. Their position and orientation defined the position and orientation of the template. Typically, a misalignment of the template along the  $X$  and/or  $Y$  direction would cause only an offset, while the components' relative position would be not affected. A rotational misalignment is compensated by the alignment of the input beams with respect to one component bonded with the template. The situation for the hexagonal interferometer is more complex, as wedged components in a polygon configuration were used. Since the input beams were aligned with respect to the optical bench an offset of the components would, as a worst case, lead to the beams not being able to interfere. Hence, it was required to relate the template to the optical bench. As a result, the fixed-point components were adjustably bonded (*cf.* Section 2.3.4). Instead of applying the silicate bonding technique, both components were optically

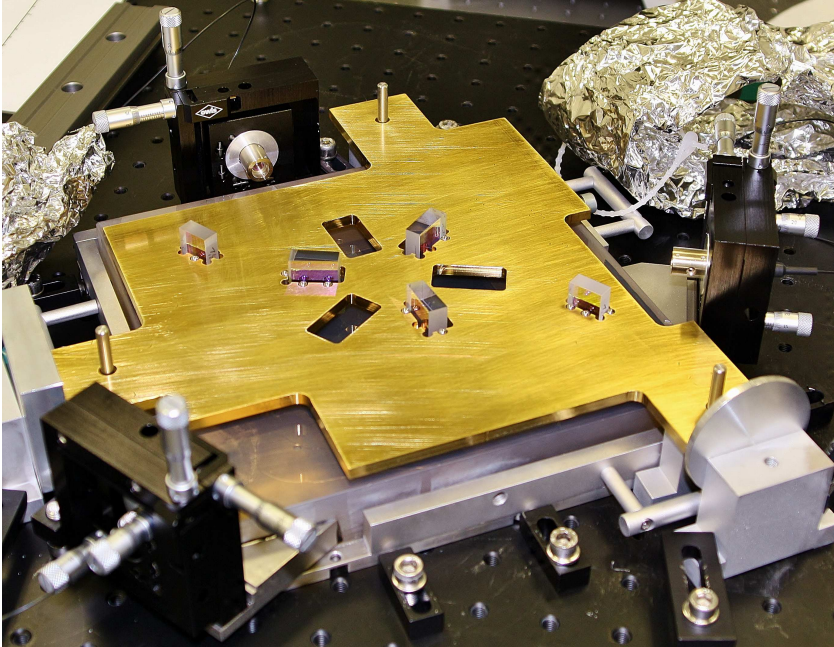


**Figure 8.7.:** Photograph of the template used to position the three beam splitters. During bonding it was mounted slightly above the baseplate and the whole assembly was tilted by an angle of  $5^\circ$ .

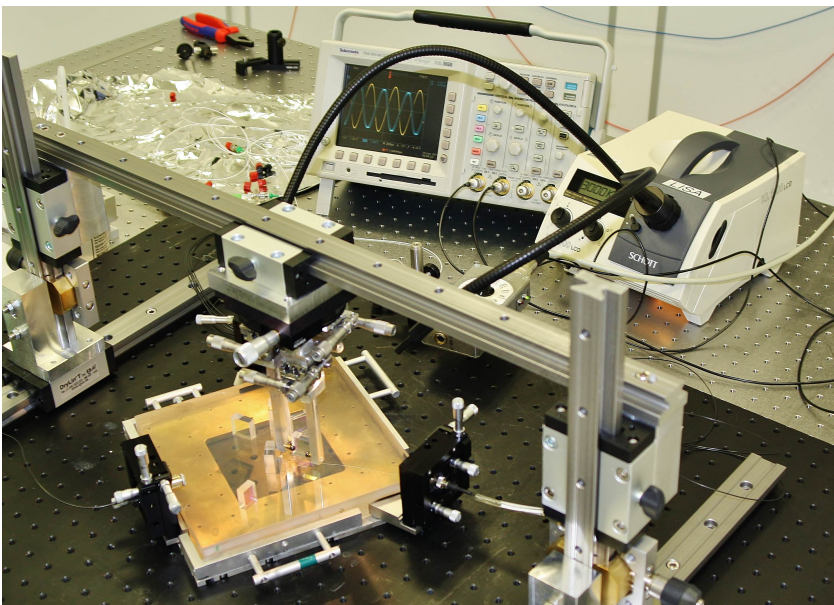


**Figure 8.8.:** Setup for alignment of one beam combiner. Three adjusters were used to align the beam combiner by monitoring the contrast on an oscilloscope.

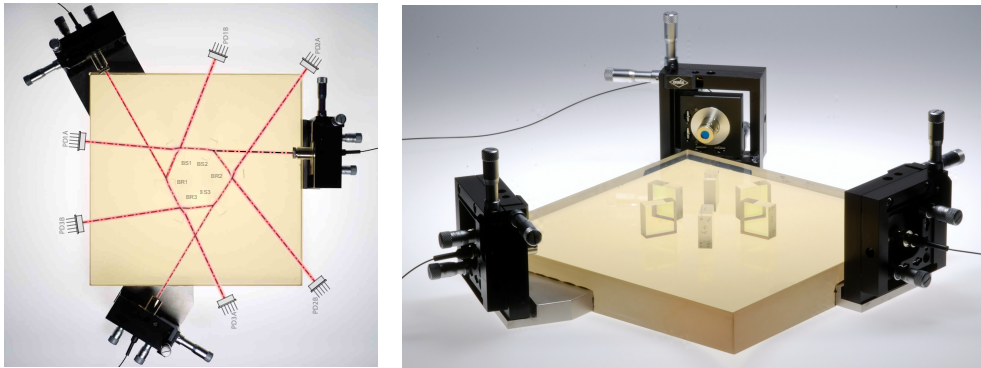


**Figure 8.9.:** Photographs of the hexagonal interferometer bonded. *Left:* Top view of the interferometer with the underlying optical layout. *Right:* Side view of the optical bench.

contacted to the baseplate. This enabled us to remove them after they were not longer needed.

### 8.2.3. Alignment of less critical components

The three beam splitters were classified as less critical in terms of their alignment. A template made of brass, shown in Figure 8.7, was used to define the position of each component. As the template was oriented with respect to the fixed-point component, the beam splitters were aligned relative to the optical bench. The template was mounted slightly above the baseplate. In order to keep the components touching the spheres during manufacturing, the combined assembly of template and baseplate was tilted by an angle of about  $5^\circ$ . A detailed description of such a template bonding procedure is given in Section 2.2. After the three beam splitters had been bonded, the two auxiliary components could be removed from the optical bench.

### 8.2.4. Alignment of the beam combiners

The last stage during manufacturing the interferometer included the alignment of the three beam combiners. As only one optimum position for each beam combiner existed, they had to be aligned by using heterodyne signals. For this purpose, two beams with a frequency difference of 1.623 kHz were injected to each interferometer, consecutively. Using the alignment tool, introduced in Section 2.3.1, each beam combiner was positioned in an iterative procedure by monitoring the contrast on an oscilloscope. A single procedure is shown in Figure 8.8. In order to maintain the possibility for supplementary installation of quasi-monolithic fibre injectors instead of using the commercial off-the-shelf

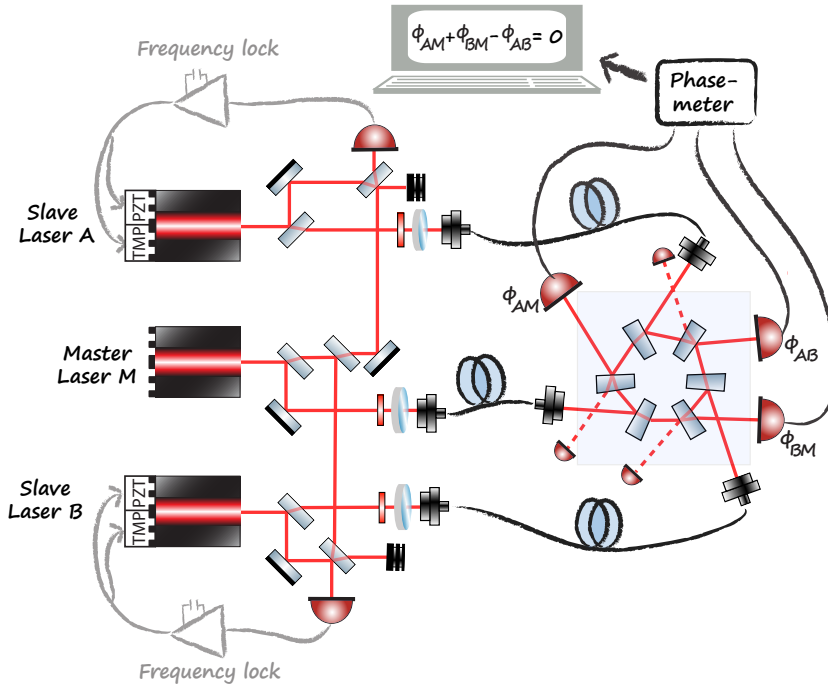


**Figure 8.10.:** Sketch of the experimental setup: Two lasers were frequency locked to the master laser prior to injecting the light into the interferometer. One single element photodiode at each RBS output port detected the longitudinal signal and processed it in the hardware-based phasemeter.

injectors, the three beam combiners were optically contacted onto the baseplate. On the one hand, this technique provides sufficient stability and, on the other hand, the components can be easily removed without damaging the bonding surface. The final interferometer after bonding is shown in Figure 8.9. The contrast obtained for each interferometer was between 80 % and 90 %.

### 8.3. Description of the experimental setup

To begin with, the optical bench as well as the beam preparation were enclosed by a plexiglass box to reduce the influence of air current and temperature fluctuations. Two lasers were frequency locked to a master laser before being injected to the optical bench, as shown in Figure 8.10. Each interferometer output was equipped with one single-element photodiode having a sufficient bandwidth of about 100 MHz. Thus, three optical signals between 3 and 6 MHz were injected into the phasemeter and the output frequencies were used. These frequencies were converted to phase, appropriately added and the residual noise was de-

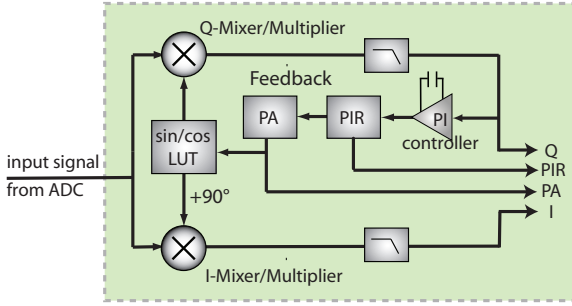


**Figure 8.11:** Schematic of the core of one digital phase-locked loop. (LUT: Look-up-table; PI: proportional Integrator; PIR: phase increment register; PA: phase accumulator)

terminated.

A non-negligible noise source in the experimental setup is time jitter in the sampling process [134]. Ideally, any two successive sampling points in an ADC are equidistant in time. However, in reality these sampling points jitter in time. As a consequence, this deviation in time appears as a fluctuating phase shift. Thus, any time jitter (leading to shifts in time  $\Delta t$ ) translates into phase deviation  $\Delta\phi$ , proportional to the signal frequency, as

$$\Delta\phi = 2\pi f_{\text{het}}\Delta t. \quad (8.3)$$

Using a so-called *pilot tone*, the time jitter can be corrected [130]. The detailed principle is explained in Section 8.3.3. For an ADC jitter correction a pilot tone  $f_{\text{pilot}} = 35 \text{ MHz}$  generated by a function generator has been split into four equivalent signals and fed to an auxiliary board attached to the main phasemeter board. The pilot tones and the interferometric signals were added by means of an operational amplifier.

The following three sections give an overview of the phase measurement system used, the offset frequency lock implemented on an FPGA and the adopted ADC jitter correction.

### 8.3.1. Phase measurement system

The purpose of the PMS is to faithfully extract the phase of the photo current generated in the photodetectors without limiting the sensitivity of the length measurement when adding significant extra noise. For the experiments described in this chapter a LISA-style MHz tracking PMS was used (Xilinx ML605 FPGA with a 4DSP FMC107 ADC card). A prototype has been developed by the AEI phasemeter team and has been made available by Oliver Gerberding. The measurement scheme for the interferometric phase readout chosen for LISA is a digital phase locked loop that tracks the signal frequency and phase. Prior to this the analogue signals were directly digitised at MHz



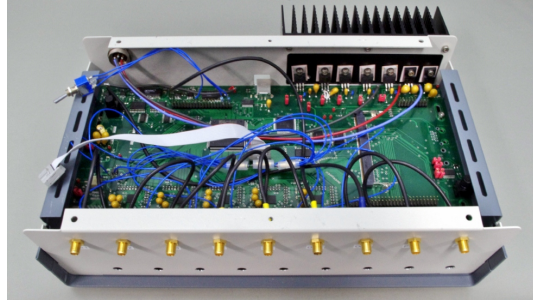


**Figure 8.12:** Photograph of the FPGA-based phasemeter used for the digital frequency lock. Image source: [139].

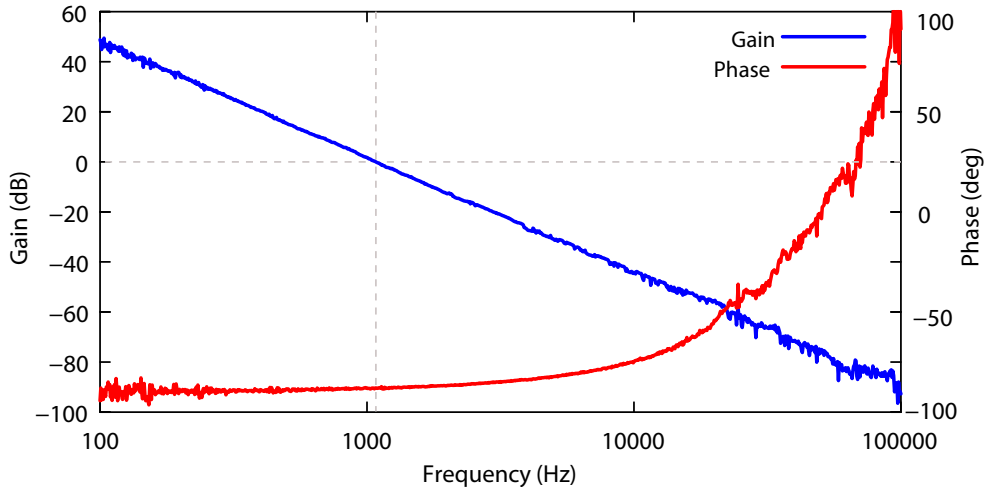
frequencies. Thus, a high bandwidth is achievable [129].

Figure 8.11 shows a schematic of such a phase readout system for one channel. The photodiode signal is converted to a voltage by the transimpedance amplifier and low-pass filtered to prevent aliasing before being digitised by an analogue-to-digital converter (ADC) at 40 MHz sampling frequency. This signal is then multiplied with a sine and cosine signal of correct frequency. The output of the multiplication is on one hand a quadrature (Q) signal, defining the phase difference between input and local oscillator signal, and on the other hand an in-phase (I) signal, being a measure for the amplitude of the beat note signal. The phase difference is used to track the signal's frequency by amplifying it by a proportional-integral (PI) amplifier before a reference frequency is added. The resulting sum is fed to a numerically controlled oscillator (NCO). The NCO is made up of a phase increment register (PIR), a phase accumulator (PA), and a sine lookup table. The feedback signal contains already the desired information about the phase and frequency of the input signal, respectively. The frequency can be obtained by reading out the PIR while the phase information is contained in the PA.

### 8.3.2. Digital offset frequency lock

The underlying principle of an offset frequency lock is to measure the difference in frequency of two lasers, e.g. by a digital PLL, and compare this signal with a reference value. This difference, the error signal, is used to control the frequency of one of the lasers, also referred to as *slave laser*, by using a PI controller.

A digital offset frequency lock has been developed and implemented on an FPGA by Nils Brause, as shown in Figure 8.12. Two laser beams, one of which served as master, have been interfered with each other and the resulting beat note was detected at a photodiode, digitised by an ADC, and fed into an FPGA. The first stage of the frequency control loop contained the DPLL.



**Figure 8.13.:** Measured open loop gain (OLG) of the digital offset frequency locked loop. Data provided by Nils Brause.

The input signal was multiplied by a local NCO at the same frequency as the signal. The output of the multiplier was used to lock the NCO frequency to the incoming signal. This tracking loop operated at 50 MHz sampling frequency  $f_s$ , meaning that the NCO frequency was updated every 0.2 ns. The minimum frequency difference that the PLL can distinguished is defined by its frequency resolution  $f_{\text{res}}$

$$f_{\text{res}} = \frac{f_s}{2^N} = \frac{50 \text{ MHz}}{2^{16}} = 763 \text{ Hz}, \quad (8.4)$$

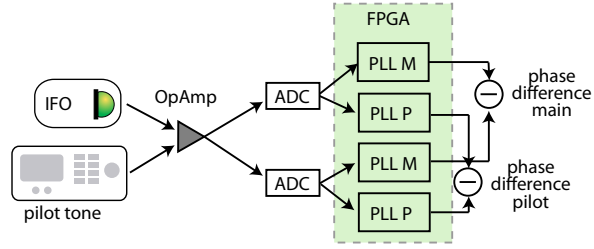
where  $N$  is the bit depth at the PIR.

Ideally, the phase and thus the frequency of the local oscillator and the incoming signal are equal. By reading out the frequency of the NCO one thus knows the frequency of the incoming beat. At the second stage this frequency is compared with a reference value and the difference is fed into a PI controller. Using a DAC, the digitised signal is converted back to an analogue signal and split into two feedback signals of different frequency ranges. One is fed to the piezo via a high-voltage amplifier, leading to length changes in the laser crystal. The other signal is used for the slower laser crystal temperature tuning.

The unity gain bandwidth of that system has been determined to be of the order of 1 kHz. The corresponding open loop gain measured is presented in Figure 8.13. Note that this frequency lock differs from a phase lock in that large and/or fluctuating frequency offsets can be programmed by adding them to the reference frequency (or, equivalently, the frequency error signal).



**Figure 8.14:** Schematic of the setup for an ADC jitter correction by means of a pilot tone generated by a function generator.



### 8.3.3. ADC time jitter noise

Using a pilot tone also referred to as *calibration tone*, the ADC time jitter noise can be corrected. This method has been investigated in both the AEI and Jet Propulsion Laboratory (JPL). Adding an ultra-stable calibration tone at a fixed frequency at the inputs of at least two ADCs, the residual phase noise measured with the PMS can be attributed to ADC time jitter noise. By tracking the interferometric signals and the pilot tones of each ADC output (in the PLL), the phase difference of two pilot tone measurements scaled with an appropriate calibration factor  $f_{\text{het}}/f_p$  can be used to correct the phase difference of the interferometric signals. A schematic of the basic principle is shown in Figure 8.14. The time jitter induced phase errors in two ADCs (denoted by the sub-index 1 and 2, respectively) can be expressed by [130]

$$\begin{aligned}
 \Delta\phi_{\text{meas1}}(f) &= f_{\text{het}} \cdot (\Delta t_s + \tau_1 + \delta\varphi_{m1}), \\
 \Delta\phi_p(f) &= f_p \cdot (\Delta t_s + \tau_1 + \delta\varphi_{p1}), \\
 \Delta\phi_{\text{meas2}}(f) &= f_{\text{het}} \cdot (\Delta t_s + \tau_2 + \delta\varphi_{m2}), \\
 \Delta\phi_p(f) &= f_p \cdot (\Delta t_s + \tau_2 + \delta\varphi_{p2}).
 \end{aligned} \tag{8.5}$$

The sampling interval is denoted by  $\Delta t_s$  and  $\tau$  is the ADC time jitter. The residual timing errors caused by either path length imbalances or cross talk are described by  $\varphi$ . Thus, the phase difference due to time jitter used to correct the signal of interest is

$$\Delta\phi_{\text{cor}} = f_{\text{het}} \cdot (\tau_1 - \tau_2) + f_{\text{het}} \cdot (\delta\varphi_{p1} - \delta\varphi_{p2}). \tag{8.6}$$

In order to correct the measured phase difference between two beat note signals, the phase difference  $\Delta\phi_{\text{cor}}$  is subtracted resulting in a residual phase error of

$$\Delta\phi_{\text{residual}}(f) = f_{\text{het}} \cdot (\delta\varphi_{m1} - \delta\varphi_{m2}) - f_{\text{het}} \cdot (\delta\varphi_{p1} - \delta\varphi_{p2}). \tag{8.7}$$

In this way, the ADC jitter is removed from the measurement of interest.

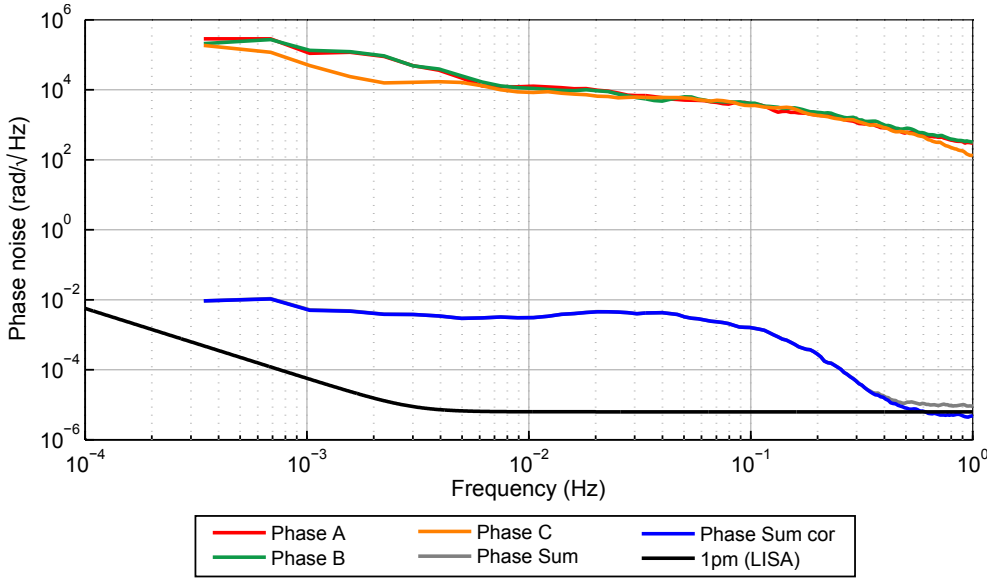
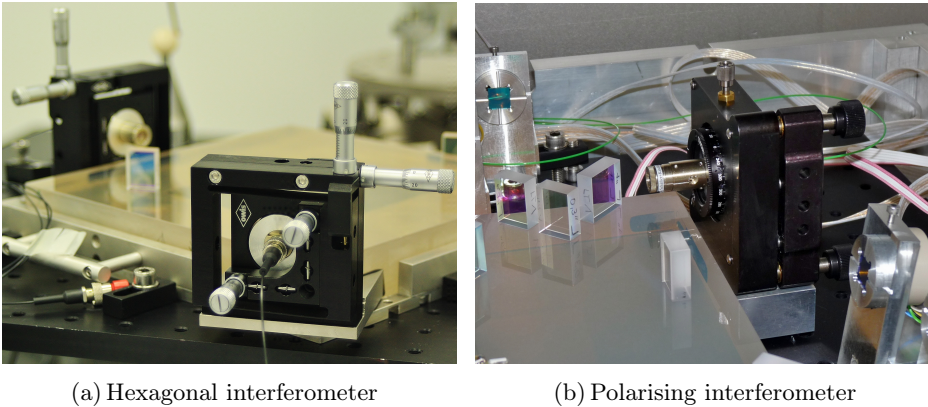


**Figure 8.15.:** Initial performance of the linearity test using three optical signals. A jitter corrections has been adopted leading to improvements around 1 Hz (blue trace).

## 8.4. Noise performance

The initial noise performance is shown in Figure 8.15. By tracking the three input signals with a frequency of approximately 3 MHz, 3 MHz and 6 MHz and combining their corresponding phase measurements, the phase noise performance of the PMS is determined. The resulting phases A, B, and C are plotted in red, green, and orange, respectively. Their appropriate combination (3 MHz + 3 MHz - 6 MHz) is depicted in solid grey. In this first result, the initial measurement in air did not fulfil the requirement. As ADC jitter is a known source of residual phase noise, a correction based on a pilot tone calibration was adopted. For this purpose, a pilot tone at fixed frequency of around 35 MHz was fed into the ADCs and thus the PLLs. By applying the correction algorithm in data post-processing, an improvement for frequencies around 1 Hz was achieved, as shown by the blue trace.

The unsatisfactory noise performance could be caused by cross talk of the beat notes, as two of them had identical frequency. For this reason it is advisable to choose frequencies considerably different, such as  $\sim 4$  MHz,  $\sim 7$  MHz, and  $\sim 11$  MHz. Another significant noise source was the occurrence of cycle slips. Therefore both the phasemeter as well as the offset frequency lock have to be refined. Furthermore, ongoing investigations showed a high potential of residual path length noise due to beam jitter across the wedge. Currently this effect



(a) Hexagonal interferometer

(b) Polarising interferometer

**Figure 8.16.:** Commercial fibre injector assemblies glued to the optical bench for the a) hexagonal interferometer and b) polarising interferometer.

on one length measurement as well as on the combined length measurements of the three interferometer are under research. Further measurements should include a zero measurement, i.e. a differential measurement of an output signal equally split. Thus, a better estimation of the noise source such as differential photodiode noise can be made.

## 8.5. Beam pointing fluctuations

The jitter of the commercial fibre injectors attached to the metal mount (Figure 8.16(a)) has been measured and compared to the beam jitter obtained with the fibre injector assemblies used in the polarising interferometer (Figure 8.16(b)). For this purpose the optical bench was enclosed by a thermal shield and the measurements were conducted in vacuum. Instead of using three laser beams in a LISA-style setup, only two beams in an LTP-based readout were injected to one interferometer. The modulation bench previously used for the polarising experiment (*cf.* Part II) provided two beams with a frequency difference of 1.623 kHz. As the input signal frequencies were in the kHz region, the LTP hardware-based phasemeter PM3 was employed. Both output ports of one interferometer were equipped with QPDs instead of SEPD.

Figure 8.17 shows the comparison of (unscaled) DWS signals obtained in the hexagonal interferometer (red trace) and the polarising interferometer (blue trace). The horizontal DWS signal  $\varphi$  is displayed by a solid trace, whilst the vertical DWS signal  $\eta$  is shown dashed. The two measurements were performed under similar conditions: vacuum of about  $10^{-6}$  mbar and enclosed by a ther-

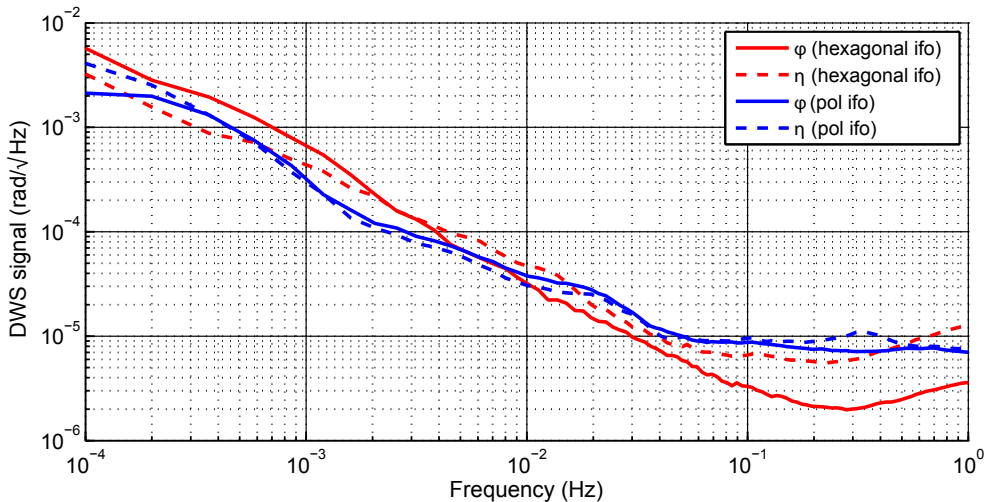


**Figure 8.17.:** Comparison between unscaled differential wave front sensing signals of the hexagonal interferometer (red) and the polarising interferometer (blue). Note that the geometrical angular fluctuations are smaller by the DWS gain factor which is typically a few 1000 rad/rad. In the case of the polarising interferometer this factor is 3800 rad/rad.

mal shield for a few days. As the fibre injector assemblies used in the hexagonal setup contained two different mounts screwed together, a worse jitter behaviour was expected with respect to the one in the polarising interferometer, where a compact and solid mount was installed. However, the unscaled results show no significant difference between the two options. Thus, no advantages or disadvantages of the different types of fibre injector assemblies could be identified at this stage. The next step will include the determination of the DWS coupling coefficient, as described in Section 5.3. This will allow us to give a reliable estimation of the exact influence of angular noise.

## 8.6. Conclusion and Outlook

The phase measurement systems of future space-based laser interferometer such as LISA or GRACE follow-on need to be able to cope with large dynamic ranges of the order of  $10^9$ . Thus, the readout is based on a tracking phase measurement system. Stringent requirements on the noise performance, functionality and linearity are demanded. A part of this thesis was devoted on the linearity tests of phase measurement systems. The underlying principle of such tests is the ability of a linear PMS to combine three phase difference outputs in such a way that the sum is virtually zero.

For this reason an optical bench consisting of three identical and symmetric

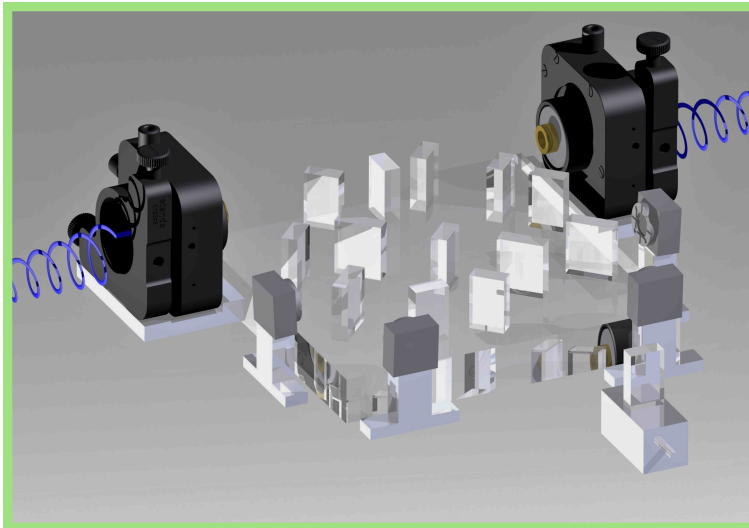
interferometers has been designed and built. In particular, the stray light was previously analysed and minimised. As a consequence, wedged beam splitters were used instead of rectangular ones. A CQP developed and used throughout this thesis has been adopted to align three input beams with respect to the optical bench. The measurement was conducted in air enclosed by a plexiglass box. Two lasers were loosely frequency locked to the master laser. Thus, three interferometric signals with heterodyne frequency of about 3 MHz, 3 MHz, and 6 MHz were read out by the PMS based on a DPLL. The initial noise performance showed no sufficient sensitivity. Reasons for this could be cross talk between the three beat notes as well as the disturbing occurrence of cycle slips in the PMS and the digital frequency lock. In order to enhance the performance various efforts have to be performed. First of all, the functionality of the digital frequency lock has to be investigated and if necessary refined to ensure a cycle slip free operation. In order to reduce fluctuations in the refractive index of air as well as in temperature the measurements need to be conducted in a vacuum environment. As beam jitter presented a problem in the current layout, it is advantageous to use quasi monolithic FIOSs instead of the commercial off-the-shelf fibre injector assemblies. This would reduce the residual phase noise caused by beam jitter coupled via the wedged beam splitter. In addition, such ultra-stable FIOSs will improve the alignment fluctuations.

As the elegant breadboard model of the LISA PM will soon be available at AEI, the ultimate linearity test will be performed. The hexagonal interferometer will be read out by three independent LISA PMs. Several data post-processing techniques of raw ranging and clock noise measurements will be verified. Thus, future investigations aim at testing all key technologies for time-delay interferometry (TDI).



## Part IV

# Ultra-stable interferometers for future geodesy missions







# 9 Joint efforts towards a transponder-type intersatellite laser ranging system

In the next generation of space-based measurements of Earth's gravitational field, laser interferometry is one of the key techniques to achieve higher spatial resolution of the time variable gravity field [140]. Several mission concepts for a follow-on mission of GRACE have been proposed: a transponder-type laser ranging system based on a heterodyne optical phase-locked loop with an accuracy level of some 10's of nanometre [28, 104] or a satellite-to-satellite laser interferometer using a homodyne optical phase locking technique [141, 142]. The latter is a mission proposed in China, called *Space Advanced Gravity Measurements* (SAGM). One of the key laboratories for the ongoing investigations concerning the SAGM is the Center for Gravitational Experiments at the Huazhong University of Science and Technology (HUST) in Wuhan, China. In order to validate their baseline scheme, a prototype heterodyne laser ranging system with a 10 m baseline has been set up. The interferometers consisted of commercial off-the-shelf components set up on a metal breadboard and conducted in vacuum within the cave laboratory, where the vibration of the floor is relative low and the temperature fluctuations are lower than  $0.03^\circ\text{C}/\text{day}$  [143]. Since the homodyne phase locked loop was at this time at a development stage, the second optical bench was replaced by a plain mirror. A total measurement noise of  $100\text{ nm}/\sqrt{\text{Hz}}$  at 100 mHz limited by frequency noise was obtained. By modulating the plain mirror attached to a nanopositioning stage with 5 nm-steps, a resolution of the laser interferometer of about  $3.2 \pm 0.3\text{ nm}$  has been determined.

In order to enhance the sensitivity of such laser ranging systems as well as to ensure space qualification, the interferometer needs to be thermally and

mechanically stable. Thus, joining technologies with high dimensional stability and a highly stable bond are required. One way to join optical components with its baseplate is adhesive bonding [144]. Although this technique does not belong to the most widely used for space applications, it has been proven recently to be principally suitable for space based metrology systems. Another possibility for building quasi-monolithic interferometers is to use the hydroxide-catalysis bonding technique (*cf.* Section 2.1). This technique has already been demonstrated to be compatible for space application [37] and performance for low-frequency measurements e.g. in the LISA measurement band [68].

The Center for Gravitational Experiments at the HUST has adopted this technique in their laboratories within the framework of this thesis. For this purpose, two heterodyne Mach-Zehnder interferometers were combined on an ultra-stable glass-ceramic baseplate. Initially, this prototype has been used to calibrate instruments with the capability of driving tiny displacements, such as nanopositioning stages and high resolution capacitive transducers with high accuracy. In the near future an optical bench sensing displacements over 10 m

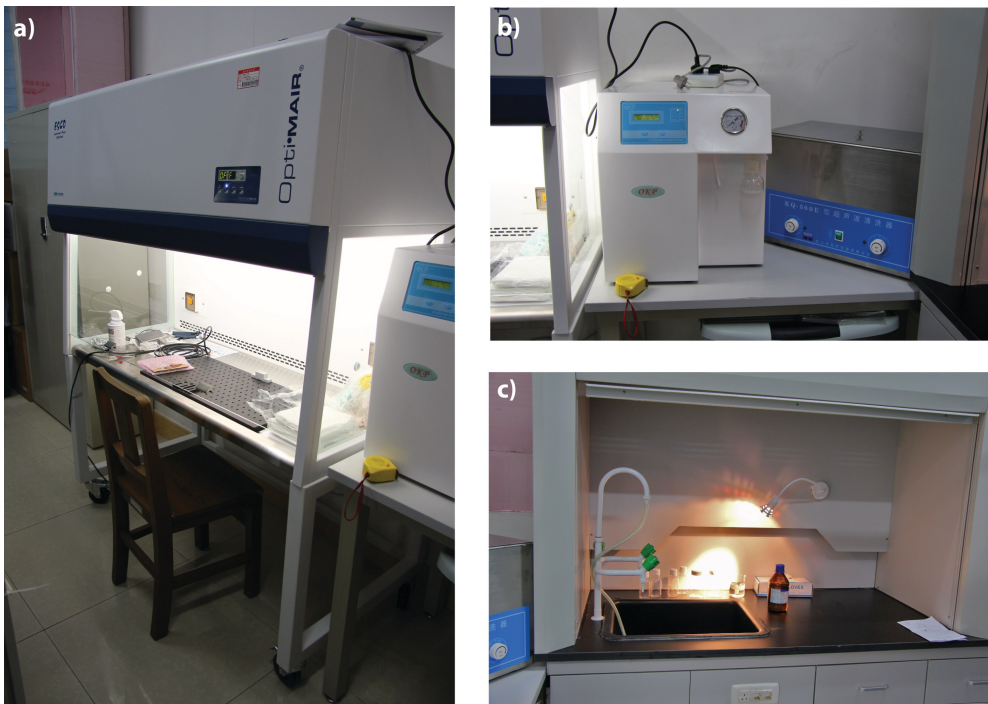


**Figure 9.1.:** Working environment: a) Flow box where the bonding was carried out b) Ultra-pure water purification systems (left) and ultra-sonic bath (right) to clean the equipment and to de-bond a component from the baseplate in case of a misalignment c) Washing basin for cleaning the substrates before each bonding process.

will be bonded. The setup will be implemented in the 10 m-prototype of the cave laboratory of the HUST to improve the currently reached sensitivity published in [142].

During my two stays in Wuhan of one week in 2009 and six weeks in 2011, the basis of building ultra-stable optical systems at HUST has been established. My contribution consisted in assisting the students in the installation of the required laboratory facilities and in construction of the first quasi-monolithic optical bench.

## 9.1. Laboratory facilities

In order to ensure a successful construction of a monolithic interferometer several arrangements had to be made beforehand. The delicate bonding procedure has to be conducted in a clean environment, optimally in a clean room better than class 1000. Therefore, the air quality in the laboratory has been improved by a laminar flow cabinet (ESCO OptiMair<sup>TM</sup>, ACB-4A1), which can be seen in Figure 9.1 a. It is providing an ISO Class 4 air cleanliness within its work zone as per ISO 14644.1 [145]. Furthermore, it was necessary to clean the components and the baseplate before bringing them into contact (*cf.* Section 2.1). For this purpose a water purification system (OKP-TX, Shanghai Laikie Instrument Co.) provided the required ultra pure water, as shown in Figure 9.1 b. In addition, a washing basin was installed close to the flow box (see Figure 9.1 c).

In case a dismounting of a recently bonded component becomes necessary, one can use an ultrasonic bath. The glass assembly should be placed for 30 minutes or longer in a detergent solution [34]. If the bonding process has not started yet it might be possible to add immediately  $\text{OH}^-$  ions to stop this process. Depending on the quality and size of the bond the damaging of the surface increases with the settling time of the bond.

## 9.2. The quasi-monolithic interferometer design

For calibration of a steering mirror, a test bench consisting of two heterodyne Mach-Zehnder interferometers has been designed, as depicted in Figure 9.2. The layout has been designed by me with the software IfoCad and visualised with OptoCad.

The interferometers can be described as follows:

- 1) The *reference interferometer* with almost equal arm lengths is detecting disturbances common to both interferometers that are external to the op-

tical bench and couple in the measurement. Thus, these common-mode fluctuations can be subtracted from the length measurement interferometer.

- 2) The *science interferometer* measured the induced position fluctuations of a mirror  $M_{\text{far}}$  mounted on a piezoelectric element using non-polarising elements with respect to a local stable mirror M22. The informations gained are used to calibrate such piezoelectric devices.

Additionally to the optical components belonging to the two interferometers four components have been added. Mirror  $M_{\text{align}}$  serves as reference for aligning the two beams parallel to the optical bench, whilst the three components TF1, TF2 and TF3 were not used optically. They defined the reference points for the template on the optical bench.

Since transmission through the optical components causes path length changes, the number of transmissions for all optical paths on the optical bench had been designed to be equal.

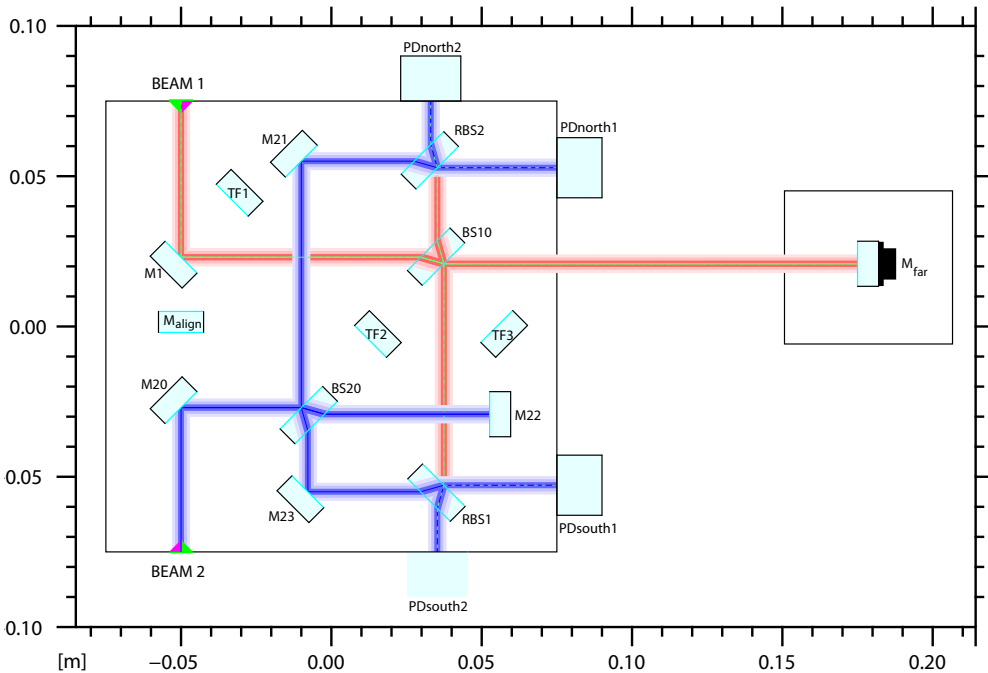


**Figure 9.2.:** OptoCad model of the laser interferometer for a calibration scheme of a far mirror mounted on a piezoelectric element.

## Properties of the optical components used

The 150 mm square baseplate is made of JGS1, a material with very low linear coefficient of thermal expansion of  $0.5 \times 10^{-6} \text{ K}^{-1}$  at room temperature [146]. This material is equivalent to Suprasil<sup>®</sup> 1 and 2 from Heraeus<sup>®</sup>. The top surface was polished to an optical surface quality of  $\lambda/8$  where  $\lambda = 633 \text{ nm}$ . Its height of 2 cm is sufficient to reduce the risk of a bending of the optical bench.

The optical components were made of fused silica, in particular JGS1, and likewise polished flat to  $\lambda/8$  over the bottom surface. These mirrors and beam splitters had a dimension of  $15 \times 25 \times 7 \text{ mm}^3$  and  $20 \times 25 \times 7 \text{ mm}^3$ , respectively. All secondary surfaces were provided with an anti-reflection coating to limit stray light and reduce stress caused by the coating of the main optical surface.

Since the components could be aligned only along the surface of the optical bench, the vertical degrees of freedom were predetermined by the components and baseplate surface. Therefore an accurate machining of the components was required. The perpendicularity of the optical surface to the bottom surface was specified for these components to be better than 5 arcseconds.

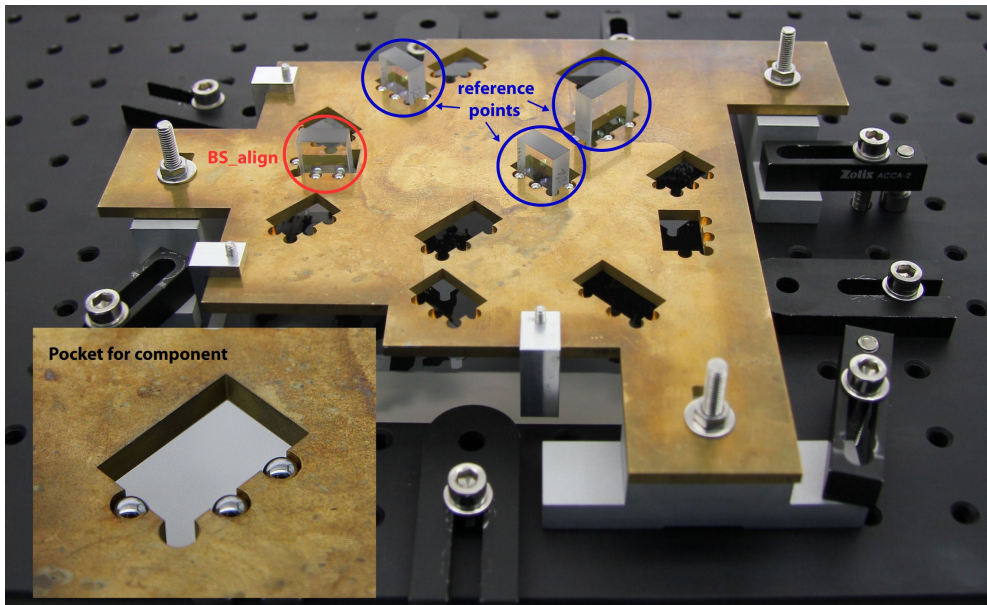


**Figure 9.3.:** Template for the components alignment. A blue circle marks the components that were finally used as reference components. The red circle marks the component used for aligning the two input beams. *Enclosed picture:* pocket with its three spheres for one component.



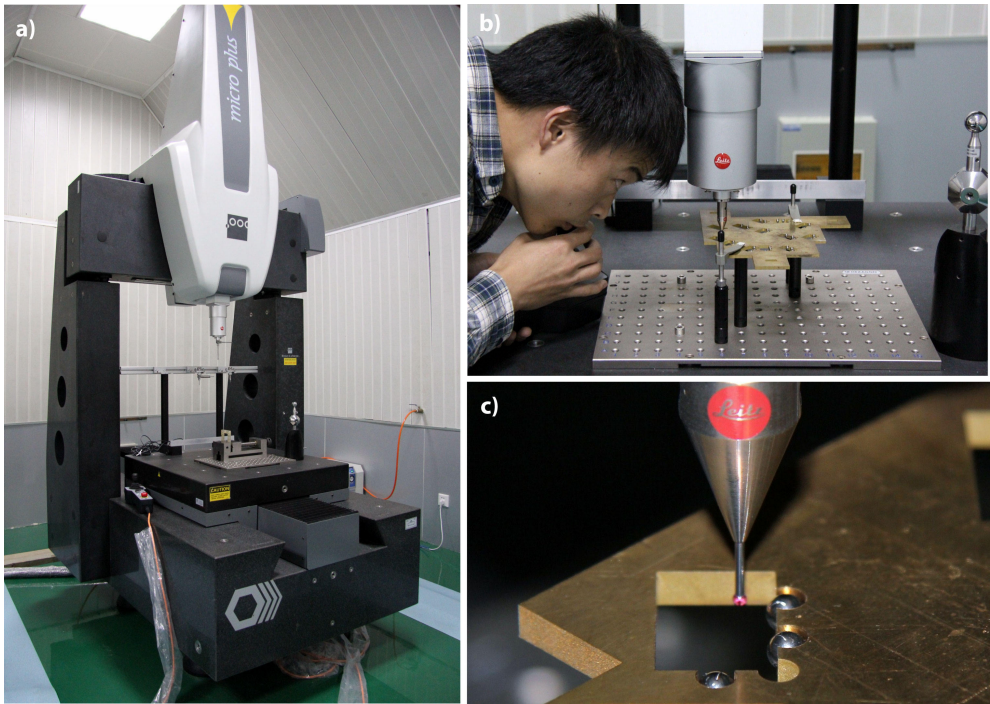


**Figure 9.4.:** a) Coordinate measurement machine b) Assembly for measuring the machining accuracy of the template c) Probe is measuring the three spheres of one pocket.

### 9.3. Manufacturing process

The interferometers were combined on the low-expansion baseplate made of JGS1 by applying the hydroxide-catalysis bonding technique [34]. Since the alignment of a component during bonding is restricted and a realignment after the bond has settled is impossible, a precise positioning procedure was required. Therefore it has been decided to adopt the template bonding technique (*cf.* Section 2.2) for all non-critical components and the technique of adjuster aided bonding to heterodyne signals (*cf.* Section 2.3.5) for the two beam combiners. The bonding solution used for all optical components had a 1:6 ratio of an aqueous sodium silicate solution to deionised water and was filtered with a 0.2  $\mu\text{m}$  pore size filter.

#### 9.3.1. Alignment of non-critical components

In order to place the optical components on the baseplate, a template made of copper was used, as shown in Figure 9.3. The machining accuracy was specified by the manufacturer to be less than 20  $\mu\text{m}$ . Before starting the bonding procedure this has been verified. Using a coordinate measuring machine (*Micro*

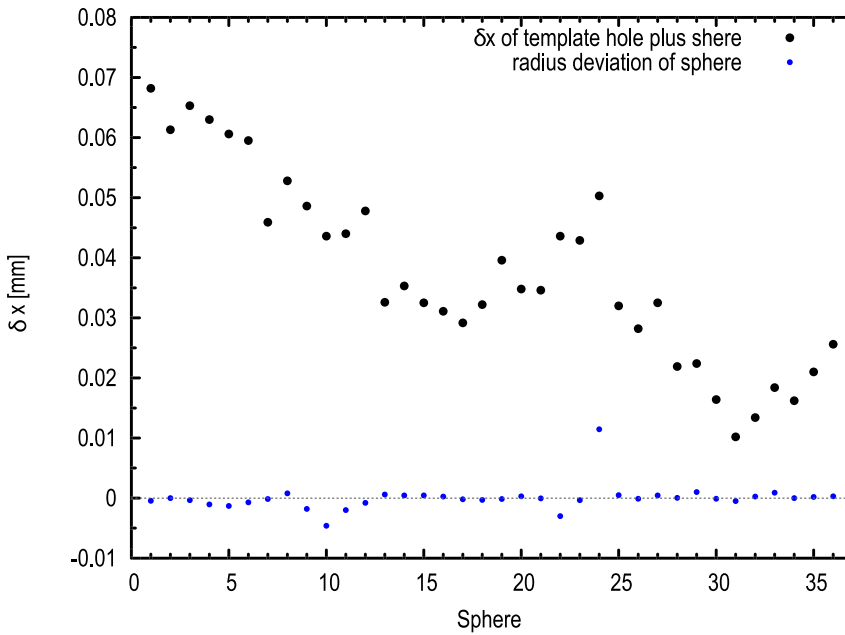


Figure 9.5.: Position deviation in  $x$  direction and radius error of each used sphere.

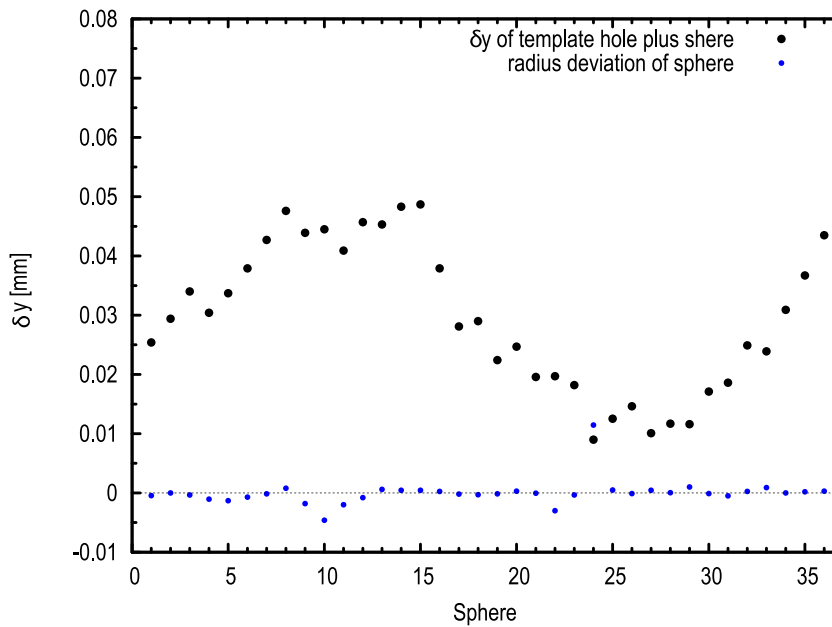
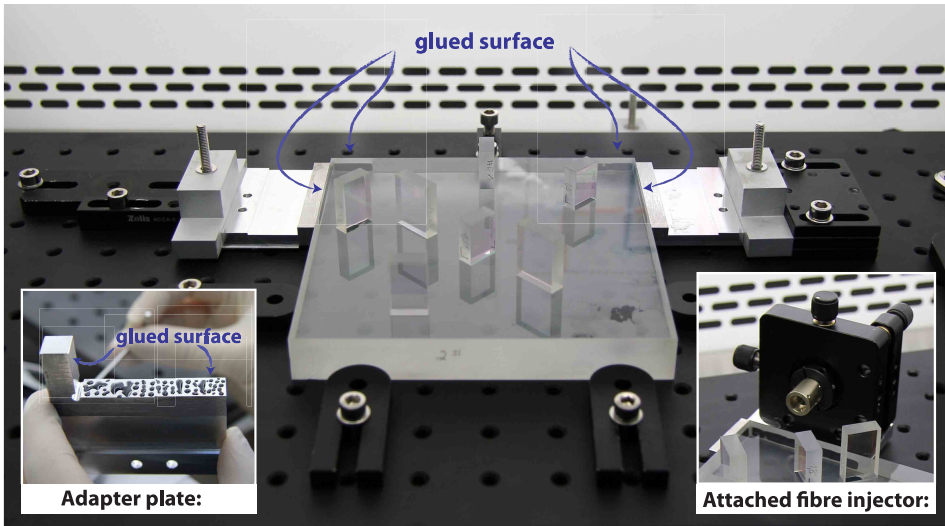


Figure 9.6.: Position deviation in  $y$  direction and radius error of each used sphere.



**Figure 9.7.:** Assembly of the optical bench with its two adapter plates during the glueing process. Picture in the left corner shows one adapter plate with its glue dots whilst the picture in the right corner shows the final attachment of one fibre injector to the baseplate.

*Plus 060806*, Hexagon Metrology), as depicted in Figure 9.4 a, the dimensions of the template with its associated reference spheres were measured. For this purpose, all spheres were placed in the holes, as shown in Figure 9.4 b, and their position with respect to the template's origin was measured. This is reflected in Figure 9.4 c. The length measuring uncertainty of the CMM used is specified to be  $0.9 \mu\text{m} + L[\text{mm}]/400$ . The results of these measurements are illustrated in Figures 9.5 and 9.6. The determined positions have been compared to the nominal values, which were obtained with IfoCad. One can see with black dots the  $x$  deviation  $\delta x$  and  $y$  deviation  $\delta y$  of each sphere's centre. To show the imperfection of the spheres the deviation of the assumed radius is plotted with blue dots. One can see that in the measurements a systematic error is present. One reason could be an imperfect calibration of the coordinate measurement machine. But in that case one would expect a constant offset (bias) and not a sinusoidal curve as is the case for  $\delta y$ . It could also be possible that the temperature changes over the whole measurement period ( $\sim$  few hours) affected the calibration. A temperature controller consisting of thermometers connected to the CMM would compensate for changes in temperature. Nevertheless, the verification demonstrated that the machining accuracy is clearly below  $100 \mu\text{m}$ . This is sufficient for our purpose. However, for a confirmation of the machining specifications the measurements need to be rerun.

During the bonding procedure the baseplate was tilted by an angle of 8 degrees



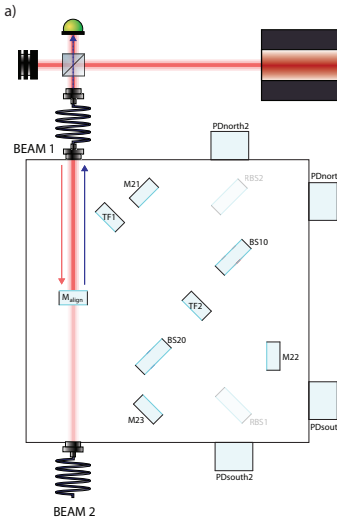


**Figure 9.8.:** Aligning the first input beam parallel to the bench's surface using a reflected beam.

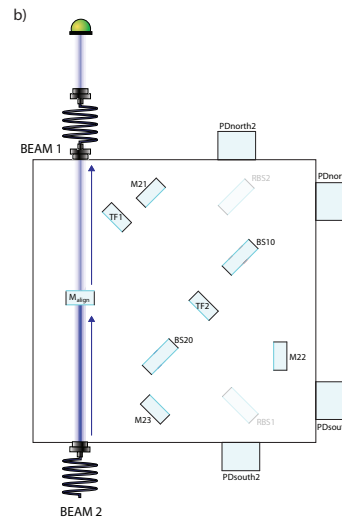


**Figure 9.9.:** Aligning the second input beam to the identical orientation and height as the first beam.

in order to keep the components being bonded in contact with the spheres. Due to gravity the component slides down until it rests against the spheres and thus has a well defined position. After applying the bonding solution the template was left in place for at least two hours until the components had settled and the bond had started to harden. This procedure has been repeated until all non-critical components had been bonded.

### 9.3.2. Alignment of critical components

The most critical alignment processes are aligning the two fibre injectors of the input beams and the two recombination beam splitters (RBS1 and RBS2). In the following these two procedures will be discussed.

#### *Input beam alignment:*

For the alignment of the fibre injectors (*60FC-4-A11-03*, Schäfter + Kirchhoff), a commercial mount with four degrees of freedom was used: tip, tilt and two translational stages. This mount has a  $2^\circ$  control of the pitch/yaw angles and a  $\pm 1.5$  mm dynamical range for the  $X/Y$  translation. The alignment actuators are fine-thread screws. A compact mount with a dimension of 6 cm (without the side screw) from a Chinese manufacturer (*OM-TZ-104-N*, CNeasy) was chosen. In order to place the mount on the intended position special adapter plates made of Invar<sup>®</sup> were designed to which finally the mount including fibre collimator were screwed. They defined the centre position of the mounts with

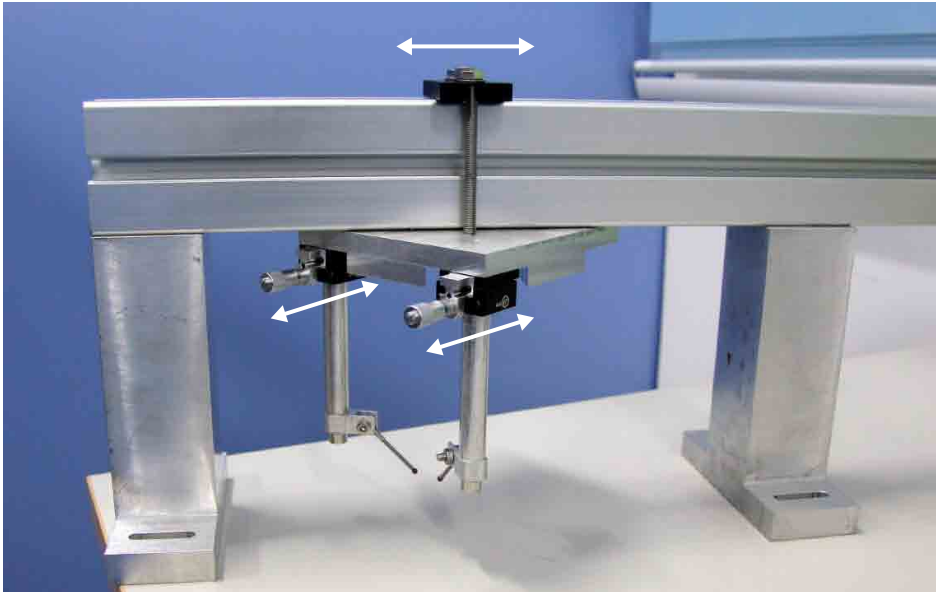


**Figure 9.10.:** Assembly of the *alignment tool*: One stable bridge with movable console. The main part consists of two translation stages where fingers terminated with small spheres are attached. The overall material is aluminium.

a machining accuracy of  $100\ \mu\text{m}$  plus a screwing accuracy of  $150\ \mu\text{m}$ . Finally, the construction of these two fibre collimators and mounts were glued with an epoxy resin (*ER 2188*, Electrotube) to the optical bench to achieve a solid connection. This process is shown in Figure 9.7.

To begin with, the polarisation state of the two beams were adjusted. The desired polarisation state was perpendicular to the plane of incidence (s-polarised). In addition, the lenses of the fibre collimators were roughly adjusted to be collimating by monitoring the beam width along the beam with a viewer card. In the next step both input beams were aligned parallel with respect to the optical bench. For this purpose component  $M_{\text{align}}$  served as reference. The reflected part of the first input beam has been coupled back to the fibre injector, as shown in Figure 9.8. Thus, the parallelism of the first beam relative to the plane of the bench to a level of the mirror's perpendicularity of less than 5 arcseconds is ensured. By coupling the transmitted part of the second input beam into the first fibre coupler, this beam has been aligned to be parallel with identical height to the first beam, as depicted in Figure 9.9. For a detailed description of the alignment procedure the reader is kindly referred to Section 4.5.

The components M10 and M20 (*cf.* Figure 9.2) were bonded subsequently to redirect the beams to the initial direction of the input beams.

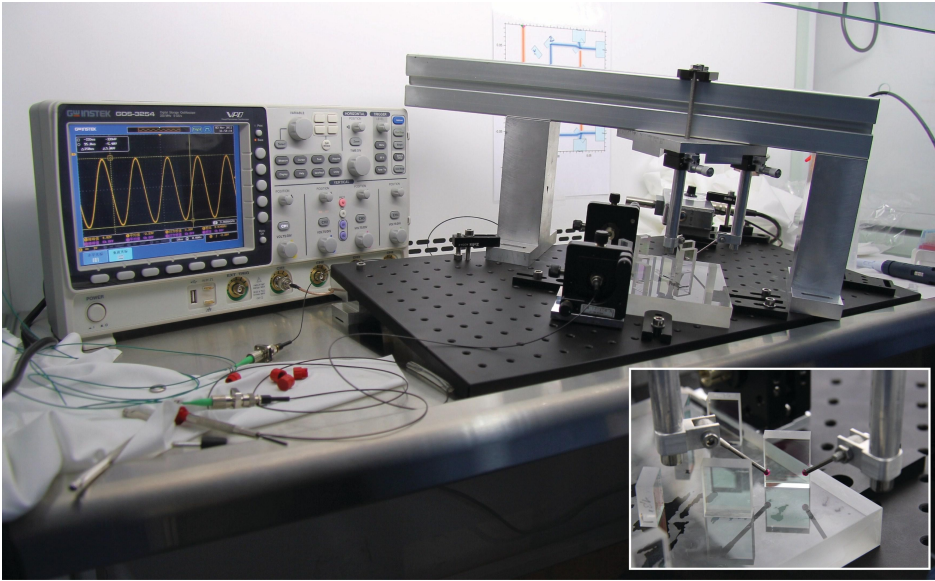


**Figure 9.11.:** Construction of the interferometer during the alignment of RBS2. The enclosed picture shows the recombining with the alignment tool fingers.

*Recombination beam splitter alignment:*

The two beam combiners had to be aligned during the bonding process by maximising the interferometric contrast. Two beams with a heterodyne frequency of 10 kHz were injected onto the optical bench. In order to align the recombiner quickly and accurately a special tool has been set up, which is shown in Figure 9.10. With this tool it was possible to align one lateral and one angular degree of freedom. The tool was composed of one stable bridge with a movable console where the main part was mounted. This part consists of two micrometer translation stages (*GCM-125001ASM*, CDHC) with mechanical fingers attached to them. These two fingers were terminated with spheres.

For the precise alignment a buffer solution was used to allow adjustment until achieving maximum contrast. As a buffer liquid n-Octane ( $C_8H_{18}$ ) was used. Once the optimum position was found the real bonding solution was applied in a scale of 0.6 micro litre per  $cm^2$ . The adopted technique of adjuster aided bonding to heterodyne signals is described in detail in Section 2.3.5. To conclude the alignment of the first recombiner RBS2 both fibre injectors were optimised and the lenses were adjusted such that the two different beam waists match each other. From then on the fibre injectors were completely defined and were depending on RBS2. Any change would have caused a loss in contrast of the corresponding reference interferometer. Figure 9.11 shows the setup used for

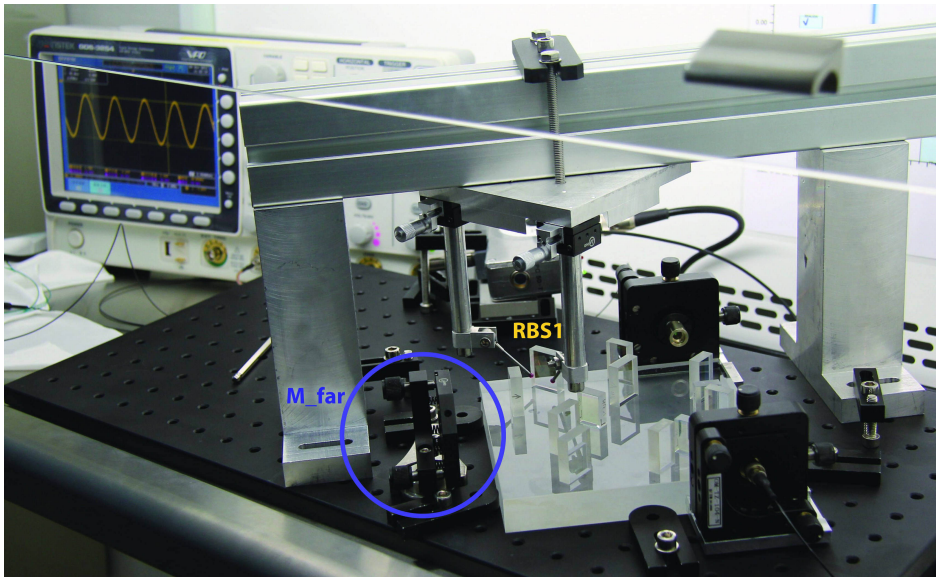


**Figure 9.12.:** Construction of the two interferometers while aligning the final recombiner RBS1. The necessary "far" mirror is set up on a commercial off-the-shelf kinematic mount and used for aligning the recombination beam splitter temporary.

aligning RBS2. One can see the optical bench under the bonding tool placed in its clean environment. On the left side the achieved contrast of  $\sim 90\%$  is displayed on an oscilloscope. The enclosed picture in the right corner shows the recombination beam splitter with the two adjusters.

In order to bond the second recombiner RBS1 the  $0^\circ$  mirror  $M_{\text{far}}$  has to be set up. Therefore, the mirror was mounted on a commercial kinematic mount with two rotational degrees of freedom: pitch and yaw. To align the mirror perpendicular to the first beam the same setup as was used as for aligning the fibre injectors. The beam was coupled back through the fibre injector while the received power was monitored by a sensitive power meter. After cleaning the bench and the optical component the adjuster aided bonding to heterodyne signals was applied. Before finally bonding the recombiner one had to control the contrast of the previously bonded interferometer. Due to the adjustability of the fibre injector mounts it was possible that they had become misaligned during the cleaning process. If necessary they had to be adjusted with respect to the reference interferometer. Afterwards the recombiner can be brought into contact with the optical bench. It was decided not to apply the hydroxide-catalysis bonding technique for the second beam combiner RBS1, but rather to optically contact ([31], [30]) this component onto the bench. The main reason for this was to teach the students how to optically contact a component.

One advantage of this technique is the possibility to remove the component if necessary. In contrast to de-bonding a component the surface of the contacted area shows no appreciable damage after dismounting the component. Figure 9.12 shows the assembly with the optically contacted RBS1 and the mounted  $0^\circ$  mirror  $M_{\text{far}}$  (circled in blue). On the oscilloscope the achieved contrast of 77 % is visible.

## 9.4. Characterisation of the optical bench

The positioning accuracy of the components was determined by measuring their position with a CMM. Due to imperfections of the components dimensions, each component was defined by only one corner point and its angle with respect to one arbitrary component on the optical bench. The calculated position errors as well as angular deviations are listed in Table 9.1. Note that they are specified with respect to the plain mirror M22. The obtained position accuracy was on average  $40 \mu\text{m}$ . However, the specification of interest was the angular deviation from the nominal angle of each component. The measured deviation from the desired orientation is in average  $400 \mu\text{rad}$ , where the beam combiners are not taken into account.

The contrast of the two interferometers was maximised by optimising the input polarisation, adjusting the couplers and by matching the power of the two input beams. The contrast achieved in the reference interferometer was 90 % and 77 % in the length measurement interferometer.

**Table 9.1.:** Accuracy characterisation of the bonded optical bench: deviation from the nominal position of the corner  $\Delta x/\Delta y$  and angular error.

Component	$\Delta x [\mu\text{m}]$	$\Delta y [\mu\text{m}]$	Angular deviation
MS10	41	59.5	3'50"
MS20	23	56.6	59"
BS10	45.9	43.7	42"
BS20	28.7	39.3	27"
M21	48	61.2	3'29"
M23	1.66	70.4	1'12"
TF1	48.7	41.6	1'6"
TF2	37.9	10.6	5"
$M_{\text{align}}$	36.6	52.7	17"
RBS1	-332.3	-275.1	2'41"
RBS2	1262.1	1257.8	6'3"

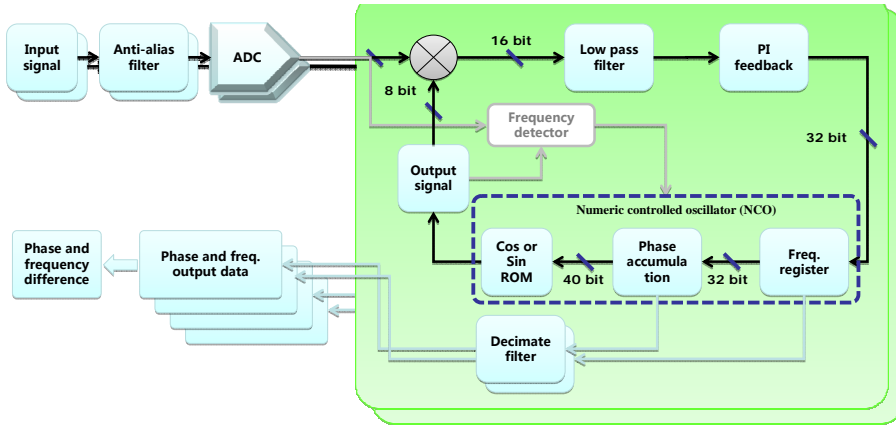


**Figure 9.13.:** Block diagram showing the FPGA-based phasemeter. Image courtesy of HUST.

## 9.5. Description of the experimental setup

In order to perform the picometre positioning control experiment, a piezo from NEC/TOKIN Co. Ltd. attached to the mirror  $M_{\text{far}}$  served as the positioning actuator. Since piezoelectric actuators exhibit an inherent hysteresis non-linearity as shown in Figure 9.14, the precision of open-loop positioning control is limited [147]. In order to reduce the positioning error induced, a heterodyne laser interferometer was used to perform a tracking control in a closed-loop system [148]. The heterodyne frequency was about 1 MHz and generated by a dual frequency source from Polytec (*DFE-A4 Series*). Using a FPGA-based phasemeter designed by Liang Yurong, the displacement of the actuated mirror

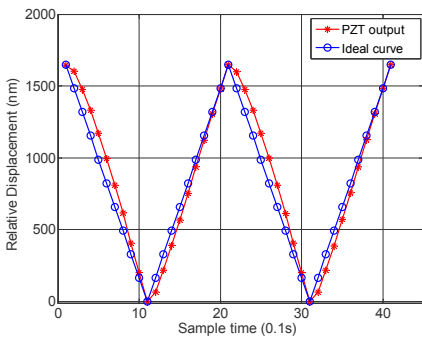


**Figure 9.14.:** The red trace shows the real displacement of the PZT, whilst the blue trace represents the ideal curve without hysteresis. Source: HUST.

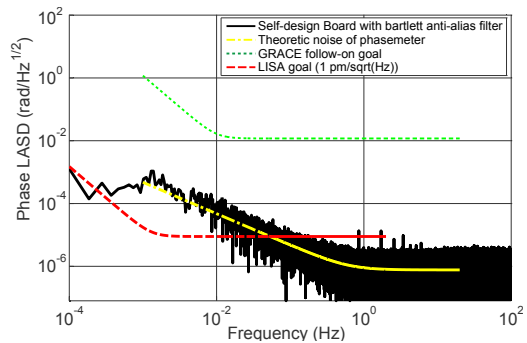


**Figure 9.15.:** Noise performance of the phasemeter used. The phasemeter has been designed and its performance has been measured by Liang Yurong at HUST.



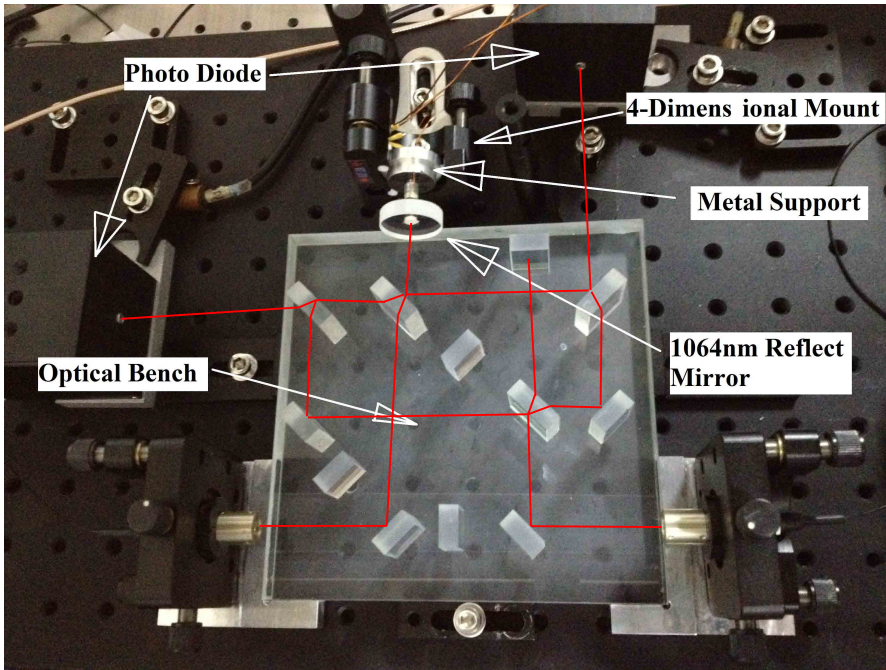


**Figure 9.16.:** Picture of the picometre positioning control system implemented in the laboratories of the Center for Gravitational Experiments. Image courtesy of HUST.

$M_{\text{far}}$  was measured. The hardware-based phasemeter was read out with a PC via a parallel port. The basic principle of this phase measurement system is similar to the prototype LISA phasemeter described in [100]. The beat note signal is passed through an anti-aliasing filter, digitised at 50 MHz by an ADC and then fed into the FPGA. The digitised signal is then multiplied by a sinusoidal signal generated by the local numerically controlled oscillator (NCO) at the same frequency as the signal. The phase difference is then fed in the controller for synchronizing the phase between local oscillator and input beat note signal. This principle is sketched in the block diagram in Figure 9.13. The obtained performance of the phasemeter is shown in Figure 9.15.

The determined displacement was compared with the desired target position to obtain the positioning error. This residual error was sent to a proportional-integral-derivative (PID) controller, programmed in LabVIEW, to compute the additional control output voltage. This voltage was added to the total control voltage and sent to the piezo via a data acquisition card (*NI-PCI-6221*). Thus, the piezo actuator moved the mirror to the target position. The experimental setup is shown in Figure 9.16.

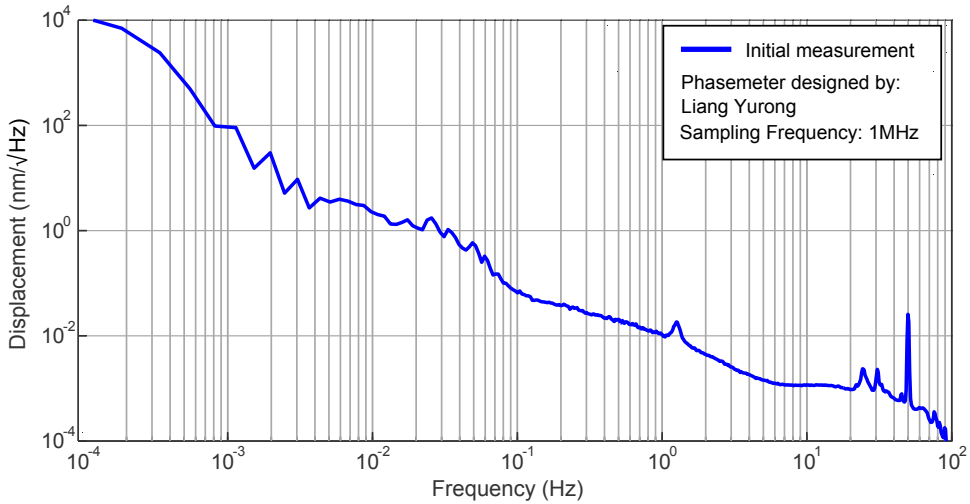


**Figure 9.17.:** Displacement noise of the measurement interferometer obtained at the laboratory of the Center for Gravitational Experiments. Image courtesy of HUST.

## 9.6. Initial noise performance

In order to assess the ability of the system to measure tiny displacements, the noise level of the interferometer without inducing displacements have been measured<sup>[1]</sup>. Hence, the piezo-actuated mirror  $M_{\text{far}}$  has been kept stable in a constant position, whilst measurements have been performed. Figure 9.17 shows the obtained displacement noise of the measurement interferometer where the reference phase was subtracted. Thus it appears that the ability of measuring displacements is about  $10 \text{ pm}/\sqrt{\text{Hz}}$  at 1 Hz increasing with  $1/f$  towards lower frequencies. Since the measurement was not conducted in vacuum, the limiting noise source can be attributed to thermal and air fluctuations influencing mainly the metal fibre injectors. Another dominant noise source is frequency noise. For instance, a typical frequency stability of the used laser diode-pumped monolithic Nd:YAG laser (*Innolight Mephisto*) is about  $1 \text{ kHz}/\sqrt{\text{Hz}}$  @ 1 Hz increasing with  $1/f$  towards lower frequencies. Assuming an arm length mismatch of 3 cm, a path length noise of about  $1 \text{ pm}/\sqrt{\text{Hz}}$  @ 1 Hz can be estimated, increasing in the same manner with  $1/f$  towards lower frequencies.

After verifying a sub-nanometre length readout, the actual experiment could be conducted. For this purpose the plain mirror  $M_{\text{far}}$  was driven by a nanopositioning stage from NEC/TOKIN Co. Ltd., operating under closed-loop positioning control. The step size was defined to be about 50 pm. Figure 9.18

<sup>[1]</sup>The measurements described in this Section were conducted by the students Duan Huizong and Liang Yurong.



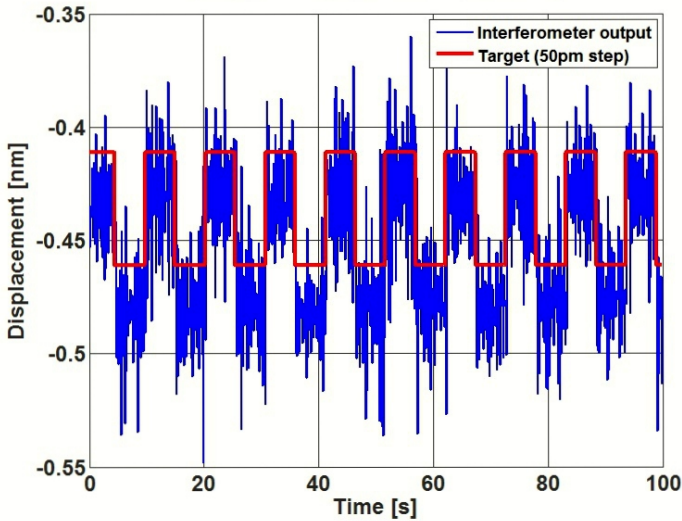


**Figure 9.18.:** Comparison of the displacement measured with the bonded interferometer and the desired displacement of the target for 50 pm step motion of the nanopositioning stage. Image courtesy of HUST.

shows the initial results. The red line represents the desired target position and the blue line represents the measured position with the interferometer. It could be demonstrated that a tracking accuracy of better than 50 pm is feasible with this setup. Further experiments are under progress.

## 9.7. Conclusion

A clean environment was set up to establish the silicon bonding technique at the Huazhong University of Science and Technology. In doing so, an optical bench containing two interferometers was set up on an ultra-stable glass ceramic base-plate. A contrast for the reference interferometer of 90 % has been achieved, and a contrast of 77 % for the science interferometer was obtained. Noise performances conducted by the students Duan Huizong and Yurong Liang revealed a displacement noise of the measurement interferometer on the order of  $10 \text{ pm}/\sqrt{\text{Hz}}$  at 1 Hz increasing with  $1/f$  towards lower frequencies. The noise performance was limited by frequency noise as well as thermal instabilities. By stepping the piezo-actuated reference mirror  $M_{\text{far}}$  with a step size of 50 pm, the desired and as measured displacement were compared. A resolution better than 50 pm has been verified.

One significant noise source in the current setup is the back reflection of the two flat mirrors. On the one hand, both beams are coupled back through the

fibre to the optical bench and cause laser intensity noise, if not eliminated by a Faraday isolator. On the other hand, a small fraction of the ghost beams is reflected from the fibre injectors and induces cavity effects. This leads to a reduction of the interferometer sensitivity. To eliminate these noise sources, the next design needs to implement some minor modifications. For instance, polarising optics could be used for redirecting beams. In Figure 9.19 such an alternative design is illustrated.

The two beam splitters BS10 and BS20 are replaced by polarising beam splitters (PBS). To control the beam direction on the optical bench a half-wave and a quarter-wave plate are used. With the first half-wave plate one can ensure that the beam is s-polarised and thus will be transmitted at the PBS. Passing twice through the second quarter-wave plate the polarisation is changed to be parallel, such that the beam is reflected at the PBS. To suppress ghost reflections at the wave plates both should be tilted by a small angle. Additionally to the existing interferometers, two output ports for an active amplitude stabilisation are optional. For this purpose two beam splitters are located directly after the fibre out coupler in both beam paths.

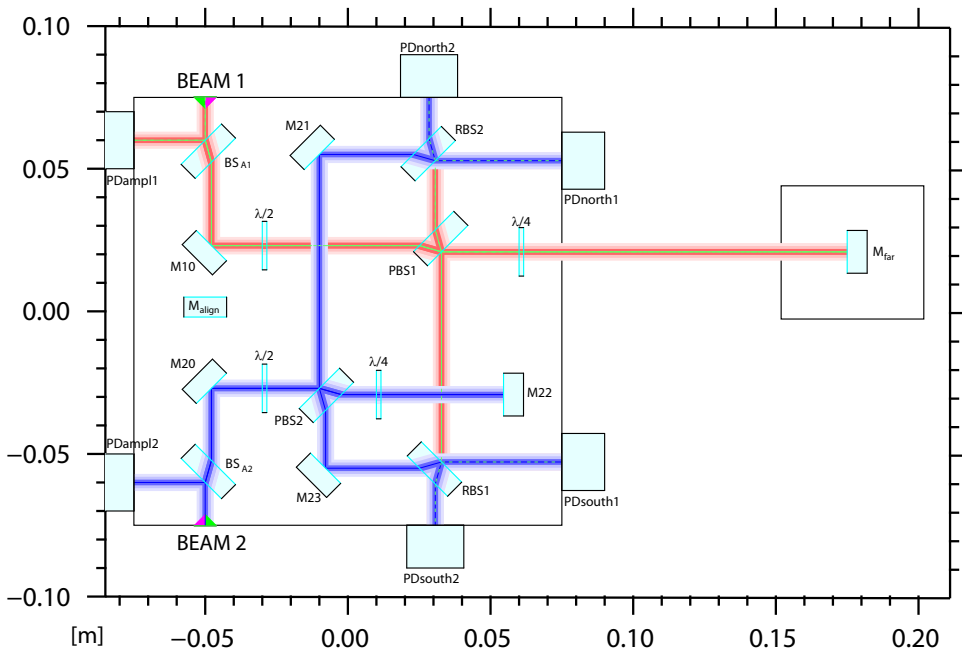


**Figure 9.19.:** OptoCad model of the improved laser interferometer. Minor modifications such as using polarising optics for beam redirection and an output for amplitude stabilisation are implemented.

# 10 Summary and Conclusion

In this thesis, several ultra-stable optical systems were developed suitable for space interferometry and the compatibility of polarising interferometry for LISA was experimentally demonstrated.

A novel technique for aligning optical components to micron accuracy has been used to construct a unique optical bench consisting of polarising optics. The implementation of polarising components enables the use of the entire light received in on-axis (normal incidence) satellite configurations. However, possible risks are driven by the thermal sensitivity of polarising optics which could modify the extinction rate, the polarising plane and the optical path length. Depending on the optical design periodical phase errors can emerge and limit the interferometric sensitivity. To assess a possible sensitivity limitation, due to polarising components, an interferometer was constructed that measures (almost) the same distance once with polarising components and once without. In order to reach the necessary sensitivity of the test setup, various noise sources were experimentally investigated and successfully suppressed. Two main noise sources were identified and mitigated by active stabilisations: the non-linear effect of optical path length difference and fluctuations of the laser frequency that translate proportionally into interferometer phase noise. Furthermore it has been shown that the polarisation state of the incoming light plays a major role. By equipping the optical bench with polarisers and controlling the incoming polarisation state of the two beams, the phase readout noise was significantly reduced by up to one order of magnitude in the frequency band between 0.3 and 30 mHz. Finally, a displacement sensitivity of better than  $1 \text{ pm}/\sqrt{\text{Hz}}$  in the frequency range of interest from 3 mHz to 1 Hz was demonstrated, but increasingly poorer towards lower frequencies. Alternatively, several noise sources were subtracted in data post-processing. These noise sources were parasitic beams due to ghost reflections (stray light) and coupling of other fluctuations into the

displacement measurement, such as alignment fluctuations, temperature noise, as well as laser frequency and intensity noise. Hence, even under non-ideal conditions it was still possible to reach the required noise performance, which leads to an improved robustness for satellite missions, in particular the LISA mission. The noise investigations were extended throughout this work with respect to thermally induced phase noise and periodic phase errors. A coupling coefficient of  $5 \times 10^{-8}$  m/K was measured from PBS temperature to displacement. This agrees with the theoretically expected value. The thermal characteristics of polarising components showed no significant difference to non-polarising components. Thus, no additional requirement for the temperature stability is needed. In order to investigate the occurrence of non-linearity induced by polarising components, several measurements were conducted: one arm length of the interferometer was intentionally varied and the response in phase was observed. By comparing the displacement in the polarising interferometer with either the displacement measured in the non-polarising interferometer or the determined displacement from the actuation voltage of the piezo, no evidence was found for periodic phase errors induced by polarising optics.

The phase measurement systems (PMS) of future space-based laser interferometers, such as LISA or GRACE follow-on, need to be able to cope with large dynamic ranges of the order of  $10^9$ . The readout is based on a tracking phase measurement system with stringent requirements on the noise performance and linearity. One part of this thesis was devoted on the linearity tests of such phase measurement systems, which could be experimentally performed for the first time in an optical setup. For this purpose, a quasi-monolithic optical bench consisting of three identical and symmetric interferometers in a hexagonal configuration has been developed. In doing so, a new technique for precise alignment of the three input beams was required. Therefore, an instrument equipped with a pair of quadrant photodiodes has been developed in the framework of a master's thesis under my direction. Using this device, referred to as *calibrated quadrant photodiode pair - CQP*, together with a suitable Coordinate Measuring Machine (CMM), absolute measurements of the propagation direction of a mm scale laser beam to an accuracy of around  $\pm 4 \mu\text{m}$  in position and  $\pm 30 \mu\text{rad}$  in angle could be realised. Using the CQP, the three input beams were aligned with respect to the optical bench. The achieved accuracy of a few microns and  $\sim 30 \mu\text{rad}$  was restricted by the CMM uncertainty and by the baseline accuracy of the CQP of approximately  $\pm 15 \mu\text{rad}$ . For the first experimental demonstration of the PMS linearity, three interferometric signals with heterodyne frequencies of 3 MHz to 6 MHz were read out by the PMS, using of a digital frequency lock. The current noise level (in air) is, as yet, still above the requirement of  $6 \mu\text{rad}/\sqrt{\text{Hz}}$  by about two orders of magnitude. Potential candidates for this excess noise are cross talk between the

---

three beat notes and cycle slips in the PMS as well as in the digital frequency lock. Ongoing investigations seem to indicate a high potential of residual path length noise of the order of a few  $\text{nm}/\sqrt{\text{Hz}}$  due to beam jitter across the wedge.

The design and construction of an optical bench focusing on a GRACE follow-on mission was addressed in the last part of this thesis. The Centre of Gravitational Experiments at the Huazhong University of Science and Technology (HUST) located in Wuhan is one of the key laboratories for the ongoing investigations concerning *Space Advanced Gravity Measurements* (SAGM) in China. Within the framework of this thesis the hydroxide-catalysis bonding technique has been adopted in their laboratories. For this purpose, two heterodyne Mach-Zehnder interferometers were combined on an ultra-stable glass-ceramic baseplate. This prototype has been used to calibrate instruments with the capability of driving tiny displacements, such as nanopositioning stages and high-resolution capacitive transducers with high accuracy.



Part V

Appendices





## Appendix A

# A CMM measurement strategies

Appendix A covers the selection of the number of measurement points when using a CMM. Furthermore it describes the probing strategies used for standard features and the definition of a proper coordinate frame for the workpiece. The latter is referred to as the *datum reference frame* [149].

## A.1. Probing strategy

A workpiece is mostly a combination of mathematical geometric features such as planes, circles, straight lines, cylinders, cones and spheres. The geometric parameters of an element (a.k.a. feature) can be determined by fitting a mathematical model to a number of measured points using fitting algorithms, typically a least square fit method. For an accurate mathematical description of a feature, a minimum number of probing points are defined. They are listed in Table A.1. For instance, three probing points are sufficient to measure a plane, while four points are required to determine a sphere. It is preferable to measure more than the minimum number of points. Thus, any form error of the workpiece's surface, as well as the measurement uncertainty, can be minimised (*cf.* Appendix B). In addition to the minimum number of points, the recommended number of points from [150] are listed in Table A.1.

Consequently, the greater the number of appropriately distributed measured points the more precise the measurement is. However, the main drawback could be the longer measuring time required to probe a feature. It is necessary to make a compromise between the desired measurement accuracy and the speed at which feedback of the results is required. For instance, the measuring duration of the three reference spheres during the adjuster-aided bonding procedure should be kept as short as possible, while a measurement accuracy of a few microns should be reached.

The probing points have to be distributed in such way that a uniform coverage of the feature being measured is ensured. However, it is not necessary that the points are equally spaced over the surface. For further information the reader is kindly referred to document *Measurement Good Practice Guide No. 41: CMM Measurement Strategies* [150]. It can be downloaded free of charge from the NIST web site.

**Table A.1.:** Number of probing points required to define a certain geometry.

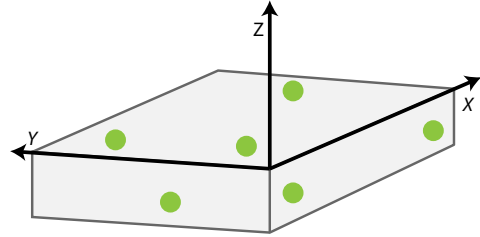
Geometric feature	Minimum number	Recommended number [150]
Straight line	2	5
Plane	3	9 (Three lines of three)
Circle	3	7 (To detect up to six lobes)
Sphere	4	9 (Three circles of three in three parallel planes)
Ellipse	4	12
Cylinder	5	12 (Circles in four parallel planes for information on straightness) 15 (Five points on each circle for information on roundness)
Cone	6	12 (Circles in four parallel planes for information on straightness) 15 (Five points on each circle for information on roundness)
Cube	6	18 (At least three per face)

## A.2. Alignment strategy

The term *alignment* defines the construction of a new coordinate system during CMM operation. For this purpose several features of a workpiece are measured and its orientation is determined. It is common to refer to such a coordinate system as *datum reference frame* [149]. It consists of three mutually perpendicular planes, three axes located at the intersection of each pair of planes, and an origin. This point is located at the intersection of the three planes.

In general, to define a datum reference frame for a rectangular workpiece that has its origin in one corner requires at least six probing points. Figure A.1 shows a rectangular optical bench with its typical coordinate system used through-

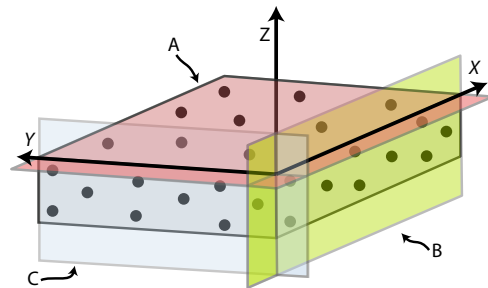
**Figure A.1:** Constructing a datum reference frame of an optical bench with 6 probing points (manual mode). Three points define the surface plane, which yields the  $Z$ -axis. With two points a line lying in the  $X$ - $Z$ -plane is defined leading to the  $X$ -axis. The final point lies in the  $X$ - $Z$ -plane and indicates the origin for the  $X$ -axis.



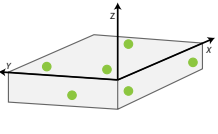
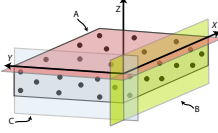
out this thesis. As mentioned earlier, three points are required to define the  $X$ - $Y$ -plane, two further points are required to define a line that lies in the  $X$ - $Z$ -plane and a final point defines the  $Y$ - $Z$ -plane. To construct a Cartesian coordinate frame the measured features need to be assigned to a certain axis. In the example described, the  $Z$ -axis is the normal vector of the probed  $X$ - $Y$ -plane with its datum point on the surface. The line represents the direction of the  $X$ -axis, where its datum point is the measured single point. The  $Y$ -axis is determined by the right-hand rule with a datum point at the line. Thus, all three axes can be defined including one origin.

Typically, this approach is used to define a coarse coordinate system, when operating the CMM in manual mode. In order to increase the measurement accuracy, more points are required and the CMM needs to be operated in computer numerically controlled (cnc) mode. These points are more accurate than measured in manual mode, because the machine motion parameters are under computer control. For the fine alignment of the datum reference frame it is recommended to probe three mutually orthogonal planes each with at least 9 points, as shown in Figure A.2. They correspond to the planes A, B, and C, as referenced in the drawing. The intersection point of these three planes defines the origin of the system. Note that the order of features (referred to as *datum*) is not irrelevant. Usually, plane A, e.g. the polished surface of the optical bench, is estimated by a least squares method and its normal vector defines the  $Z$ -axis. Then plane B is estimated analogously with the additional constraint

**Figure A.2:** Defining a datum reference frame of an optical bench in cnc-mode. Three planes are probed, each with 9 points. The normal vector of plane A is the  $Z$ -axis. The intersection line between this plane and plane B yields the  $X$ -axis. The piercing point of the intersection line with plane C as well as the intersection point of all three planes gives the origin of the system.



**Table A.2.:** Two different alignment strategies for a datum reference frame: 1) CMM is manually operated; 2) CMM is operated in cnc-mode.

Mode	Geometric feature	Number of points	Coordinate frame
Manually	Plane	3	
	Straight line	2	
	Point	1	
CNC	Plane (A)	9	
	Plane (B)	9	
	Plane (C)	9	

of being perpendicular to plane A. The intersection line between plane A and plane B is the  $X$ -axis. The last feature- plane C- is finally estimated with the constraint that it must be orthogonal to both plane A and plane B. Clearly, plane C could be used instead of plane B for constructing the intersection line and the associated  $Y$ -axis. However, to minimise measurement uncertainties the same alignment strategy should always be performed. Furthermore, in most of the adopted alignment strategies the origin was defined by the piercing point of the intersection line and plane C.

Table A.2 lists both adopted alignment strategies. It distinguishes between the manually and the cnc operated CMM measurement procedure. In addition, the workpiece along with its probing points and the associated coordinate frame is visualised for each strategy.

## Appendix B

## B

## Measurement uncertainty for Coordinate Measuring Systems

The measurement uncertainty is a very important part of the measurement result obtained with a coordinate measuring system. Such a measurement result is complete only if it is accompanied by a statement of its uncertainty. The evaluation of a CMM measurement uncertainty, particularly with regard to the applications described throughout this thesis, will be described in this appendix. Therefore, various sources of uncertainty, such as operator-selectable actions as well as environmental conditions, and methods for quantifying the CMM performance will be briefly discussed. A detailed description is beyond the scope of this appendix, but can be found in full extent in several publications [151–158].

The measurement uncertainty is described in accordance with the ISO *Guide to the Expression of Uncertainty in Measurement* (GUM, [151]) recommended by the Joint Committee for Guides in Metrology. At first, the difference between measurement error and measurement uncertainty shall be stated. The *measurement error* is the difference between the value measured with a CMM and the “true” value. Usually, this true value is unknown and with it the measurement error. One exception is the calibration procedure of the probe head or the performance evaluation of the CMM. The latter exactly evaluates the measurement error. The test method used, standardised in ISO 10360-2:2009, involves repeated measurements at well-calibrated dimensional artefacts. The results are used to determine the difference between the measured value and the calibrated value, that is the measurement error, and the uncertainty of the calibrated artefact, which is typically sufficiently small. Even though the artefact is well-calibrated, multiple measurements under identical conditions will yield

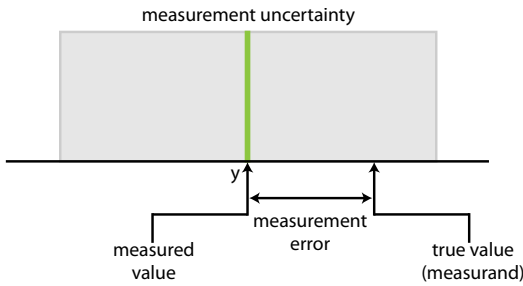


**Figure B.1:** Illustration of the measurement error and measurement uncertainty in the case of a rectangular distribution.

different results. This variation of all measurement errors represents the *measurement uncertainty*. As shown in Figure B.1, the measurement uncertainty is centred symmetrically about the measured value  $y$ . It can be interpreted as the ignorance about the true value of the measurement.

In general, characteristics such as length or diameter can be expressed as a single number leading to a one-dimensional uncertainty region. However, most measurements need several values to specify their results, such as a point in space. Its uncertainty can be described by a three-dimensional uncertainty region about the measured point in space, associated with an “uncertainty cloud”. Since the uncertainty of the CMM varies with its different axes, the cloud will not be spherical but rather elongated along the axis with the highest uncertainty [152]. Due to the complexity of the system, the cloud will not be static. Its size will vary in time, since the CMM responds to external influences such as thermal gradients, deformation due to workpiece loading and wear or damage of the granite table [153]. Typically, uncertainty due to workpiece loading can be excluded for the applications used throughout this thesis. Besides the errors caused by the CMM structure, foremost among the factors contributing to the total system measurement uncertainty are the environmental conditions, in particular the thermal environment leading to changes in the workpiece size, as well as measurement-specific and operator-selectable factors [54]. For instance, the probe approach direction, probe orientation, probe velocity as well as the probing force have to be taken into account. Commonly, the sources of CMM uncertainties can be divided into five categories: hardware, workpiece, probing strategy, fitting and evaluation algorithms, as well as external factors [154].

### Combined standard uncertainty

The various uncertainty sources can be grouped into two categories, in which the measured value and the associated uncertainty are estimated by either statistical methods (also referred to as type A method of evaluation) or by “other means” (also referred to as type B method of evaluation) [155]. The type A method of evaluation is used if the feature is measured several times under

unchanged conditions and multiple values are determined. In contrast, the uncertainty of a feature that is measured only once, is obtained by using a type B method of evaluation. Further, this method can be applied for input quantities, that are evaluated from models involving additional quantities, or that include previous measurement and/or calibration data, as well as manufacturer's specifications. Each uncertainty source is represented by its standard deviation. This standard uncertainty  $u(x_i)$  is quantified as the square root of the variance of the distribution. The output quantity  $y$  (e.g. the desired feature, such as the length of a workpiece) depends on the input quantities  $x_i$  ( $i = \{0, \dots, N - 1\}$ ), and has  $N$  different sources of measurement uncertainty. The combined uncertainty of a measurement result  $u_c(y)$  is taken to represent the estimated standard deviation of the measurement result [155]. This combined standard uncertainty is obtained by appropriately combining all known sources of uncertainties in a root sum of squares manner, which is given by

$$u_c(y) = \sqrt{\sum_{i=1}^N (c_i u(x_i))^2} = \sqrt{\sum_{i=1}^N u_i^2(y)}. \quad (\text{B.1})$$

The factors  $c_i$  are called *sensitivity coefficients* and describe how the output quantity  $y$  varies with changes in the input quantities. That is the importance of the uncertainty source with respect to the total uncertainty. The method applied in Equation (B.1) is called the *law of propagation of uncertainty* [155].

### Expanded uncertainty

The statement of the estimated measurement uncertainty is incomplete without an associated level of confidence. In particular, this is of importance for some commercial, industrial and regulatory applications. Typically, the measurement uncertainty corresponds to some level of confidence in the measured value. The GUM recommends the term *expanded uncertainty* to describe an interval in which the measured value can be expected to lie with a specific level of confidence. To obtain the expanded uncertainties  $U$ , the combined uncertainty is multiplied by a *coverage factor*  $k$

$$U = k \cdot u_c(y), \quad (\text{B.2})$$

where  $k$  is a real positive number. The value of the coverage factor is dependent on the desired level of confidence and usually lies in the range of 2 to 3 (*student's t-distribution*). Typically, the expanded uncertainty covers a level of confidence of 95 %, that is twice the standard deviation ( $k = 2$ ). For instance, a  $k$  factor of 1 will yield a level of confidence of about 68 %, whereas a value of 3 for the coverage factor defines an interval having a level of confidence greater than 99 % [155].

## B.1. Sources of CMM uncertainties

In order to understand how measurement uncertainty propagates through the CMM system, it is useful to describe the measurement process. Hence, the sources of uncertainty and their impact on the measurement can be understood.

### Machine error

In general, a CMM is tested for conformance to its maximum permissible error (MPE) of length measurement according to [54]. This is done by the manufacturer and describes only what errors can be expected for specific measurement tasks under ideal conditions, such as a perfect workpiece, a room temperature of 20 °C, optimal measurement-specific factors and a “reference” probe, e.g.  $L_{\text{stylus}}: 50 \text{ mm}$ ,  $r_{\text{tipball}} = 2.5 \text{ mm}$ . For the CMM used throughout this thesis (DEA GLOBAL Advantage) the *length measuring uncertainty* is specified according ISO 10360-2 [159] by

$$u_m = 1.5 \mu\text{m} + \frac{L}{333000}, \quad (\text{B.3})$$

where  $L$  is the length being evaluated.

### Sampling uncertainty

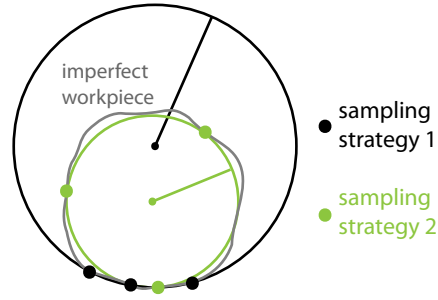
However, such ideal conditions are uncommon. Usually the operator selects a different probe or stylus configuration as for specifying  $u_m$ , which affects the CMM hardware performance. Since the CMM used determines the position of the probe within its measurement volume of  $0.7 \times 1 \times 0.5 \text{ m}^3$  by calculating the centre of the tip ball, additional information is required to determine the points on the workpiece surface. Such information can be the size of the tip ball, the stylus length, the probing force and its approach velocity, including the vector that describes the direction toward which the probe is moving at the time of probing. Hence, the CMM hardware performance depends on dynamic errors and is determined by the uncertainty in the point coordinate of the tip ball centre, the probing speed and direction, probe approach distance, the effective size of the tip ball, acceleration settings and workpiece length. The effective size of the tip ball includes any factors obtained by the probe calibration, in particular its radius and stylus bending that is specific to the probe in use. According to [54] and ISO 10360-2 [159], the *probing uncertainty*, also referred to as probing error, for the CMM used is given by

$$\sigma_p = 1.7 \mu\text{m}. \quad (\text{B.4})$$

In order to express the point coordinate uncertainty, it is necessary to add to the probing uncertainty the errors induced by a different stylus being used.



**Figure B.2:** An imperfect workpiece as source of measurement uncertainty: a perfect circle is measured with two different sampling strategies. By considering a perfect CMM without uncertainty, the form error of the workpiece produces different results. In the case of the first sampling strategy the measurement uncertainty is disastrously larger.



Additionally, the uncertainty of calibration must be taken into consideration. Thus, the value for the additional probing error due to the stylus  $\sigma_{\text{stylus}}$  can be determined from the probe calibration procedure. Typically, this value is of the order of  $2\ \mu\text{m}$  for the most frequently used stylus. Consequently, the point coordinate error is given by [152] as

$$\sigma_{\text{pc}} = \sqrt{\sigma_{\text{p}}^2 + \sigma_{\text{stylus}}^2}. \quad (\text{B.5})$$

Since the CMM measures only individual points in space, a mathematical process is required to fit these points to an ideal geometry. For this reason the measured points are analysed by the CMM software PC-DMIS to produce the desired geometric result. In most cases a least squares algorithm is implemented. The obtained accuracy depends largely on the selected sampling strategy. A carefully considered sampling strategy includes an appropriate number and position of the points on the workpiece surface being measured. Otherwise, a poor sampling strategy corresponds to a large sensitivity coefficient  $c$ , yielding a large uncertainty of the computed result [160]. For instance, by assuming a perfect CMM without measurement uncertainty, a measurement with a finite number of sampling points will not necessarily lead to a correct result. Since the workpiece has some geometric imperfections, resulting from the manufacturing or fixturing process, repeated measurements with a finite probing strategy (with randomly located points), will yield different results. This effect is illustrated in Figure B.2, where an imperfect circle is measured twice with different probing strategies but each time with the minimum number of points required to define it. In both cases the best fit circle is not identical to the actual workpiece geometry. In addition, it is shown that the first probing strategy has a much larger uncertainty than the second probing strategy. Hence, the sensitivity coefficient corresponds to the distribution of the sampling points and thus to the sampling strategy. However, even an infinite number of sampling points will have residuals as a consequence of the imperfect workpiece. Consequently, workpiece form errors cannot be neglected and are a significant source of measurement uncertainty, especially when using finite sampling strategies.



**Figure B.3:** A perfect circle is measured with two different probing strategies assuming an imperfect CMM with a point coordinate error. In both cases the modelled geometry is not identical to the real workpiece. Again, the first probing strategy yields a significantly larger measurement uncertainty.

In contrast, by assuming a perfect workpiece without form errors while the CMM is now imperfect, a finite sampling strategy will result in different characteristics. In Figure B.3, a perfect circle is probed twice with three randomly distributed points. Due to the measurement uncertainty in the point coordinate, the measured points will vary. Thus, a different centre or diameter is determined each time. This can be reduced by having numerous sampling points with an appropriate distribution on the workpiece’s surface. Once again, the probing strategy, including its distribution, assigns the sensitivity coefficient, which assesses the measurement uncertainty.

In reality, both CMM and workpiece are imperfect. Both will introduce residuals in the fitting algorithm. Therefore they are sources of uncertainty when finite sampling strategies are adopted. As a result, a *sampling uncertainty*  $u_{\text{sampling}}$  is defined to quantify the effect of finite sampling

$$u_{\text{sampling}} = \frac{\sigma_{\text{pc}}}{\sqrt{n - x}}, \quad (\text{B.6})$$

where  $n$  is the number of probing points and  $x$  the minimum number of points required to define a given feature. Table A.1 of Appendix A lists the minimum number of points for an accurate mathematical description of a feature along with the recommended number of points as cited in [150].

### Thermal uncertainty

Ideally, the temperature of the measuring environment, the CMM as well as the workpiece should be 20 °C [161]. Mostly, the room temperature was about 20.5 °C depending on the equipment in operation and the number of persons in the room. The CMM used includes an adaptive structural thermal compensation technology. At the three measurement scales of the CMM as well as an arbitrary point (granite table, reference sphere or workpiece) a number of thermal sensors capable of reading the temperature are installed. Software reads these data and compensates for the current thermal state of the machine, so

that the influence of temperature variations is virtually cancelled over a wide range [52]. However, this CMM's thermal compensation system does not correct for thermal errors induced by the workpiece. Consequently, it is necessary to correct for a non-uniform, temporally changing temperature distribution of the workpiece. As the workpieces used throughout this thesis are usually stored in the clean room, the workpiece temperature can be considered identical to the room temperature.

The change in workpiece size for a given temperature change can be expressed by the coefficient of linear thermal expansion,  $\alpha_w$ . In order to correct its length to the required 20°C, the following expression can be used [156]

$$L_{20^\circ\text{C}} = L + L\alpha(20^\circ\text{C} - T), \quad (\text{B.7})$$

where  $L_{20^\circ\text{C}}$  is the length at 20°C while  $L$  is the length being considered,  $T$  [C] is the temperature at which the length was measured. By considering the law of propagation of uncertainty, the standard uncertainty of Equation (B.7) can be expressed by

$$u[L_{20^\circ\text{C}} - L] = \sqrt{L^2 u_{\alpha_w}^2 [\alpha_w] (20^\circ\text{C} - T)^2 + L^2 \alpha^2 u_T^2 [(20^\circ\text{C} - T)]}. \quad (\text{B.8})$$

The first term includes the uncertainty in the measurement of the expansion coefficient, while the second term includes the uncertainty of the thermometer used to measure the temperature.

In general, the coefficient of thermal expansion of a certain material is not known with any certainty, because it is difficult to measure it in the laboratory and it varies with the batch of the material. Typically, a common value for the material from e.g. an engineering data book is taken. Therefore it is recommended to assume a  $\pm 10\%$  variation in that number [152]. Hence, the uncertainty  $u_{\alpha_w}$  associated with the coefficient of thermal expansion of the workpiece is given by [156]

$$u_{\alpha_w} = c_T \cdot 0.1 \cdot \alpha_w. \quad (\text{B.9})$$

The sensitivity coefficient,  $c_T$ , specifies the temperature distribution. Mostly, a rectangular (“box car”) distribution can be assumed (in our applications), that is that a given temperature in the range is equally likely. For a rectangular distribution the uncertainty of  $\alpha$  is divided by the square root of three, corresponding to a factor of approximately 0.6 [162]. In contrast, for a normal distribution, which can usually be assumed when uncertainties are imported, such as from a calibration certificate, the uncertainty needs to be divided by 2 corresponding to a factor of 0.5.

A further uncertainty in the length correction is due to uncertainty in the temperature determination as well as variation of the temperature with time [156]. The uncertainty due to variation of temperature of the workpiece can be calculated by

$$u_{\delta T_w} = c_T \cdot (T_{\max,w} - T_{\min,w}), \quad (\text{B.10})$$

where  $T_{\max,w}$  and  $T_{\min,w}$  are the maximum and the minimum temperatures of the workpiece.

Using the error in the temperature measurement device  $\epsilon(T)_D$ , which can be obtained from the calibration certificates, the last contribution to the uncertainty of the length correction is

$$u_{TD} = c_T \cdot \epsilon(T)_D. \quad (\text{B.11})$$

Hence, the thermally induced uncertainty  $u_T$  in the workpiece can be expressed by [163]

$$u_T = \sqrt{\text{UNE}_w^2 + \text{LUTM}_w^2}. \quad (\text{B.12})$$

With the uncertainty of the nominal thermal expansion of the workpiece

$$\text{UNE}_w = \sqrt{L^2 \cdot \alpha_w^2 \cdot (20^\circ - T)^2} \quad (\text{B.13})$$

and the length uncertainty due to the temperature measurement of the workpiece

$$\text{LUTM}_w = \sqrt{L^2 \cdot \alpha_w^2 \cdot u_{\delta T_w}^2 + L^2 \cdot \alpha_w^2 \cdot u_{TD}^2}. \quad (\text{B.14})$$

## Datum uncertainty

Most of the adopted features are associated with a datum reference frame (*a.k.a* coordinate frame). For instance, to define such a system for a rectangular part with flat surfaces, such as an optical bench that has its origin in one corner, would require at least six probing points (*cf.* Figure A.1, Appendix A). As shown in the drawing, three points define the  $X$ - $Y$ -plane (primary datum A), two points define a line, lying on the  $X$ - $Z$ -plane (secondary datum B), and a final point in the  $Y$ - $Z$ -plane (tertiary datum C). These datum items, which have to be measured in addition to the desired features, have associated measurement uncertainties. Hence, the total uncertainty is affected by *datum uncertainties*. However, if size features are evaluated, a datum uncertainty is not applicable. In such a case the size of a feature is independent of the datum reference frame [152].

Understanding the principle of an alignment strategy, as described in Section A.2, it is apparent that the probed features do not equally influence the datum

uncertainty, and thus the assigned sensitivity coefficient has to be adapted. Since the primary datum defines the first axis, it controls three degrees of freedom. Note that a rigid body is defined by six degrees of freedom. The secondary datum, which yields a line, controls two degrees of freedom. Consequently, the last tertiary datum controls only one degree of freedom. Thus, the datum uncertainty can be expressed by [152]

$$u_{\text{datum}} = \sqrt{\left(\frac{3}{6} \cdot u_{\text{primary}}\right)^2 + \left(\frac{2}{6} \cdot u_{\text{secondary}}\right)^2 + \left(\frac{1}{6} \cdot u_{\text{tertiary}}\right)^2}. \quad (\text{B.15})$$

The uncertainty for each datum is the individual uncertainty of the probed feature and needs to be calculated individually. In general, Equation (B.6) weighted with a sensitivity coefficient can be used to roughly estimate the uncertainty.

Different uncertainty sources which play a role in the applications presented in this thesis, were introduced. Clearly, not all of them have the same contribution of importance to the overall uncertainty. By considering independent sources, the combined uncertainty from Equation (B.1) becomes

$$u_c = \sqrt{u_m^2 + u_{\text{sampling}}^2 + u_T^2 + u_{\text{datum}}^2}. \quad (\text{B.16})$$

## B.2. Performance evaluation

A CMM is mainly used for three different applications throughout this thesis. On the one hand it is used for adjustable bonding (*cf.* Section 2.3.4), where in principle three spheres serving as references are probed. Their precise coordinates are of significant importance. They determine how accurately a component can be placed on an optical bench by using such a technique. On the other hand, the position and orientation of already bonded components are measured to be able to correct for misplacements. Another application includes the use of a CQP (*cf.* Chapter 3). This is a device for measuring the physical position of a beam in space, required to be probed by a CMM. Its accurate position and orientation in space are essential to obtain high accuracy in the determination of the beam's propagation direction.

It is of high interest how accurately such applications can be realised. Thus, three representative applications are used to evaluate the achievable accuracy. The different uncertainty sources contributing to the measurement uncertainty are calculated and the expanded uncertainty is given.

**Table B.1.: Example 1:** Uncertainty analysis for an adjuster located 280 mm (straight line) from the origin of the optical bench. Its sphere has a diameter of 5 mm.

Source of uncertainty	Probability distribution	Formula	Standard uncertainty [ $\mu\text{m}$ ]
Machine	Normal	$1.5 + \frac{280}{333}$	2.34
Sampling	Normal	$\sqrt{\frac{1.7^2 + 2^2}{25 - 4}}$	0.57
Thermal: UNE	Rectangular	$\sqrt{0.005^2 \cdot (0.6 \cdot 0.1 \cdot 4.5 \times 10^{-6})^2 \cdot 0.5^2}$	0.00067
LUTM	Rectangular/ Normal	$\frac{\sqrt{(0.005^2 \cdot (4.5 \times 10^{-6})^2 \cdot (1 \cdot 0.6)^2) \dots}}{\dots + (0.005^2 \cdot (4.5 \cdot 10^{-6})^2 \cdot (0.1 \cdot 0.5)^2)}$	0.014
Thermal uncertainty		$\sqrt{0.0067^2 + 0.14^2}$	0.016
Datum	Normal	$\sqrt{\left(\frac{3}{6} \cdot 0.54\right)^2 + \left(\frac{2}{6} \cdot 0.54\right)^2 + \dots}$ $\dots \left(\frac{1}{6} \cdot 0.54\right)^2$	0.34
Combined uncertainty		$\sqrt{2.34^2 + 0.57^2 + 0.016^2 + 0.34^2}$	2.43
Expanded uncertainty		$2 \cdot u_c$	4.86

**Example 1: Adjustable bonding**

The obtained measurement uncertainty for an adjuster used to define the position of an optical component during bonding associated with a sphere is analysed and listed in Table B.1. The sphere is located 280 mm away from the origin of the optical bench, leading to a length measurement uncertainty due to the machine structure of

$$u_m = 1.5 \mu\text{m} + \frac{280 \text{ mm}}{333} = 2.34 \mu\text{m}. \tag{B.17}$$

The sphere is measured with 25 probing points, thus the sampling uncertainty is

$$u_{\text{sampling}} = \sqrt{\frac{1.7^2 \mu\text{m}^2 + 2^2 \mu\text{m}^2}{25 - 4}} = 0.57 \mu\text{m}. \tag{B.18}$$

The position of the sphere's centre is related to the optical bench frame, which is determined with the approach described in Section A.2. For this purpose

three planes have been probed with at least nine sampling points using the same stylus. Consequently, the uncertainty of each datum by considering a normal probability distribution is

$$u_{\text{plane}} = \sqrt{\frac{1.7^2 \mu\text{m}^2 + 2^2 \mu\text{m}^2}{9 - 3}} \times 0.5 = 0.54 \mu\text{m}. \quad (\text{B.19})$$

By considering Equation B.15, the assigned datum uncertainty is approximately  $0.34 \mu\text{m}$ . The sphere is made of silicon nitride and has a CTE of  $4.5 \times 10^{-6}/\text{K}$ . Assuming a rectangular temperature distribution of the thermal expansion coefficients with a 10% variation, an uncertainty in the CTE of the workpiece can be estimated to:

$$u_{\alpha_w} = 0.6 \times 0.1 \times 4.5 \frac{10^{-6}}{\text{K}} = 2.7 \times 10^{-7}/\text{K}. \quad (\text{B.20})$$

Considering a mean temperature of  $20.5^\circ\text{C}$  and a sphere's diameter of 5 mm, an uncertainty of the nominal thermal expansion of the workpiece of  $0.00067 \mu\text{m}$  can be determined. In order to estimate the length uncertainty due to temperature measurement of the workpiece, one has to consider the uncertainty due to variation of the workpiece's temperature, given by

$$u_{\delta T_w} = 0.6 \cdot (21 - 20)^\circ\text{C} = 0.6^\circ\text{C}, \quad (\text{B.21})$$

and the uncertainty contribution due to the error in the temperature measuring device

$$u_{mTD} = 0.5 \cdot 0.1^\circ\text{C} = 0.05^\circ\text{C}. \quad (\text{B.22})$$

As the error  $\epsilon_D$  was obtained from the data sheet, being of the order of 0.1, a normal distribution of probability is assumed. Taking Equation B.12 into account, a combined uncertainty due to temperature is calculated to be  $0.016 \mu\text{m}$ . Finally, a combined uncertainty of  $2.43 \mu\text{m}$  can be calculated, resulting in an expanded uncertainty of  $4.86 \mu\text{m}$ .

### ***Example 2: Position measurement of an optical component***

The second example, shown in Table B.2, represents a position measurement of an optical component (material: Suprasil<sup>®</sup>) bonded onto an optical bench made of Clearceram<sup>®</sup>. In order to define the optical bench frame, the approach described in Section A.2 has been adopted: three planes were probed with at least nine sampling points using the same stylus. Hence, the uncertainty of each datum by considering a normal probability distribution is

$$u_{\text{plane}} = \sqrt{\frac{1.7^2 \mu\text{m}^2 + 2^2 \mu\text{m}^2}{9 - 3}} \times 0.5 = 0.54 \mu\text{m}, \quad (\text{B.23})$$

**Table B.2.: Example 2:** Uncertainty analysis for the determination of the distance of an optical component located in the centre of the optical bench to the origin. The component's footprint is  $20 \times 20 \times 7 \text{ mm}^3$ . The dominating sampling uncertainty is introduced by the unused small side surface of the component ( $20 \times 7 \text{ mm}^2$ ), which can only be probed with 5 points.

Source of uncertainty	Probability distribution	Formula	Standard uncertainty [ $\mu\text{m}$ ]
Machine	Normal	$1.5 + \frac{140}{333}$	1.92
Sampling	Normal	$\sqrt{\frac{1.7^2 + 2^2}{5-3}}$	1.86
Thermal:			
UNE <sub>OB</sub>	Rectangular	$\sqrt{0.14^2 \cdot (0.6 \cdot 0.1 \cdot 2 \times 10^{-8})^2 \cdot 0.5^2}$	$8.4 \times 10^{-5}$
LUTM <sub>OB</sub>	Rectangular/ Normal	$\frac{\sqrt{(0.14^2 \cdot (2 \times 10^{-8})^2 \cdot (1 \cdot 0.6)^2) + \dots}}{\dots (0.14^2 \cdot (2 \times 10^{-8})^2 \cdot (0.1 \cdot 0.5)^2)}$	$1.7 \times 10^{-3}$
UNE <sub>c</sub>	Rectangular	$\sqrt{0.02^2 \cdot (0.6 \cdot 0.1 \cdot 5.1 \times 10^{-7})^2 \cdot 0.5^2}$	$0.306 \times 10^{-3}$
LUTM <sub>c</sub>	Rectangular/ Normal	$\frac{\sqrt{(0.02^2 \cdot (5.1 \times 10^{-7})^2 \cdot (0.1 \cdot 0.6)^2) \dots}}{\dots + (0.02^2 \cdot (5.1 \times 10^{-7})^2 \cdot (1 \cdot 0.5)^2)}$	0.006
Thermal uncertainty		$\sqrt{0.08^2 + 0.22^2 + 0.31^2 + 0.8^2}$	0.006
Datum	Normal	$\sqrt{\left(\frac{3}{6} \cdot 0.54\right)^2 + \left(\frac{2}{6} \cdot 0.54\right)^2 + \dots}$ $\dots \left(\frac{1}{6} \cdot 0.54\right)^2$	0.34
Combined uncertainty		$\sqrt{1.92^2 + 1.86^2 + 0.006^2 + 0.34^2}$	2.69
Expanded uncertainty		$2 \cdot u_c$	5.38

resulting in an assigned datum uncertainty of about  $0.34 \mu\text{m}$ . The component is located in the centre of the optical bench ( $L = 140 \text{ mm}$ ) and has a footprint of  $20 \times 20 \times 7 \text{ mm}^3$  ( $l = 20 \text{ mm}$ ). This yields a length measurement uncertainty due to the machine structure of

$$u_m = 1.5 \mu\text{m} + \frac{140 \text{ mm}}{333} = 1.92 \mu\text{m}. \quad (\text{B.24})$$

For the determination of its position, three planes were probed: the optical surface ( $20 \times 20 \text{ mm}^2$ ) with at least nine points and both remaining planes



(top and side surface with  $20 \times 7 \text{ mm}^2$ ) with five points. Thus the sampling uncertainty is dominated by the smallest surface size and is

$$u_{\text{sampling}} = \sqrt{\frac{1.7^2 \mu\text{m}^2 + 2^2 \mu\text{m}^2}{5 - 3}} = 1.86 \mu\text{m}. \quad (\text{B.25})$$

The intersection point of all three planes yields the desired corner point of the component. This coordinate was related to the origin of the optical bench frame.

To estimate the total measurement uncertainty, both the thermal influence on the optical bench and the component have to be considered. As Clearceram has an CTE of  $2 \times 10^{-8}/\text{K}$ , the uncertainty of nominal thermal expansion of the optical bench can be calculated to be

$$\text{UNE}_{\text{OB}} = 0.14 \cdot (0.6 \cdot 0.1 \cdot 2 \times 10^{-8}) \cdot (20^\circ\text{C} - 20.5^\circ\text{C}) = 8.4 \times 10^{-11} \text{m}. \quad (\text{B.26})$$

Taking Equations (B.21) and (B.22) into account, a length uncertainty due to temperature measurements of the optical bench can be estimated to be about

$$\text{LUTM}_{\text{OB}} = \sqrt{(0.14 \cdot 2 \times 10^{-8} \cdot 0.6)^2 + (0.14 \cdot 2 \times 10^{-8} \cdot 0.05)^2} = 1.7 \times 10^{-9} \text{m}. \quad (\text{B.27})$$

In the same manner the uncertainty contribution to the total measurement uncertainty due to thermal influence on the component is determined. Assuming a CTE for Suprasil<sup>®</sup> of  $5.1 \times 10^{-7}$  and a maximum length of 0.02 m, an  $\text{UNE}_c$  of  $3.06 \times 10^{-10}$  m and a  $\text{LUTM}_c$  of  $6.14 \times 10^{-9}$  m can be estimated. Thus, the thermal uncertainty of about  $0.006 \mu\text{m}$  is negligible. Consequently, the combined uncertainty for measuring the position of a component on the optical bench is  $2.69 \mu\text{m}$  with an expanded uncertainty of  $5.38 \mu\text{m}$ .

### Example 3: CQP

The centre of the CQP's aperture defines the origin of the associated coordinate system (BCF). An uncertainty in that coordinate would lead to an uncertainty in the required beam centroid. For this reason an estimation of this uncertainty is calculated and listed in Table B.3. The aperture represented by a circle has a diameter of 15 mm and is probed with at least 15 points. Hence, the machine and sampling uncertainties are

$$u_m = 1.5 \mu\text{m} + \frac{15 \text{ mm}}{333} = 1.54 \mu\text{m} \quad (\text{B.28})$$

and

$$u_{\text{sampling}} = \sqrt{\frac{1.7^2 \mu\text{m}^2 + 2^2 \mu\text{m}^2}{15 - 3}} = 0.75 \mu\text{m}, \quad (\text{B.29})$$

respectively.

Considering a CTE for Invar<sup>®</sup> of  $2 \times 10^{-6}/\text{K}$  and Equations (B.21) as well

**Table B.3.: Example 3:** Uncertainty analysis for the measurement of the origin of the CQP  $O_{BCF}$ . It is mainly defined by the aperture located on the front side of the CQP. The circle has a diameter of 15 mm and the CQP's material is Invar<sup>®</sup>.

Source of uncertainty	Probability distribution	Formula	Standard uncertainty [μm]
Machine	Normal	$1.5 + \frac{15}{333}$	1.54
Sampling	Normal	$\sqrt{\frac{1.7^2 + 2^2}{15 - 3}}$	0.75
Thermal:			
UNE	Rectangular	$\sqrt{0.015^2 \cdot (0.6 \cdot 0.1 \cdot 2 \times 10^{-6})^2 \cdot 0.5^2}$	$9 \times 10^{-4}$
LUTM	Rectangular/ Normal	$\frac{\sqrt{(0.015^2 \cdot (2 \times 10^{-6})^2 \cdot (1 \cdot 0.6)^2) + \dots}}{\dots(0.015^2 \cdot (2 \times 10^{-6})^2 \cdot (0.1 \cdot 0.5)^2)}$	0.018
Thermal uncertainty		$\sqrt{9 \times 10^{-8} + 0.018^2}$	0.018
Datum	Normal	$\sqrt{\left(\frac{3}{6} \cdot 0.54\right)^2 + \left(\frac{2}{6} \cdot 0.54\right)^2 + \dots}$ $\dots\left(\frac{1}{6} \cdot 0.38\right)^2$	0.33
Combined uncertainty		$\sqrt{1.54^2 + 0.75^2 + 0.018^2 + 0.33^2}$	1.75
Expanded uncertainty		$2 \cdot u_c$	3.50

as (B.22), the uncertainty contribution caused by thermal influence has been determined to be about 0.018 μm. As the orientation BCF is determined by probing two planes with 9 points and the origin is defined by measuring the circle using 15 probing points, the datum uncertainty can be calculated as follows:

The primary and secondary datum items can be estimated using Equation (B.19) to 0.54 μm each. Since the centre of the circle defines the origin and controls only one degree of freedom, the tertiary datum uncertainty can be expressed by

$$u_{\text{circle}} = \sqrt{\frac{1.7^2 \mu\text{m}^2 + 2^2 \mu\text{m}^2}{15 - 3}} \times 0.5 = 0.38 \mu\text{m}. \quad (\text{B.30})$$

Thus, an expanded measurement uncertainty of 3.50 μm results.

## Appendix C

# C CMM measurement program for adjustable bonding

Appendix C shows a compact PC-DMIS script for the entire adjuster-aided bonding technique based on the CMM. It can be divided into five parts: *i*) the assignment of several parameters, such as the moving points and reference points (line 23-51), *ii*) the alignment of the optical bench with respect to the MCS (line 52-131), *iii*) the positioning of the first sphere including the alignment of ACF (line 132-287), *iv*) the positioning of the second sphere (line 288-447), and finally *v*) the positioning of the third sphere forming a three-point reference for the optical component to be bonded (lines 448-602). Various comments have been included in the script highlighted in green.

```

1 PART NAME   : polifo_m8
  REV NUMBER  :
  SER NUMBER  :
  STATS COUNT : 1

START        =ALIGNMENT/START,RECALL:,LIST=YES
             ALIGNMENT/END
             LOADPROBE/KU_3X50
             MODE/MANUAL

11 $$.
  ,-- Anfahr- und Rückfahrweg sowie die Fahrgeschwindigkeit definiert -----
  ,-- Sicherheitsabstand von Tasterspitze zur Oberfläche einstellen -----
  ,-- für Polifo sollte mindestens 2lmm gewählt werden -----
  ;
             PREHIT/ 5
             RETRACT/ 5
             CHECK/ 10,1
             MOVESPEED/ 100
             FORMAT/TEXT, , ,HEADINGS,SYMBOLS, ;NOM,TOL,MEAS,DEV,OUTTOL, ,
             RECALL/ALIGNMENT,INTERNAL,START
21 LOADPROBE/KU_3X50
             TIP/T1A5B90, SHANKIJK=-0.087, 0, 0.996, ANGLE=90

31 $$.
  ,--Zuweisungen der einzelnen Bewegungspunkte und angestrebten CMM Punkten-----
  ;
  ,-----KUGEL 1 entspricht Kugel F von M8-----
  ;
             ASSIGN/BWPTX_KUG1 = 3.22183*(-1)+100
             ASSIGN/BWPTY_KUG1 = -83.5653*(-1)+100
             ASSIGN/BWPTZ_KUG1 = 13
             ASSIGN/NWX_KUG1   = 0.393398*(-1)+100
             ASSIGN/NWY_KUG1   = -80.7369*(-1)+100

```

## C. CMM measurement program for adjustable bonding

```

ASSIGN/NWZ_KUG1 = 13
$$.
,--KUGEL 2 entspricht KUGEL B von M8-----
$
ASSIGN/BWPTX_KUG2=7.11091*(-1)+100
ASSIGN/BWPTY_KUG2=-82.5046*(-1)+100
ASSIGN/BWPTZ_KUG2=13.
41  ASSIGN/NWX_KUG2= 9.93934*(-1)+100
ASSIGN/NWY_KUG2=-79.6762*(-1)+100
ASSIGN/NWZ_KUG2=13.
$$.
,--KUGEL 3 entspricht KUGEL A von M8-----
$
ASSIGN/BWPTX_KUG3=14.182*(-1)+100
ASSIGN/BWPTY_KUG3=-89.5757*(-1)+100
ASSIGN/BWPTZ_KUG3=13
ASSIGN/NWX_KUG3=17.0104*(-1)+100
ASSIGN/NWY_KUG3=-86.7473*(-1)+100
51  ASSIGN/NWZ_KUG3=13
$$.
,-- manuelle Ausrichtung der optischen Bank -----
,-- Oberfläche mittels drei Punkten -----
,-- x-Achse mittels einer zwei-Punkt-Linie -----
,-- y-Achse mittels einem Punkt -----
$
OBERFL_MAN =FEAT/PLANE, CARTESIAN, TRIANGLE
THEO/<168.449,87.581,-7>,<0,0,1>
61  ACTL/<131.28,220.159,-513.161>,<-0.0822782,-0.0004745,0.9966093>
MEAS/PLANE,3
...
ENDMEAS/
LIN1 =FEAT/LINE, CARTESIAN, UNBOUNDED
THEO/<50,194.19,-33.655>,<0,-1,0>
ACTL/<136.731,248.994,-519.994>,<0.9999974,-0.0022916,0>
MEAS/LINE,2,WORKPLANE
...
ENDMEAS/
PKT1 =FEAT/POINT, CARTESIAN
71  THEO/<101.714,10,-23.872>,<0,-1,0>
ACTL/<121.319,237.379,-515.992>,<-0.9971105,-0.0353108,0.0672587>
MEAS/POINT,1
...
ENDMEAS/
A1 =ALIGNMENT/START,RECALL:START,LIST=YES
ALIGNMENT/LEVEL,ZPLUS,OBERFL_MAN
ALIGNMENT/ROTATE,YPLUS,TO,LIN1,ABOUT,ZPLUS
ALIGNMENT/TRANS,ZAXIS,OBERFL_MAN
ALIGNMENT/TRANS,XAXIS,LIN1
81  ALIGNMENT/TRANS,YAXIS,PKT1
ALIGNMENT/END
$$.
,-- CNC Modus für die Ausrichtung der Platte -----
,-- Oberfläche der Platte mittels mindestens 4 Pkt (je mehr desto besser) -----
,-- X-Achse als Ebene mittels 4 Punkten -----
,-- Y-Achse als Ebene mittels 4 Punkten -----
,-- Bewegungspunkte setzen -----
,-- ACHTUNG: Taster durchfährt den kürzesten Weg zwischen A und B -----
$
91  MODE/DCC
EBENEX =FEAT/PLANE, CARTESIAN, TRIANGLE
THEO/<65.27,-0.106,-12.178>,<-0.0023874,-0.9999971,-0.0003106>
ACTL/<65.269,-0.12,-12.256>,<-0.0024648,-0.9999969,-0.0003054>
MEAS/PLANE,8
...
ENDMEAS/
OBERFL_CNC =FEAT/PLANE, CARTESIAN, TRIANGLE
THEO/<49.212,47.489,0>,<-0.0000067,0.0000076,1>
101 ACTL/<49.214,47.471,0.004>,<0.0000323,0.0000629,1>
MEAS/PLANE,7
...
ENDMEAS/
EBENEY =FEAT/PLANE, CARTESIAN, TRIANGLE
THEO/<0.016,60.9,-10.681>,<-0.9999999,0.0003965,0.0000425>
ACTL/<-0.136,60.916,-10.764>,<-0.9999999,0.0004722,0.0001826>
MEAS/PLANE,8
...
ENDMEAS/
LIN_SZ =FEAT/LINE, CARTESIAN, UNBOUNDED, NO
111 THEO/<-0.008,0.049,-11.438>,<-0.0000424,0.0003107,-1>
ACTL/<-0.165,0.041,-11.513>,<-0.0001825,0.0003058,-0.9999999>

```

```

CONSTR/LINE,INTOF,EBENEX,EBENEY
LIN_SY =FEAT/LINE,CARTESIAN,UNBOUNDED,NO
THEO/<0.014,54.204,0>,<-0.0003965,-0.9999999,0.0000076>
ACTL/<-0.137,54.206,0.006>,<-0.0004722,-0.9999999,0.0000629>
CONSTR/LINE,INTOF,OBERFL_CNC,EBENEY
$$
,-- Durchstoßpunkt der Schnittlinie mit der Oberfläche -----
$
121 PKT_DST_OL =FEAT/POINT,CARTESIAN,NO
THEO/<-0.007,0.046,0>,<-0.0003965,-0.9999999,0.0000076>
ACTL/<-0.163,0.037,0.009>,<-0.0004722,-0.9999999,0.0000629>
CONSTR/POINT,PIERCE,LIN_SY,EBENEX
A1_cnc =ALIGNMENT/START,RECALL:A1,LIST=YES
ALIGNMENT/LEVEL,ZPLUS,OBERFL_CNC
ALIGNMENT/ROTATE,YMINUS,TO,LIN_SY,ABOUT,ZPLUS
ALIGNMENT/TRANS,XAXIS,PKT_DST_OL
ALIGNMENT/TRANS,YAXIS,PKT_DST_OL
ALIGNMENT/TRANS,ZAXIS,PKT_DST_OL
131 ALIGNMENT/END
$$
,-- Taster drehen nach 45/-45 -----
$
TIP/T1A45B-45, SHANKIJK=-0.502, 0.555, 0.663, ANGLE=58.167
$$
,-- Bewegungspunkt zur 1. Koordinate aus dem C Programm -----
,-- der Radius der Kugel muss in Richtung des Normvektors der -----
,-- Komponentenoberfläche abgezogen werden -----
$
141 $$
,-- Manuelle Messung der Toolstange um Normvektor für Kugel 1 zu ermitteln -----
,-- hierfür Ebene mit 4 Punkten abtasten -----
,-- Ebene_Stange -----
$
MODE/MANUAL
,-- Manuelle Messung der Kugel 1 mit 5 Punkten -----
$
EBENE_STANGE=FEAT/PLANE,CARTESIAN,TRIANGLE
151 THEO/<4.41,-1.606,9.961>,<-0.9999773,-0.0027562,-0.0061522>
ACTL/<101.034,176.68,30.875>,<-0.7046068,0.7095735,-0.0058891>
MEAS/PLANE,4
...
ENDMEAS/
$$
,-- Die manuell angetastete Kugel 1 wird in X,Y und Z zu Null gesetzt -----
,-- Ausrichtung: Yplus 'drehen Raum' auf Ebene_Stange -----
,-- Kugl_man ist X,Y und Z Nullpunkt -----
$
161 KUG1_MAN =FEAT/SPHERE,CARTESIAN,OUT
THEO/<0.199,0.077,-0.006>,<-0.0000312,-0.0000227,1>,4.99
ACTL/<99.164,180.181,12.581>,<0,0,1>,4.986
MEAS/SPHERE,5
...
ENDMEAS/
ASSIGN/NWX_KUG1_MAN=(-0.70711*(NWX_KUG1-KUG1_MAN.X-AX_KUG1)-0.70711*(NWX_KUG1-KUG1_MAN.Y-AY_KUG1))
DIM LAGE3= LOCATION OF SPHERE KUG1_MAN
AX NOMINAL +TOL -TOL MEAS DEV
X NWX_KUG1 0.050 0.050 99.164 -0.443
171 Y NWY_KUG1 0.050 0.050 180.181 -0.556
END OF DIMENSION LAGE3
A_KUG1_MAN =ALIGNMENT/START,RECALL:A1_cnc,LIST=YES
ALIGNMENT/LEVEL,ZPLUS,
ALIGNMENT/ROTATE,YPLUS,TO,EBENE_STANGE,ABOUT,ZPLUS
ALIGNMENT/TRANS,XAXIS,KUG1_MAN
ALIGNMENT/TRANS,YAXIS,KUG1_MAN
ALIGNMENT/TRANS,ZAXIS,KUG1_MAN
ALIGNMENT/END
$$
181 ,-- Einschalten des CNC MODUS -----
$
MODE/DCC
PREHIT/ 1
RETRACT/ 1
$$
,-- Variablendeklaration für die Verschiebewerte in X und Y-Richtung der Kugel 1--
$
ASSIGN/X_VERSCH_KUG1=0
ASSIGN/Y_VERSCH_KUG1=0
191 ASSIGN/XTEMP_KUG1=0
ASSIGN/YTEMP_KUG1=0

```

## C. CMM measurement program for adjustable bonding

```

ASSIGN/AX_KUG1=0
ASSIGN/AY_KUG1=0
$$-----
,-- Einfügen einer Sprungmarke falls die Kugel 1 nochmal gemessen werden soll -----
NOCHMAL KUGEL1=LABEL/
$$-----
,-- neue Ausrichtung falls die Kugel 1 mehrmals nachjustiert werden muss -----
201 A_KUG1_VER =ALIGNMENT/START,RECALL:A_KUG1_MAN,LIST=YES
      ALIGNMENT/TRANS_OFFSET,XAXIS,AX_KUG1
      ALIGNMENT/TRANS_OFFSET,YAXIS,AY_KUG1
      ALIGNMENT/END
$$-----
,-- Messung der Kugel 1 im CNC Modus mit den eingestellten Verschiebewerten -----
,-- und der Richtung des Ebenen_Stange-Normvektors an der Kugel 1 -----
,-- mit F9 können die Parameter der Kugel und der Messung angepasst werden -----
211 ,-- Radius anpassen und WICHTIG: Startwinkel anpassen !!! -----
KUG1_CNC =FEAT/CONTACT/SPHERE,CARTESIAN,OUT,LEAST_SQR
      THEO/<-0.02,-0.02,0>,<EBENE_STANGE.I,EBENE_STANGE.J,EBENE_STANGE.K>,5
      ACTL/<0.688,0.063,0.004>,<0,0.9999827,-0.0058891>,<4.999
      TARG/<-0.02,-0.02,0>,<EBENE_STANGE.I,EBENE_STANGE.J,EBENE_STANGE.K>
      START ANGLE 1=0,END ANG 1=360
      START ANGLE 2=34,END ANG 2=90
      ANGLE VEC=<-0.0276492,-0.9962468,0.0820234>
      SHOW FEATURE PARAMETERS=NO
      SHOW CONTACT PARAMETERS=YES
      NUMHITS=25,NUMROWS=3
      SAMPLE HITS=0
      AVOIDANCE MOVE=NO,DISTANCE=0
      SHOW HITS=YES
      ...
$$-----
,--- Ausrichtung an der Grundplatte -----
DIM LAGE1= LOCATION OF SPHERE KUG1_CNC
231 AX  NOMINAL          +TOL      -TOL      MEAS      DEV
      X  NWX_KUG1_MAN    0.002      0.002      0.688      1.394
      Y  NWY_KUG1_MAN    0.002      0.002      0.063      0.142
      Z  -0.000          0.002      0.002      0.004      0.004
END OF DIMENSION LAGE1
      RECALL/ALIGNMENT,INTERNAL,A1_cnc
$$-----
,-- Berechnung des zu verschiebenden Wertes -----
ASSIGN/DIFFERENZ1_X=NWX_KUG1-KUG1_CNC.X
241 ASSIGN/DIFFERENZ1_Y=NWY_KUG1-KUG1_CNC.Y
      ASSIGN/VERSCHIEBUNG1_X=(0.70711*DIFFERENZ1_X+0.70711*DIFFERENZ1_Y)
      ASSIGN/VERSCHIEBUNG1_Y=(-0.70711*DIFFERENZ1_X+0.70711*DIFFERENZ1_Y)
$$-----
,--- Auswertung der Kugel 1 (Nullpunkt an der Grundplatte) -----
DIM LAGE11= LOCATION OF SPHERE KUG1_CNC
251 AX  NOMINAL          +TOL      -TOL      MEAS      DEV
      X  VERSCHIEBUNG1_X 0.002      0.002      99.608      99.610
      Y  VERSCHIEBUNG1_Y 0.002      0.002      180.739      180.739
END OF DIMENSION LAGE11
DIM LAGE2= LOCATION OF SPHERE KUG1_CNC
      AX  NOMINAL          +TOL      -TOL      MEAS      DEV
      X  NWX_KUG1         0.050      0.050      99.608      0.001
      Y  NWY_KUG1         0.050      0.050      180.739      0.002
      Z  -0.006           0.050      0.050      12.585      12.591
END OF DIMENSION LAGE2
$$-----
,--- Anzeige des Messergebnisses der Kugel 1 auf dem Bildschirm -----
,--- Dateipfad und Name anpassen -----
261 CS7=REPORT/LEGACY, FILENAME= C:/PC-DMISDATEN/M8KUG1_CNC.RPT
      ENDREPORT/
      RECALL/ALIGNMENT,INTERNAL,A_KUG1_VER
$$-----
,--- Abfrage, ob die Kugel 1 erneut gemessen werden soll -----
C1 =COMMENT/YESNO,NO,Soll Kugel 1 nochmal gemessen werden ?
$$-----
,--- IF Schleife um dem JA/NEIN zu steuern -----
271 IF/C1.INPUT=="JA"

```

```

$$$$
,--- Eingabe der Verschiebe-Werte für die Kugel 1 -----
$
C_XKUG1=COMMENT/INPUT,'Verschiebung der Kugel 1 in X-Richtung [mm] eingeben!'
C_YKUG1=COMMENT/INPUT,'Verschiebung der Kugel 1 in Y-Richtung [mm] eingeben!'
$$$$
,--- die eingegebenen Werte werden in Variablen geschrieben -----
$
281      ASSIGN/XTEMP_KUG1=X_VERSCH_KUG1
      ASSIGN/YTEMP_KUG1=Y_VERSCH_KUG1
      ASSIGN/X_VERSCH_KUG1=C_XKUG1.INPUT
      GOTO/NOCHMAL KUGEL1
$$$$
,--- Ende der IF Schleife -----
$
      END_IF/
      RECALL/ALIGNMENT,INTERNAL,A1_cnc
      TIP/T1A45B-110, SHANKIJK=0.239, 0.721, 0.65, ANGLE=-29.217
291 $$$$
,----- Bewegungspunkt zur 2. angeforderten Koordinate aus dem C Programm -----
$
$$$$
,-- Manuelle Messung der Toolstange um Normvektor für Kugel 2 zu ermitteln --
,-- hierfür Ebene mit 4 Punkten abtasten -----
$
      MODE/MANUAL
      EBENE2_STANGE=FEAT/PLANE,CARTESIAN,TRIANGLE
301      THEO/<4.41,-1.606,9.961>,<-0.9999773,-0.0027562,-0.0061522>
      ACTL/<88.854,178.275,30.249>,<-0.7335592,-0.6795792,-0.0079361>
      MEAS/PLANE,4
      ...
      ENDMEAS/
$$$$
,--- Manuelle Messung der Kugel 2 mit 5 Punkten -----
$
      KUG2_MAN =FEAT/SPHERE,CARTESIAN,OUT
      THEO/<0.199,0.077,-0.006>,<-0.0000312,-0.0000227,1>,4.99
311      ACTL/<90.066,179.676,11.281>,<0,0,1>,4.985
      MEAS/SPHERE,5
      ...
      ENDMEAS/
      ASSIGN/NWX_KUG2_TEST=NWX_KUG2-KUG2_MAN.
      ASSIGN/NWY_KUG2_TEST=NWY_KUG2-KUG2_MAN.Y
      ASSIGN/NWX_KUG2_MAN=(-0.70711(NWX_KUG2_TEST-AX_KUG2)+0.70711(NWY_KUG2_TEST-AY_KUG2))
      ASSIGN/NWY_KUG2_MAN=(-0.70711(NWX_KUG2_TEST-AX_KUG2)-0.70711(NWY_KUG2_TEST-AY_KUG2))
      DIM LAGE6=LOCATION OF SPHERE KUG2_MAN
      AX      NOMINAL      +TOL      -TOL      MEAS      DEV
321      X      NWX_KUG2      0.050      0.050      90.066      0.006
      Y      NWY_KUG2      0.050      0.050      179.676      0.000
      Z      -0.006      0.050      0.050      11.281      11.287
      END OF DIMENSION LAGE6
$$$$
,----- manuelle Ausrichtung der Kugel 2 -----
$
      A_KUG2_MAN =ALIGNMENT/START,RECALL:A1_cnc,LIST=YES
      ALIGNMENT/LEVEL,ZPLUS,
      ALIGNMENT/ROTATE,YMINUS,TO,EBENE2_STANGE,ABOUT,ZPLUS
331      ALIGNMENT/TRANS,XAXIS,KUG2_MAN
      ALIGNMENT/TRANS,YAXIS,KUG2_MAN
      ALIGNMENT/TRANS,ZAXIS,KUG2_MAN
      ALIGNMENT/END
$$$$
,--- Einschalten des CNC MODUS -----
$
      MODE/DCC
      PREHIT/ 1
      RETRACT/ 1
341 $$$$
,-- Variablendeklaration für Verschiebewerte in X und Y-Richtung der Kugel 2 --
$
      ASSIGN/X_VERSCH_KUG2=0
      ASSIGN/Y_VERSCH_KUG2=0
      ASSIGN/XTEMP_KUG2=0
      ASSIGN/YTEMP_KUG2=0
      ASSIGN/AX_KUG2=0
      ASSIGN/AY_KUG2=0
$$$$
,-- einfügen einer Sprungmarke falls Kugel 2 nochmal gemessen werden soll -----
$
351      NOCHMAL KUGEL2=LABEL/

```

## C. CMM measurement program for adjustable bonding

```

$$-----
,--- neue Ausrichtung falls die Kugel 2 mehrmals nachjustiert werden muss -----
$
A_KUG2_VER =ALIGNMENT/START,RECALL:A_KUG2_MAN,LIST=YES
            ALIGNMENT/TRANS_OFFSET,XAXIS,AX_KUG2
            ALIGNMENT/TRANS_OFFSET,YAXIS,AY_KUG2
            ALIGNMENT/END
$$-----
361 ,--- Messung der Kugel 2 im CNC Modus mit den eingestellten Verschiebewerten ---
    ,--- und der Richtung des Ebenen_Stange-Normvektors an der Kugel 2 -----
    $
KUG2_CNC   =FEAT/CONTACT/SPHERE,CARTESIAN,OUT,LEAST_SQR
            THEO/<0,0,0>,<-0.3564643,0.6707147,0.6504422>,.5
            ACTL/<-0.006,-0.005,-0.001>,<-0.3564643,0.6707147,0.6504422>,.5001
            TARG/<0,0,0>,<-0.3564643,0.6707147,0.6504422>
            START_ANGLE 1=0,END_ANGLE 1=360
            START_ANGLE 2=35,END_ANGLE 2=90
            ANGLE_VEC=<-0.0276492,-0.9962468,-0.0820234>
371 SHOW FEATURE PARAMETERS=NO
    SHOW CONTACT PARAMETERS=YES
        NUMHITS=25,NUMROWS=3
        SAMPLE_HITS=0
        AVOIDANCE_MOVE=NO,DISTANCE=0
        SHOW_HITS=YES
        ...
DIM LAGE4= LOCATION OF SPHERE KUG2_CNC
AX  NOMINAL          +TOL      -TOL      MEAS      DEV
X   NWX_KUG2_MAN    0.002      0.002      -0.006    0.032
381 Y   NWY_KUG2_MAN 0.002      0.002      -0.005    0.557
Z   0.000            0.002      0.002      -0.001    -0.001
END OF DIMENSION LAGE4
$$-----
,--- Ausrichtung der Grundplatte -----
$
            RECALL/ALIGNMENT,INTERNAL,A1_cnc
$$-----
,--- Auswertung der Kugel 2 (Nullpunkt an der Grundplatte) -----
$
391 DIM LAGE5= LOCATION OF SPHERE KUG2_CNC
AX  NOMINAL          +TOL      -TOL      MEAS      DEV
X   NWX_KUG2        0.002      0.002      90.058    -0.002
Y   NWY_KUG2        0.002      0.002      179.677   0.001
D   5.000            0.002      0.002      5.001     0.001
END OF DIMENSION LAGE5
$$-----
,--- Berechnung des zu verschiebenden Wertes -----
$
401 ASSIGN/DIFFERENZ2_X=NWX_KUG2-KUG2_CNC.X
    ASSIGN/DIFFERENZ2_Y=NWY_KUG2-KUG2_CNC.Y
    ASSIGN/VERSCHIEBUNG2_X=(+0.70711*DIFFERENZ2_X-0.70711*DIFFERENZ2_Y)
    ASSIGN/VERSCHIEBUNG2_Y=(+0.70711*DIFFERENZ2_X+0.70711*DIFFERENZ2_Y)
$$-----
,--- Anzeige des Messergebnisses der Kugel 2 auf dem Bildschirm -----
,--- schreibe in Datei -----
$
DIM LAGE10= LOCATION OF SPHERE KUG2_CNC
AX  NOMINAL          +TOL      -TOL      MEAS      DEV
X   VERSCHIEBUNG2_X 0.002      0.002      90.058    90.056
411 Y   VERSCHIEBUNG2_Y 0.002      0.002      179.677   179.677
Z   -0.006           0.002      0.002      11.280    11.287
END OF DIMENSION LAGE10
CS7=REPORT/LEGACY, FILENAME= C:/PC-DMIS DATEN/M8KUG2_CNC.RPT
ENDREPORT/
RECALL/ALIGNMENT,INTERNAL,A_KUG2_VER
$$-----
,--- Abfrage ob die Kugel 2 erneut gemessen werden soll -----
$
421 C2 =COMMENT/YESNO,NO,Soll Kugel 2 nochmal gemessen werden ?
$$-----
,--- IF Schleife um dem JA/NEIN zu steuern -----
$
            IF/C2.INPUT=="JA"
$$-----
,--- Eingabe der Verschiebe Werte für die Kugel 2 -----
$
C_XKUG2=COMMENT/INPUT,'Verschiebung die Kugel 2 in X-Richtung [mm] eingeben!'
C_YKUG2=COMMENT/INPUT,'Verschiebung die Kugel 2 in Y-Richtung [mm] eingeben!'
431 $$-----
    ,--- die eingegebenen Werte werden in Variablen geschrieben -----

```



```

$
$
ASSIGN/XTEMP_KUG2=X_VERSCH_KUG2
ASSIGN/YTEMP_KUG2=Y_VERSCH_KUG2
ASSIGN/X_VERSCH_KUG2=C_XKUG2.INPUT
ASSIGN/Y_VERSCH_KUG2=C_YKUG2.INPUT
ASSIGN/AX_KUG2=XTEMP_KUG2+X_VERSCH_KUG2
ASSIGN/AY_KUG2=XTEMP_KUG2+Y_VERSCH_KUG2
$
$
441 ,--- Sprungbefehl zu Sprungmarke der Kugel 2 -----
$
GOTO/NOCHMAL KUGEL2
$
$
,--- Ende der IF Schleife -----
$
END_IF/
RECALL/ALIGNMENT,INTERNAL,A1_cnc
TIP/T1A45B-110,SHANKIJK=0.239,0.721,0.65,ANGLE=-29.217
$
$
451 ,--- Bewegungspunkt zur 3. Koordinate aus dem C Programm -----
$
MOVE/POINT,NORMAL<BWPTX_KUG3,BWPTY_KUG3,BWPTZ_KUG3>
$
$
,----- Manuelle Messung der Toolstange -----
,----- hierfür Ebene mit 4 Punkten abtasten -----
$
MODE/MANUAL
EBENE3_STANGE=FEAT/PLANE,CARTESIAN,TRIANGLE
461 THEO/<4.41,-1.606,9.961>,<-0.9999773,-0.0027562,-0.0061522>
ACTL/<80.855,184.971,28.678>,<-0.7318063,-0.6814593,-0.0085252>
MEAS/PLANE,4
...
ENDMEAS/
$
$
,--- Manuelle Messung der Kugel 3 mit 5 Punkten -----
$
KUG3_MAN =FEAT/SPHERE,CARTESIAN,OUT
THEO/<0.199,0.077,-0.006>,<-0.0000312,-0.0000227,1>,4.99
471 ACTL/<83.019,186.698,12.296>,<0,0,1>,4.984
MEAS/SPHERE,5
...
ENDMEAS/
DIM LAGE7= LOCATION OF SPHERE KUG3_MAN
AX NOMINAL +TOL -TOL MEAS DEV
X NWX_KUG3 0.050 0.050 83.019 0.029
Y NWY_KUG3 0.050 0.050 186.698 -0.050
Z -0.006 0.050 0.050 12.296 12.303
END OF DIMENSION LAGE7
ASSIGN/NWX_KUG3_DIFF=NWX_KUG3-KUG3_MAN.X
481 ASSIGN/NWY_KUG3_DIFF=NWY_KUG3-KUG3_MAN.Y
ASSIGN/NWX_KUG3_MAN=(-0.70711(NWX_KUG3_DIFF-AX_KUG3)+0.70711(NWY_KUG3_DIFF-AY_KUG3))
ASSIGN/NWY_KUG3_MAN=(-0.70711(NWX_KUG3_DIFF-AX_KUG3)-0.70711(NWY_KUG3_DIFF-AY_KUG3))
$
$
,----- manuelle Ausrichtung der Kugel 3 -----
$
A_KUG3_MAN =ALIGNMENT/START,RECALL:A1_cnc,LIST=YES
ALIGNMENT/LEVEL,ZPLUS,
ALIGNMENT/ROTATE,YMINUS,TO,EBENE3_STANGE,ABOUT,ZPLUS
491 ALIGNMENT/TRANS,XAXIS,KUG3_MAN
ALIGNMENT/TRANS,YAXIS,KUG3_MAN
ALIGNMENT/TRANS,ZAXIS,KUG3_MAN
ALIGNMENT/END
$
$
,--- einschalten des CNC MODUS -----
$
MODE/DCC
PREHIT/1
RETRACT/1
$
$
501 ,-- Variablendeklaration für Verschiebewerte in X und Y-Richtung der Kugel 3 --
$
ASSIGN/X_VERSCH_KUG3=0
ASSIGN/Y_VERSCH_KUG3=0
ASSIGN/XTEMP_KUG3=0
ASSIGN/YTEMP_KUG3=0
ASSIGN/AX_KUG3=0
ASSIGN/AY_KUG3=0
$
$
,--- einfügen einer Sprungmarke falls Kugel 3 nochmal gemessen werden soll ---
$
511 NOCHMAL KUGEL3=LABEL/
$

```

## C. CMM measurement program for adjustable bonding

```

$$-----
,--- neue Ausrichtung falls die Kugel 3 mehrmals nachjustiert werden muss -----
$
A_KUG3_VER =ALIGNMENT/START,RECALL:A_KUG3_MAN,LIST=YES
            ALIGNMENT/TRANS_OFFSET,XAXIS,AX_KUG3
            ALIGNMENT/TRANS_OFFSET,YAXIS,AY_KUG3
            ALIGNMENT/END
$$-----
521 ,--- Messung der Kugel 3 im CNC Modus mit den eingestellten Verschiebewerten ---
,--- und der Richtung des Ebenen_Stange-Normvektors an der Kugel 3 -----
$
KUG3_CNC =FEAT/CONTACT/SPHERE,CARTESIAN,OUT,LEAST_SQR
          THEO/<0,0,0>,<-EBENE3_STANGE.I,-EBENE3_STANGE.J,-EBENE3_STANGE.K>,5
          ACTL/<-0.055,0.012,-0.001>,<0,0.9999637,0.0085252>,5
          TARG/<0,0,0>,<-EBENE3_STANGE.I,-EBENE3_STANGE.J,-EBENE3_STANGE.K>
          START ANGLE 1=0,END ANG 1=360
          START ANGLE 2=30,END ANG 2=90
          ANGLE VEC=<-0.0276492,-0.9962468,-0.0820234>
531 SHOW FEATURE PARAMETERS=NO
          SHOW CONTACT PARAMETERS=YES
              NUMHITS=25,NUMROWS=3
              SAMPLE HITS=0
              AVOIDANCE MOVE=NO,DISTANCE=0
              SHOW HITS=YES
          ...
          DIM LAGE8= LOCATION OF SPHERE KUG3_CNC
          AX  NOMINAL      +TOL      -TOL      MEAS      DEV
          X   NWX_KUG3_MAN  0.002      0.002      -0.055     -0.110
541  Y   NWY_KUG3_MAN  0.002      0.002      0.012      0.027
          Z   0.000        0.002      0.002      -0.001     -0.001
          END OF DIMENSION LAGE8
          $$-----
          ,--- Ausrichtung an der Grundplatte -----
          $
          RECALL/ALIGNMENT,INTERNAL,A1_cnc
          $$-----
          ,--- Auswertung der Kugel 3 (Nullpunkt an der Grundplatte) -----
          $
551 DIM LAGE9= LOCATION OF SPHERE KUG3_CNC
          AX  NOMINAL      +TOL      -TOL      MEAS      DEV
          X   NWX_KUG3     0.002      0.002      82.991     0.001
          Y   NWY_KUG3     0.002      0.002      186.746    -0.001
          Z   -0.006       0.002      0.002      12.296     12.302
          END OF DIMENSION LAGE9
          $$-----
          ,--- Berechnung des zu verschiebenden Wertes -----
          $
          ASSIGN/DIFFERENZ3_X=NWX_KUG3-KUG3_CNC.X
561  ASSIGN/DIFFERENZ3_Y=NWY_KUG3-KUG3_CNC.Y
          ASSIGN/VERSCHIEBUNG3_X=(+0.70711*DIFFERENZ3_X-0.70711*DIFFERENZ3_Y)
          ASSIGN/VERSCHIEBUNG3_Y=(+0.70711*DIFFERENZ3_X+0.70711*DIFFERENZ3_Y)
          $$-----
          ,--- Anzeige des Messergebnisses der Kugel 3 auf dem Bildschirm -----
          ,--- Dateipfad und Name anpassen -----
          $
          DIM LAGE12= LOCATION OF SPHERE KUG3_CNC
          AX  NOMINAL      +TOL      -TOL      MEAS      DEV
          X   VERSCHIEBUNG3_X  0.002      0.002      82.991     82.992
571  Y   VERSCHIEBUNG3_Y  0.002      0.002      186.746    186.746
          END OF DIMENSION LAGE12
          CS7=REPORT/LEGACY, FILENAME= C:/PC-DMIS DATEN/M8KUG3_CNC.RPT
          ENDREPORT/
          RECALL/ALIGNMENT,INTERNAL,A_KUG3_VER
          $$-----
          ,--- Abfrage ob die Kugel 3 erneut gemessen werden soll -----
          $
          C3 =COMMENT/YESNO,NO, Soll Kugel 3 nochmal gemessen werden ?
          $$-----
581 ,--- IF Schleife um dem JA/NEIN zu steuern -----
          $
          IF/C3.INPUT=="JA"
          $$-----
          ,--- Eingabe der Verschiebe Werte für die Kugel 3 -----
          $
          C_XKUG3=COMMENT/INPUT,'Verschiebung der Kugel 3 in X-Richtung [mm] eingeben!'
          C_YKUG3=COMMENT/INPUT,'Verschiebung der Kugel 3 in Y-Richtung [mm] eingeben!'
          $$-----
          ,--- die eingegebenen Werte werden in Variablen geschrieben -----
          $
591 ASSIGN/XTEMP_KUG3=X_VERSCH_KUG3

```

```

ASSIGN/YTEMP_KUG3=Y_VERSCH_KUG3
ASSIGN/X_VERSCH_KUG3=C_XKUG3.INPUT
ASSIGN/Y_VERSCH_KUG3=C_YKUG3.INPUT
ASSIGN/AX_KUG3=XTEMP_KUG3+X_VERSCH_KUG3
ASSIGN/AY_KUG3=XTEMP_KUG3+Y_VERSCH_KUG3
GOTO/NOCHMAL KUGEL3

$$$
-----
,--- Ende der IF Schleife -----
601 ,-----$
        END_IF/
        RECALL/ALIGNMENT,INTERNAL,A1_cnc
DIM LAGE13= LOCATION OF SPHERE KUG3 CNC
AX      NOMINAL      +TOL      -TOL      MEAS      DEV
X      NWX_KUG3      0.002      0.002      82.991     0.001
Y      NWY_KUG3      0.002      0.002      186.746    -0.001
END OF DIMENSION LAGE13
DIM LAGE14= LOCATION OF SPHERE KUG2 CNC
AX      NOMINAL      +TOL      -TOL      MEAS      DEV
611 X      NWX_KUG2      0.002      0.002      90.058     -0.002
Y      NWY_KUG2      0.002      0.002      179.677    0.001
END OF DIMENSION LAGE14
DIM LAGE15= LOCATION OF SPHERE KUG1 CNC
AX      NOMINAL      +TOL      -TOL      MEAS      DEV
X      NWX_KUG1      0.002      0.002      99.608     0.001
Y      NWY_KUG1      0.002      0.002      180.739    0.002
END OF DIMENSION LAGE15
CS7 =REPORT/LEGACY, FILENAME= C:/PC-DMIS DATEN/M8_CNC.RPT
      ENDREPORT/

```



## Appendix D

# D Alignment plan

As the layout of the optical bench for testing the influence of polarising optics on the interferometric sensitivity has been developed, a sophisticated alignment plan had to be worked out. This was required to ensure the manufacturability of the optical bench since the precise position alignment of the components was done by means of a coordinate measuring machine (CMM). The outcome of this is an alignment plan as shown in Figure D.1 and described in the following:

- 1) Glue the adapter plates for both fibre injector mounts onto the baseplate. Both plates have well defined positions.
- 2) Bond the mirror  $BS_{ALIGN}$  for aligning the two beams to each other.
- 3) Screw both pre-assembled fibre injectors in place.
- 4) Align the height of both fibre injectors by measuring their centre with the CMM. Note that the accuracy is limited mainly by the centre accuracy of the fibre core.
- 5) Adjust with a beam analyser the lenses in both fibre injectors to ensure a collimated beam.
- 6) Use a polarimeter to adjust the orientation of the fibre injectors and subsequent the orientation of both polarisers mounted at the collimator's output.
- 7) Align the two beams to each other.
- 8) Bond the beam splitter  $BS1$  directing the first beam to the interferometers.
- 9) Bond the mirror  $M2$  to direct the second beam to its power monitor.

- 10) Bond the beam splitter BS2 directing the second beam to the interferometers.
- 11) Bond the mirror M13 directing the second beam to the recombiner of the reference interferometer.
- 12) Bond mirror M1 to direct the first beam to its power monitor.
- 13) Bond mirror M11.
- 14) Bond beam splitter BS4 directing the second beam to the reference and frequency interferometers.
- 15) Bond beam splitter BS10 and direct the beams to the reference and frequency interferometers.
- 16) Bond beam splitter BS5 directing one beam to the  $0^\circ$ -mirror and the other one through the polarising optics.
- 17) Bond mirror M4 directing the second beam to the  $0^\circ$ -mirror through the polarising optics.
- 18) Bond the PBS to multiplex the transmitted beam from M4 to the  $0^\circ$ -mirror and reflecting the beam coming from M3 to the recombiner.
- 19) Bond the  $0^\circ$ -mirror M3.
- 20) Bond mirror M5 directing the second beam to the recombination beam splitter for the non-polarising interferometer.
- 21) Bond mirror M6.
- 22) Glue both mounts including the wave plates in place. Special care has to be taken to tilt the assembly less than  $1.5^\circ$  and that the beam impinge in the centre of the wave plate surface.
- 23) Align the orientation of the two wave plates consecutively.
- 24) Bond beam splitter BS13 separating the first beam to the measurement and to the auxiliary interferometers.
- 25) Bond beam splitter BS14 directing the first beam to the recombiner of the reference and frequency interferometer, respectively.
- 26) Align in real-time and bond the recombiner BR11 for the frequency interferometer.

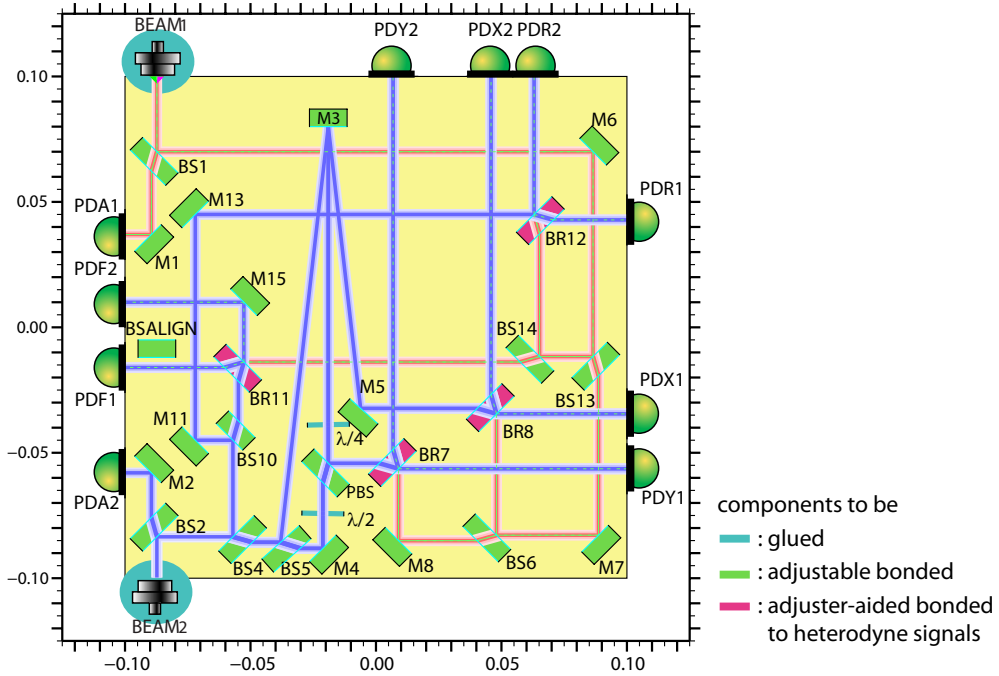


**Figure D.1.:** Alignment plan for the components of the optical bench for testing polarising components. The different colours indicate the alignment and bonding technique involved.

- 27) Re-adjust the two lenses while monitoring the contrast of the frequency interferometer.
- 28) Re-adjust the mounts of the collimators while monitoring the contrast of the frequency interferometer. Ideally the DWS signal should be monitored.
- 29) Align in real-time and bond the recombiner BR12 for the reference interferometer.
- 30) Bond mirror M7.
- 31) Bond beam splitter BS6 directing one part of the first beam to the recombiner of the non-polarising interferometer.
- 32) Bond mirror M8 directing the first beam to the recombiner of the polarising interferometer.
- 33) Align in real-time and bond the recombiner BR7 for the polarising interferometer.

- 34) Align in real-time and bond the recombiner BR8 for the non-polarising interferometer.



# Bibliography

- [1] Albert Einstein, *Die Grundlage der allgemeinen Relativitätstheorie*, Annalen der Physik, Band 49 **7**, (1916). 1
- [2] S. van der Putten, *Thermal Lensing in Virgo and Polynomial Search: An All-sky Search for Gravitational Waves from Spinning Neutron Stars in Binary Systems* (Vrije Universiteit, 2011). 1
- [3] A. Einstein, *Zur Quantentheorie der Strahlung*, Physikalische Zeitschrift **18**, 121 (1917). 1
- [4] H. Kogelnik and T. Li, *Laser Beams and Resonators*, Appl. Opt. **5**, 1550 (1966). 2
- [5] A. E. Siegman and L. Fellow, *Laser beams and resonators: The 1960s*, IEEE J. Sel. Top. Quantum Electron 2000 .
- [6] A.E. Siegman, *Laser beams and resonators: Beyond the 1960s*, Selected Topics in Quantum Electronics, IEEE Journal of **6**, 1389 (2000). 2
- [7] S. Hild and the LSC, *The status of GEO 600*, Classical and Quantum Gravity **23**, S643 (2006). 2
- [8] The LIGO Scientific Collaboration, *A gravitational wave observatory operating beyond the quantum shot-noise limit* , Nature Physics **7**, (2011). 2
- [9] B P Abbott *et al.*, *LIGO: the Laser Interferometer Gravitational-Wave Observatory*, Reports on Progress in Physics **72**, 076901 (2009). 2
- [10] C. Bradaschia *et al.*, *The VIRGO Project: A wide band antenna for gravitational wave detection*, Nuclear Instruments and Methods in Physics Research Section A: Accelerators, Spectrometers, Detectors and Associated Equipment **289**, 518 (1990). 2
- [11] M. Ando and the TAMA Collaboration, *Current status of the TAMA300 gravitational-wave detector*, Classical and Quantum Gravity **22**, S881 (2005). 2

- [12] K. Yamamoto *et al.*, *Current status of the CLIO project*, Journal of Physics: Conference Series **122**, 012002 (2008). 2
- [13] S. Hild *et al.*, *Sensitivity studies for third-generation gravitational wave observatories*, Classical and Quantum Gravity **28**, 094013 (2011). 2
- [14] B. Tapley, S. Bettadpur, M. Watkins and C. Reigber, *The gravity recovery and climate experiment: Mission overview and early results*, Geophys. Res. Lett. **31**, L09607 (2004). 2, 5
- [15] B.S. Sheard *et al.*, *Intersatellite laser ranging instrument for the GRACE follow-on mission*, Journal of Geodesy 1 (2012). 2, 7
- [16] *LISA assessment study report* (<http://sci.esa.int/science-e/>, 2011), Vol. ESA/SRE(2011)3. 3, 73, 152
- [17] O Jennrich, *LISA technology and instrumentation*, Classical and Quantum Gravity **26**, (2009). 3
- [18] S. A. Hughes, *LISA sources and science*, arXiv:0711.0188 (to be published by Classical and Quantum Gravity) . 3
- [19] Yan Xia *et al.*, *Orbit design for the Laser Interferometer Space Antenna (LISA)*, SCIENCE CHINA Physics, Mechanics & Astronomy **53**, 179 (2010), 10.1007/s11433-010-0100-7. 3
- [20] Karsten Danzmann *et al.*, *LISA technology - concept, status, prospects*, Classical and Quantum Gravity **20**, S1 (2003). 3
- [21] M. Armano *et al.*, *LISA Pathfinder: the experiment and the route to LISA*, Classical and Quantum Gravity **26**, 094001 (2009). 4
- [22] S. Vitale *et al.*, *LISA and its in-flight test precursor SMART-2*, Nucl. Phys. B (Proc. Suppl.) **110**, 209 (2002). 4
- [23] V. Hruba *et al.*, *Colloid thrusters for the new millennium, ST7 DRS mission*, IEEE Aerospace Conference Proceedings **1-6**, 202 (2004). 4
- [24] Gerhard Heinzel *et al.*, *Laser Ranging Interferometer for GRACE follow-on*, ICSO conference proceedings (9-12 October 2011). 6
- [25] P.L. Bender, R.S. Nerem and J.M. Wahr, *Possible Future Use of Laser Gravity Gradiometers*, Space Science Reviews **108**, 385 (2003). 6
- [26] M. Stephens *et al.*, *Interferometric Range Transceiver for Measuring Temporal Gravity Variations*, 4th annual Earth Science Technology Conference (ESTC) (2004).

- [27] S. Nagano *et al.*, *Development of a simulator of a satellite-to-satellite interferometer for determination of the Earth's gravity field*, Review of Scientific Instruments **76**, 124501 (2005).
- [28] R. Pierce *et al.*, *Intersatellite range monitoring using optical interferometry*, Appl. Opt. **47**, 5007 (2008). 6, 175
- [29] J. Leitch *et al.*, *Laboratory Demonstration of Low Earth Orbit Inter-Satellite Interferometric Ranging*, Conference on Lasers and Electro-Optics/Quantum Electronics and Laser Science and Photonic Applications Systems Technologies 1754 (2005). 6
- [30] L. Rayleigh, *A Study of Glass Surfaces in Optical Contact*, Proceedings of the Royal Society A: Mathematical, Physical and Engineering Sciences **156**, 326 (1936). 11, 186
- [31] V. Greco, F. Marchesini and G. Molesini, *Optical contact and van der Waals interactions: the role of the surface topography in determining the bonding strength of thick glass plates*, Journal of Optics A: Pure and Applied Optics **3**, 85 (2001). 11, 186
- [32] K. Numata, Amy Kemery and Jordan Camp, *Thermal-Noise Limit in the Frequency Stabilization of Lasers with Rigid Cavities*, Phys. Rev. Lett. **93**, 250602 (2004). 11
- [33] A. Preston, B. Balaban, G. T. Boothe and G. Mueller, *Stable Materials and Bonding Techniques for Space-Based Optical Systems*, NASA Science Technology Conference (NSTC2007) (2007). 11
- [34] S. Rowan, J. Hough and E. Eliffe, *Silicon carbide bonding*, Patent Number US2007/0221326A1, (2007). 11, 14, 15, 177, 180
- [35] D.-H. Gwo, in *Two unique aspects of gravity probe-B star-tracking space telescope: (1) focal-plane roof-edge diffraction and (2) fused-quartz bonding for 2.5-Kelvin applications*, edited by Pierre Y. Bely and James B. Breckinridge (SPIE, 1998), No. 1, pp. 892–903. 11
- [36] D.-H. Gwo *et al.*, *The Gravity Probe-B star-tracking telescope*, Advances in Space Research **32**, 1401 (2003).
- [37] C. W. F. Everitt *et al.*, *Gravity Probe B: Final Results of a Space Experiment to Test General Relativity*, Phys. Rev. Lett. **106**, 221101 (2011). 11, 176
- [38] B Willke *et al.*, *The GEO 600 gravitational wave detector*, Classical and Quantum Gravity **19**, 1377 (2002). 11

- [39] G. M. Harry and the LIGO Scientific Collaboration, *Advanced LIGO: the next generation of gravitational wave detectors*, Classical and Quantum Gravity **27**, 084006 (2010). 11
- [40] M. V. Plissi *et al.*, *Aspects of the suspension system for GEO 600*, Review of Scientific Instruments **69**, 3055 (1998). 12
- [41] S. Goßler *et al.*, *Damping and tuning of the fibre violin modes in monolithic silica suspensions*, Classical and Quantum Gravity **21**, S923 (2004).
- [42] N. A. Robertson *et al.*, *Quadruple suspension design for Advanced LIGO*, Classical and Quantum Gravity **19**, 4043 (2002).
- [43] A. V. Cumming *et al.*, *Design and development of the advanced LIGO monolithic fused silica suspension*, Classical and Quantum Gravity **29**, 035003 (2012). 12
- [44] Ewan .D. Fitzsimons, *Techniques for Precision Interferometry in Space*, PhD Thesis, University of Glasgow, (2010). 12, 29, 36, 38, 61, 83
- [45] F. Steier *et al.*, *Construction of the LISA back-side fibre link interferometer prototype*, Classical and Quantum Gravity **26**, 175016 (2009). 12
- [46] E. J. Elliffe *et al.*, *Hydroxide-catalysis bonding for stable optical systems for space*, Classical and Quantum Gravity **22**, S257 (2005). 14
- [47] A. A. van Veggel *et al.*, *Hydroxide catalysis bonding of silicon carbide*, Journal of the European Ceramic Society **28**, 303 (2008). 14
- [48] S. Reid *et al.*, *Influence of temperature and hydroxide concentration on the settling time of hydroxy-catalysis bonds*, Physics Letters A **363**, 341 (2009). 14
- [49] Gerhard Heinzl, *A framework of C subroutines to plan and optimize the geometry of laser interferometers*, (2011). 16
- [50] [www.quick-ohm.de/](http://www.quick-ohm.de/). 19
- [51] International Organisation for Standardisation, *ISO 22093:2011 Industrial automation systems and integration – Physical device control – Dimensional Measuring Interface Standard (DMIS)*, (2011). 20
- [52] Hexagon Metrology GmbH:, <http://www.hexagonmetrology.de>. 20, 209
- [53] PC-DMIS:, <http://www.pcdmis.com/>. 20

- [54] *Methods for Performance Evaluation of Coordinate Measuring Machines, ASME B 89.4.1-1997: An American National Standard : Engineering Drawing and Related Documentation Practices* (American Society of Mechanical Engineers, 1997). 20, 26, 204, 206
- [55] *Encoders for Linear Motors in the Electronics Industry*, Dr. Johannes Heidenhain GmbH, 11/2007. 22
- [56] W. van Vliet, *Development of a Fast Mechanical Probe for Coordinate Measuring Machines*, PhD Thesis, Eindhoven University of Technology, (1996), iISBN 90-386-0168-9. 22
- [57] D. Flack, in *Measurement Good Practice Guide NO. 43: CMM Probing*, edited by National Physical Laboratory (National Physical Laboratory, 2011), iISSN 1368-6650. 22
- [58] D. Flack, *Measurement Good Practice Guide NO. 42: CMM Verification* (National Physical Laboratory, 2001), iISSN 1368-6550. 26
- [59] Personal communication with Gerhard Heinzl. 29
- [60] 2011 Christoph Mahrtdt, *Contrast and heterodyne efficiency* . 29
- [61] E. D. Fitzsimons *et al.*, *Initial interferometric pre-investigations for LISA*, Journal of Physics: Conference Series **154**, 12034 (2009). 29
- [62] M. Sommerfeld, *Development of a calibrated quadrant photodiode pair (CQP)*, Diploma thesis, Leibniz University Hanover, (2010). 36, 40, 47, 49
- [63] Physics Instrumente (PI) GmbH; *6-Axis Hexapod: low-profile, precision parallel-kinematic system; H-824*, [www.physikinstrumente.com/](http://www.physikinstrumente.com/) . 37
- [64] ER2188 data sheet; [www.electrolube.com/](http://www.electrolube.com/). 41
- [65] <http://www.pacificsensor.com/>, *Pacific Silicon Sensor Quadrant Series Data Sheet: QP50-6-18u-SM*. 41
- [66] I.N. Bronstein and K.A. Semendjajew, *Taschenbuch der Mathematik, 25* (Verlag Harry Deutsch GmbH, 1999). 48, 49
- [67] Gunnar Stede, *Interferometrische Charakterisierung von Retroreflektoren für satellitengestützte Erdschwerefeldbestimmungen*, Diploma thesis, Leibniz Universität Hannover, 2011. 57
- [68] L. d’Arcio *et al.*, *Optical bench development for LISA*, ICSO conference proceedings (4-8 October 2010). 61, 176

- [69] J. Burkhardt *et al.*, Technical Report No. LISA project document: LOB-TN-007-05-ASD, ASTRIUM. 61
- [70] Dennis Weise, Technical Report No. LISA project document: LOB-ASD-TN-006-02, ASTRIUM. 64
- [71] R. C. Quenelle, *Nonlinearity in Interferometer Measurements*, Hewlett-Packard journal **34**, 10 (1983). 65
- [72] C. M. Sutton, *Non-linearity in length measurement using heterodyne laser Michelson interferometry*, Journal of Physics E: Scientific Instruments **20**, 1290 (1987). 65, 125
- [73] J. M. De Freitas and M. A. Player, *Importance of rotational beam alignment in the generation of second harmonic errors in laser heterodyne interferometry*, Measurement Science and Technology **4**, 1173 (1993). 66
- [74] J.M. De Freitas and M.A. Player, *Polarization Effects in Heterodyne Interferometry*, Journal of Modern Optics **42**, 1875 (1995).
- [75] C.-M. Wu and C.-S. Su, *Nonlinearity in measurements of length by optical interferometry*, Measurement Science and Technology **7**, 62 (1996).
- [76] C.-M. Wu, *Periodic nonlinearity resulting from ghost reflections in heterodyne interferometry*, Optics Communications **215**, 17 (2003). 72
- [77] C.-M. Wu and R. D. Deslattes, *Analytical Modeling of the Periodic Nonlinearity in Heterodyne Interferometry*, Appl. Opt. **37**, 6696 (1998). 68
- [78] C.-M. Wu, John Lawall and Richard D. Deslattes, *Heterodyne Interferometer with Subatomic Periodic Nonlinearity*, Appl. Opt. **38**, 4089 (1999).
- [79] S.J.A.G. Cosijns, H. Haitjema and P.H.J. Schellekens, *Modeling and verifying non-linearities in heterodyne displacement interferometry*, Precision Engineering **26**, 448 (2002).
- [80] W. Hou and W. Cui, in *Society of Photo-Optical Instrumentation Engineers (SPIE) Conference Series*, Vol. 7133 of *Society of Photo-Optical Instrumentation Engineers Conference Series* (SPIE, 2008). 67
- [81] W. Hou and G. Wilkening, *Investigation and compensation of the nonlinearity of heterodyne interferometers*, Precision Engineering **14**, 91 (1992).
- [82] V.G. Badami and S.R. Patterson, *A frequency domain method for the measurement of nonlinearity in heterodyne interferometry*, Precision Engineering **24**, 41 (2000).

- [83] D.J. Loner *et al.*, *Laser Polarization State Measurement in Heterodyne Interferometry*, CIRP Annals - Manufacturing Technology **52**, 439 (2003).
- [84] A.E. Rosenbluth and N. Bobroff, *Optical sources of non-linearity in heterodyne interferometers*, Precision Engineering **12**, 7 (1990). 66
- [85] Leonard S. Cutler, *Frequency stabilized laser system*, Patent number 3534292 (1970). 66
- [86] M.-S. Kim and S.-W. Kim, *Two-Longitudinal-Mode He-Ne Laser for Heterodyne Interferometers to Measure Displacement*, Appl. Opt. **41**, 5938 (2002). 66
- [87] Felipe Guzmán Cervantes, *Gravitational wave observation from space: Optical measurement techniques for LISA and LISA Pathfinder*, PhD Thesis, Leibniz Universität Hannover, (2009). 70, 87, 93, 104, 114
- [88] M. Perreur-Lloyd *et al.*, *Optical Bench EBB Design Definition File*, LISA project document: LOB-UGL-TN-008.2-11 (2011). 83
- [89] Takayuki Kishi *et al.*, *Material Characteristics of CLEARCERAM<sup>®</sup>-Z HS for Use in Large Diameter Mirror Blanks*, SPIE Astronomical Instrumentation Conference (2010). 85
- [90] J.N. Reddy, *Theory and Analysis of Elastic Plates and Shells, Second Edition, Series in Systems and Control Series* (Taylor & Francis, 2006). 85
- [91] Roland Fleddermann, *Interferometry for a space-based gravitational wave observatory: Reciprocity of an optical fiber*, PhD Thesis, Leibniz Universität Hannover, (2011). 85, 104, 121, 158
- [92] www.ohara-gmbh.com, *Ultra-Low Expansion Glass-Ceramics: Clearceram<sup>®</sup>-Z, OHARA<sup>®</sup>*. 85
- [93] M. Hoek *et al.*, *Radiation hardness study on fused silica*, Nuclear Instruments and Methods in Physics Research Section A: Accelerators, Spectrometers, Detectors and Associated Equipment **595**, 190 (2008). 86
- [94] <http://heraeus-quarzglas.com> : Quartz Glass for Optics: Data and Properties (2011). 86, 142, 143, 159
- [95] Antonio Francisco García Marín, *Minimisation of optical pathlength noise for the detection of gravitational waves with the spaceborne laser interferometer LISA and LISA Pathfinder*, PhD Thesis, Leibniz Universität Hannover, (2007). 87, 115, 119

- [96] S. Anza *et al.*, *The LTP experiment on the LISA Pathfinder mission*, *Class. Quantum Grav.* **22**, 125 (2005). 87
- [97] T. J. Kane and R. L. Byer, *Monolithic, unidirectional single-mode Nd:YAG ring laser*, *Opt. Lett.* **10**, 65 (1985). 88
- [98] A. Ksendzov *et al.*, in *Measurement of spatial filtering capabilities of single mode infrared fibers*, edited by John D. Monnier, Markus Scholler and William C. Danchi (SPIE, 2006), No. 1, p. 626838. 88
- [99] O. Wallner *et al.*, *Minimum length of a single-mode fiber spatial filter*, *J. Opt. Soc. Am. A* **19**, 2445 (2002). 88
- [100] Vinzenz Wand, *Interferometry at low frequencies: Optical phase measurement for LISA and LISA Pathfinder*, PhD Thesis, Leibniz Universität Hannover, (2007). 91, 105, 189
- [101] G. Heinzel *et al.*, *Investigation of noise sources in the LTP interferometer*, AEI Hannover, University of Glasgow, EADS Astrium Deutschland **S2-AEI-TN-3028**, (2005). 91, 113, 114
- [102] J Rose, A. *et al.*, *Architecture of Field-Programmable Gate Arrays*, *Proceedings of the IEEE* **81**, 1013 (1993). 92, 104
- [103] G. Heinzel *et al.*, *The LTP interferometer and Phasemeter*, *Class. Quantum Grav.* **21**, 581 (2004). 92, 104, 117
- [104] Marina Dehne *et al.*, *Laser interferometer for spaceborne mapping of the Earth's gravity field*, *Journal of Physics: Conference Series* **154**, 012023 (2009). 92, 175
- [105] P. Hidnert and H.S. Krider, *Thermal expansion of aluminum and some aluminum alloys*, *Journal of Research of the National Bureau of Standards* **48**, 209 (1952). 93
- [106] F Steier *et al.*, *The end-to-end testbed of the optical metrology system on-board LISA Pathfinder*, *Classical and Quantum Gravity* **26**, 094010 (2009). 93
- [107] Frank Steier, *Interferometry techniques for spaceborne gravitational wave detectors*, PhD Thesis, Leibniz Universität Hannover, (2008). 94
- [108] Bengt Edlén, *The Refractive Index of Air*, *Metrologia* **2**, 71 (1966). 106
- [109] J. Sanjuan *et al.*, *Thermal diagnostics front-end electronics for LISA Pathfinder*, *Review of Scientific Instruments* **78**, 104904 (2007). 108



- [110] M. Tröbs and G. Heinzel, *Improved spectrum estimation from digitized time series on a logarithmic frequency axis*, **39**, 120 (2006). 108
- [111] M. Tröbs and G. Heinzel, *Corrigendum to “Improved spectrum estimation from digitized time series on a logarithmic frequency axis” [Measurement 39 (2006) 120-129]*, **42**, 170 (2009). 108
- [112] J. Bogenstahl *et al.*, *LTP fibre injector qualification and status*, Journal of Physics: Conference Series **154**, 012011 (2009). 110
- [113] G. Wanner *et al.*, *Methods for simulating the readout of lengths and angles in laser interferometers with Gaussian beams*, Optics Communications (2012). 110
- [114] E. Morrison, B. J. Meers, D. I. Robertson and H. Ward, *Experimental demonstration of an automatic alignment system for optical interferometers and Automatic alignment of optical interferometers*, Appl. Opt. **33**, 5037 (1994). 110, 138
- [115] E. Morrison, B. J. Meers, D. I. Robertson and H. Ward, *Automatic alignment of optical interferometers*, Appl. Opt. **33**, 5041 (1994). 110
- [116] www.thorlabs.com. 112
- [117] V. Wand *et al.*, *Noise sources in the LTP heterodyne interferometer*, Classical and Quantum Gravity **23**, S159 (2006). 113
- [118] J. Noda, K. Okamoto and Y. Sasaki, *Polarization-maintaining fibers and their applications*, Lightwave Technology, Journal of **4**, 1071 (1986). 116
- [119] K. Mochizuki, Y. Namihira and Y. Ejiri, *Birefringence variation with temperature in elliptically clad single-mode fibers*, Appl. Opt. **21**, 4223 (1982). 116
- [120] F. Guzmán Cervantes *et al.*, *Subtraction of test mass angular noise in the LISA technology package interferometer*, Applied Physics B: Lasers and Optics **90**, 395 (2008). 124, 138
- [121] Personal communication with Ewan Fitzsimons. 124
- [122] C.-M. Wu and R. D. Deslattes, *Analytical modeling of the periodic non-linearity in heterodyne interferometry*, **37**, 6696 (1998). 126
- [123] R. Fleddermann *et al.*, *Successful demonstration of stray light subtraction in data post-processing for the LISA backlink fiber non-reciprocity experiment*, to be published in . 132

- [124] Michael Tröbs, *Laser development and characterization for the spaceborne interferometric gravitational wave detector LISA*, PhD Thesis, Leibniz Universität Hannover, (2005). 134
- [125] W.C. Lindsey and Chak Ming Chie, *A survey of digital phase-locked loops*, Proceedings of the IEEE **69**, 410 (1981). 151
- [126] B. Ware *et al.*, *Phase Measurement System for Inter-Spacecraft Laser Metrology*, Earth Science Technology Conference (2006). 151
- [127] M.R. Marcin, *Digital receiver phase meter for LISA*, Instrumentation and Measurement, IEEE Transactions on **54**, 2446 (2005). 151
- [128] R. J. Cruz *et al.*, *The LISA benchtop simulator at the University of Florida*, Classical and Quantum Gravity **23**, S751 (2006). 151
- [129] I. Bykov *et al.*, *LISA phasemeter development: Advanced prototyping*, Journal of Physics: Conference Series **154**, 012017 (2009). 151, 165
- [130] Juan José Esteban Delgado, *Laser ranging and data communication for the Laser Interferometer Space Antenna*, PhD Thesis, Leibniz Universität Hannover, (2012). 151, 152, 153, 164, 167
- [131] G. Ascheid and H. Meyr, *Cycle Slips in Phase-Locked Loops: A Tutorial Survey*, Communications, IEEE Transactions on **30**, 2228 (1982). 152
- [132] D. Hess, *Cycle Slipping in a First-Order Phase-Locked Loop*, Communication Technology, IEEE Transactions on **16**, 255 (1968).
- [133] D. Rytter and H. Meyr, *Theory of phase tracking systems of arbitrary order: Statistics of cycle slips and probability distribution of the state vector*, Information Theory, IEEE Transactions on **24**, 1 (1978). 152
- [134] D. Shaddock *et al.*, *Overview of the LISA Phasemeter*, Vol. 873 of *American Institute of Physics Conference Series*, Laser Interferometer Space Antenna: 6th International LISA Symposium **873**, (2006). 152, 164
- [135] O. Gerberding *et al.*, *LISA phasemeter core: Readout of a space-borne gravitational wave detector*, in preparation (2012). 152, 153
- [136] M. de Berg, M. van Kreveld, M. Overmars and O. Schwarzkopf, *Computational Geometry: Algorithms and Applications*, Second (Springer-Verlag, 2000), p. 367. 156
- [137] J. Fernández, B. Tóth, L. Cánovas and B. Pelegrín, *A practical algorithm for decomposing polygonal domains into convex polygons by diagonals*, TOP **16**, 367 (2008). 156

- [138] Zerodur<sup>®</sup> data sheet:, <http://www.schott.com>. 158
- [139] Nils Brause, *Bau und Test eines Phasenmeters*, Diploma thesis, Leibniz Universität Hannover, (2011). 165
- [140] P. L. Bender, J. L. Hall, J. Ye and W. M. Klipstein, *Satellite-Satellite Laser Links for Future Gravity Missions*, *Space Science Reviews* **108**, 377 (2003). 175
- [141] S. Nagano *et al.*, *Displacement measuring technique for satellite-to-satellite laser interferometer to determine Earth's gravity field*, *Measurement Science and Technology* **15**, 2406 (2004). 175
- [142] Hsien-Chi Yeh *et al.*, *Intersatellite laser ranging with homodyne optical phase locking for Space Advanced Gravity Measurements mission*, *Review of Scientific Instruments* **82**, (2011). 175, 177
- [143] H. B. Tu *et al.*, *Performance measurements of an inertial sensor with a two-stage controlled torsion pendulum*, *Classical and Quantum Gravity* **27**, (2010). 175
- [144] S. Ressel *et al.*, *Ultrastable assembly and integration technology for ground- and space-based optical systems*, *Appl. Opt.* **49**, (2010). 176
- [145] OptiMAIR data sheet:, <http://escoglobal.com/>. 177
- [146] JGS1, <http://www.newrise-llc.com/fused-silica.html>. 179
- [147] Ping Ge and Musa Jouaneh, *Modeling hysteresis in piezoceramic actuators*, *Precision Engineering* **17**, 211 (1995). 188
- [148] Ping Ge and Musa Jouaneh, *Tracking control of a piezoceramic actuator*, *Control Systems Technology*, *IEEE Transactions on* **4**, 209 (1996). 188
- [149] M. R. McCaleb, *A Conceptual Data Model of Datum Systems*, *J. Res. Natl. Inst. Stand. Technol.* **104**, 349 (1999). 199, 200
- [150] D. Flack, *Measurement Good Practice Guide N0. 41: CMM Measurement Strategies* (National Physical Laboratory, 2011), issue 2. 199, 200, 208
- [151] International Organization for Standardization, *Guide to the expression of uncertainty in measurement (GUM)-Supplement 1: Numerical methods for the propagation of distributions* (Geneva, 2004). 203
- [152] R.J. Hocken and P.H. Pereira, *Coordinate Measuring Machines and Systems*, Vol. Second Edition of *Manufacturing Engineering And Materials Processing* (CRC Press, 2012). 204, 207, 209, 210, 211

- [153] A. Weckenmann, M. Knauer and T. Killmaier, *Uncertainty of coordinate measurements on sheet-metal parts in the automotive industry*, Journal of Materials Processing Technology **115**, 9 (2001). 204
- [154] R.G. Wilhelm, R. Hocken and H. Schwenke, *Task Specific Uncertainty in Coordinate Measurement*, CIRP Annals - Manufacturing Technology **50**, 553 (2001). 204
- [155] B.N. Taylor and C. E. Kuyatt, *Guidelines for Evaluating and Expressing the Uncertainty of NIST Measurement Results*, NIST Technical Note **1297**, (1994). 204, 205
- [156] I. Lira and G. Cargill, *Uncertainty analysis of positional deviations of CNC machine tools*, Precision Engineering **28**, 232 (2004). 209, 210
- [157] Wolfgang Kessel, *Meßunsicherheit, ein wichtiges Element der Qualitätssicherung*, PTB Mitteilungen **108**, 377 (1998).
- [158] Wolfgang Kessel, *Measurement uncertainty according to ISO/BIPM-GUM*, Thermochemica Acta **382**, 1 (2002). 203
- [159] International Organisation for Standardisation, *ISO 10360-2:2009 Geometrical product specifications (GPS) – Acceptance and reverification tests for coordinate measuring machines (CMM) - Part 2: CMMs used for measuring linear dimensions*, 2009. 206
- [160] W. Weekers, *Compensation for Dynamic Errors of Coordinate Measuring Machines*, PhD Thesis, Technische Universiteit Eindhoven, 1996. 207
- [161] International Organisation for Standardisation, *ISO 1:2002: Geometrical Product Specifications (GPS) - Standard reference temperature for geometrical product specification and verification*, (2008). 208
- [162] S. Bell, *A Beginner's Guide to Uncertainty of Measurement, Measurement good practice guide No.11* (National Physical Laboratory, 2001). 209
- [163] International Organisation for Standardisation, *ISO/TR 16015:2003: Geometrical product specifications (GPS) – Systematic errors and contributions to measurement uncertainty of length measurement due to thermal influences*, (2010). 210

## List of publications

- [Dehne1] **M. Dehne**, M. Tröbs, G. Heinzel and K. Danzmann, *Verification of polarising optics for the LISA optical bench*, Optics Express, **20**, 25, (2012).
- [Dehne2] **M. Dehne**, M. Sommerfeld, M. Tröbs, G. Heinzel and K. Danzmann, *Building an ultra-stable optical bench for testing polarising optics in interferometry*, to be published in Journal of Physics: Conference Series, 1<sup>st</sup> quarter of 2013.
- [Dehne3] **M. Dehne**, F. Guzmán Cervantes, B. Sheard, G- Heinzel, K. Danzmann, *Laser interferometer for spaceborne mapping of the Earth's gravity field*, Journal of Physics: Conference Series **154**, 012023 (2009)
- [Sheard] B. Sheard, **M. Dehne**, O. Gerberding, H. Heinzel, C. Mahrtdt, V. Müller, and K. Danzmann, *Laser interferometry for future satellite gravimetry missions*, GEOTECHNOLOGIEN Science Report **17**, 160 (2010).
- [Meier] T. Meier, B. Willke, **M. Dehne** and K. Danzmann, *Investigation of the Self-Injection Locked Behaviour of a Continuous Wave Nd:YAG Ring Laser* in Conference on Lasers and Electro-Optics/International Quantum Electronics Conference (Optical Society of America), 2009.
- [Arcio] L. d'Arcio, J. Bogenstahl, **M. Dehne**, C. Diekmann, E. D. Fitzsimons, R. Fleddermann, E. Granova, G. Heinzel, H. Hogenhuis, C. J. Killow, M. Perreur-Lloyd, J. Pijenburg, D. I. Robertson, A. Shoda, A. Sohmer, A. Taylor, M. Tröbs, G. Wanner, H. Ward, D. Weise, *Testing the LISA optical bench*, ICSO conference proceedings (9-12 October 2011).
- [Heinzel] G. Heinzel, B. Sheard, N. Brause, K. Danzmann, **M. Dehne**, O. Gerberding, C. Mahrtdt, V. Müller, D. Schütze, G. Stede, W. Klippstein, W. Folkner, R. Spero, K. Nicklaus, P. Gath, D. Shaddock, *Laser Ranging Interferometer for GRACE follow-on*, ICSO conference proceedings (9-12 October 2011).

---

## Project documents

---

- [PD1] **M. Dehne**, G. Heinzel, *Building an ultra-stable optical bench by applying the hydroxide-catalysis bonding technique*, AEI-HUST-TN-01.3, 2012
- [PD2] M. Tröbs, J. Bogenstahl, **M. Dehne**, C. Diekmann, E. Granova, A. Shoda, G. Wanner, G. Heinzel, *Test of interferometry concept*, LOB-AEI-TN-5.1, 2010
- [PD3] **M. Dehne**, C. Diekmann, E. Fitzsimons, R. Fleddermann, G. Heinzel, C. Killow, J. Pijnenburg, M. Tröbs, M. Vogt, D. Weise, *Prototypes Description, Design and Test Plan*, LOB-ASD-TN-4-13, 2010

# Acknowledgements

There are many people to whom I am very much indebted and it is a pleasure to express my gratitude towards them here. First of all, I want to thank Karsten Danzmann for his crucial support and encouragement. He gave me the opportunity to be part of his institute with an overwhelming atmosphere, and I am truly grateful to him for this.

Secondly, I would like to thank Gerhard Heinzl for supervising this thesis and thus allowing me to learn from him. I am enormously indebted to him for all the support and good advice he gave, including all the times he pulled me through the difficulties of programming in particular IfoCad. I appreciate his vast knowledge of physics and electronics. His influence is strongly reflected in this work. Gerhard, I am grateful in every possible way and hope to keep up our collaboration in the future.

I thank Christian Ospelkaus for agreeing to serve as the second referee to this thesis and Jakob Flury to chair my thesis defence. Thank you for taking time out from your busy schedule!

A very special thanks goes out to Hsien-Chi Yeh for giving me the opportunity to work in his friendly group in Wuhan. For creating a pleasant working atmosphere I truly thank Lù Ying Xin, Duan Huizong and Li hong Yin. During both times in China I was honoured to meet very warm and gentle people who made my stay a nice residence. In particular Xuefei Gong, Gao Wei, Yang Ran, Yan-Zheng Bai, Liang Yurong and Lau Riunqiu. I appreciate Albrecht Rüdiger's time to give me a great many of helpful hints about China. Xiè xie!

This acknowledgement will be incomplete without mentioning the AEI secretary (Kirsten Labove, Brigitte Gehrman and colleagues), the IT (Konrad Mors and colleagues), Karl-Heinz Zwick-Meinheit for having always an open door if questions arose from vacuum systems or Clean room related stuff, the electronic workshop (Heiko zur Mühlen, Andreas Weidner and Philipp Kormann), and finally the mechanic workshop team (Jan Diedrich, Philipp Schauzu and colleagues) without your efforts and hard work most of my experiments could not have been performed. You guys rock!

An honourable mention goes to my office mates past and present: Paul Cochrane, Roland Fleddermann, Ben Sheard and Christoph Mahrtdt. You guys have always been a source of entertainment and discussions on a variety of subjects. In particular I would like to thank Christoph for all discussions from physics to nature and being my conference and hiking mate.

Likewise, I thank Martin Sommerfeld for being a cheerful friend during the countless shifts in the clean room and for calming me down if the CMM operated unexpected. Tschakka! In the same manner I thank Oliver Gerberding and Nils Brause for providing me the phasemeters I needed to perform my last experiment.

I am obliged to many of my colleagues who supported me and proof-read this thesis. They are, in alphabetical order: Albrecht Rüdiger, Ben Sheard, Christian Diekmann, Christoph Mahrtdt, Gerhard Heinzl, Heather Audley, Henning Kaufer, Katrin Dahl, Markus Otto, Michael Britzger, Michael Tröbs and Oliver Gerberding. Thank you for using your precious time to read this thesis!

An undertaking such as a PhD is greatly alleviated if one can rely on friends and family and thus I warmly thank my parents and my sister as well as the Kaufer family for continued support. Finally, I thank Henning for his benign attitude towards being ignored for the last 5 months whilst I was writing. I would not have made it without you!

**Thanks all of you for making these past few years unforgettable!**



# CURRICULUM VITAE

---

## Personal informations

Name Marina Lamprini Dehne  
Nationality German and Greek  
Date of birth 25.05.1981  
Place of birth Hannover, Germany  
Family status unmarried

## School Education

08/1987 - 07/1991 Grundschule, Hannover  
08/1991 - 05/1993 Orientierungsstufe, Hannover  
06/1992 - 07/2000 Gymnasium (Abitur), Hannover  
08/1987 - 05/1995 Grundschule Meterstraße & Gymnasium, Hannover  
(griechischer Unterricht)

## University Education

10/2000 - 02/2007 Studies of physics at the Leibniz Universität Hannover,  
Graduate with Diploma  
Diploma Thesis *Untersuchungen zum Self-Injection-Locking eines Hochlei-  
stungs-Ringlasers*  
04/2007 - 11/2012 Doctoral studies at the Albert-Einstein Institute in Hannover  
10/2011 - 11/2011 Visiting scientist at the Huazhong University of Science  
and Technology (HUST) in China

